RECHARGE QUANTIFICATION AND CONTINENTAL FRESHWATER LENS DYNAMICS IN ARID REGIONS:

APPLICATION TO THE MERTI AQUIFER (EASTERN KENYA)

PhD thesis presented at the Centre for Hydrogeology
and Geothermics of the University of Neuchâtel

For the degree of

Doctor in Science

by

Lucien Blandenier

Defended on September 2, 2015

Accepted by the following Jury:

Prof. Pierre Perrochet, director, Université de Neuchâtel
Dr Ellen Milnes, co-director, Université de Neuchâtel
Prof. Philip Brunner, co-director, Université de Neuchâtel
Prof. Rachida Bouhlila, Ecole Nationale d'Ingénieurs de Tunis
Prof. André Mermoud, Ecole Polytechnique Fédérale de Lausanne

UNIVERSITÉ DE
NEUCHÂTEL

Faculté des sciences
Secrétariat-décanat de Faculté
Rue Emile-Argand 11
2000 Neuchâtel - Suisse
Tél: + 41 (0)32 718 2100
E-mail: secretariat.sciences@unine.ch

IMPRIMATUR POUR THESE DE DOCTORAT

**La Faculté des sciences de l'Université de Neuchâtel
autorise l'impression de la présente thèse soutenue par**

Monsieur Lucien Blandenier

Titre:

"Recharge quantification and continental freshwater lens dynamics in arid regions: application to the Merti aquifer (eastern Kenya)"

sur le rapport des membres du jury composé comme suit:

- Prof. Pierre Perrochet, Université de Neuchâtel, directeur de thèse
- Prof. Philip Brunner, Université de Neuchâtel, co-directeur de thèse
- Dr Ellen Milnes, Université de Neuchâtel, co-directrice de thèse
- Prof. Rachida Bouhlila, Ecole Nationale d'Ingénieurs de Tunis, Tunisie
- Prof. André Mermoud, Ecole Polytechnique Fédérale de Lausanne, Suisse

Neuchâtel, le 16 novembre 2015 Le Doyen, Prof. B. Colbois

B. Colbois.

Abstract

The Dadaab refugee camp, the largest refugee camp in the world with a population of approximately 400’000 persons, is located in the arid to semi-arid eastern Kenya, close to the Somali border. The only permanent water resource for the refugees and the host communities comes from the Merti aquifer which consists in a large continental freshwater lens of 250 km by 50 km surrounded by salty water. The increasing groundwater abstractions as well as signs of increasing salinity and uncertainty on the water level depletion led to the necessity to better characterise the aquifer recharge and the dynamics between the freshwater lens and the surrounding salty water.

Firstly, a new methodology was developed for quantifying the concentrated groundwater recharge through a physically-based coupled surface/groundwater numerical model reproducing inundated surfaces during flood events which is calibrated with inundated surfaces derived from satellite images. Secondly, the dynamics of freshwater lenses are investigated with a series of synthetic numerical models. These models aim to analyse the effect of the recharge rates and mechanisms (rainfall, concentrated recharge) on the freshwater lens geometries and to compare these geometries with the observed geometry of the freshwater lens of the Merti aquifer. These two approaches are cross-validated owing to a groundwater monitoring network of twenty high time-resolution devices installed over the whole freshwater lens in September 2013. Finally, results from these three axes are combined in a regional numerical model.

The approaches developed in this study allowed to quantify a concentrated groundwater recharge to be between 195 and 329 x 10^6 m^3/y. Diffuse recharge contributing to the freshwater lens is estimated to be between 12 and 62 x 10^6 m^3/y. Compared to these recharge rates, the current groundwater extraction (about 4.8 x 10^6 m^3/y), is considered as sustainable on the regional scale. However, this recharge is about 50 to 100 higher than the axial flow estimated with the gradient and the transmissivities obtained with pumping tests. This discrepancy led to postulate the presence of a multi-layer aquifer much thicker than the currently exploited horizon but with uncertainties on its thickness and the vertical salinity gradient.

The synthetic numerical model revealed a very high inertia of the Merti aquifer and confirmed that the recharge of the aquifer is mainly controlled by concentrated recharge on flood plains in the upstream area of the freshwater lens. The high inertia of the aquifer is consistent with the very small groundwater level and electrical conductivity variations observed with the monitoring network.

As conclusion, this work opens new perspectives for the quantification of groundwater recharge in arid to semi-arid areas occurring during large scale flood events. However, it also showed the necessity to continue the monitoring of the aquifer and to carry out further investigations on the aquifer thickness if further exploitations are foreseen.

Résumé

Avec une population de près de 400'000 personnes, le camp de réfugiés de Dadaab est le plus grand au monde. Il est situé dans la région semi-aride de l'est du Kenya, proche de la frontière somalienne. L'unique ressource permanente en eau potable pour les réfugiés et les communautés locales provient de l'aquifère de Merti, qui consiste en une large lentille d'eau douce souterraine de 250 km sur 50 km, et qui est entourée par de l'eau salée. L'augmentation des volumes pompés, des signes d'augmentation de la salinité de l'eau et l'incertitude sur la diminution du niveau de l'eau souterraine ont fait prendre conscience du risque d'épuisement de la ressource. Ces observations ont abouti à la nécessité de mieux caractériser la recharge de l'aquifère ainsi que la dynamique entre la lentille d'eau douce et l'eau salée environnante.

Dans un premier temps, une nouvelle méthodologie a été développée pour quantifier la recharge concentrée à travers un modèle numérique, basé sur la physique des écoulements, couplant l'eau souterraine et l'eau de surface. Ce modèle a eu pour but de reproduire les surfaces inondées durant les crues et a été calibré à l'aide d'images satellites. Deuxièmement, la dynamique de la lentille d'eau douce a été investiguée par une série de modèles numériques synthétiques. Ces modèles ont permis d'analyser les effets des taux de recharge et leurs mécanismes (pluie, recharge concentrée) sur la géométrie de la lentille et de comparer ces géométries simulées avec la géométrie réelle de la lentille de l'aquifère de Merti. Ces deux approches ont été contre-validées à l'aide d'un réseau de monitoring de l'eau souterraine composé de vingt stations de mesures à haute résolution temporelle (15 min), installé sur toute la lentille en septembre 2013. Finalement, les résultats de ces trois axes de recherche ont été combinés dans un modèle numérique régional.

L'approche développée dans cette étude a permis de quantifier une recharge concentrée entre 195 et 329 x 10^6 m^3/a. La recharge diffuse sur la lentille d'eau douce est quant à elle estimée entre 12 et 62 x 10^6 m^3/a. Comparée à ces taux de recharge, l'extraction courante de l'eau souterraine (environ 4.8 x 10^6 m^3/a) est considérée comme durable à l'échelle de l'aquifère. Cependant, la recharge totale est environ 50 à 100 fois plus grande que l'inféroflux traversant le niveau exploité, calculé à l'aide du gradient hydraulique de l'aquifère et des valeurs de transmissivité issues des essais de pompage. Cet écart a mené à postuler la présence d'un aquifère multi-couche considérablement plus épais qu'uniquement l'horizon couramment exploité, mais avec une importante incertitude sur son épaisseur et sur le gradient vertical de salinité entre la lentille d'eau douce et l'eau salée sous-jacente.

Les modèles numériques ont révélé la très grande inertie de l'aquifère et ont également confirmé que la recharge a principalement lieu de manière concentrée lors des évènements de crue, juste en amont de la lentille d'eau douce. La grande inertie de l'aquifère est cohérente avec les faibles variations des niveaux d'eau et de la conductivité électrique (salinité) observées avec le réseau de monitoring.

En conclusion, ce travail ouvre de nouvelles perspectives pour la quantification de la recharge en milieu aride à semi-aride lors d'évènements de crue. Il a également permis de mettre en avant la nécessité de poursuivre le monitoring de l'aquifère et de mener de nouvelles investigations sur l'épaisseur de l'aquifère afin de confirmer les résultats de la recharge.

Executive summary

This executive summary presents the main results and recommendations of the PhD study "Recharge quantification and continental freshwater lens dynamics in arid regions: application to the Merti aquifer (Eastern Kenya)", which was conducted at the Center for Hydrogeology of the University of Neuchâtel (Switzerland), financed by the Swiss Agency for Development and Collaboration (SDC) and in collaboration with the United Nation High Commissioner for Refugee (UNHCR). This study aimed to assess the sustainability of the exploitation of the Merti aquifer that is the only permanent freshwater resource of the Dadaab refugee camp, the largest refugee camp in the world with a population varying between 350'000 and 450'000 persons. The increase of the camp population since its settlement in the early 1990s and the related increasing groundwater abstractions led to the concern of groundwater level depletion and risk of salinization.

The particular hydrogeological setting of the Merti aquifer is characterised by the combination of the vast aquifer size, the semi-arid to arid conditions and the interplay between fresh water surrounded by brackish-salty groundwater. Moreover, the hydrology of the basin is characterised by major periodic inundations caused by the intermittent Ewaso Ng'Iro River. In the past, these inundations led to the formation of a swamp, the so-called Lorian Swamp, located at the end of the permanent path of the Ewaso Ng'Iro River and directly upstream of the freshwater lens. Nowadays, this area is not anymore permanently wet but the recurrent inundations are still supposed to play a major role for the groundwater recharge.

The geological and hydrogeological characterisation of the aquifer was carried out through the analysis of geological maps, boreholes logs, hydrodynamical data obtained from pumping tests and groundwater levels as well as electrical conductivity data from historical data and from a monitoring network of 20 devices installed within the framework of this project. The analysis of the geology allowed to define the geometry of the aquifer, which is located within a large Miocene sedimentary basin, composed of a succession of coarse and fine layers of sediments (Fig. 1). The granulometry and the hydraulic conductivity of the sediments diminish towards the border of the basin. The freshwater lens develops in the central zone with high hydraulic conductivities.

The main focus of this study was to develop a new methodology for quantifying the concentrated groundwater recharge under the Lorian Swamp through a physically-based coupled surface/groundwater numerical model reproducing inundated surfaces during flood events and which was calibrated with inundated surfaces derived from satellite images. This methodology allowed to quantify an average annual concentrated groundwater recharge between 195 and 329 x 10^6 m^3/y. The diffuse recharge was estimated between 12 and 62 x 10^6 m^3/y, yielding a total recharge ranging between 207 and 391 x 10^6 m^3/y.

These results pointed out a discrepancy between literature values of recharge, the transmissivity measured by pumping tests and the transmissivity required to accommodate the estimated recharge, which is about 50 to 100 higher than estimations of the groundwater flow through the exploited aquifer horizon (the Merti beds). This led to the hypothesis that the Merti aquifer is an aquifer system composed of numerous water bearing horizons located within the coarse-sedimentary succession, of which only the first horizon (the so-called Merti beds) is currently exploited.

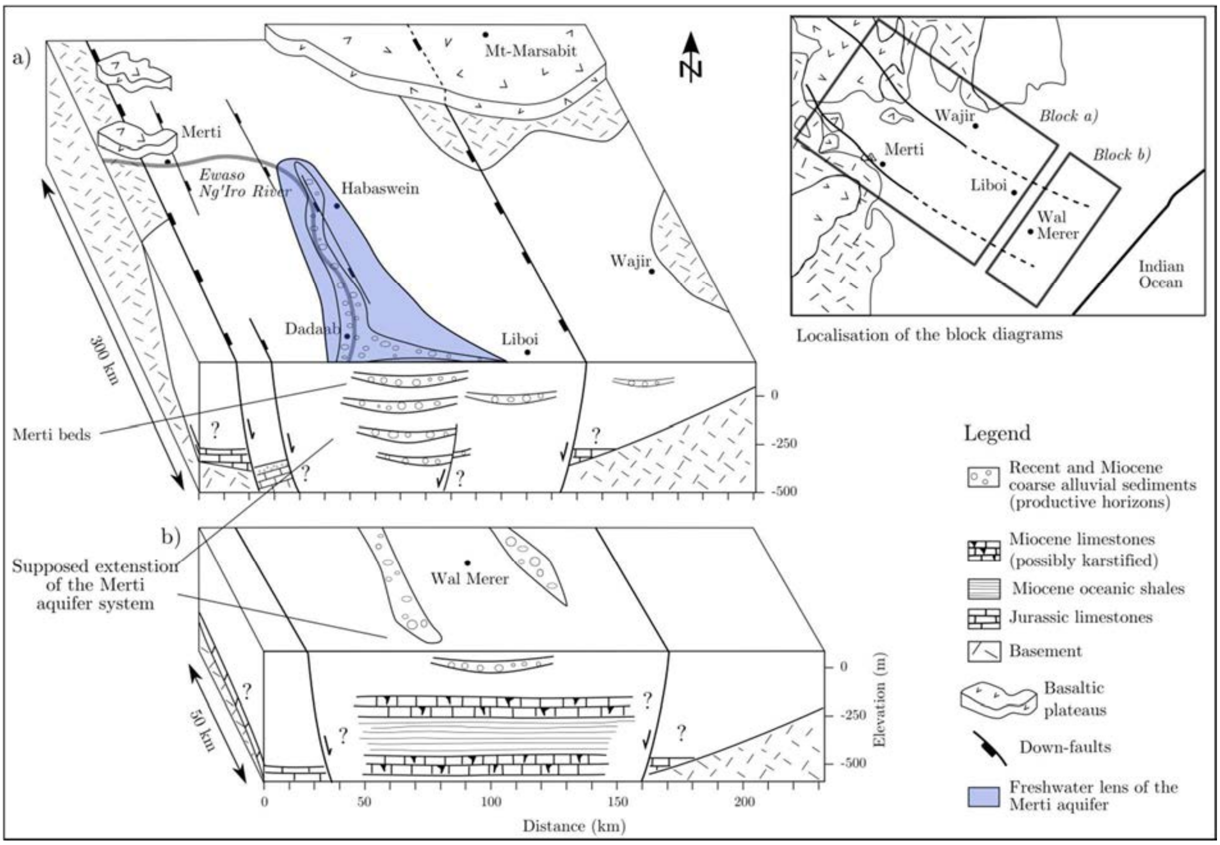

Fig. 1: Conceptual geological model of the Merti aquifer. The basin is delimitated at its border by normal faults and, in some places, by tilted blocks associated to the rifting of the Anza basin. Successive coarse horizons are likely to be found at several depths (block a). Within the lower part of the aquifer, Miocene limestones separated from marine shales are present at a depth of 250 and 500 m (block b). Beyond the limit of the graben, the basement is covered by only few tens or hundreds meters of sediments. Coarse sediments dominate within the center of the basin while the fine sediments proportion increases towards the border of the basin.

In order to cross-validate these recharge rates, a second approach was adopted, investigating the dynamics of a freshwater lens in response to such recharge rates. This was done with a series of numerical models. These models aimed to analyse the effect of the recharge rates and mechanisms (rainfall, concentrated recharge) on the freshwater lens geometries and to compare these geometries with the observed geometry of the freshwater lens of the Merti aquifer. This approach confirmed of the concentrated recharge as the predominant recharge mechanism, being more than 80 % of the total recharge.

Thus, the recharge results and the proposed aquifer system suggest that deeper horizons may contain fresh to brackish groundwater (Fig. 2) below the Merti beds. However, the depth of the transition between the fresh and brackish water remains unknown since no deep water prospection has been done in the area.

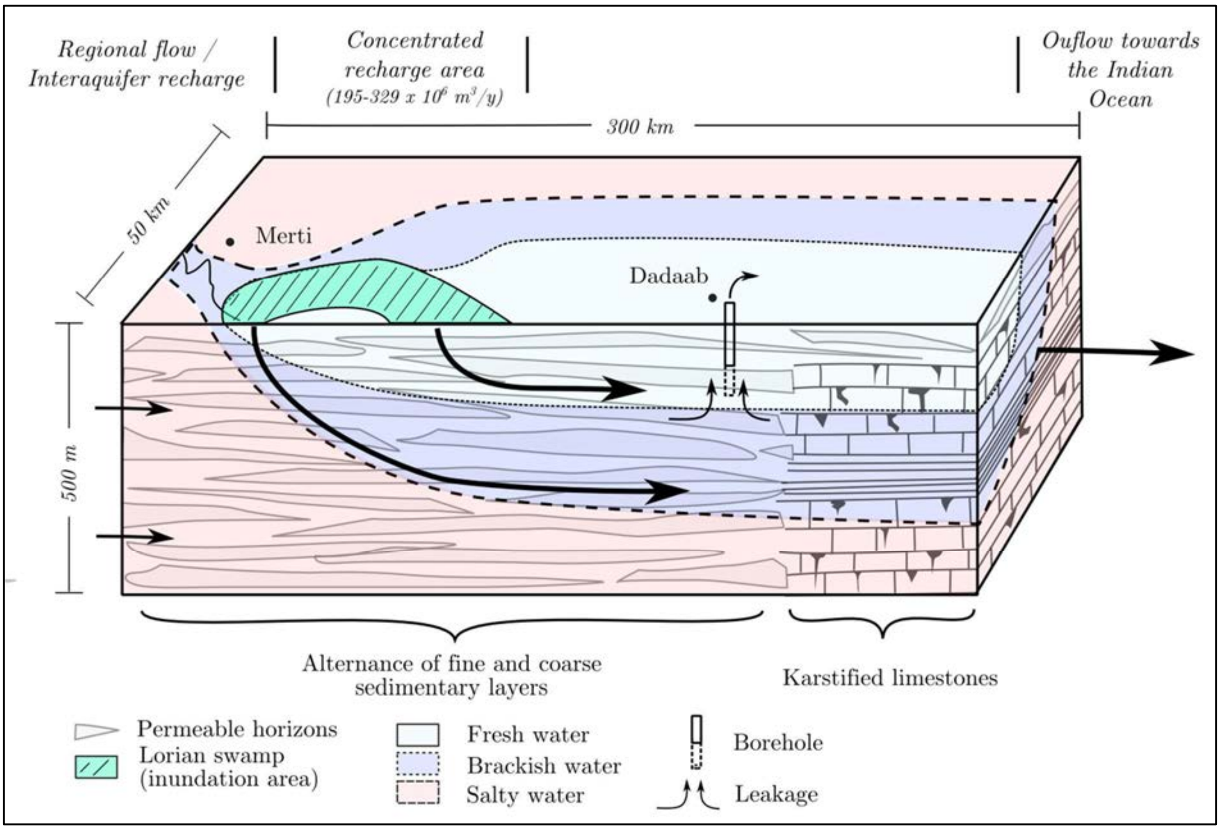

Fig. 2: Conceptual model of the Merti aquifer system. The Merti aquifer consists in a succession of fine and coarse sedimentary layers, where the Merti beds are only the upstream uppermost. Freshwater recharge occurs mainly as concentrated recharge over the Lorian Swamp area (between 195 and 329 x 10^6 m^3/y). From this location, the freshwater lens develops in width and thickness. Part of this freshwater recharge is diluted with the surrounding brackish and salty water. Diffuse recharge over the freshwater lens ranges between 12 and 62 x 10^6 m^3/y.

The very stable water levels and electrical conductivity values measured through the groundwater monitoring support the hypothesis of deeper freshwater bearing horizons which act as a “buffer” between the exploited horizon (the Merti beds) and the deeper brackish/saline water. Thus, the possibility of contamination of the wells by upconing of saline water from the underlying layers of the aquifer system is reduced due to the probable presence of the fresh water between the Merti beds and the underlying saline/brackish water. Furthermore, the numerical modelling carried in this study showed that the risk of migration of saline water from the lateral saline zones is insignificant on the regional scale.

However, locally, especially close to the border of the freshwater lens, as in Hagadera (south of Dadaab), signs of salinity increase were observed (up to 100 µS/cm during a period of few years), which requires to carefully consider the salinity evolution. These increases remain low and electrical conductivities of these boreholes remain below the value of 2'000 µS/cm, which is the limit considered for potable water.

Considering only the Merti beds, groundwater axial flow is estimated to be 5 to 8 x 10^6 m^3/y. Comparing this to the 4.8 x 10^6 m^3/y of extractions shows that the upper limit of exploitation of the Merti beds has been reached and calls for careful monitoring.

Hence, in order to investigate the potential of the underlying freshwater resources, it was recommended to drill deep exploration boreholes (350 m), in the upstream area, close to the Lorian Swamp, as well as in the area of refugee camp. Such boreholes would allow to better evaluate the available freshwater resource and the risk of contamination of the boreholes by upconing of saline water. Additionally, it would also allow to confirm the estimation of the groundwater recharge by estimating the flow of freshwater through the entire aquifer system and not only through the Merti beds.

Since groundwater salinity along the edges of the freshwater is the higher, it is recommended to maintain the groundwater monitoring network. This data is essential for the understanding of the groundwater dynamics but also to identify precursory signs of rapid salinity increase and to adapt the groundwater extraction strategy. If the groundwater extraction should be increased at the refugee camps, then it is recommended to increase extraction in the area of the central freshwater lens (Dagahaley and Ifo) and not in Hagadera.

Finally, an extension of the monitoring network over the concentrated recharge area (the Lorian Swamp) may allow to better understand and quantify the recharge mechanism of the aquifer, and thus, its sustainability. Such monitoring networks are also a valuable tool for technicians in charge of the day-to-day exploitation of the wells, for instance for the monitoring of the pumping duration or the identification of well degradation (e.g. clogging).

Keywords

Groundwater, Recharge, Arid areas, Remote sensing, Numerical modelling, Continental freshwater lens, Monitoring, Flooding.

Acknowledgements

The acknowledgments are usually the last words written in the manuscript of the PhD. It's the opportunity for me to remember the various steps of this work and the people who supported me during these four years.

This project was an incredibly rich scientific, professional and human adventure which allowed me to meet fascinating people in the domain of humanitarian aid and hydrogeology, to discover the context of the refugee camps (or at least part of it!) and work in the spectacular landscape and environment of the Turkana region, in the north of Kenya. So, for all this, I would like to sincerely thank all the people who have made this project possible and who accompanied and supported me during this experience.

First of all, I want to thank Ellen Milnes, my co-director, who invested for the elaboration and realisation of this project who proposed me to join this adventure. Thank you also to Philip Brunner and Pierre Perrochet, my two other supervisors. I would like to define their support and accompanying with the following words: creativity, encouragement, scientific rigor and endless enthusiasm!

Thanks also to the institutions that founded and supported this project: the Swiss Humanitarian Aid (SHA) and the United Nations High Commissioner for Refugees (UNHCR). In particular, I want to thank Marc-André Bünzli, the Head of the Expert Group WES, for his great interest on this study and his very constructive and relevant inputs, as well as Dominique Porteaud, Murray Burt and Claudia Perlongo, Heads of the WASH department at the UNHCR in Geneva, who guided me within the twists and turns of the UN administration and made the challenging field work of this thesis possible.

I also want to thank the members of the jury and the scientific committee of this thesis: Cédric Egger, Olivier Senegas, Yves Haeberlin, Rachida Bouhlila and André Mermoud.

I also express my gratitude to all those who supported the field side of this project in Nairobi, Dadaab, Kakuma and Auvernier: Andrea Cippà, Patrick Galli, Christel Dischinger, Patrick D'Aoust, Bernard Chamoux, Kebede Asegedew, Osman Ahmed, Matthew Binyiri, Jecinta Mwongeli, Dominic Gachanja, and the staff from the Earth-Water company as well as Thierry Schneider and Christine Koch from the Tetraedre company in Auvernier. A particular thought goes to Jonathan with whom I spent 7 weeks in the refugee camp of Kakuma.

This PhD was also an enriching period at the Center for Hydrogeology of the University of Neuchâtel. Many thanks to my PhD colleagues, Post-docs, senior lecturers for the numerous discussions, sharing of experiences, helping hands and the nice moments. Particular thanks to Cécile, Claire, Greg, Lorienne, the two Guillaume, Andrea, Dom, Pierik, Paco, Jaouhar, Fabio, Fabien, Oli, Léa and Nico. Of course, without forgetting Roberto, our dream technician!

Finally, before entering in the core of this study, I let the reader enjoy some pictures from Pierik from the Kakuma field campaign of October – November 2012.


KING'S
COLLECTION


ALPHA TAILORING
AFRICAN DRESSMAKING
ALL FASHION
ARMANI KINYOZI
FOIX ZERO
DRC

Contents

Chapter 1

Introduction

1.1 Background

Over the past decades, armed conflicts combined with harsh arid climatic conditions in the Horn of Africa have led to internal displacement and migration of populations. As an example of such migration, the civil war in Somalia led to the creation of the Dadaab refugee camp in the early 1990s. This camp is located in eastern Kenya, close to the Somali border. Initially, the Dadaab camp was planned to host up to 90'000 refugees as an emergency solution.

In 2004, however, 150'000 refugees were hosted in the now semi-permanent camp. The population increase accelerated dramatically to 465'000 refugees in 2011 due to the devastating drought (www.data.unhcr.org), Dadaab becoming the biggest refugee camp in the world. Its actual population varies between 350'000 and 450'000 refugees, distributed into five sub-camps: Dagahaley, Ifo, Ifo 2, Hagadera and Kambioos, Dadaab being the village hosting the UNHCR and NGOs staff (Fig. 1.1).

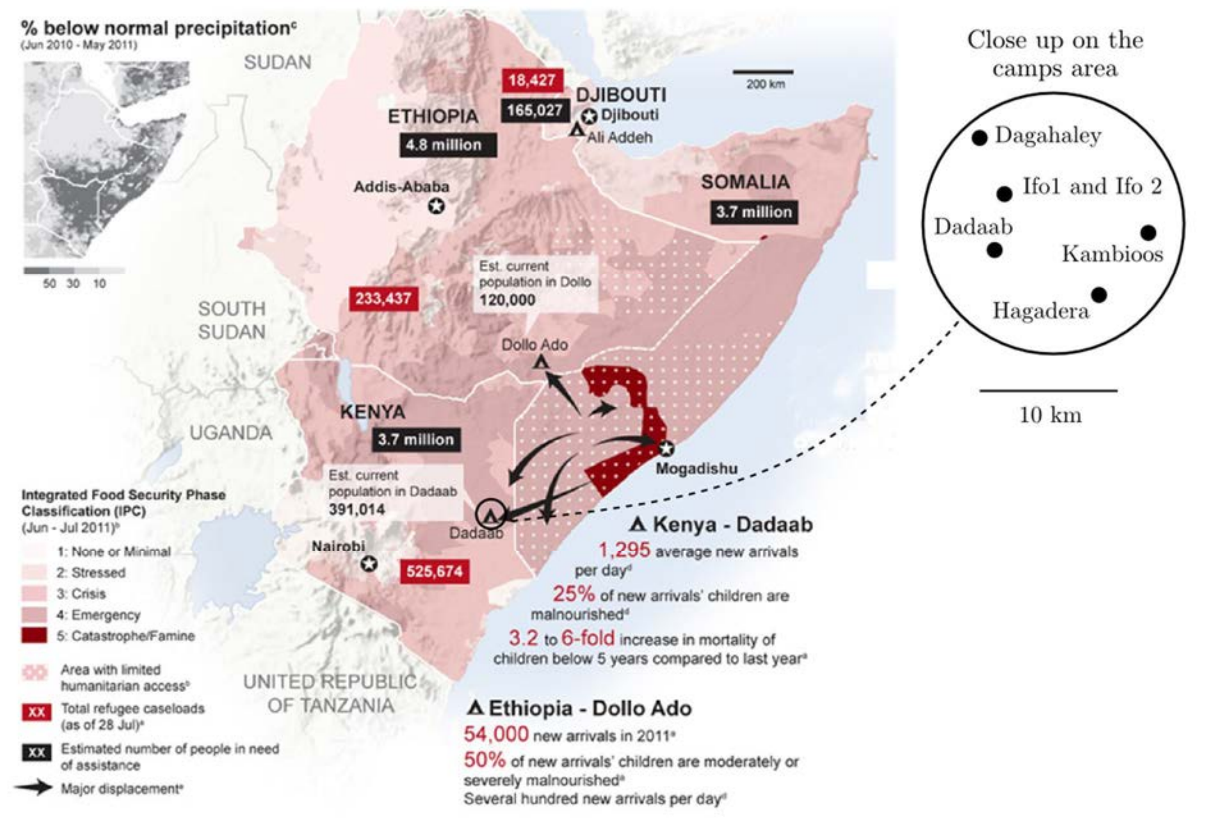

Fig. 1.1 : Humanitarian crisis situation in the Horn of Africa at the beginning of the project, in 2011. Food security classification and major displacement (OCHA, 2011, http://www.unfpa.org). The Dadaab refugee camp is located close to the Somali border and is subdivided into five camps (Dagahaley, Ifo, Ifo2, Hagadera, Kambioos) plus Dadaab that hosts the UNHCR and NGOs staff.

Humanitarian crises led to innumerable challenges for authorities, host communities and humanitarian actors, but also for applied research. One of these challenges and a key component of public health is water supply: both the necessary quantity and quality of water have to be guaranteed. In the case of Dadaab, where water supply entirely relies upon groundwater exploited from the so-called Merti aquifer, at a depth of 150 m, ensure both quantity and quality of water is crucial.

The critical growth of the Dadaab refugee camps combined with the transition towards semi-permanent settlement led to conflict situations with the host community, the latter accusing the refugee operation of depleting the groundwater reserves. As a result, the importance of assessing the sustainability of groundwater management within this changing demographic context became clear, for which an extensive hydrogeological study was necessary.

The Swiss government released substantial funds during the 2011 crisis in order to address the water scarcity issue in the Horn of Africa, while UNHCR invested in a novel groundwater monitoring system, providing the required ground data for the understanding of hydrogeological processes. The present PhD thesis is a joint outcome of the 2011 emergency funding by the Swiss development cooperation (SDC) and the United Nation High Commissioner for refugees (UNHCR), and was carried out at the Center for Hydrogeology of the University of Neuchâtel (CHYN).

The particular hydrogeological setting of the Merti aquifer is characterised by the combination of the vast aquifer size, the semi-arid to arid conditions and the interplay between fresh and brackish groundwater. Moreover, the hydrology of the basin is characterised by major periodic inundations caused by the intermittent Ewaso Ng'Iro River, which drains a large catchment north of Mt-Kenya (Fig. 1.2). In the past, these inundations led to the formation of a swamp, the so-called Lorian Swamp, located at the end of the permanent path of the Ewaso Ng'Iro River and directly upstream of the freshwater lens. Nowadays, this area is not anymore permanently wet but the recurrent inundations are still supposed to play a major role for the groundwater recharge.

Similar hydrogeological and hydrological environments can be found all around the sub-Saharan region or in other arid/semi-arid regions, and are so far not well understood, neither the processes of groundwater recharge, nor the evolution and dynamics of the freshwater lenses.

The work which forms the basis for the present thesis was carried out against this general backcloth and attempts to make a contribution towards developing a comprehensive approach allowing quantification of recharge processes in continental mega-aquifers in semi-arid/arid regions and towards a better understanding of the dynamics of freshwater lenses in continental context. It uses the Merti aquifer and Dadaab as a case-study.

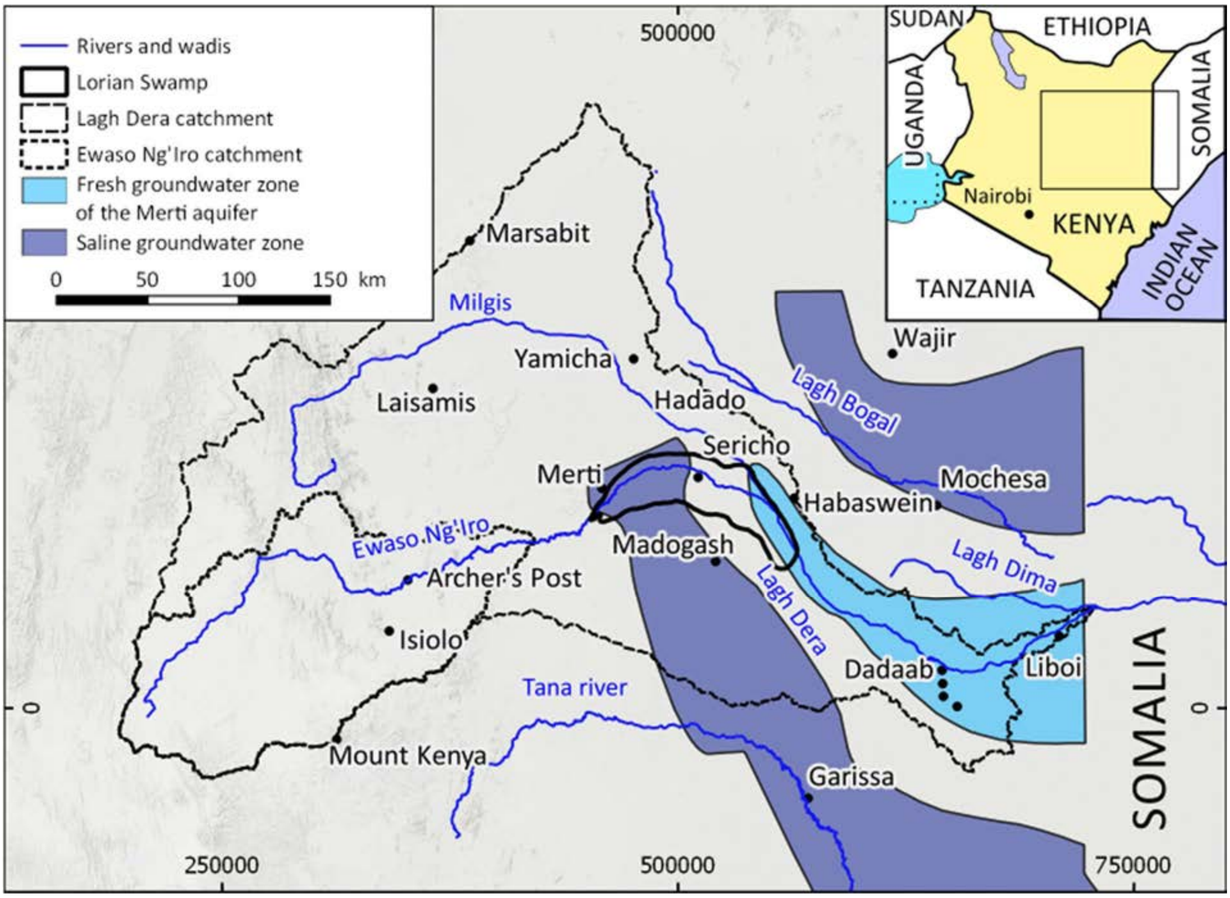

Fig. 1.2: Map of the Merti aquifer, showing the fresh and the saline groundwater domains in light and dark blue, respectively (modified after Swarzenski and Mundorff, 1977). The recurrent inundations of the Ewaso Ng'Iro River over the Lorian Swamp are supposed to play a major role for the groundwater recharge of the Merti aquifer.

1.2 Recharge in arid and semi-arid areas – the need for a coupled surface/groundwater approach

Despite scarcity of surface water in arid to semi-arid areas, surface and groundwater flow are closely linked: groundwater flow is constrained by the geology of the aquifer, but also by the recharge from the surface water. Dynamics of recharge from the surface is complex. Surface water infiltrates into the subsurface. Part of the infiltrated water then percolates deeper toward the aquifer and constitutes the recharge. The other part of the infiltrated water is evapotranspired back to the atmosphere.

Additionally to migration of water from the surface to the groundwater, the processes of diffuse and concentrated recharge have to be distinguished (Fig. 1.3). Diffuse recharge includes areal distributed recharge from rainfall or irrigation while concentrated recharge (also called focussed, localised or indirect recharge (Lerner, 1997)) refers to recharge under water surface accumulations such as rivers, lakes or inundated plains (Scanlon et al., 2006).

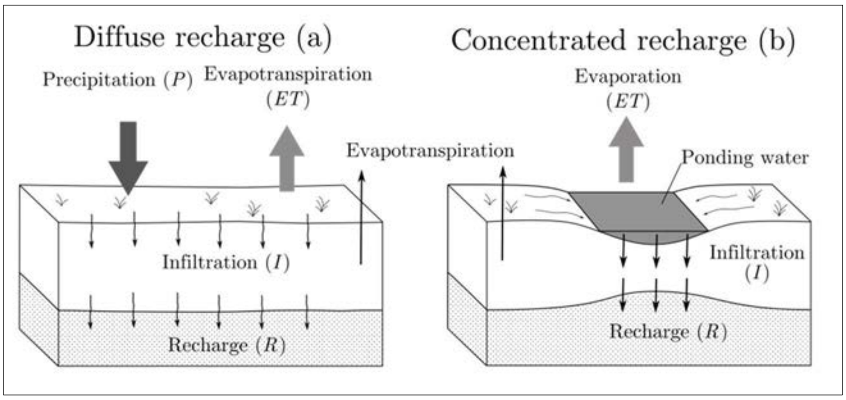

Fig. 1.3: Schematic model for diffuse recharge (a) and concentrated recharge (b)

Numerous methods have been developed in order to quantify these processes, in particular in arid and semi-arid areas where quantification of groundwater recharge is crucial for assessing the groundwater sustainability. These methods allow the estimation of recharge by investigating the surface-water dynamics, the unsaturated zone or the saturated zone, using various techniques such as chemical tracers, physical techniques, or numerical modelling (Scanlon et al., 2002; Shanafield and Cook, 2014).

Groundwater recharge based on surface-water data is commonly estimated using a simple water budget (e.g. Lerner 1997):

$$R = Q_{up} - Q_{down} + \sum Q_{in} - \sum Q_{out} - E_a - \frac{\Delta S}{\Delta t} \qquad (1.1)$$

where R is recharge rate, Q_{up} and Q_{down} are flows at the upstream and downstream ends of the considered section, Q_{in} and Q_{out} refer to tributary inflows and outflows along the reach and E_a is the evaporation from surface water and stream bed, and ΔS is change in channel and unsaturated-zone storage over change in time Δt.

Numerous analytical and numerical flood-routing models based on this general equation have been developed, using water discharge rates at gauging stations (Jordan, 1977; Lerner et al., 1990; Morin et al., 2009; Sorman and Abdulrazzak, 1993). Integrated hydrological models using distributed precipitation were also developed for simulating the transmission losses within the river bed of an ephemeral river in Eastern Egypt (Gheith and Sultan, 2002). However, such models require accurate and several gauging stations along the river to validate the results. Besides, they often neglect the influence of evaporation and groundwater evapotranspiration during and after the flood as well as the complex temporal dynamics and the complexity of the unsaturated zone (Brunner et al., 2011). The development of fully integrated physically based hydrological models such as *HydroGeoSphere* allows to couple surface water and groundwater flow and to solve complex flow problems, in particular better considering the evapotranspiration and unsaturated zone dynamics (Brunner and Simmons, 2012).

For shallow aquifers, groundwater level increase during short periods allows to estimate the variation of groundwater volume after a delimitated recharge event (Healy and Cook, 2002). Additionally, in steady state, calculation of the underflow through a cross-section of an aquifer can be done by multiplying the transmissivity of the aquifer by the hydraulic gradient and the aquifer section. However, this method can lead to significant uncertainty because of the high variability of the transmissivity.

Chemical methods complete the panel of tools available for estimating the groundwater recharge from the unsaturated zone (Edmunds, 2010). Environmental tracer methods, such as the chloride mass-balance (CMB) have been widely used in arid to semi-arid areas where drainage is low, giving results for diffuse recharge ranging from 0.05 to about 100 mm/y (Scanlon et al., 2002). However, methods investigating the unsaturated zone, such as CMB but also lysimeter or chemical tracers generally apply to small scale regions because they are difficult to interpolate on larger scale.

Chemical methods are also widely used for assessing the recharge focusing on the saturated zone. These methods include analysis of historical tracers such as bomb-pulse tritium (^{3}H), chlorofluorocarbons (CFC) and the ^{3}He/^{3}H ratio that allows to assess ages of groundwater recharge for recent periods (up to 50 year). Older recharge ages, from 200 to 20’000 years, can be estimated with the radioactive decay of ^{14}C. The chloride mass-balance (CMB) method can also be used for investigating the saturated zone but results could be up to two times higher than for the unsaturated zone (Scanlon et al., 2002).

As discussed, each of these methods has its own relevance specific to each site and each issue to be addressed. Combining various methods on a same site allows to cross-validate results and to improve the system understanding. However, regardless of the approach, the recharge quantification in arid or semi-arid areas remains challenging due to the specific constraints in arid and semi-arid regions. Data are generally limited in such regions because of the remoteness of the study sites and limited means of some governments. Besides, arid and semi-arid regions are characterised by high temporal variability of rainfall and flood events which are difficult to fully integrate into conceptual and numerical models.

Recent developments in remote sensing introduced new perspectives for addressing these lacks, especially for large scale studies. The large spatial cover of images satellites can be used to create spatially distributed input parameters for a model or to constrain models during the calibration (Brunner et al., 2007). Salama et al., (1994) used Landsat images and aerial photographs for delimitating recharge and discharge areas in Western Australia. Multispectral and radar (passive microwave) images were also used to identify surface water (Carbonneau and Piégay, 2012; Jackson, 2002; Matgen et al., 2007; Mc Feeters, 1996; Ordoyne and Friedl, 2008).

Despite the growing possibilities of numerical simulations, especially with the arrival of coupled surface-groundwater models, and despite the recent development of remote sensing products with high temporal and spatial resolution, methods coupling both approaches remain rare to inexistent for quantifying recharge in arid or semi-arid regions. This study proposes a new method combining the potential of remote sensing products and coupled surface-groundwater simulation tools, in order to quantify recharge.

1.3 Freshwater lens dynamics

In semi-arid and arid areas, freshwater lenses commonly develop along ephemeral rivers and streams or below flood plains, and are often the only permanently available water resource (Wheater et al., 2010). Continental freshwater lenses are characterised by specific dynamic behaviours that need to be understood in order to assess the sustainability of this particular groundwater resource under given exploitation schemes.

The dynamics between freshwater and salty/brackish water have been studied for many decades. In particular, variable density flow has been extensively studied in coastal contexts where seawater intrusions often occur (e.g. Cheng, 2004; Steyl and Dennis, 2010; Werner, 2009). Implications of seawater intrusions on water management and soil and groundwater salinization have also been widely discussed in literature (e.g. Essaid, 1990; Essink, 2001; Milnes and Renard, 2004; Milnes et al., 2006; Sophocleous and Ma, 1998; Vengosh, and Rosenthal, 1994).

However, despite the numerous examples of continental saline groundwater bodies, in particular in arid to semi-arid contexts (van Weert et al., 2009), freshwater lens dynamics in these contexts is less documented than seawater intrusion and studies generally focus on smaller scales. Thorne et al. (1990) identified a freshwater lens along the Murray River (Australia). Age, origin and stability of this lens were further investigated by Cartwright et al. (2010) by means of hydrodynamic investigations (piezometry and surface water elevation) and geochemistry (major ions, $\delta^{18}O$, ^{14}C activities, ^{3}H concentrations). They identified five main aspects that have to be investigated when studying continental freshwater lenses along loosing streams : "*(1) the controls on the location of the lens; (2) the time-scales over which the water in the lens is replenished; (3) the extent of mixing between the water in the lens and the regional groundwater; (4) whether the lens is recharged directly from the river or through the floodplains; and (5) whether the lens is stable, growing or degrading under the current hydrogeological conditions* ". In this latter study area, it was found that recharge of the lens is mainly controlled by the river levels and mainly occurs through the river bank, and not through the flood plain. They highlighted the control of aquifer lithology on the freshwater lens extension.

Another Australian example of a freshwater lens was investigated by Cendón et al. (2010) beneath the Cooper Creek floodplain. The freshwater lens is located over a shallow regional saline groundwater and crops out in a 'waterhole' of about 50 m by 400 m along the ephemeral streambed. The freshwater is located in unconsolidated fluvial sands and is covered by a layer of 2 to 7 m of impermeable mud. Investigations revealed that the waterhole is fully connected with the surrounding freshwater lens and is the preferential route for recharge during major flood events related to monsoonal cycles. This is supported by stable groundwater isotopes ($\delta^{2}H$ and $\delta^{18}O$) which have a homogeneous signature, and by the total dissolved solids that increase with the distance to the waterhole, up to 5'000 and 15'000 mg/l at a distance of 1'000 m.

A further example of a continental freshwater lens is found in the hyper-arid climate of Central Oman. Young et al. (2004) detected this freshwater lens below a topographic depression of 60 km^2 using a geophysical method and confirmed its presence by drilling boreholes. Isotope analyses showed that the lens is recharged by modern water from rare cyclonic rainfall events. However, the current dynamics of the lens was not investigated.

In Africa, numerous saline aquifers and local or regional freshwater bodies can be found (van Weert et al., 2009), such as in the Western Sahara Aquifer System, the Nubian Sandstone Aquifer System, the Niger Delta and the Kalahari-Karoo aquifer. The characterisation of these aquifer systems very rarely includes the dynamics between fresh and saline water. One example of this dynamics characterisation is given by Bauer et al. (2006) for the Shashe River Valley aquifer, south of the Okavango Detla in Northern Botswana. The temporal dynamics of the groundwater salinity of the aquifer, located around an ephemeral stream was modelled using coupled flow/transport models. These models allowed to assess the importance of evapotranspiration and pumping and to reproduce the long term evolution of the freshwater lens.

These literature examples reveal a high variability of contexts in which continental freshwater lenses may exist. Two main parameters controlling the dynamics of a freshwater lens can be identified: firstly, the recharge dynamics, which depend on the surface water dynamics; and secondly, the geological and soil settings which determine the possibility of water to infiltrate and controls surface-groundwater interaction. Some freshwater lens replenishments are controlled by major flood events, while others are dominated by infiltration through the river bank and thus depend on the water level in the river and not on inundation or flood events.

Up to now, continental freshwater lens dynamics have been studied through case-by-case analysis and mostly on small scales, combining geochemical, hydrodynamic, geological or numerical modelling approaches. In this study, we aim to develop a numerical approach that allows the assessment of the recharge mechanisms (volumes, concentrated or diffuse recharge) by comparing simulated and observed freshwater lens geometry and which can be applied for characterising the Merti aquifer and other continental freshwater lenses, in particular for large-scale contexts.

1.4 The Merti aquifer site

In the 1960s and 1970s, the Merti aquifer has been largely studied to develop agro-pastoralism within the Merti-Dadaab region (Arnold, 1952; Mundorff and Swarzenski, 1970; Swarzenski and Mundorff, 1977; Wanyeki, 1979). These works established the basis of the understanding of the aquifer, in particular describing the geology of the area and identifying the presence of the large continental freshwater lens (Fig. 1.2). The groundwater resource study of the Merti aquifer restarted in the 1990s with the creation of the Dadaab refugee camps (Gachanja and Tole, 2002; Lane, 1995; WRAP, 1991). In 2004, GIBB updated the understanding of the aquifer carrying out a large groundwater field campaign and compiling the massive pre-existenting data. A first numerical model, aiming to assess the impact of the increasing groundwater extraction on the groundwater quality and levels was developed by Earth Water Ltd (2012).

In parallel to these groundwater-oriented investigations, numerous studies focused on the larger geological settings of the Anza Graben, a minor associated rift system of the East African Rift in which the Merti aquifer developed (Bosworth and Morley, 1994; Greene et al., 1991; Hendrie et al., 1994; Nyagah, 1995; Reeves et al., 1987; Winn et al., 1993).

These numerous studies allowed to establish a first conceptual model of the aquifer. This previous conceptual model, which is presented below, will be further investigated in the next chapters of this study.

- The development of the Anza Graben created a large and deep sedimentary basin (several thousands of meters) which is filled by Cretaceous, Paleogene and Neogene sediments.
- The upper part of the basin (about 600 meters) is constituted of an intercalation of fine and coarse alluvial to peri-marine sediments of Miocene and Pliocene ages;
- A late Miocene horizon of coarse sediments, called the “Merti beds”, is located at a depth of 90 to 50 meters and is 20-40 meters thick.
- This water-bearing horizon, that constitutes the productive unit of the Merti aquifer, extents over 200 km from Habaswein to Dadaab and Liboi, and possibly downstream. It is several tens of kilometres wide. The shape of this main productive layer coincides with the freshwater part of the aquifer (Fig. 1.4), while the areas

surrounding this freshwater lens are characterised by brackish (2’000 to 10’000 µS/cm) to saline water (higher than 10’000 µS/cm).

Recharge of the aquifer was also estimated by various methods (Table 1.1). Estimations vary between 2.6 x 10^6 m^3/y and 33 x 10^6 m^3/y. These estimations are quite rough and do not distinguish between diffuse and concentrated recharge. From the description given in these reports it is assumed that these estimations refer to the freshwater recharge supplying the freshwater lens. Thus, in order to assess the vertical recharge flux, these figures are normalised by the surface of the freshwater lens between the Lorian Swamp and Liboi (the downstream limit before the freshwater lens become brackish) (Table 1.1).

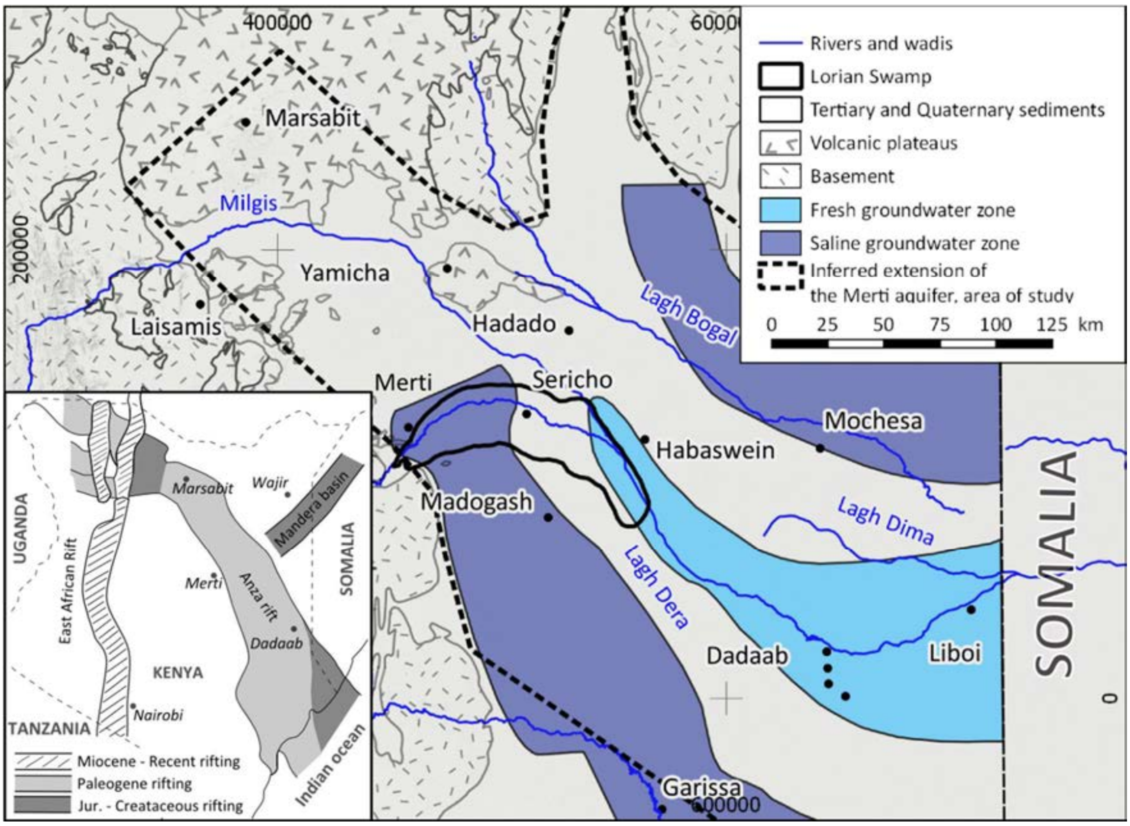

Fig. 1.4: General overview the Merti aquifer and the fresh and saline groundwater zones. The Merti aquifer is supposed to extend upstream of the freshwater lens as defined by Swarzenski (1977) and to be delimited laterally by the border of the Anza Rift and upstream by the topographic watershed limit of the Marsabit volcanic plateau, which covers the Tertiary sediments in which the aquifer developed.

The various methods used for the recharge estimation can lead to significant uncertainties. The method based on the groundwater underflow computed from hydraulic gradient, section and transmissivity indicates recharge between 3.3 and 4.6 x 10^6 m^3/y (Lane, 1995; Swarzenski and Mundorff, 1977; Wanyeki, 1979; WRAP, 1991). This method may give reliable estimations if the regional transmissivity is well defined. Also, even though the aquifer has been described with a thickness of 20 to 40 meters, its exact thickness is not documented and could therefore lead to considerably higher transmissivities.

Based on decreasing Cl^- concentrations between the upper part of the aquifer (Yamicha triangle) and Habaswein, GIBB (2004) suggested high freshwater recharge around Habaswein in order to dilute the salinity observed in the upper part of the aquifer. They estimated the freshwater recharge to be at least ten times higher than at the Yamicha triangle, that is 3.3 and 33 x 10^6 m^3/y respectively.

Source	Calculation method	Recharge volume (10^6 m^3/y)	Vertical flux (mm/y)
Swarzenski *et al* (1977)	Groundwater flux at Liboi	2.6 – 3.9	0.21
Wanyeki (1979)	Finite difference model	3.8	0.30
Wanyeki (1979)	Groundwater flux at Liboi	4.7	0.38
WRAP (1991)	Groundwater flux	2.4, at the Yamicha triangle	0.19
		0.9, at the Ewaso Ng'iro River	0.07
Lane (1995)	Groundwater flux at Habaswein	1.2	0.10
GIBB 2004	Dilution ratio	3.3 and 33, at the Yamicha triangle and Ewaso Ng'Iro River	2.90

Table 1.1: Recharge estimations from previous studies. The vertical recharge flux is normalised by the surface of the freshwater lens surface (12'500 km^2). Locations are shown on Fig. 1.4.

These studies also discussed the main possible recharge mechanisms. The main hypothesis is that recharge occurs periodically during flood events of the Ewaso Ng'Iro River beneath large inundations over the Lorian Swamp area. The Ewaso Ng'Iro River drains a large watershed west of Mt-Kenya and is permanent up to Archer's Post (Fig. 1.2). From Archer's Post, the river becomes ephemeral and reaches the Lorian Swamp only during major floods, i.e. about once per year. Wanyeki (1979) estimated that once every ten year, major flood would lead to significant recharge volume of up to 30 x 10^6 m^3. However, his approach is based on the total river discharge volume during the flood event and does not consider evapotranspiration. Estimation of the recharge is presented graphically in Fig. 1.5. This figure will be completed in the next chapters in order to compare the various recharge estimations. Extraction was estimated in the refugee camp in 2011 to 3.2 x 10^6 m^3/y and to 1.6 x 10^6 m^3/y outside the camp in 2003, for a total of 4.8 x 10^6 m^3/y for the entire aquifer in 2003 (Earth Water Ltd, 2012).

Recharge is also supposed to occur along other ephemeral rivers of the Merti basin, such as the Lagh Dera and Lagh Bogal rivers (Fig. 1.4). But again, no precise and solid quantification of this recharge was presented.

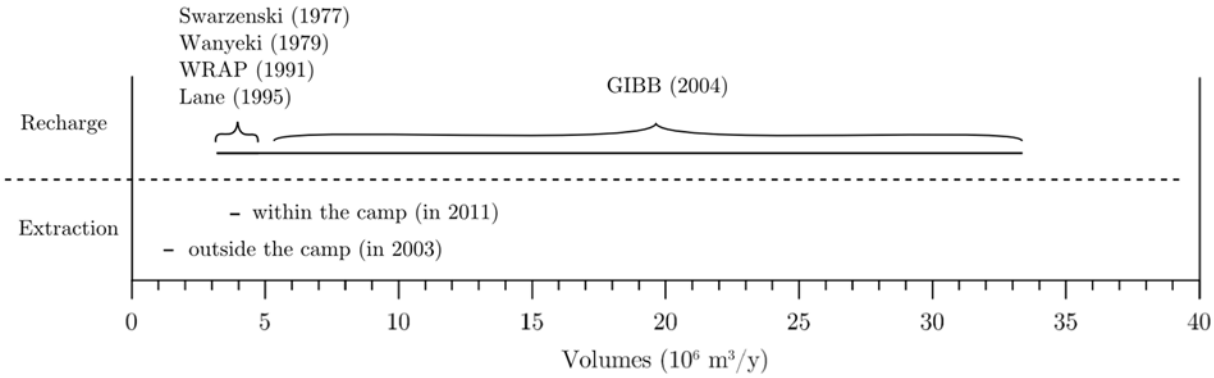

Fig. 1.5: Annual recharge estimations from previous studies and extraction rate within and outside the Dadaab refugee camp.

The basaltic plateaus located north-west of the freshwater lens at Merti, Yamicha, Laisamis and the Mt-Marsabit were also suggested as preferential recharge areas due to the supposed higher precipitation rate over these plateaus, and possibly due to the basalt fracturation. However, these two hypotheses were not strongly demonstrated.

Another mechanism is suggested via localised infiltration in sinkholes within carbonate rocks (GIBB, 2004) at Oresaboru (few kilometres north of Merti) and Shantabak (between Habaswein and Madogash). However this type of recharge is assumed to be limited because of the small extension of the carbonate rocks, as they were only described at these locations.

In the previous studies, five geochemical campaigns were carried out since 1974 (GIBB, 2004; Gachanja and Tole, 2002; Ingraham and Matthews, 1988; Lane, 1995; Pearson and Swarzenski, 1974; Sklash and Mwangi, 1991), using analyses of ^{2}H, ^{3}H, ^{18}O, ^{14}C and ^{87}Sr isotopes. Following hypotheses about recharge dynamics were established, indicating that the Merti aquifer water is composed from very old to recent water :

1) δ^{18}O and δ^{2}H analyses reveal that water from the central Merti aquifer (between Dadaab and Habaswein) is significantly isotopically depleted, indicating that recharge is made up of water coming from higher areas (i.e. the upper Ewaso Ng'Iro catchment) or occurred during a more humid period (paleorecharge).

2) Recent recharge in shallow groundwater systems along the Ewaso Ng'Iro River and in volcanic regions is validated by tritium data. Unusually high values found at Sericho, Shantabak and Sabule are interpreted as recent recharge during the 1997/1998 ENSO (El Niño Southern Oscillation) or earlier ENSO events.

3) ^{14}C isotopic analyses suggest recent to very old recharge ages which could be associated with recent or previous known wet periods: (1) recent recharge; (2) around 2'700 years BP; (3) 9'200 years BP; and (4) 14'200 years BP. Younger ages are found around Habaswein and Gurufa.

Finally, based on the current understanding of the aquifer, Earth Water Ltd (2012) elaborated a finite-difference groundwater model in order to predict the groundwater depletion and salinity evolution at Dadaab, according to two different recharge scenarios (6.8 and 32.2 x 10^6 m^3/y) and assuming increasing abstraction rates due to growing populations. They concluded that, from 2035 onwards, drawdown at Dadaab could reach 2.4 to 8.2 meters and that pumped water at boreholes close to the edge of the freshwater could become brackish with electrical conductivities beyond 8'000 µS/cm. The results of this first numerical model of the Merti aquifer reveal the risk of a degradation of the groundwater quality and quantity, and the necessity to undertake further investigations.

Up to now, only local increases of salinity at the edge of the freshwater lens were measured and little to inexistent depletion of static water level could be observed. However, mid to long term degradation of the groundwater quality and level could have dramatic humanitarian, social and economic consequences. To avoid such consequences, a better understanding of the Merti aquifer is required.

1.5 Approach and structure of the thesis

The present thesis follows two main objectives. The first one is to propose new methods for (1) estimating groundwater recharge in arid to semi-arid areas, using the high potential of remote sensing products and of a fully integrated, physically based flow model (*HGS*); and (2) for quantifying the dynamics of large scale continental freshwater lenses. The second objective is to better characterise the Merti aquifer, in particular by applying these new methods but also by the interpretation of geological and hydrogeological field data (the piezometry, well tests, groundwater electrical conductivities and hydrochemistry).

Chapter 2 describes the overall geological and hydrogeological characteristics of the Merti aquifer. The geometry and hydrodynamic characteristics of the aquifer are described based on geological and well test data. The characterisation of the aquifer is completed with the spatial and temporal analysis of the piezometry and groundwater electrical conductivities. For this purpose, historical data collected since Swarzenski (1977) are used, as well as high resolution temporal data acquired with a network of 20 monitoring devices installed in 2013 in the framework of this research project. This chapter provides the basis for the conceptual model of the Merti aquifer and the latter numerical model.

The method for quantifying concentrated groundwater recharge developed in this research work is presented in Chapter 3. This method relies on an integrated physically coupled groundwater / surface water flow model, calibrated by satellite images of inundation surfaces. Based on the recharge quantified for six inundation events, average annual groundwater recharge is computed converting the statistical distribution of the river discharge rates into a recharge distribution. Additionally to the concentrated recharge quantification, estimation of areal recharge (diffuse recharge) is approached using remote sensing products and values found in literature for similar environments.

Chapter 4 explores the dynamics of a synthetic continental freshwater lens inspired from the Merti aquifer geometry. The dynamics of this freshwater lens is assessed under various recharge conditions (concentrated recharge, diffuse recharge and various rates) and aquifer characterisation (e.g. transmissivity) using geometric indicators (size and shape of the freshwater lens). The effect of pumping is also evaluated observing the modification of the freshwater lens geometry. Comparison with the actual Merti aquifer is carried out in order to cross-validate hypotheses of recharge conditions suggested in chapter 3.

In chapter 5, a conceptual and a numerical model of the Merti aquifer are elaborated. The conceptual model is established using results from recharge quantification and the freshwater lens dynamics, as well as interpretations of geological and field data of chapter 2. This conceptual model serves as basis for the development of the regional numerical model. This numerical model is used to test hypothesis of the conceptual model.

Finally, conclusions, perspectives and recommendations are discussed in chapter 6.

Chapter 2

Geological and hydrogeological characterisation of the Merti aquifer

2.1 Introduction

The aim of this chapter is to characterise the main geological and hydrogeological features of the Merti aquifer in order to set the framework for the further investigations on groundwater recharge (chapter 3) and the freshwater lens dynamics quantification (chapter 4). Eventually, these three pillars will serve as base for the development of the conceptual and regional numerical models of chapter 5.

First, the aquifer geometry and the main lithostratigraphic units are interpreted by the analysis of the geological units and structures (faults). This step allows to define the main hydrostratigraphic units with qualitative hypotheses on hydraulic behaviour. Then, hydrodynamic characterisation of the aquifer is refined with the analysis of piezometry, well test data and hydrochemical distributions and evolution. This analysis, which integrates historical and recent field data, allows to define more precisely the areas of high transmissivities but also to interpret the effect of recharge over the Lorian Swamp on the observed piezometry.

2.2 Geometry and geology of the Merti aquifer

The analysis of the geology serves to define as accurately as possible the geometry and the major units of the aquifer. First, the large scale setting of the geology is presented. Secondly a more detailed description of the Merti beds (the main aquifer formation) and the quaternary deposits and soils is given, with a focus on hydrostratigraphic characteristics.

2.2.1 Regional geological setting

The Merti aquifer is located within a large tertiary sedimentary basin, between the East African Rift (EAR) and the passive margin of the Indian Ocean. This basin (Fig. 2.1) was created along a minor associated rift system of the large EAR, the Anza Rift, that was mainly active during the Paleogene (Bosworth and Morley, 1994; Reeves et al., 1987).

Sedimentary rocks in the basin consist of an alternation of high energy environment depositional sediments (mainly sands and some gravels) and low energy depositional environment sediments (clays and silts). Some rare limestones are present, which formed in shallow marine depositional environment. These rocks are deposited over the pre-existant Mesozoic sedimentary units and the Precambrian basement.

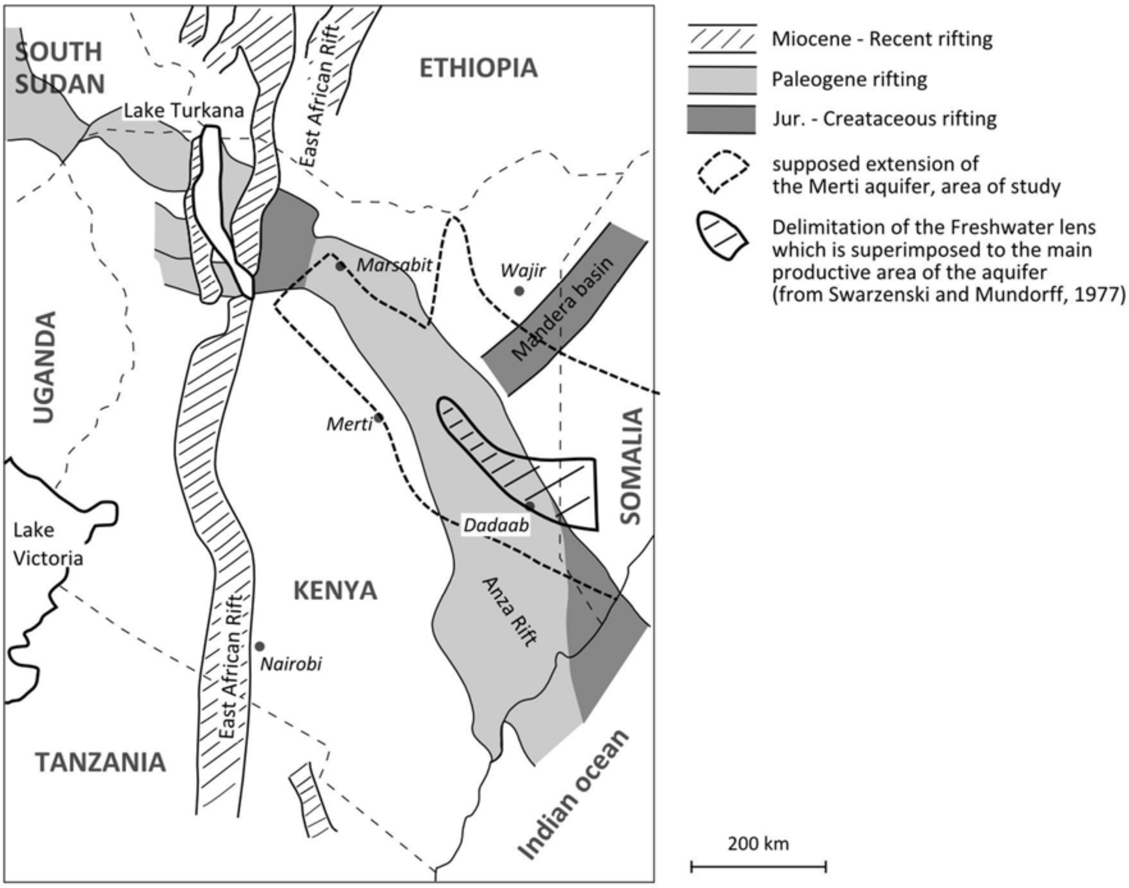

Fig. 2.1: Tectonic map of the East African Rift and the Anza Rift in which the Merti aquifer develops (modified after Hendrie et al., 1994 and Rop, 2011). The freshwater lens as defined by Swarzenski and Mundorff (1997) is superimposed to the main productive area of the Merti aquifer.

The dynamics of sedimentation within the Anza Rift is constrained by normal fault systems but also by eustatic sea level fluctuations that affect the sedimentation facies of the formations (Nyagah, 1995). The major structure is the Lagh Bogal Fault crossing the area northwest-southeast under the entire Marsabit plateau up to Habaswein (Fig. 2.2). Various normal faults and minor grabens associated to the large extension context were also identified by the same author. From Middle Miocene, faulting considerably decreased or stopped, suggesting that faults do not significantly affect the more recent layers. Since Middle Miocene, volcanism started over the basin and formed high reliefs (Mt-Kenya and Mt-Marsabit) and plateaus covering part of the Tertiary sediments.

The main characteristics of the basement, Mesozoic and Cenozoic rocks are presented below with a hydrostratigraphic overview.

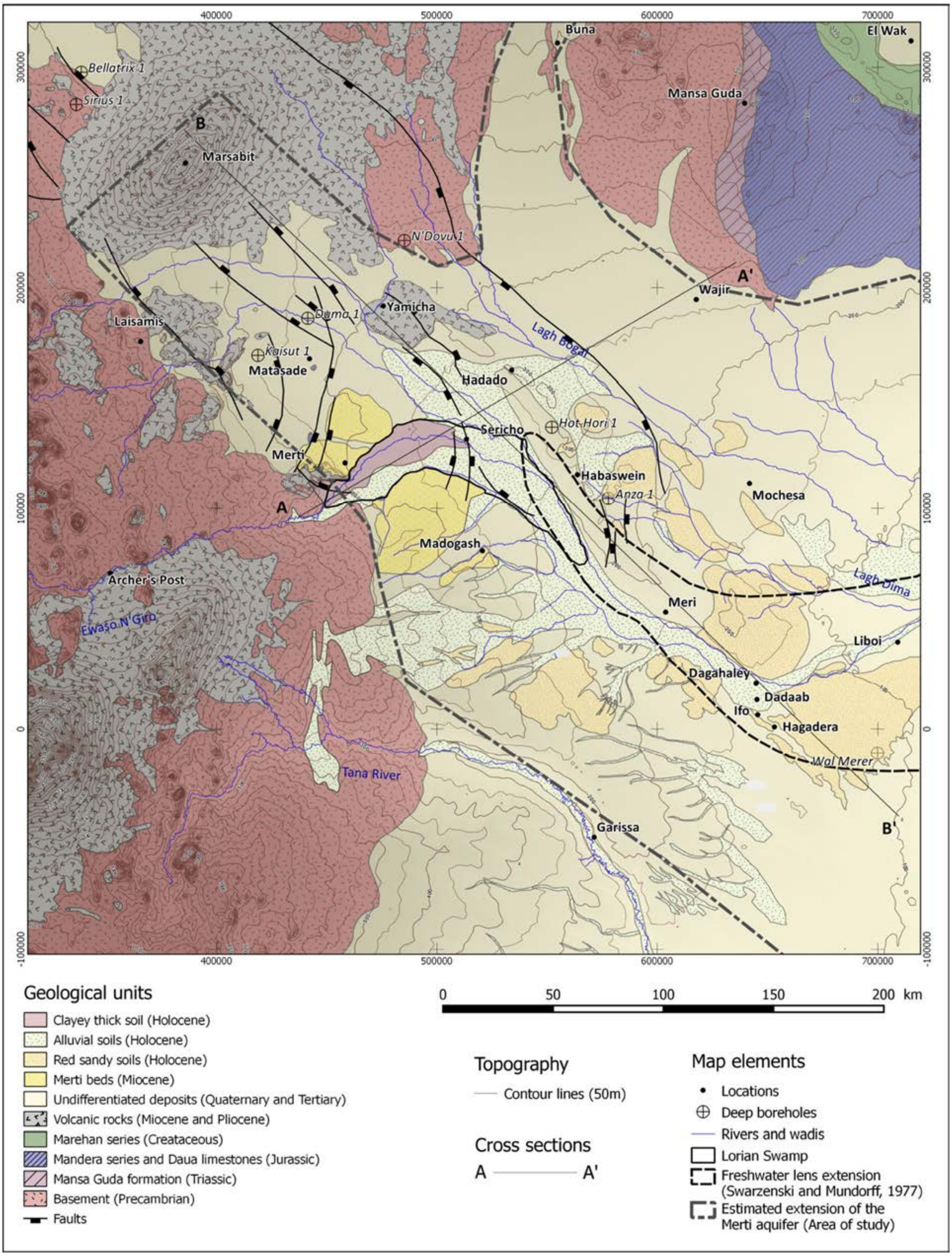

Fig. 2.2: Geological map of the Merti area compiled from the sources : GIBB, 2004; Lane, 1995; Swarzenski and Mundorff, 1977; Kenyan Water Resources Management Authority (WRAP).

Precambrian Basement

North, west and southwest of the Merti aquifer, the basement present under the sedimentary piles consists of metamorphic rocks of Precambrian and Paleozoic ages. It includes quartzites, granulites, gneisses, schists and amphibolites, intruded by granites, gabbros and others salic to ultramafic rocks.

Basement rocks are characterised by fracture porosity and low hydraulic conductivity. Swarzenski and Mundorff (1977) reported that water production at boreholes usually yield less than 10 litres per minute. In rare cases, some boreholes produce between 25 litres per minute to more than 100 litres per minute.

Carboniferous and Permian rocks, included in the basement unit, do not crop out within the Merti aquifer. Remnants are visible south of the Tana River but they are covered northward by Mesozoic and Cenozoic deposits. Carboniferous and Permian rocks are not of relevance for the Merti aquifer. Indeed, they are neither found as reservoirs nor as infiltration areas.

Mesozoic

Except for a Jurassic outcrop in Matasade and south east of Merti, the Mesozoic formations are not identified in the Merti aquifer area. Triassic is present north of Wajir (north of the Merti aquifer) in a subsiding basin, and south of the Tana River. It consists of consolidated conglomerates, sandstones, siltstones and shales, contained in the Mansa Guda formation.

Jurassic rocks mainly crop out in the subsiding basin northeast of Wajir. This basin is not of interest for the study because it is separated of the Merti aquifer by basement rocks. The limestones cropping out locally in Matasade and south east of Merti are interpreted as the upper part of tilted blocks at the edge of the graben. These limestones are capped by unconformable quarzitic sandstones (Bosworth and Morley, 1994). They are described by Gachanja and Tole (2002) as karstified and sinkholes were identified within this formation.

In the centre of the Anza Rift, the Jurassic formations are found at several thousand of meters below the surface. In the upper area of the Merti aquifer area, the Jurassic was not encountered in boreholes despite an investigation depth of 4’000 to 5’000 meters (Fig. 2.3). At Garissa, in the border of the rift system, the Jurassic formation is found at a depth of 1040 m. At Wal Merer, 30 km east of Hagadera, Early Cretaceous is still present up to a depth of 3’800 m (Nyagah, 1995).

The early Cretaceous formation is not well known over the basin. The compiled stratigraphic section of Fig. 2.3 shows the very great thickness of the Cretaceous formation up to several thousands of meters. Additionally, Aptian and Albian are present as marine strata in the Northern Lamu embayment, at Wal-Merer-1 at a depth of 1470 m (Bosworth and Morley, 1994; Winn et al., 1993).

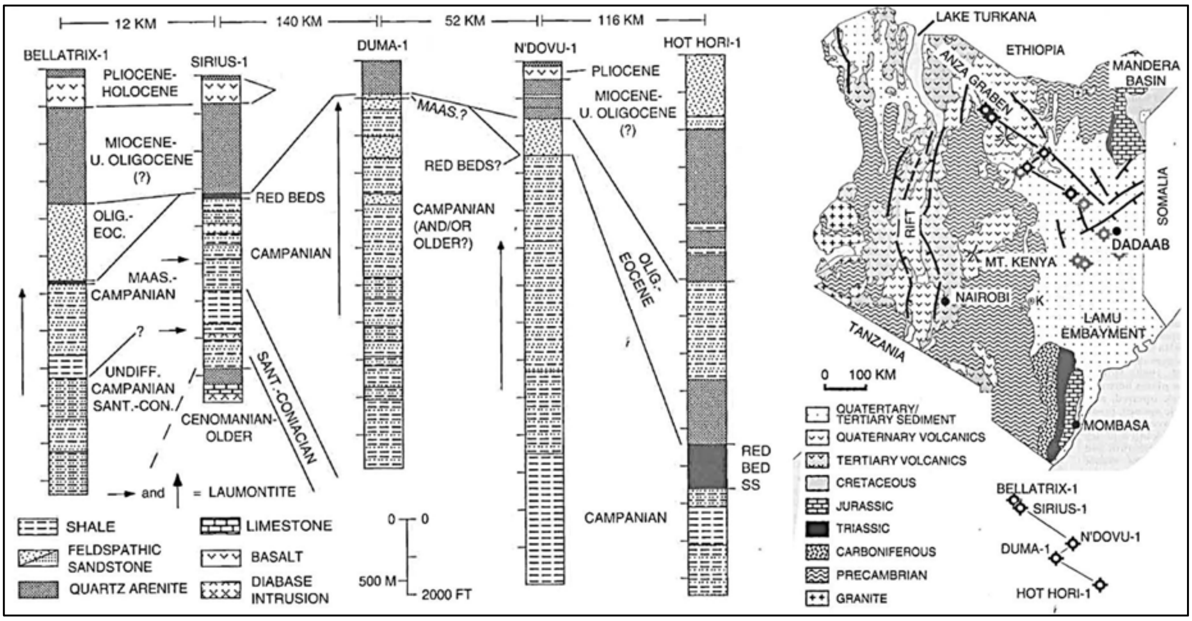

Fig. 2.3: Stratigraphic sections of the Anza rift (reprinted from Winn et al., 1993).

The schematic cross-section of Fig. 2.4 summarises the vertical distribution of the rocks between the two shoulders of the graben, up to a depth of 6000 m, along the section shown in Fig. 2.2. This figure illustrates the importance of the normal fault system for the depositional dynamics of the Mesozoic and Tertiary formations. Laterally, the Jurassic limestones found in the Merti area are interpreted as tilted-blocks along the western border of the Anza graben.

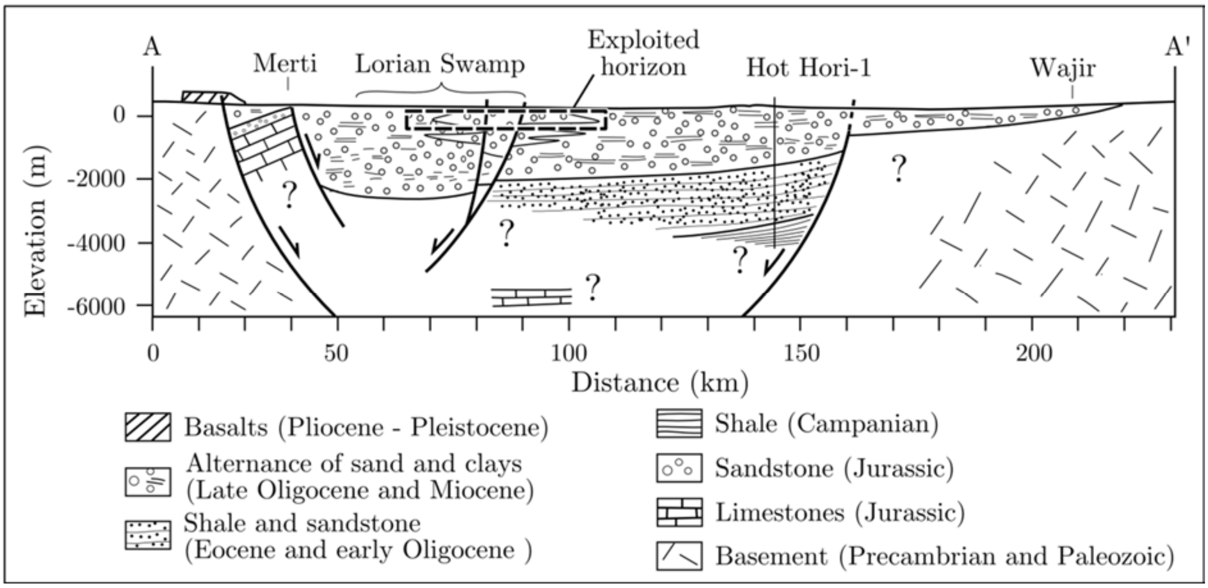

Fig. 2.4: Schematic cross-section of the Anza Graben. The graben is delimited laterally by normal faults, which leads to the deposition of several thousand meters of Cenozoic sediments in the middle of the basin. Laterally, tilted blocs with Jurassic cover are presumed. These blocks crop out in few locations along the western border. At the base of the basin, presence of Jurassic limestones is expected. Over the shoulder of the basin, a thickness of few tens or hundreds meters of late Tertiary sediments is present. The Merti aquifer developed within the Late Oligocene and Miocene formation. The exact thickness of the aquifer is not documented. Sources: geological map of Kenya 1:3'000'000, Bosworth and Morley, 1994 and Winn et al., 1993.

These limestones present at the edge of the rift basin could possibly lead to a complementary connected aquifer system, which could be dominated by karstic flows, underlying the unconsolidated Tertiary Merti aquifer. However, according to the geological map, the Jurassic rocks are not directly in contact with the main recharge area (the Lorian Swamp), which is around 30-40 km east of the tilted block. Furthermore, these rocks crop out more than 20 km south and north of the Ewaso Ng'Iro River, making difficult the possibility of the Ewaso Ng'Iro to infiltrate into this formation.

Cenozoic

The upper part of the Anza graben is filled with Paleogene and Neogene formations that constitute the reservoir of the Merti aquifer. Thickness of these sediments highly varies from the center of the Anza Rift to the shoulders. East of Marsabit, the thickness of Cenozoic sediments ranges from 0 to 600 m while within the basin, the Miocene sediments reach a thickness from 300 to 600 m (Bosworth and Morley, 1994). Eocene and Oligocene formations reach several hundreds of meters of thickness at Hot-Hori (Fig. 2.3 and Fig. 2.4)

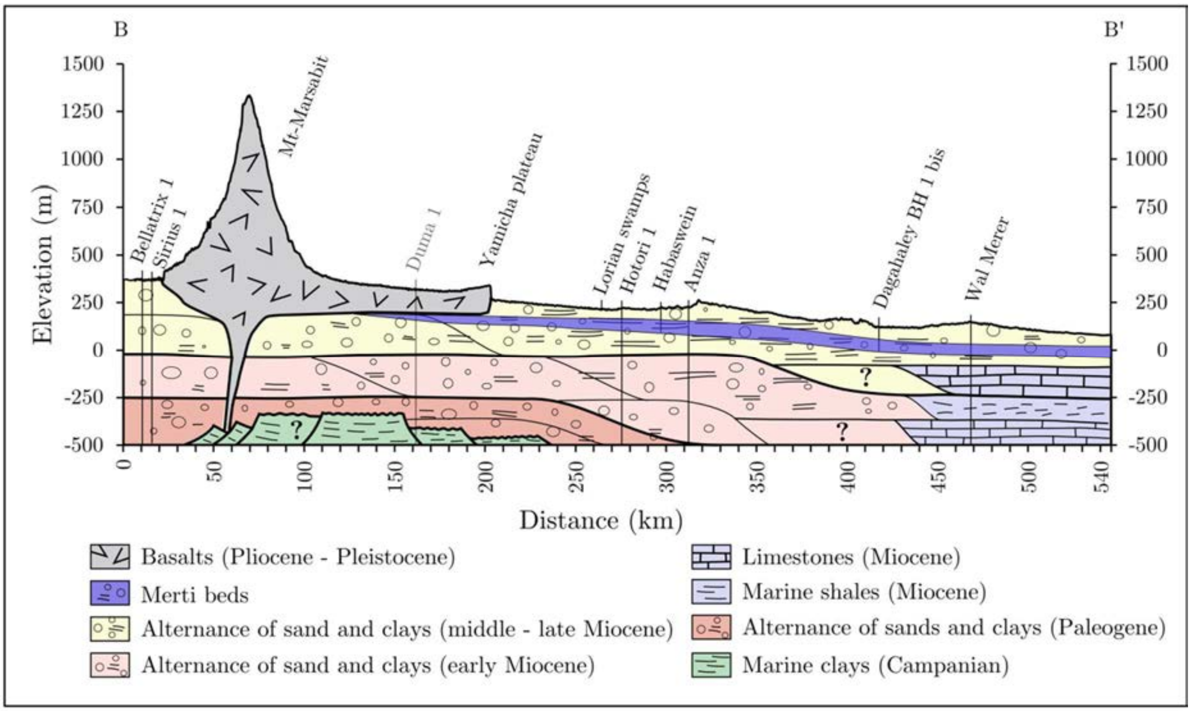

Fig. 2.5: Schematic geological cross-section of the Merti aquifer, interpreted from the borehole logs described by Bosworth and Morley (1994), Nyagah (1995) and Winn et al. (1993). Downstream, oceanic Miocene limestones could be karstified and lead to significant increase of the transmissivity. The transition between the Miocene oceanic sediments (clays and limestones) and the continental deposits is not known. Campanian marine shales are interpreted as the upper part of tilted block along the border of the Anza graben. The exploited productive layer of the Merti beds is located within the middle to late Miocene formation. Deeper productive horizons are probable.

Uplift and a drop of sea level during the late Miocene and Pliocene induced an increase of the river gradient and the deposition of predominantly fluvial clastic deposits that include the Merti beds formation, the groundwater productive horizon (Fig. 2.5). Some rare carbonate rocks can be encountered, such as in north of Merti and between Madogash and Habaswein. Towards the ocean, Miocene alluvial sediments are replaced by two thick limestone layers separated by marine shales (Fig. 2.4). These limestones, encountered in the Wal Merer borehole, could be karstified and lead to a significant increase of the transmissivity.

Early Miocene large marine/fluvial connection with the Lake Turkana (northwestern Kenya) is suggested by the presence of a whale marine fossil found in late Burdigalian fluvial deposits around the lake Turkana (Bosworth and Morley, 1994). This connection implies the presence of a large peri-marine channel that extended beyond the Mt-Marsabit during some periods of the Miocene, indicating a possible stratigraphic continuity upstream the lower part of the Anza Rift.

Pliocene-Pleistocene volcanic plateaus

Many volcanic areas are present in the western and northwestern region of the Merti aquifer. Except for the Mt-Marsabit that culminates to 1700 m, the plateaus overlook the surrounding plain of about 100 m. Basalts were deposited during a period from the Late Miocene to the Pleistocene. K/Ar analysis (Brotzu et al., 1984; Key et al., 1987) indicate that the Mt-Marsabit and the Yamich plateau are the youngest volcanic rocks of the basin (0.7 to 1.7 Ma) while the Merti and Laisamis are dated between 9.9 and 12.2 Ma.

Deposition of sediments continued during and after the creation of basaltic formation. At the exploratory Sirius-1 borehole (Fig. 2.3), the basalts are covered by a 40-60 m thick layer of coarse sediments (Bosworth and Morley, 1994). It is also assumed that the Yamicha plateau is an extension of the Mt-Marsabit with a connection under the recent deposits, as suggested in Fig. 2.5.

Because of their low fracturing, basalt formations are considered as low permeable units. Evidences supporting this assumption are the poor number of boreholes drilled in this formation and their low specific capacity. Two boreholes are located on the Marsabit plateau with a specific capacity of 0.4 and 0.5 $m^3/h/m$ while specific capacity over the central Merti aquifer are around 1 and 2 order of magnitude higher. Furthermore, the last important fracturation period goes back to the Early Miocene and did not significantly affect the basalt formation.

2.2.2 Description of the Merti beds and quaternary deposits

This section focuses more specifically on the stratigraphic levels that contain the freshwater, the Merti beds, and on quaternary soils and deposits that control the infiltration processes.

Merti beds

The Merti beds, located in the Middle to Late Miocene, refer to the exploited productive horizon of the Merti aquifer. In the Merti area, it has a thickness of 10 to 20 m and is found at about 90 m depth (GIBB Ltd, 2004; Swarzenski and Mundorff, 1977). In the region of Dadaab, it has a thickness between 20 and 40 m and is found at a depth of around 150 m.

The Merti beds are a fluvial detrital formation made up of friable to semi consolidated gravel, grit, sand, silt and clay, generally intercalated in lenticular beds. Variation in the local sedimentation dynamic and in the origin of the detrital material could explain the spatial granulometry variation, as for instance the clay content. Clay is a product of basalt erosion while basement igneous and metamorphic rocks are more likely to produce coarser siliceous sediments.

The thickness and depth of the Merti beds is based on groundwater well logs (up to 250 m deep) and not on deeper boreholes. Deeper boreholes (Fig. 2.4 and Fig. 2.5) describe all the Miocene deposits as an alternating succession of fine and coarse fluviatile and perimarine sediments but without giving details on the exact thickness and depth of these layers. Thus it remains possible that others productive horizons can be found below the “first” exploited horizon (i.e. the Merti beds), up to a depth of 500 m, or even deeper.

The extent of the coarser horizon of the Merti aquifer is probably superimposed on the “freshwater” part of the aquifer: freshwater infiltrating and recharging the aquifer will preferentially goes into formations of higher permeabilities, than in fine sediments layers. The productive zone of the Merti aquifer extent is thus located along a line from the Lorian Swamp up to the Somali border and between two major drainage ways of the area: the Ewaso Ng'Iro River and the Lagh Dera wadi. This extent represents about 200 km long and 20 to 90 km wide. A clayey sediment layer of about 50 meters thickness overlies the Merti beds, making the Merti aquifer confined over the largest part of its extent (GIBB Ltd, 2004).

Furthermore, two major outcrops of the Merti beds are described on both sides of the Ewaso Ng’Iro close to Merti. Nevertheless, because of the high vertical heterogeneity of the Miocene formation, there is no evidence that these beds are in continuity with the horizons encountered in more downstream boreholes.

Soils

Soils on basement rocks are generally characterized by a sandy or clayey loam texture, well-drained, red to reddish brown, moderately organic and often stony (Lane, 1995). They can be permeable.

Soils above the Tertiary sedimentary basin are very variable and their exact limits are not well defined. Data from the WRAP study (1991), satellite images and descriptions from Lane

(1995) and Swarzenski and Mundorff (1977) were used to create the synthetic distribution proposed in the geological map of Fig. 2.2.

Between Merti and Sericho, the soil of the Lorian Swamp is constituted of a layer of hard clays or brownish-gray clays of 3 to 4 m thick, found 0.5 to 1 m below land surface. Deeper clays are also found from about 7 to 20 m. Spatial and vertical succession of this material allows formation of small local perched aquifer but with an overall moderate permeability at the large scale. Quaternary deposits and soils over the upper part of the Lorian Swamp between Merti and Sericho are likely to have a low permeability.

Alluvial soils from the central plain are mainly deposited along ephemeral streams along the Lagh Dera wadi and its vicinity. Similar deposits could also be found on both sides of the Lagh Bogal and the Lagh Dera wadi tributaries. They are likely to be clayey to sandy clayey loams with local dominance of sand and gravels (as downstream of Sericho). They are reddish brown to grey, mainly organic but slightly calcareous, and relatively thick. They may be very permeable.

Sedimentary plain soils of the "*red sandy plains*" are mainly present North of Dagahaley and east of Dadaab. These soils are described as "*well to excessively well drained, deep and friable reddish brown loamy coarse sand*". They are characterized by a lack of runoff and, they may be a possible direct recharge route.

The remains of soils in the central eastern part of the aquifer are formed by "sealing loam plains" and are comprised in the "undifferentiated" Tertiary and Quaternary deposits. They are composed of coarse to fine sandy clay loams. Generally deep, their permeability is rather low.

Soils from volcanic area are described as well drained clayey loams, dark reddish brown, richly organic and deep around Mt Kenya, Nyabeni and Marsabit. On the Merti, Laisamis and Yamicha Plateaux, soils are well to imperfectly drained, reddish brown, organic and calcareous, and relatively shallow. According to Lane, permeability of soil on volcanic rocks is considered as variable.

2.2.3 Conclusions on the geology of the Merti aquifer

The succession of coarse (water bearing) layers lead to develop the concept of the Merti aquifer system, of which only the first horizon, called "the Merti beds" is well known and exploited for the water production. The coarse layers occur mainly along the central area of the basin and may be found up to a depth of 500 m or even deeper, within the Miocene formation. The development of the Merti aquifer system is delimited laterally by a system of normal faults of the Anza Graben (Fig. 2.6).

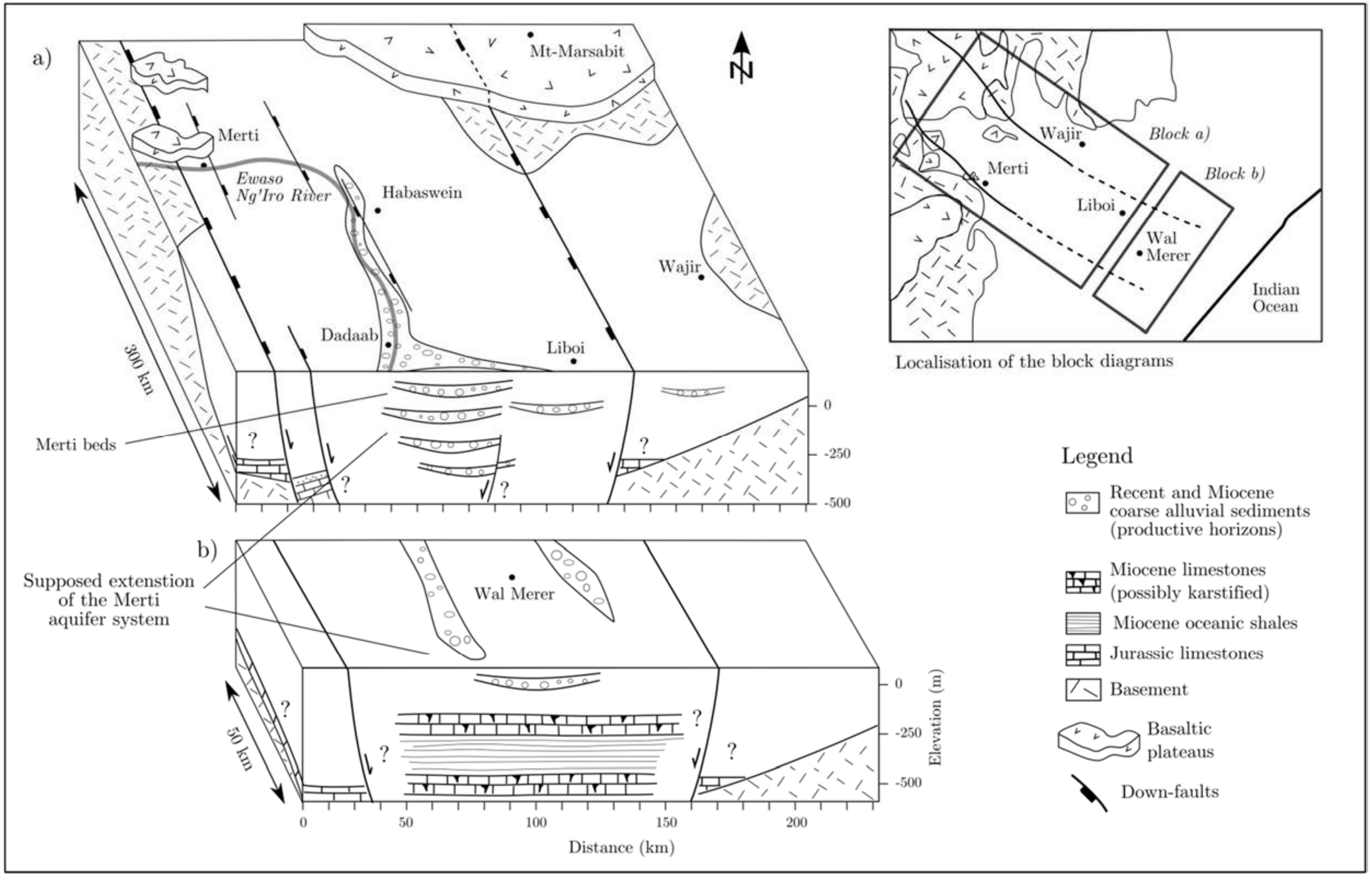

Fig. 2.6: Conceptual geological model of the Merti aquifer system. The basin is delimitated at its border by normal faults and, in some places, by tilted blocks associated to the rifting. Successive coarse horizons are likely to be found at several depths (block a). Within the lower part of the aquifer, Miocene limestones separated from marine shales are present at a depth of 250 and 500 m (block b). Beyond the limit of the graben, basement could be covered by few tens or hundreds meters of sediments. Coarse sediments dominate within the center of the basin while fine sediments proportion increases toward the border of the basin.

Granulometry and thickness tend to diminish from the center of the Merti aquifer toward the border. Beyond the major normal faults, over the shoulder of the basin, the aquifer is either delimited by basement rocks or is extended by thinner sedimentary basin (i.e. towards Wajir or west of Dadaab). Sediments over the shoulders of the basin were probably deposited in lower energy environments and are thus likely to have lower permeabilities.

At some locations, between the Tertiary sediments and the basement, Jurassic limestones may be found, either at the shoulder of the graben, as it is probably the case at a depth of around 1'000 m at Garissa (Nyagah, 1995) or as tilted blocks at both sides of the Ewaso Ng'Iro River at Merti. Because of either their depth or their distance to the freshwater lens, these limestones are probably not, or marginally, in hydraulic connection with the permeable layers of the Merti beds.

Within the lower part of the aquifer, the presence of possibly karstified Miocene limestones could lead to significantly higher transmissivity.

2.3 Hydrogeological characterisation of the Merti aquifer

The analysis of groundwater levels, transmissivities and electrical conductivity is used to refine the conceptual model based on the geology. Firstly, the regional piezometry is used to assess the dynamics of the aquifer on a large scale. Secondly, the temporal dynamics of the groundwater is assessed by mid-term observations of groundwater levels within the refugee camp area and by a high temporal resolution monitoring of groundwater level and electrical conductivities between September 2013 and March 2015. Then, the transmissivity and the specific capacity (the ratio between the water level and the drawdown) distribution allows to identify areas with a similar transmissivity and spatial trends of the transmissivity. The data from the monitoring network was also used to carry out a pumping test in order to characterise the aquifer and to identify possible underlying productive horizons not reached by boreholes. Finally, electrical conductivity and major ion distributions over the entire Merti aquifer are discussed and compared with the distribution of the transmissivities in order to confirm hypotheses.

2.3.1 Regional piezometry

The regional piezometric map (Fig. 2.7) was elaborated from static water level data. Since water levels are likely to vary over time, a piezometric map usually shows the hydraulic head distribution at a defined time. The various previous field campaigns led to a temporal "mosaic" of data which are not representative for a specific time window. However, considering the uncertainty of the terrain elevation (about 2-10 m), the low gradient of the groundwater table (less than 1‰ in the lower part of the aquifer) and the low variation of static water level (about 2 meters at the Dadaab refugee camp over the past 20 years), this data could be compiled and give an overview of the water table on a large scale. Furthermore, GIBB (2004) compared their own data with the ones of Swarzenski (1977) and Lane (1995) and they did not find significant differences between the water levels between these three temporal windows.

Additionally to recent data collected during this study, piezometric data are compiled from the following studies: Swarzenski (1977), Wanyeki (1979), Lane (1995) GIBB (2004), Earth-Water (2012). The data have been cleaned: erratic values have been removed, terrain elevation have been completed with the SRTM digital elevation model for the missing values. Furthermore, values have been sorted between the deep aquifer and local perched aquifers. All the data are available in the appendix A.

A major continuous and mostly confined aquifer is considered from Mt-Marsabit foothill, up to Liboi. Downstream of Liboi, the groundwater levels are not documented. However, in the south-southwest, despite the lack of data, the ocean is considered as the "final" limit of the aquifer. Laterally, the aquifer is limited westerly and northerly by the contact between the basement and the sedimentary formations. Between Yamicha and Liboi, the water table is generally located about 110 to 130 m below the terrain surface. Over the Lorian Swamp, this unsaturated zone thickness decreases dramatically up to 20-30 m.

The Merti aquifer presents an overall slightly low gradient over most part of the aquifer. Between Habaswein and Dadaab, the gradient is around 0.7 ‰. Downstream of Dadaab, the gradient becomes very low with a slope of 20 m for about 200 km, giving a value of 0.1‰. This observation is consistent with the hypothesis that the Miocene limestones are karstified, increasing the transmissivity and lowering the groundwater base level (Fig. 2.6, block b).

Northwest of Habaswein, piezometric lines become closer to each other over the Lorian Swamp area, revealing a groundwater "bulge". This observation is consistent with the hypothesis that recharge mainly takes place over the Lorian Swamp. The higher observed hydraulic gradient could also be explained by possible lower hydraulic conductivity over this area.

Upstream, from Hadado, the aquifer becomes shallower and possibly unconfined. The hydraulic gradient remains low up to the foothill of the Mt-Marsabit volcanic plateau, except a band south of the Yamicha basaltic plateau. The higher gradient at this location could either be explained by higher local recharge or by a smaller transmissivity of the aquifer. The groundwater level beneath the Mt-Marsabit is not known. The absence of boreholes over this location (personal communication from ICRC[1] staff) suggests that groundwater is hardly exploitable because of its depth or small hydraulic conductivity.

---

[1] International Committee of the Red Cross

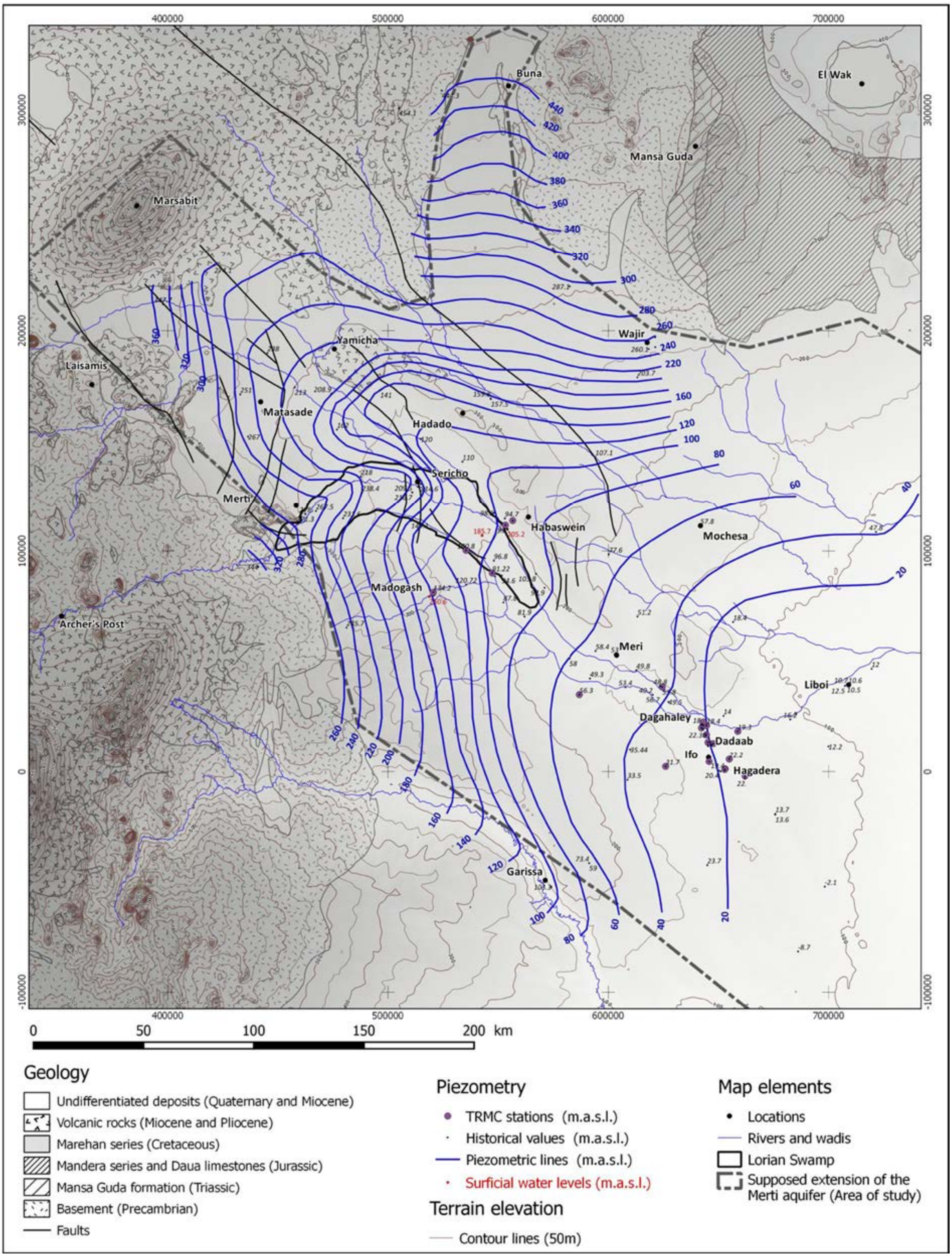

Fig. 2.7: Regional piezometric map of the Merti aquifer based on data from Swarzenski and Mundorff 1977, Lane 1995, GIBB 2004 and own data.

West of the Merti aquifer, towards the basement, piezometric lines become closer than on the central Merti aquifer. This feature is interpreted by lower transmissivities values, resulting of lower hydraulic conductivities or lower aquifer thickness.

The north of the basin between Hadado and Buna is poorly documented. It is separated from the main Merti aquifer by the Lagh Bogal fault. Despite the small number of boreholes on both sides of the fault, no evidence of hydraulic discontinuity is observed between these two basins. The higher gradient over this region suggests that transmissivity is moderate or low.

2.3.2 Mid-term groundwater level evolution at the Dadaab refugee camp

A major compilation of groundwater level data was carried out by GIBB (2004) for the period 1994-2003 for 14 boreholes within the refugee camp area (Dagahaley, Ifo and Hagadera). This compilation shows that most of the water levels decreased less than one meter during this period. The graphics from GIBB are reprinted in Appendix B.

For the Dagahaley boreholes, water level decrease ranges between 0.5 and 1.3 meters. One borehole (Dagahaley 4) was decommissioned in May 2002 and regained, in a single year, the pre-pumping level of 1994. At Ifo, the pumping of groundwater started in 1998. Before this year, water levels show fluctuations of half a meter. Then, until summer 2000, the level decreased by 0.6 to 0.7 m and finally stabilised or even slightly increased again by 0.3 m. At Hagadera, between 1995 (year of commissioning) and June 2001, the water level decreased by 0.2 to 0.9 m and then stabilised until summer 2003. It is interesting to note that even if most of borehole's water levels are inversely linked to the abstraction rates, water levels in some boreholes increase or stabilise while abstraction rates are maintained (Ifo 1 from Jan. 2000, Hagadera 2, 3 and 5 from Jul. 2001), or even increased (Dagahaley 6 from Feb. 2001, Ifo 2 from Jun. 2000, Ifo 5 Jun. 2001, Ifo 6 from Jan. 2001). This observation leads to two possibilities: firstly, this behaviour may be due to erratic values caused by the manual measuring of water levels (for instance inconsistency of the measurement during dynamic or static water level), or secondly, due to changes in pumping in boreholes close to the ones observed.

Without long term observations, and because of the thick unsaturated zone, it is difficult to link the groundwater level variations to recharge dynamics. Furthermore, the high pumping rates within the camps may locally significantly influence the dynamics of the water levels and make difficult to separate the influence of pumping to the influence of local or regional recharge. However, it seems unlikely that the aquifer, in its downstream part, reacts quickly to recharge events since the major event of 1998 (the second major event between 1949-2011) is not recorded by the piezometry. The nearest next increase of water levels are those observed since 2000 but it is not possible to say if these increases are related to the 1998 recharge event or to an older one.

2.3.3 High temporal resolution monitoring of water level and electrical conductivity

Annual evolution of groundwater level and salinity has been observed between September 2013 and March 2015 thanks to a network of twenty monitoring devices, distributed over the entire freshwater lens (Fig. 2.8) and measuring the water pressure and the electrical conductivity. The monitoring devices measure every 15 minutes the groundwater level with immerged pressure probes in boreholes and the electrical conductivity (EC) with EC probes installed in the rising mains. The daily maximum water level is extracted. EC values are extracted during pumping (when the rising main is full of water), that is at daily minimum water level. EC values outside periods of pumping are not considered.

Within the framework of this project, nine devices were installed within the Dadaab refugee camp and eleven in the upper part of the aquifer, between the Lorian Swamp and the refugee camp area. Five of them, without pumping, are used as observation stations for monitoring the undisturbed static groundwater levels (Gurufa BGP BH, Dagahaley BH 3 (old), Dagahaley BH 9 (old), Mathagissa Jica BH and Kambioos BH 2).

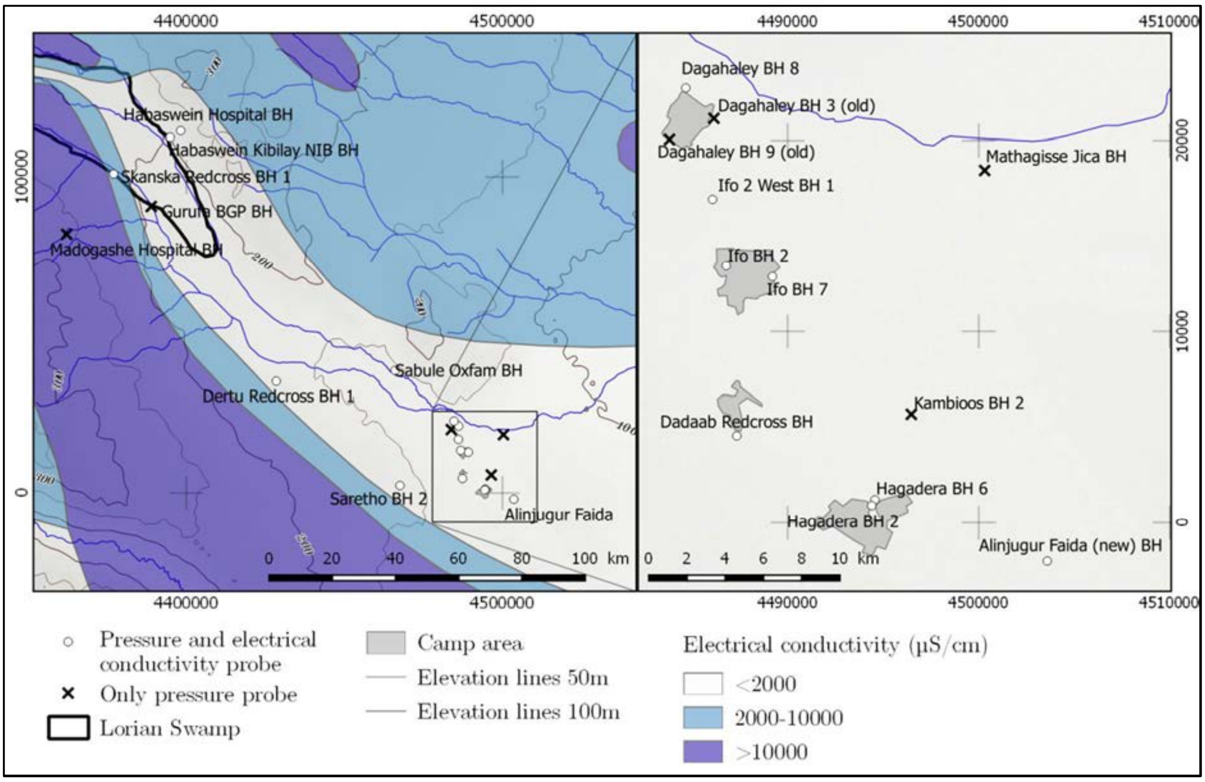

Fig. 2.8: Groundwater monitoring network, showing the location of the 20 monitoring devices. They are located within the Merti aquifer freshwater lens, between the major supposed recharge area of the Lorian Swamp and the Dadaab refugee camp. The zoom on the right side of the figure shows the distribution of the 9 devices within the Dadaab refugee camps.

Groundwater static levels over the Merti aquifer show a great stability during the recorded period, with up to 10-20 cm variation (Fig. 2.9). Only the Madogashe Hospital borehole shows a bigger variation of up to 2 meters, which may be explained by lower transmissivity of this boreholes (1.2 10^{-4} m^2/s), that is more than one order of magnitude lower than the other boreholes.

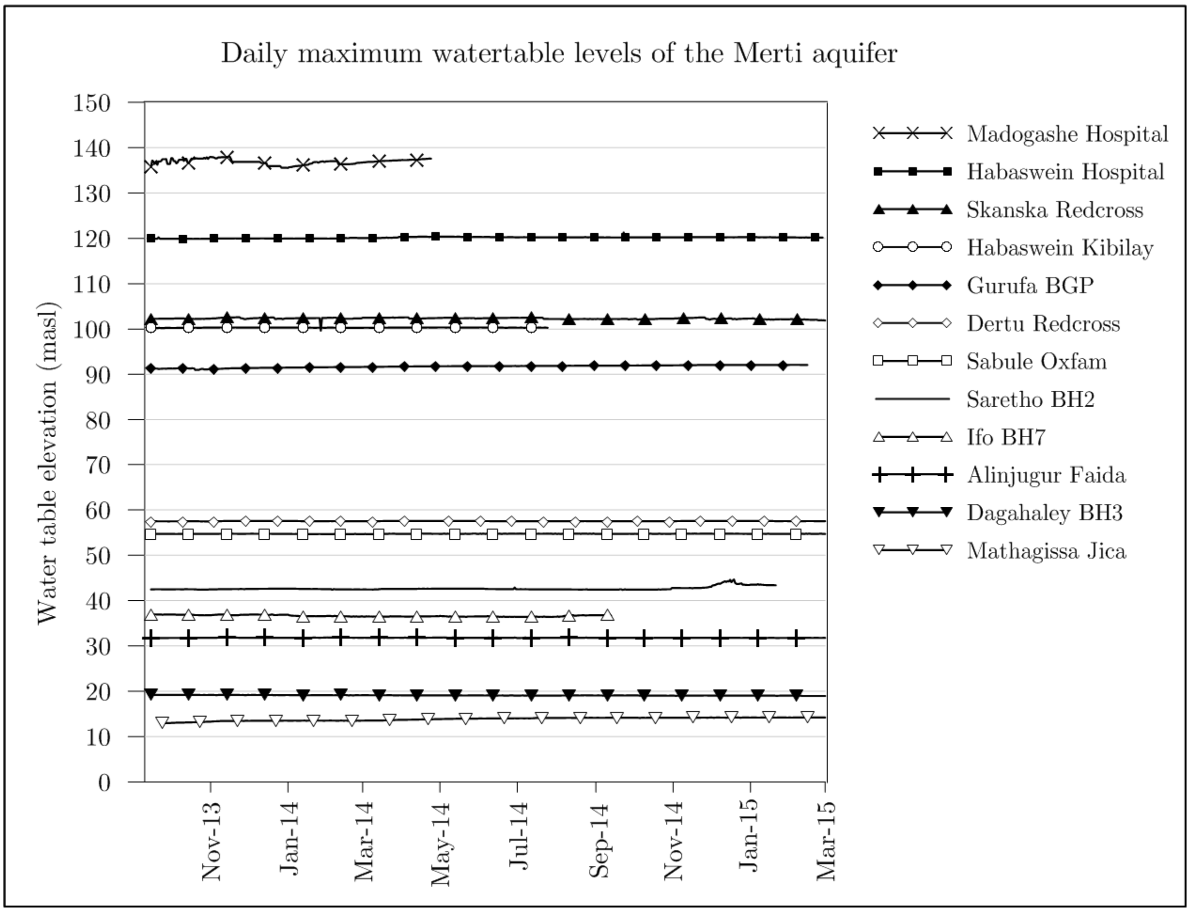

Fig. 2.9: Water table elevations of observation stations over of the Merti aquifer. In the lower part, only representative stations are selected.

On a smaller scale, the analysis of individual borehole water level data did not point out significant groundwater level depletion or irrefutable recharge events. Eight relevant graphs are discussed below (Fig. 2.10 to Fig. 2.17). The rest of the graphs are presented in Appendix C. These graphs show the daily minimum and daily maximum water levels as well as the EC during pumping for boreholes equipped with pumps.

The borehole at Habaswein Hospital (Fig. 2.10) shows a slight increase of 30 cm of the water level at the end-March 2014. This increase could either be the effect of local recharge or due to pumping rate changes in the boreholes or in a near borehole. Between February and March 2014, the borehole was exploited every day, which is illustrated by the constant difference between maximum and minimum water levels. After this period, at the end of March 2013, pumping did not take place every day (daily minimum water level curve is close to the daily maximum water level curve), allowing the static water level to rise. Furthermore, this period of groundwater level increase was preceded by precipitation that possibly caused groundwater recharge. The EC during pumping days remains fairly stable around 1’275 µS/cm.

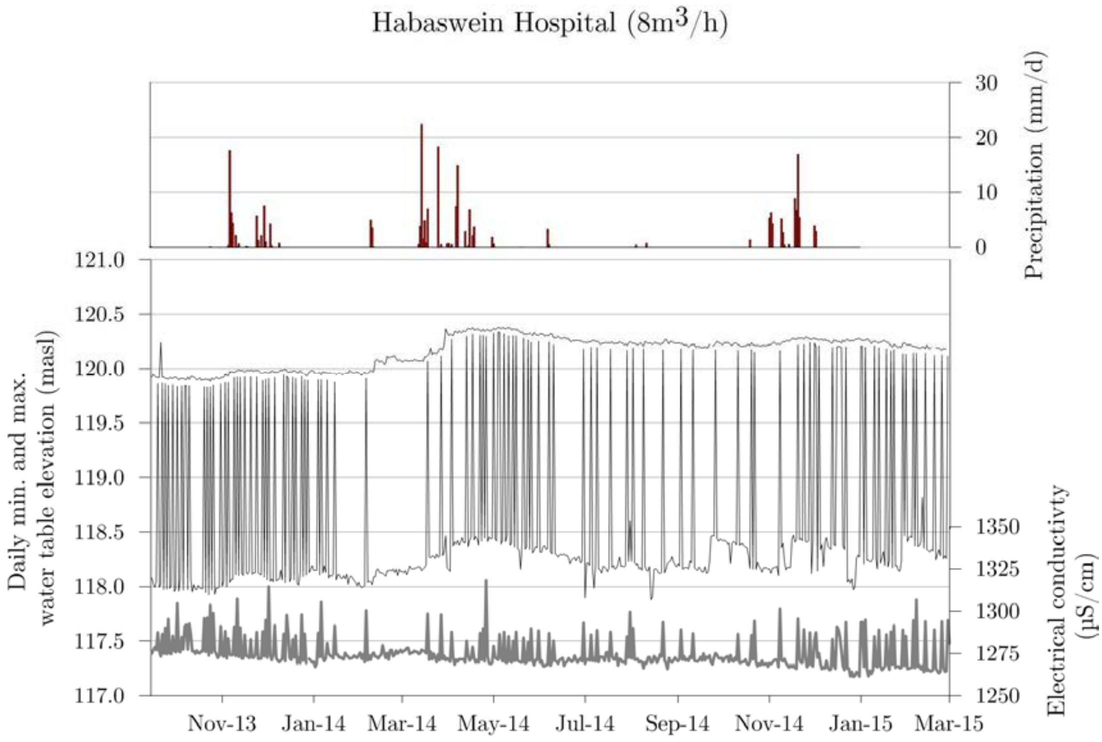

Fig. 2.10: Groundwater monitoring at Habaswein Hospital. Daily minimum and maximum water levels (static water level) and electrical conductivity measured in the rising main. Precipitations are extracted from the FEWS-net data (http://www.fews.net/).

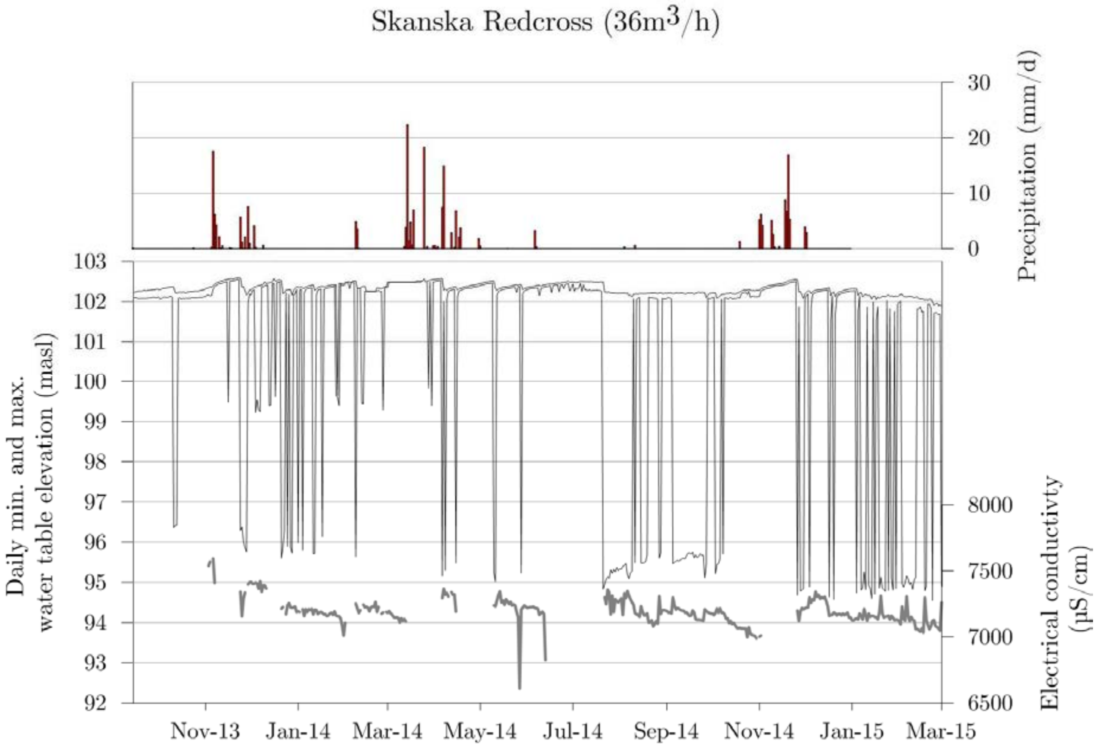

Fig. 2.11: Groundwater monitoring at Skanska Redcross. Daily minimum and maximum water levels (static water level) and electrical conductivity measured in the rising main. Precipitations are extracted from the FEWS-net data (http://www.fews.net/).

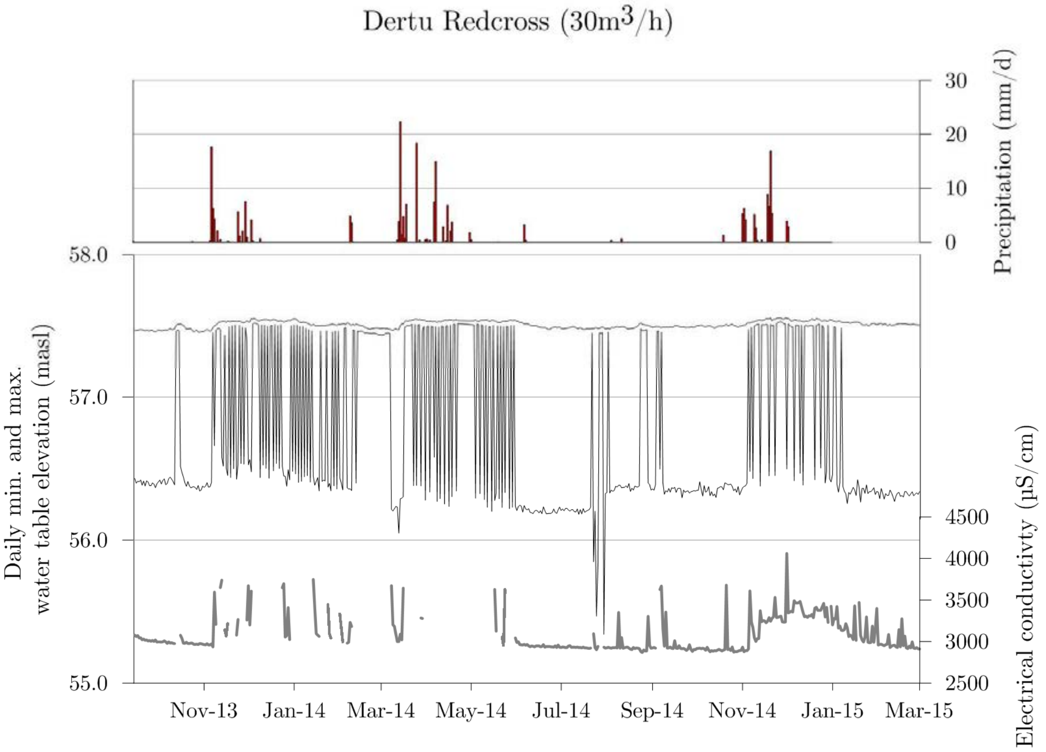

Fig. 2.12: Groundwater monitoring at Dertu Redcross. Daily minimum and maximum water levels (static water level) and electrical conductivity measured in the rising main. Precipitations are extracted from the FEWS-net data (http://www.fews.net/).

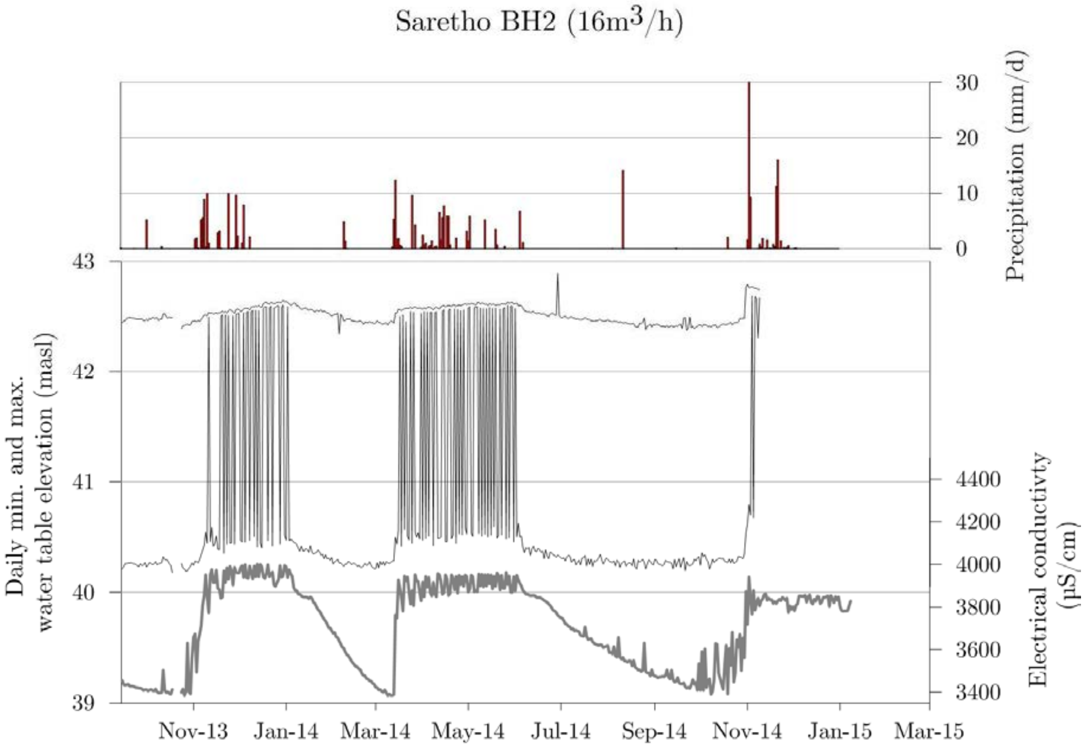

Fig. 2.13: Groundwater monitoring at Saretho BH2. Daily minimum and maximum water levels (static water level) and electrical conductivity measured in the rising main. Precipitations are extracted from the FEWS-net data (http://www.fews.net/).

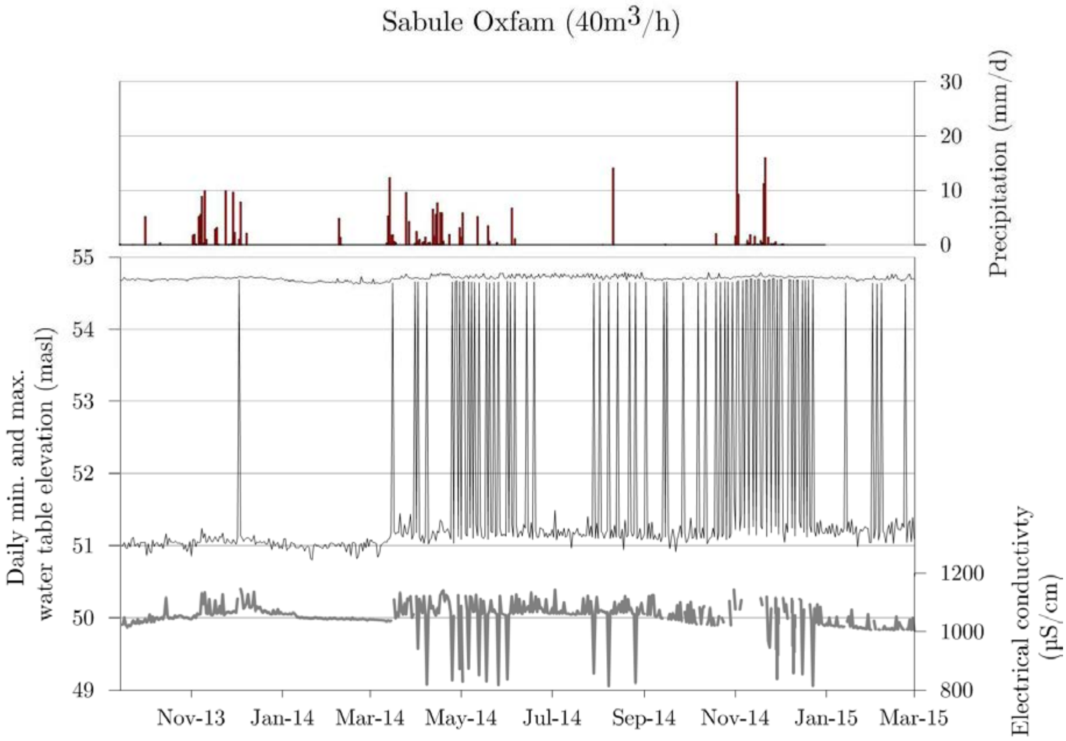

Fig. 2.14: Groundwater monitoring at Sabule Oxfam. Daily minimum and maximum water levels (static water level) and electrical conductivity measured in the rising main. Precipitations are extracted from the FEWS-net data (http://www.fews.net/).

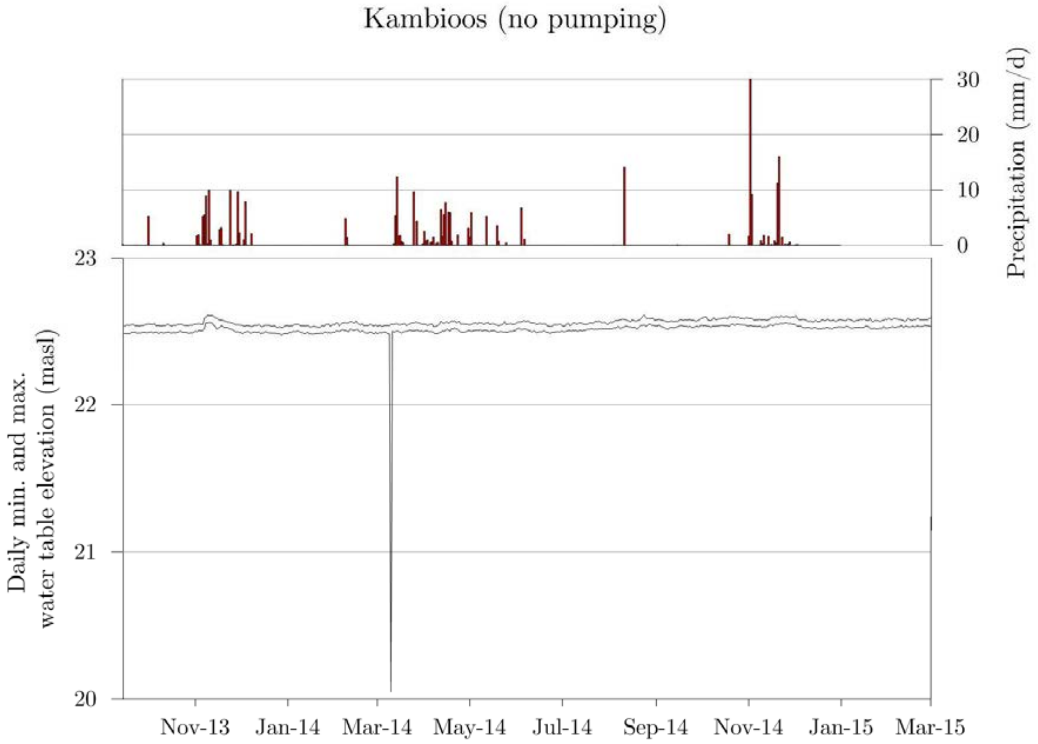

Fig. 2.15: Groundwater monitoring at Kambioos. Daily minimum and maximum water levels (static water level). Precipitations are extracted from the FEWS-net data (http://www.fews.net/).

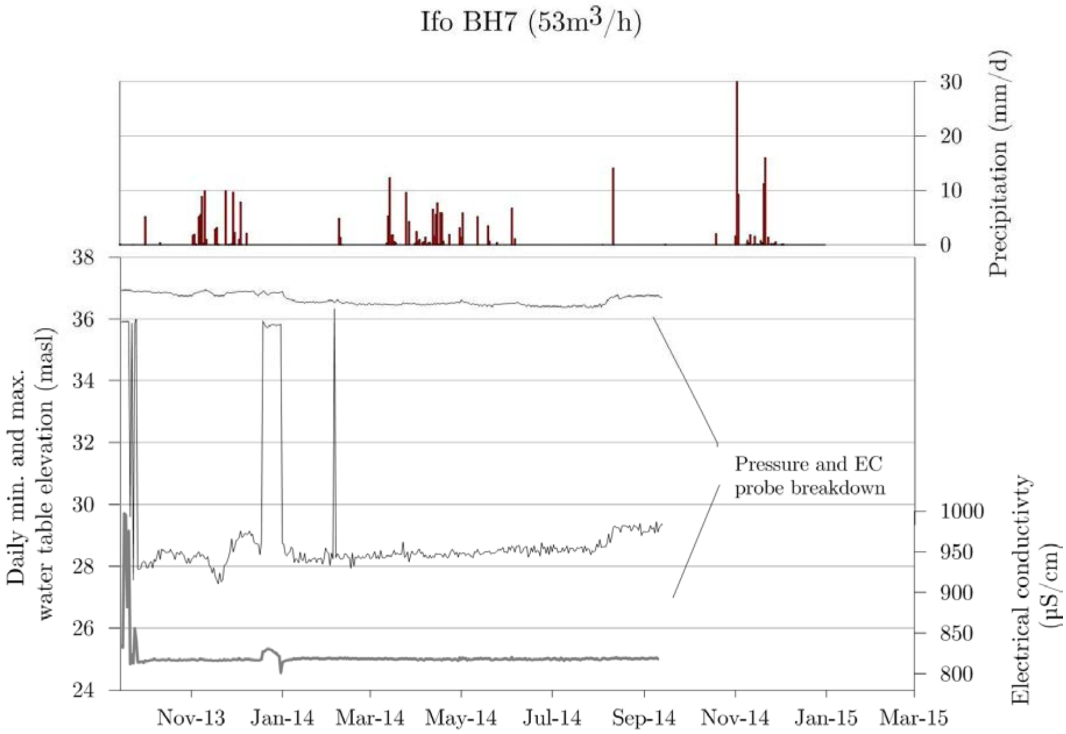

Fig. 2.16: Groundwater monitoring at Ifo BH7. Daily minimum and maximum water levels (static water level) and electrical conductivity measured in the rising main. Precipitations are extracted from the FEWS-net data (http://www.fews.net/).

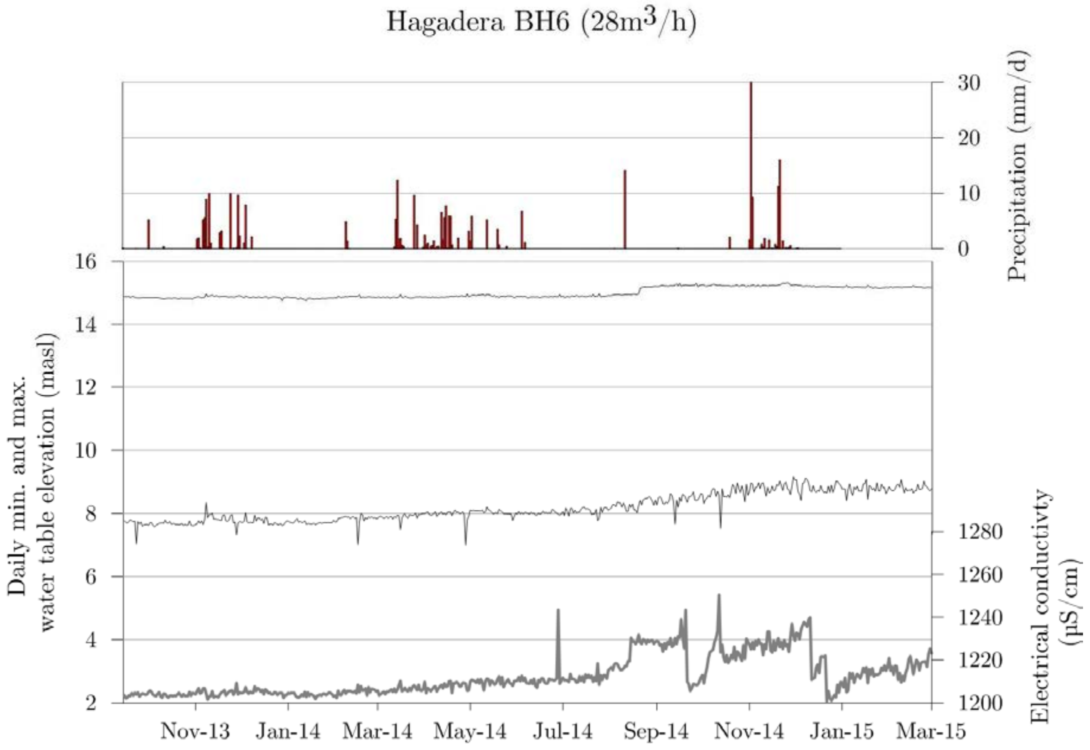

Fig. 2.17: Groundwater monitoring at Hagadera BH6. Daily minimum and maximum water levels (static water level) and electrical conductivity measured in the rising main. Precipitations are extracted from the FEWS-net data (http://www.fews.net/).

At the Skanska Redcross borehole (Fig. 2.11), which is located close to Habaswein, but at the edge of the freshwater lens area, the static water level is also influenced by the rate of pumping: periods without pumping (when daily minimum and maximum water level curves are close) show a slight increase of water level before it falls when pumping starts again. EC at this location (around 7'000 µS/cm) is significantly higher than in other stations, confirming the presence of a brackish area between the freshwater lens area and the surrounding saline water, but remains fairly stable.

Also close to the brackish limit, at Dertu Redcross and Saretho (Fig. 2.12 and Fig. 2.13), electrical conductivities range between 3'000 and 3'800 µS/cm. The EC at Saretho decreases of about 400 µS/cm during period for which pumping takes place every day, as between January and March 2014 and between April and November 2014. This indicates, that, at this location, high pumping rate periods mobilise fresher groundwater than period of non-daily pumping. Static water levels show little variation (20 cm) between periods of high and low pumping rates.

The Sabule Oxfam borehole (Fig. 2.14), which is located in the middle part of the Merti aquifer, also shows very stable daily minimum and maximum water level. As for Saretho, the EC shows a slight decrease between January and March 2014 and between end-December 2014 and March 2015, which is also interpreted as a mobilisation of fresher groundwater during high pumping rate.

In the lower part of the aquifer (around the Dadaab refugee camp), the Kambioos observation station (Fig. 2.15) also indicates very little variation of the groundwater level. This borehole is not in use and was equipped by the monitoring devices in order to observe the undisturbed groundwater level evolution. The peak in early-March 2014 is probably due to a short period of pumping in the boreholes.

The Ifo BH7 and the Hagadera BH6 boreholes (Fig. 2.16 and Fig. 2.17) also show very little variation of the groundwater levels. Concerning the EC, it remains stable for the Ifo BH7 but becomes instable at the Hagadera BH6, with values between 1'200 and 1'250 µS/cm. These variations, even moderate, could either be interpreted as the sensitivity to salinization of the groundwater near the brackish area or by an alteration of the EC probe.

2.3.4 Transmissivity and specific capacity

Only few complete pumping tests have been carried out on the Merti aquifer with the Theis method by Wanyeki (1979), Lane (1995) and GIBB (2004). Additional estimations of transmissivity is established with the Dupuit formula (Eq 2.1) using discharge rate and drawdown data at the boreholes monitored with the monitoring devices. The radius of the boreholes (r_1) were estimated to be 10 cm and the radius of influence (R) to be 25 m. Due to the logarithmic function involved in this formula, the radius of influence does not significantly influence the transmissivity estimation.

$$T = \frac{Q}{2\pi S_0} \ln\left(\frac{R}{r_1}\right) \qquad (2.1)$$

With: T = Transmissivity (m^2/s)
Q = Pumping rate (m^3/s)
S_0 = Drawdown (m)
R = Radius of influence (m)
r_1 = Radius of the borehole (m)

Computed transmissivities with the Dupuit method show values ranging between 3 x 10^{-4} and 3 x 10^{-3} m^2/s (Table 2.1) while previous estimations range between 2 x 10^{-4} and 5 x 10^{-3} m^2/s. The highest values are found in the lower part of the Merti aquifer at Liboi and around the Dadaab refugee camps but also in Merti (Fig. 2.18). The large variation of transmissivities within these areas reveals the impact of the boreholes penetration into the aquifer but also, especially in Merti, the spatial variability of the aquifer hydrodynamical properties. Pumping tests carried out at Ifo BH8 by Milnes (2010) indicates a transmissivity of 7.4 x 10^{-3} m^2/s, that is close to the maximum value (Dertu Redcross) measured in previous studies. Borehole logs do not indicate the depth and length of the screened section. However, this section is assumed to be located within the productive layer of the aquifer, with a length of about 20-30 m.

Well	Madogashe hospital	Habaswein Kibilay	Habaswein hospital	Skanska Redcross	Dertu Redcross	Sabule Oxfam	Saretho BH2
So	2	2	2	6	1	3.5	2
Q (m^3/h)	1	10	8	36	30	40	16
Q (m^3/s)	0.0003	0.003	0.002	0.010	0.008	0.011	0.004
T (m^2/s)	1.2 x 10^{-4}	1.2 x 10^{-3}	9.8 x 10^{-4}	1.5 x 10^{-3}	7.3 x 10^{-3}	2.8 x 10^{-3}	2.0 x 10^{-3}

Well	Dagahaley BH8	Ifo2 west BH1	Ifo BH2	Ifo BH7	Dadaab Redcross	Hagadera BH2	Hagadera BH6
So	5	4	6	9	2.5	11	7
Q (m^3/h)	27	56	30	56	16	40.5	28
Q (m^3/s)	0.008	0.016	0.008	0.016	0.004	0.011	0.008
T (m^2/s)	1.3 x 10^{-3}	3.4 x 10^{-3}	1.2 x 10^{-3}	1.5 x 10^{-3}	1.6 x 10^{-3}	9.0 x 10^{-4}	9.8 x 10^{-4}

Table 2.1: Transmissivity estimated with the Dupuit formula. Drawdown *So* is measured with the monitoring devices. *Q* was noted during the reconnaissance and implantation mission. Radius of boreholes is estimated at 0.1 m. Based on borehole logs, the exploited aquifer thickness is estimated at 40 m. Radius of influence is estimated at 25 m. Sources: Wanyeki (1979), Lane (1995) and GIBB (2004).

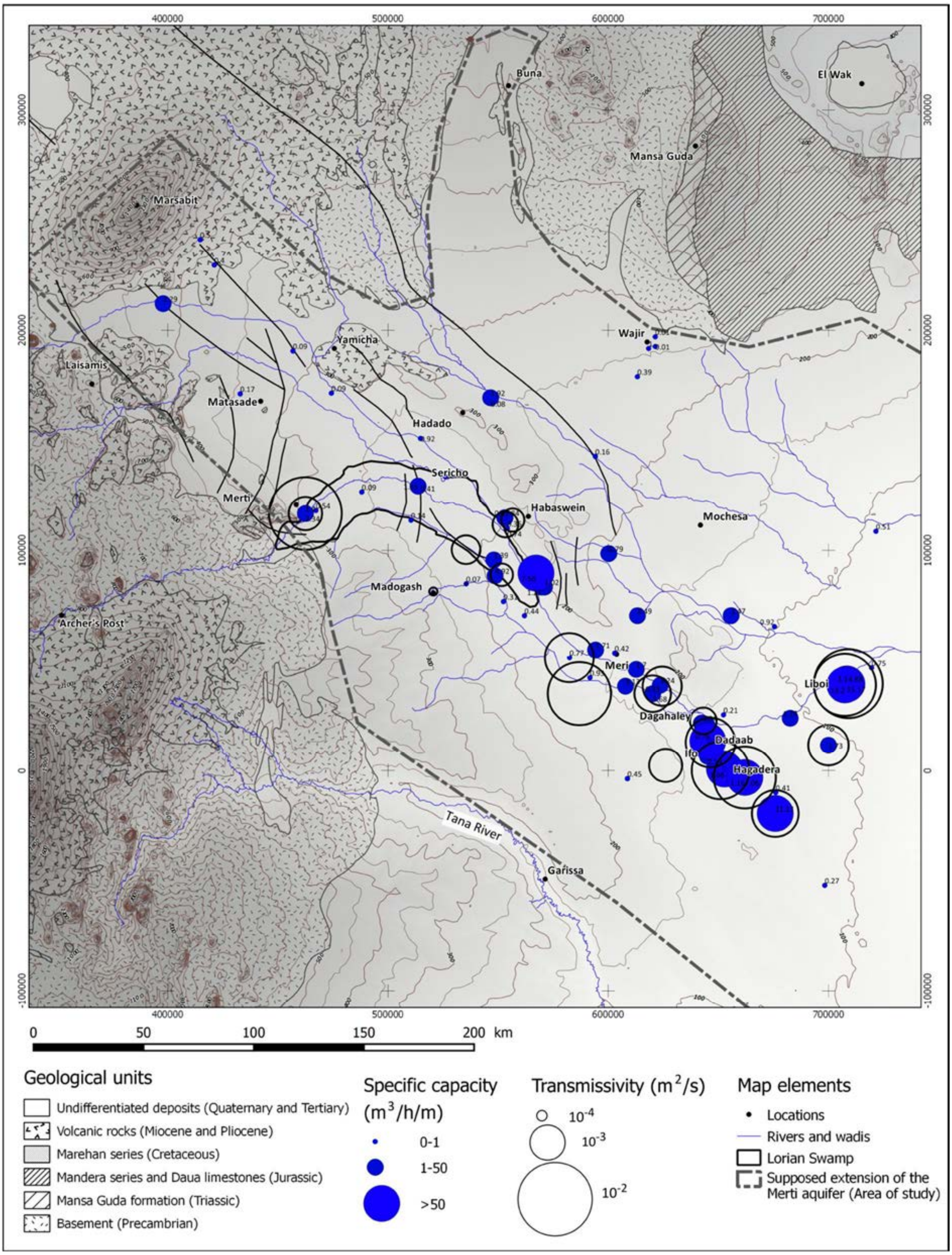

Fig. 2.18: Specific capacity and transmissivity map. Source: Wanyeki (1979), Lane (1995) and GIBB (2004) and own data.

Assuming a transmissivity of 7.4 x 10^{-3} m^2/s, an aquifer width of 50 km (the width of the freshwater lens) and a gradient of 0.7 ‰ between Habaswein and Dadaab, the underflow through the exploitable horizon of the aquifer (the Merti beds) is around 8 x 10^6 m^3/y. This value is slightly higher than the previous estimations which range between 2.6 and 4.7 x 10^6 m^3/y (see section 1.4, Table 1.1). Available drilling logs are reproduced in Appendix D.

Because of the few pumping tests, the transmissivity distribution is completed with the specific capacity values, which is the ratio between abstraction rate and drawdown (Eq 2.2). Specific capacity is expressed in $m^3/h/m$ or m^2/h.

$$S_c = \frac{Q}{S_0} \qquad (2.2)$$

Where : S_c is the specific capacity ($m^3/h/m$)
Q is the abstraction rate (m^3/h)
S_0 is the drawdown

Even though this data is less informative than transmissivity, it allows to make relative comparison on a large scale using the maximum available data (Fig. 2.18). The distribution of the specific capacities confirms partly the observation based on transmissivities, with high values at Liboi and around Dadaab, but also south of Habaswein. The high transmissivity values found at Merti and east of Meri are not clearly identified with the specific capacity approximation.

However, the specific distribution reveals a concentration of high values along the Hagadera – Meri axis, which extends up to Habaswein and Sericho with more intermediate values. On the western side of the aquifer (at Matasade, between Sericho and Merti, towards Madogash and west of Ifo), very low values are found (about 3 orders of magnitude lower) confirming the hypothesis of a lower transmissivity zone suggested by the piezometric analysis.

Additionally, it should also be noticed that newer boreholes give higher specific capacity values either because of a deeper aquifer penetration or because older boreholes could suffer from degradation or clogging, leading to well losses.

2.3.5 Storativity and pumping test interpretation

A more detailed pumping test interpretation was carried out with data from the Dagahaley BH3-old monitoring station (Fig. 2.8). This monitoring station is located 10 m close to the Dagahaley BH3-new (which is not equipped with a pressure probe) and allows to carry out pumping test. However, because of the poor time resolution (15 min), the beginning of the curve is difficult to define precisely and could lead to uncertainty of the parameter fitting, in particular of the determining of the transmissivity and the storativity.

Nevertheless, despite this data limitation, the analysis of the behaviour of the drawdown and derivative curves allows to identify two possible analytical aquifer models consistent with the observed data. These models are the infinite linear constant head boundary model and the leaky aquifer model. Since there is no surface water which could impose a constant head boundary close to the borehole, the model of a leaky aquifer is accepted. The model of the leaky aquifer is also known as the Hantush and Jacob solution (1955) which describes the drawdown of a confined aquifer recharged by an overlying or underlying aquifer (the drained layer) through a confining aquitard layer. Further descriptions of these analytical models, including the two above-mentioned models and the diagnostic methodology is discussed by Renard et al. (2009). This result supports the presence of a multi-layer and confined aquifer, as it was suggested by the geological interpretation (Fig. 2.5 and Fig. 2.6). This model is illustrated in Fig. 2.19 below.

If this model is confirmed, the Merti aquifer should be considered as an aquifer system composed of several permeable layers, of which the first is the Merti beds.

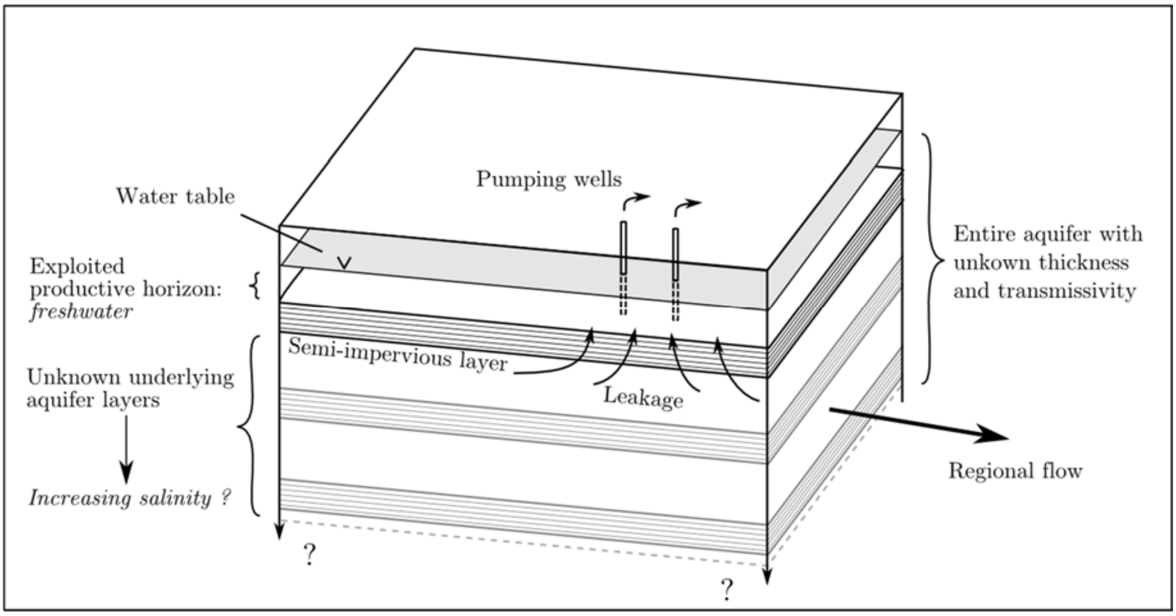

Fig. 2.19: Schematic bloc diagram of a section of the Merti aquifer illustrating the known exploited productive layer (the Merti beds) of the aquifer as well as the possible deeper productive layer constituting the entire Merti aquifer system.

The solution of the model also indicates a transmissivity and a storativity of around 1.2 x 10^{-3} m^2/s and 3.5 x 10^{-3} respectively. Given a screened length of the well of 40 m, the estimated hydraulic conductivity is about 3 x 10^{-5} m/s. As mentioned above, these values should be considered with care because of the rough time resolution of the data. Drawdown and diagnostic plot of the pumping test are shown in Fig. 2.20. Complete results of the model are given in Appendix E. Assuming a hypothetic aquitard thickness of 20 m, the computed solution indicates an aquitard conductivity of 1.2 x 10^{-5} m/s.

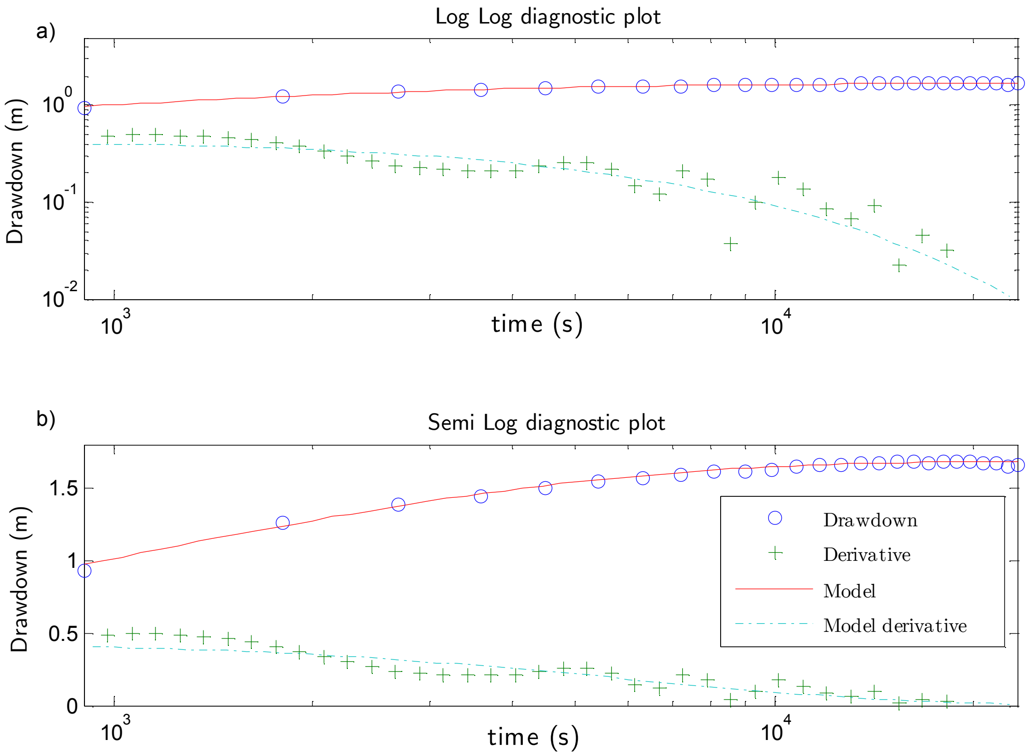

Fig. 2.20: Drawdown data (circles) and its derivative (crosses) of the Dagahaley BH3-old borehole during pumping on the 2nd of October 2013. The observed data are well reproduced by the Hantush and Jacob (1955) solution for a leaky aquifer. Data are plotted on log-log scales (a) and semi-log scale (b).

The Hantush and Jacob solution does not allow to estimate directly the transmissivity of the drained layer but it could be approached using the hypotheses of validation of the Hantush and Jacob solution developed by Neuman & Witherspoon (1969). These hypotheses postulate that the Hantush and Jacob solution remains valid as long as the hydraulic head in the drained layer does not decline. This condition is assumed to be valid if the pumping time is short enough as formulated in Eq 2.3:

$$t < \frac{S'(b')^2}{10bK'} \qquad (2.3)$$

or if the drained layer is thick enough (Eq (2.4)

$$b''K'' > 100bK \qquad (2.4)$$

where

t	time since pumping began (s)
S'	storativity of the aquitard (-)
b	thickness of the confined layer (m)
K	hydraulic conductivity of the confined layer (m/s)
K'	vertical hydraulic conductivity of the aquitard (m/s)
K''	hydraulic conductivity of the drained layer (m/s).
b'	thickness of the aquitard (m)
b''	thickness of the drained layer (m)

Looking at the drawdown and derivative curves in Fig. 2.20, one can assume that the model fairly well reproduces the observations and that one of these two conditions is valid. The first condition, based on the pumping duration, is difficult to assess because of the uncertainty related to the parameters of Eq 2.3. However, a guess with conservative values (Table 2.2) indicates that this time-based condition is not met after a pumping period longer than 6 minutes. This indicates that the drained aquifer transmissivity condition (Eq (2.4) should be true, or partially true.

b	b'	S'	K'	t (s)	t (min)
20 m	20 m	0.002	1.2×10^{-5}	3.33×10^{2}	6

Table 2.2: Estimation of the time for which the time-based condition of the Hantush and Jacob solution is valid. The b' and K' parameters are obtained from the pumping data interpretation illustrated in Fig. 2.20. The S' is estimated by multiplying the hypothetic thickness of the aquitard by a typical storativity value of 1×10^{-4} 1/m.

However, as discussed above, the uncertainties on the confining aquitard and the rough time resolution of the drawdown data at the beginning of the pumping implies to consider this approach with care. Nevertheless, the observation that the model reasonably fits the drawdown curve after almost 6 hours of pumping (that is 60 times the time computed in Table 2.2) supports the hypotheses of a high transmissive underlying aquifer below the exploited one.

In order to confirm this hypothesis, it would be necessary to carry out longer pumping tests with adequate time resolution measurements in various boreholes.

2.3.6 Electrical conductivity map and major ions

Electrical conductivity has been measured at numerous boreholes within the Merti aquifer over the last 60 years, providing a large overview of the mineralisation of the groundwater. Groundwater mineralisation is subdivided into three classes: a) freshwater (up to 2’000 µS/cm); b) moderately mineralised, or brackish (from 2’000 to 10’000 µS/cm); c) highly mineralised, or saline (greater than 10'000 µS/cm). Changes in EC since 1957 show locally significant variation of the salinity but all the sampling points (except Hadado and Garbatula) stay within the same class. This observation allows to elaborate a map showing the regional distribution of the salinity within the Merti aquifer (Fig. 2.21).

Spatial distribution of electrical conductivities

This distribution confirms the presence of a freshwater area along the Habaswein – Dadaab – Liboi axis. Along this axis, values are particularly low, mainly below 1000 µS/cm. North of this axis, groundwater is moderately mineralised with exceptions at some locations, for instance in Diff and along the Lagh Bogal wadi, between Wajir and Habaswein.

Southwest of the Habaswein – Dadaab – Liboi axis, groundwater is highly mineralised with values between 10'000 µS/cm and 20'000, and even up to 36'000 µS/cm at Garissa. From this point of view, the Tana River (Fig. 2.18) seems to be disconnected from groundwater, avoiding groundwater recharge from the Tana River.

The area of the Lorian Swamp is less uniform than the rest of the aquifer. The central corridor of the Lorian Swamp from Merti to Sericho is characterised by quite low EC but closely flanked by moderate to high EC values. This is interpreted by a possibly recurrent input of freshwater along this path, replacing locally saline groundwater by fresh water. However, the close high EC values along this path suggest a relative low permeability around this area, avoiding a further propagation of the fresh water.

Upstream of Yamicha and Matasade, EC values are moderate. This upper limit between intermediate and low EC possibly coincides with the former limit of sea water influence.

Variations of electrical conductivities over time

Generally, temporal variations of electrical conductivities over the aquifer are lower than the spatial variations between the different fresh, brackish and saline water zones. Evolution of the salinity should be interpreted carefully since EC values could have been sampled from several boreholes at a same location because of the numerous boreholes and their replacements.

Fig. 2.21 shows that boreholes located within the freshwater lens show variable changes of the EC over time. Some of them indicate a small decrease of the salinity of about 100-200 µS/cm (Shantabak, Kumahumato, and Alinjugur) or slight increases of about 150 µS/cm (Wal Merer). Locations with numerous boreholes (Habaswein, Liboi, Ifo and Hagadera) show significant variability of the EC (up to 400 µS/cm) over the time but also at a same time, possibly because of the variability in the borehole penetration depths. The slight increasing trend of EC observed, could indicate a migration of brackish water because of the high rate of pumping at these locations (several m^3/h by borehole, for a total of 3.5×10^6 m^3/y for the entire Dadaab refugee camps). However, the increase at each of these locations remains lower than the difference between the maximum and minimum value (difference = 200 µS/cm at Habaswein and Ifo, and 300 µS/cm at Hagadera).

In Dadaab, where boreholes are less numerous, EC show more homogenous values. Considering the measurement since 1990, the salinity increases progressively by 300 µS/cm. At Dimanyale, the EC increased dramatically of 400 µS/cm since 1970.

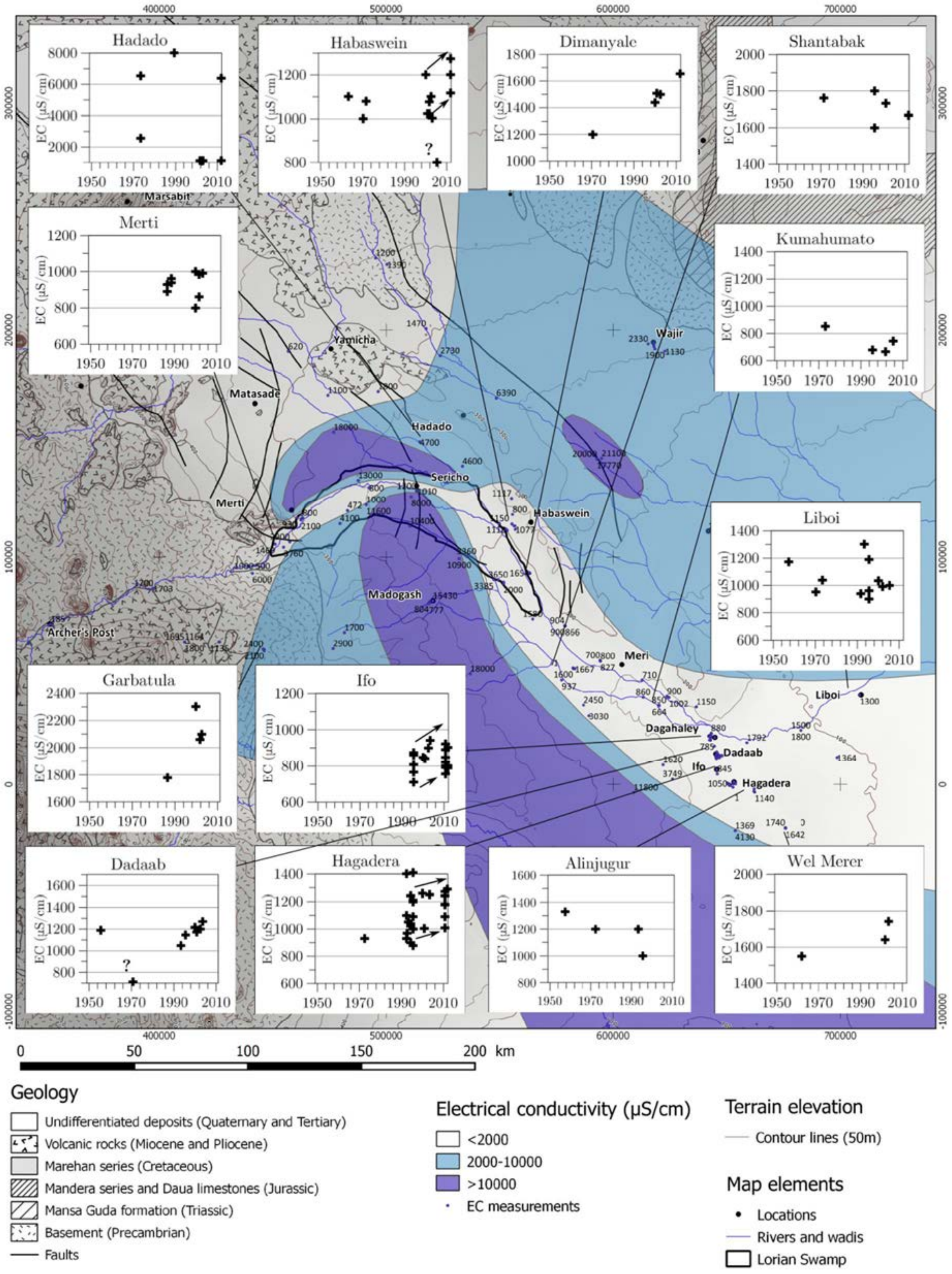

Fig. 2.21: Electrical conductivity map of the Merti aquifer and long term electrical conductivity (EC) time series for selected locations. Three classes of mineralisation are derived from the EC data: fresh water (up to 2'000 µS/cm), moderately mineralised (from 2'000 to 10'000 µS/cm) and highly mineralised (>10'000 µS/cm). Because of commissioning and decommissioning of boreholes over time, EC time series at each location are compiled from several different boreholes. On the regional scale, the temporal variation of EC is lower than the variation between classes. Source: Lane (1995), GIBB (2004) and own data.

Close to the salinity class limits, as at Hadado and Garbatula, variations are significant. The differences of EC at Hadado (from 1'500 to 8'000 µS/cm) are probably due to the different boreholes depths that were sampled and to the influence of the saline water body in the west, that could induce high lateral and vertical heterogeneity of the EC. Additionally, the lowest EC values (1'500 and 2'400 µS/cm) suggest the probable continuation of the main water-bearing formations (Fig. 2.6) which is found downstream. At Garbatula, the borehole is located within the basement and is thus more vulnerable to water quality degradation related to pumping.

The temporal and spatial distribution of the EC supports the hypothesis of a relative stable aquifer on the large scale, with local significant variations at the border of the freshwater lens or related to the different boreholes penetration depths and long term exploitation, by the migration of underlying more mineralised water. However, the exact depth of this supposed underlying mineralised water is not documented by the data available. The implications for the exploitation of the groundwater for the Dadaab refugee camp are discussed within the conclusion of this chapter (Section 2.3.7).

Major ions

The distribution of the EC measurements is consistent with the distribution of the major ions, as shown with the Stiff diagrams on Fig. 2.22. As for the EC, water chemistry is likely to vary over time, thus, this map presents a regional overview of the chemistry of the Merti aquifer and its surrounding. Local and temporal variations of the groundwater chemistry may occur.

This figure, which includes analyses of the 2011 Earth-Water field campaign analysed at the Center for Hydrogeology of the University of Neuchâtel, as well as results from previous studies indicate that the freshwater lens and its close surrounding is mainly dominated by the Na + K and HCO_3 poles. In the brackish zones, Na and Cl concentrations dramatically increase and mostly dominate the composition of groundwater. However, in some places (Kurdi, Madogashe, Lagh Boghal), significant amounts of SO_4 or Mg can be found. This presence of SO_4 suggests the presence of localised evaporitic deposits at these locations. Groundwaters sampled in the bedrock or basaltic rocks, between Merti and the Mt-Kenya, indicate higher concentrations of Mg. All hydrochemical data since 1956 data are compiled in appendix F.

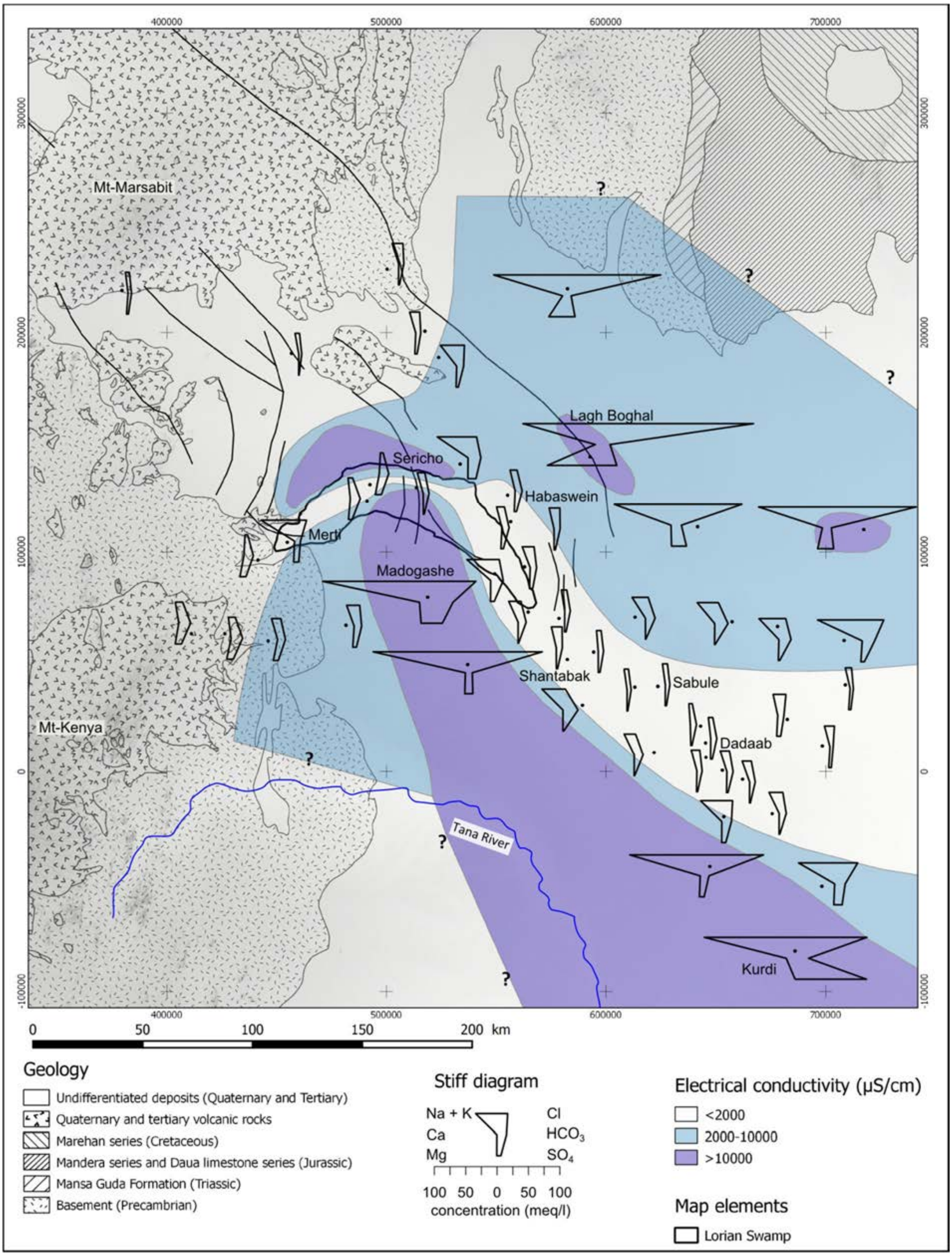

Fig. 2.22: Majors elements of the Merti aquifer (Stiff diagrams). Sources: GIBB, 2004 and own data.

2.3.7 Conclusions of the hydrogeological characterisation of the Merti aquifer

The analysis of the transmissivity, specific capacity and the regional piezometry of the Merti aquifer allowed to define the main domains of the aquifer (Fig. 2.23). The "central Merti aquifer", is characterised by high transmissivity values between Habaswein and the Dadaab refugee camp. Upstream, this channel is extended by an intermediate transmissivity zone, the "upper Merti aquifer". Downstream, towards the ocean, the dramatically decreasing gradient suggests an increasing transmissivity. An enlargement of the conductive channel is also suggested south-east by the high specific capacity measured at Liboi. Laterally, from the upper/central aquifer zones towards the basement, the higher hydraulic gradient and the lower specific capacities requires lower transmissivities. The main recharge area, identified over the Lorian Swamp, induces a piezometric "bulge" west of Habaswein (Fig. 2.7).

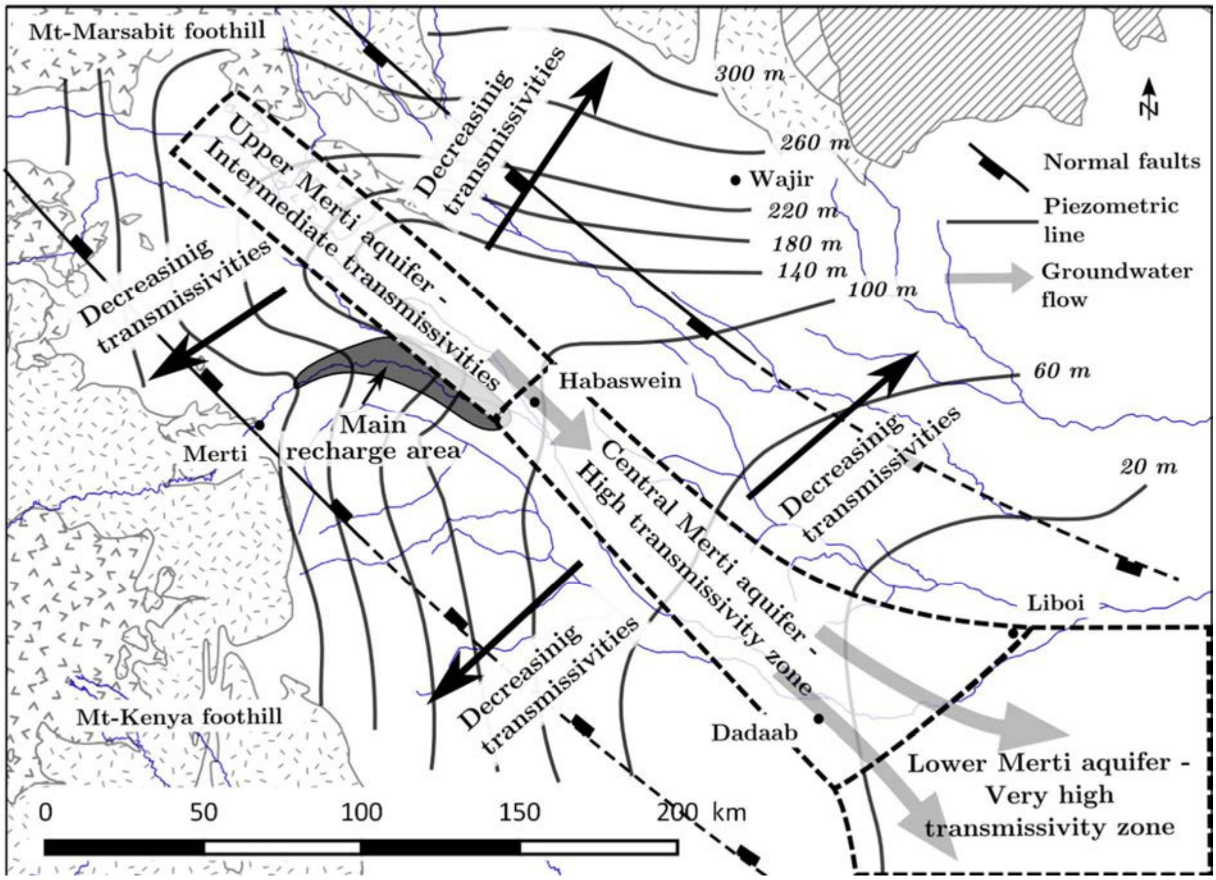

Fig. 2.23 : Synthetic model of the transmissivities distribution, main recharge area and regional groundwater flow.

Spatial distribution of electrical conductivities and majors ions concentrations revealed the presence of a freshwater lens superimposed on the high transmissive channel identified with hydrodynamic data. According to the laterally surrounding brackish and saline waters, recharge should mainly take place over the downstream part of the Lorian Swamp with possible further contribution towards Dadaab. The small width of fresh water between Merti and Sericho suggests that recharge along this path is limited and does not propagate because of a relative low permeability. Temporal evolutions of electrical conductivity values suggest a rather stable freshwater lens on the large scale, with local rebalancing due to pumping, especially close to the brackish water zones.

The interpretation of pumping data (Fig. 2.20) allowed to characterise the currently exploited layer of the Merti aquifer as confined and leaky. This observation suggests that the aquifer is not limited to the first exploited horizon but may in fact be a multi-layer aquifer that extends deeper down. This analysis is consistent with the geological description of the Middle to Late Miocene deposits within the Anza Graben, which indicate a succession of fine and coarse levels (2.2.2). This model would imply to consider the Merti aquifer as an aquifer system composed of several layers, of which the first is the Merti beds formation.

Implications for the groundwater exploitation for the Dadaab refugee camp

For the exploitation of the groundwater for the Dadaab refugee camp, two conclusions can be made based on the temporal evolution and spatial distribution of the electrical conductivity. Firstly, on a large scale, no serious concern remains on the overall evolution of the groundwater quality. The freshwater lens doesn't show a dramatic increase of salinity on the short term (Appendix C) and the mid-term observations (Fig. 2.21). The evolution of the electrical conductivity mostly increased by a maximum of 50 to 100 µS/cm within the last twenty years and remains in all zones of the freshwater lens below the threshold of 2000 µS/cm, considered as the limit for potable water.

Secondly, locally, the exploitation of the groundwater of the freshwater presents some risks, specifically close to the limit between the fresh and brackish water, as in Hagadera where the electrical conductivity shows the highest values compared to the rest of the Dadaab refugee camp. These risks come from a possible salinisation of the wells from brackish or saline underlying water (upconing). Because of the uncertainty on the local lithostratigraphy and the depth the transition between the fresh and the brackish water, these risks are difficult to quantify. However, they should be considered seriously. In order to quantify the evolution of the salinity and to limit these risks, it is recommended to continue a permanent monitoring of the groundwater, in particular for the sensitive wells close to the limit between the fresh and the brackish water (at Hagadera).

Furthermore, as a general recommendation and according to these risks of salinisation close to the previous mentioned limit, the exploitation of the groundwater should be encouraged toward the center of the aquifer where the freshwater lens shows the lowest risk of salinisation. Additionally, due to the supposed presence of brackish and saline water below the freshwater lens, an extraction strategy with more, but shallower boreholes should be preferably chosen in opposition to deeper boreholes.

Chapter 3

Quantification of concentrated and diffuse recharge of the Merti aquifer

3.1 Introduction

Groundwater recharge is defined by Healy (2010) as "*the downward flow of water reaching the water table, adding to groundwater storage*". Along the route of water from the surface to water table, the recharge is preceded by infiltration, which is the entry of water into the unsaturated zone. Infiltration can be considered as potential recharge because the infiltrated water may flow down to the water table and become recharge, or it can also be evapotranspired and return to the atmosphere. Because the Merti aquifer has an unsaturated zone of up to 100 m, the difference of dynamics of infiltration and recharge is very important: the infiltrated water could percolate during several months or even years before reaching the water table.

Two different recharge processes with very different dynamics are identified: the "diffuse recharge" and the "concentrated recharge". The diffuse recharge is related to recharge occurring at large scale by precipitation (Fig. 3.1a). In arid to semi-arid areas, the diffuse recharge rate is very low (few percent, or even lower), because of the little difference between precipitation and evapotranspiration. However, this mechanism takes place over very large areas, and volumes can therefore be significant. On the other hand, concentrated recharge refers to recharge taking place below delimited surface waters (Fig. 3.1b). This recharge mechanism occurs on a smaller spatial extension than the diffuse recharge but vertical recharge rates may be much higher. Because of the high difference in spatial and temporal dynamics between these two recharge processes, different approaches are required to quantify them.

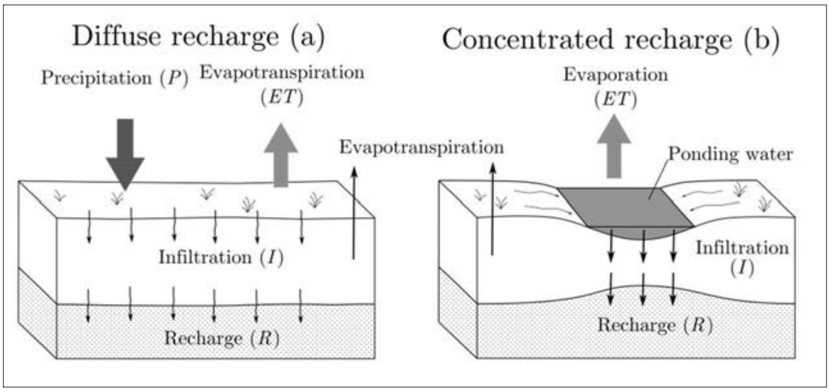

Fig. 3.1: Schematic illustration for diffuse recharge (a) and concentrated recharge (b).

The relative contribution of these two recharge processes is not well understood. Thus, the quantification of both processes is crucial for understanding the entire Merti aquifer system. This chapter presents new methods for estimating recharge, based on numerical modelling and remote sensing analyses.

First, the regions where diffuse and concentrated recharge occur are differentiated by means of the Normalised Difference Water Index (*NDWI*) which allows to distinguish inundated areas (section 3.2). This index is derived from multispectral satellite images.

Then, over the regions where no significant inundations occur (Fig. 3.1a), the diffuse recharge is estimated by comparison with diffuse recharge rate estimations of similar environments (section 3.3). The spatial distribution of the diffuse recharge is approached by a vertical water balance, which is the difference between precipitation (P) and evapotranspiration (ET). However, the uncertainty of the P et ET data have to be taken into account and does not allow to use this approximation as absolute value.

Finally, in order to quantify concentrated recharge (Fig. 3.1b), a fully coupled surface-groundwater finite-element model (*HydroGeoSphere*) is developed, based on river discharge data, precipitation and a digital elevation model (section 3.4). The model is calibrated to reproduce the extent of inundated surfaces with the *NDWI* images by varying a ground conductance of soil. *NDWI* inundation images are used to calibrate the hydraulic conductivity in order to reproduce simulated inundated surface close to the observed ones. Recharge is then derived from the infiltration over the inundated areas by subtracting the evapotranspiration from the soil once the inundation is over.

3.2 Identification of regions of diffuse and concentrated recharge

Based on the spectral property of water, inundated areas can be identified using satellite multispectral optical methods.

The *NDWI*, initially developed by Gao (1996) to identify vegetation liquid water, could be used to identify surface water from space (Campos et al., 2012; Ordoyne and Friedl, 2008; Soti et al., 2009), and thus delimitate the region where concentrated recharge dominates.

The *NDWI* is based on the reflectance of near infrared (NIR) and short wave infrared bands (SWIR) of satellite images. The reflectance of the first band does not vary with the presence of water, while the second one varies significantly (Fig. 3.2a). Applying a normalised difference index (Eq 3.1), Gao pointed out a linear relation between the water depth and the *NDWI* (Fig. 3.2b). In this present study, *NDWI* images were derived from the MOD09A1 MODIS[2] images with bands 2 (0.841 – 0.876 µm) and 5 (1.230 – 1.250 µm). These images have a spatial resolution of 1 km.

---

[2] MODIS is the acronym for Moderate Resolution Spectroradiometer. MODIS is an instrument aboard the Terra and Aqua satellites. Terra MODIS and Aqua MODIS are viewing the entire Earth's surface every 1 to 2 days, acquiring data in 36 spectral bands, or groups of wavelengths. The MOD09A1 product has a spatial resolution of 1 km and a time resolution of 8 days.

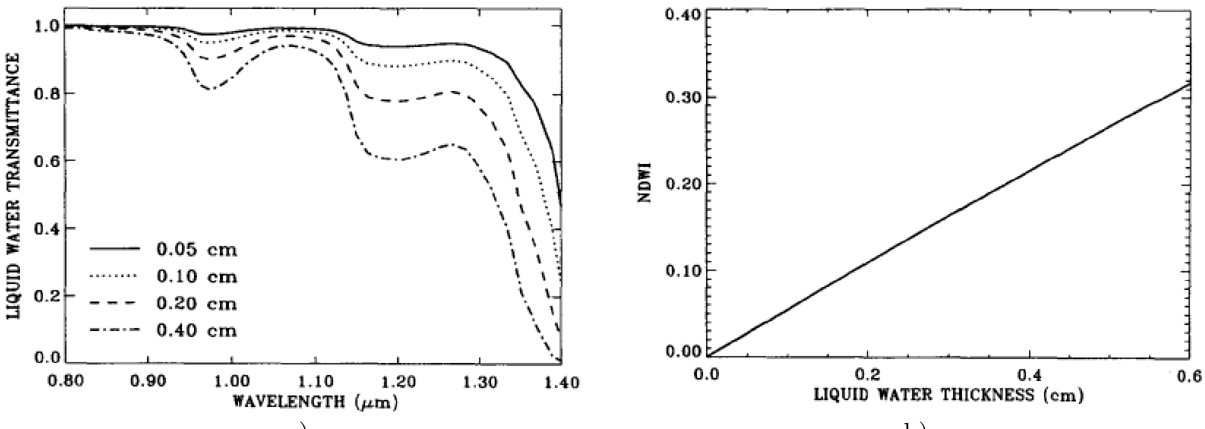

a) b)

Fig. 3.2: a) Liquid water transmittance vs wavelength. Transmittance at 1.24 µm varies more than at 0.86µm. b) The *NDWI* increases linearly with water thickness (Reprinted from Gao, 1996).

$$NDWI=\frac{NIR\text{-}SWIR}{NIR+SWIR}=\frac{(band\ 2)\text{-}(band\ 5)}{(band\ 2)+(band\ 5)} \qquad (3.1)$$

where :		
	NIR	is the near-infrared reflectance, measured by the band 2 of the MODIS satellite
	SWIR	is the shortwave infrared reflectance (band 5 of MODIS satellite)

The *NDWI* index produces images with continuous values ranging from -1 and 1, representing in relative terms the water depth. In order to distinguish wet from dry pixels, a threshold has to be defined. This threshold, which is calibrated by comparing a reference inundation map (Fig. 3.3) realised by the Darthmouth Flood Observatory from October to December 2006 during a major flood event (Anderson and Brakenridge, 2006), is fixed at 0.10. Pixels above 0.10 are considered as inundated and pixels below this threshold as dry. The same threshold value was also found by Soti et al. (2009) in Northern Senegal. Based on this threshold, every 8-days period images, derived from the MOD09A1 product for the period 2000-2012, are classed to binary images identifying if pixel are considered inundated or not. This classification allows to have a continuous approximation of the inundated area with a time resolution of 8 days, that is the time resolution of the MOD09A1 product.

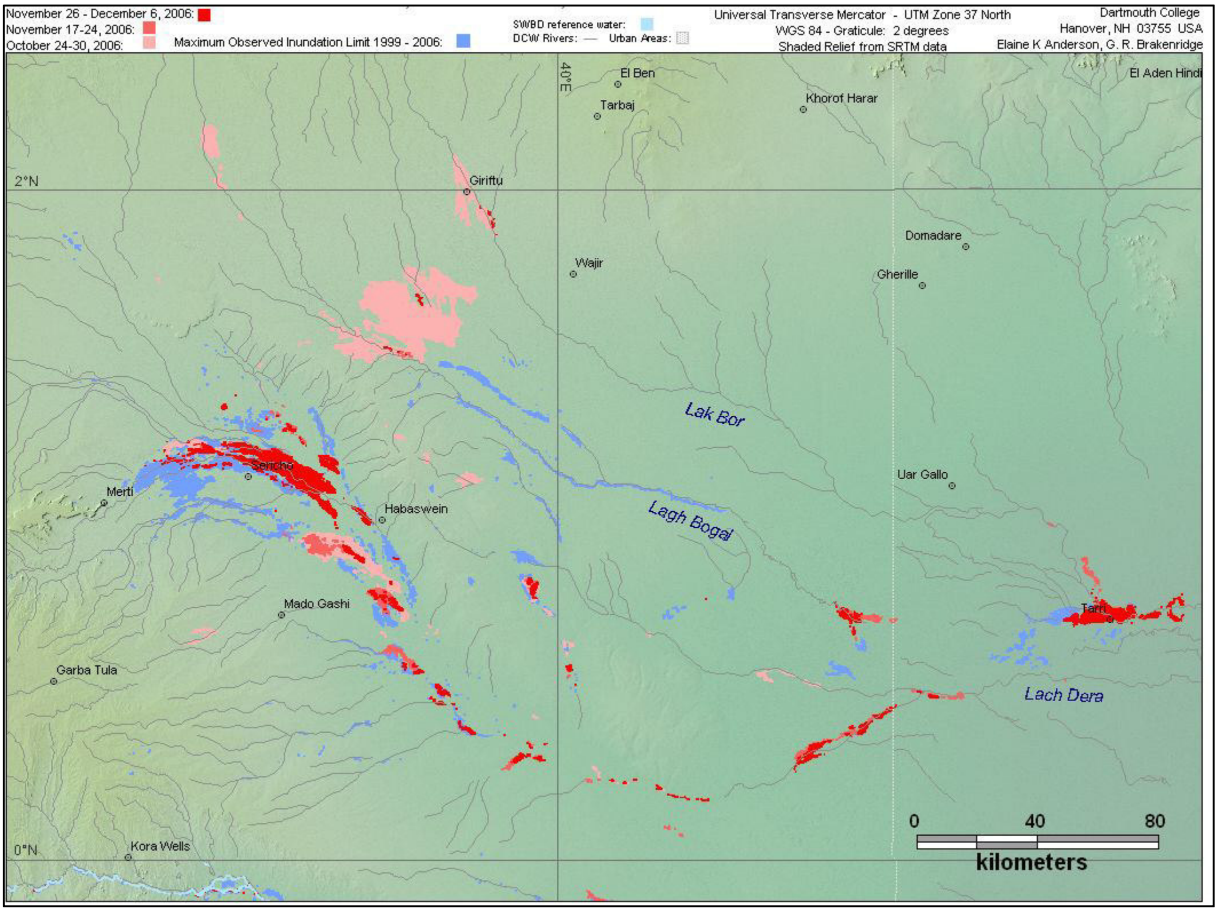

Fig. 3.3: Inundation map of the major flood event in October-December 2006. This map is used as reference map for the calibration of the *NDWI* threshold (Reprinted from Anderson and Brakenridge, 2006).

Examples of binary reclassification during the major reference flood event in 2006 are shown on the three maps in Fig. 3.4. The first image (a) shows the *NDWI* before the inundation. The second one (b) illustrates the peak of the inundation between the 17^{th} and the 24^{th} of November 2006. This image reproduces satisfactorily the reference inundation image of Fig. 3.3 during the same period (in dark red on the reference image). The last image (c) is extracted during the recession.

NDWI images could be used over a long period in order to distinguish recurrently inundated areas where concentrated recharge occurs, from areas where diffuse recharge occurs, with less inundations.

For this purpose, an annual average map of inundated days was established (Fig. 3.5), cumulating each 8-days classified *NDWI* maps during the period 2000-2012 and dividing by 13 years. This map reveals the high frequency of inundations over the Lorian Swamp area with more than 25 days per year (on annual average). Other areas over the Merti catchment are rarely inundated. Other inundated areas beyond the Merti aquifer are also revealed by this method, such as the Garissa River and areas north of the Mt-Marsabit. Parallel lines of inundated pixels visible on the close up are due to artefact present on some 8-days images.

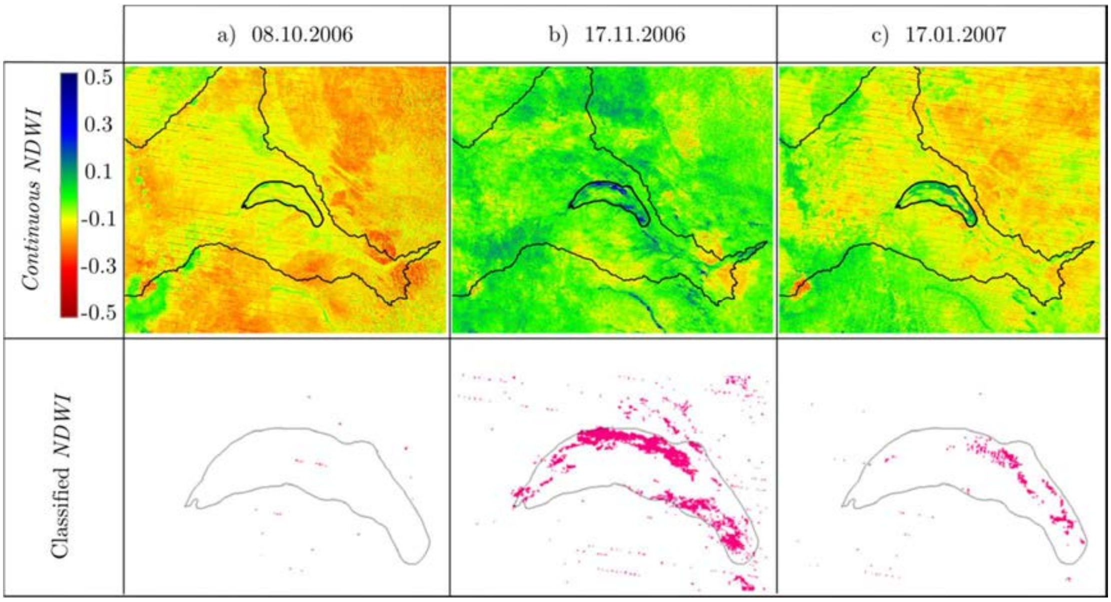

Fig. 3.4: Continuous *NDWI* and binary classified *NDWI* maps before (a), during (b) and at the end (c) of the 2006-2007 flood event. *NDWI* maps are displayed over the entire Merti basin. Classified maps are a close up of the Lorian Swamp area. The image between the 17th and 23rd of November (b) reproduces fairly well the inundation surface of the reference inundation image during this same period (Fig. 3.3). The thin black line on the continuous *NDWI* maps shows the limit of the Ewaso Ng'Iro/Lagh Dera catchment.

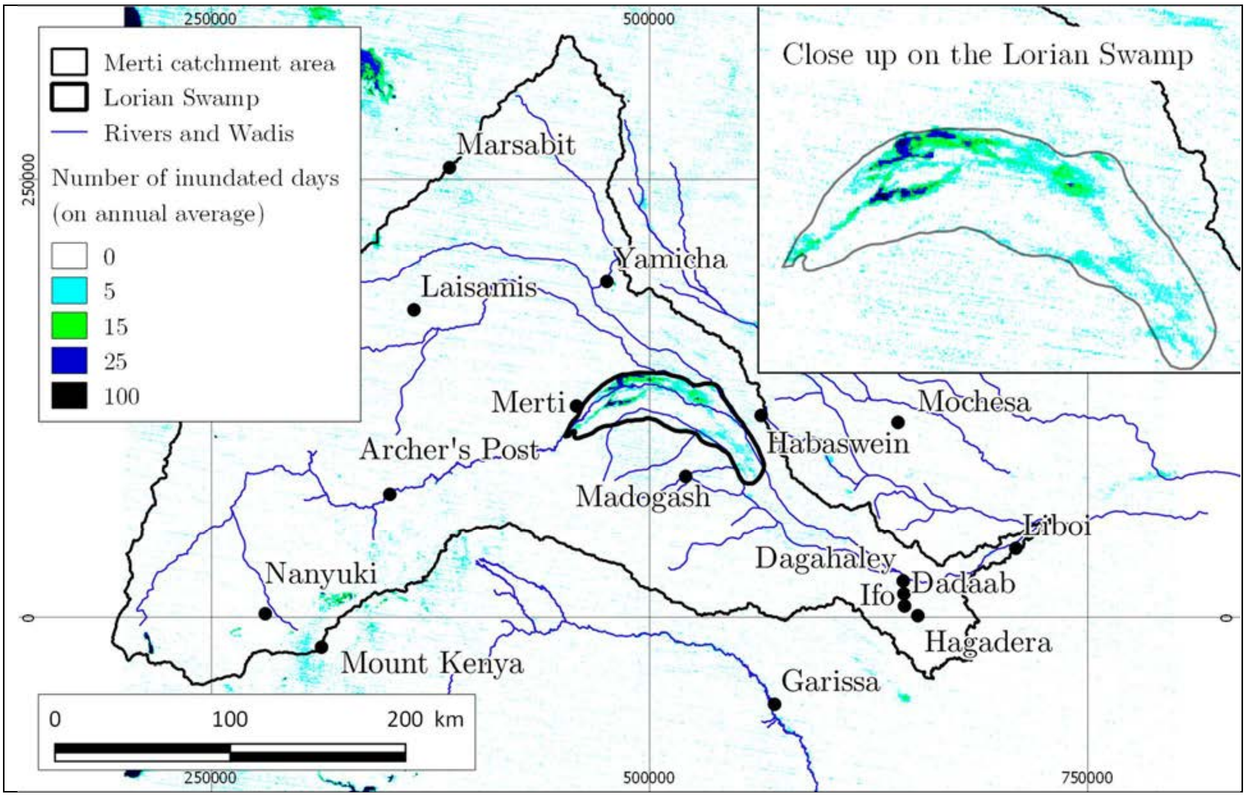

Fig. 3.5: Annual average of inundated days for the period 2000-2012, computed with 8-day binary *NDWI* images. The concentrated recharge occurs predominantly over the Lorian Swamp, where inundation is recurrent, while diffuse recharge occurs over the rest of the Merti aquifer and the Ewaso Ng'Iro catchment.

This analysis shows that concentrated recharge predominantly occurs over the Lorian Swamp whereas diffuse recharge dominates over the rest of the domain. This observation allows to consider that concentrated recharge occurs only over the Lorian Swamp and that diffuse recharge occurs over the rest of the Merti basin area. The recurring inundated surfaces identified with MODIS satellite images is consistent with the delimitation of the freshwater channel between Sericho and Merti identified with electrical conductivity values shown on the map in Fig. 2.21.

3.3 Diffuse recharge - large scale approach

Over areas where no surface runoff is present, the diffuse recharge can be approached by the difference between precipitation (*P*) and evapotranspiration (*ET*). However, because the precipitation and evapotranspiration have very similar values in semi at semi-arid regions and because the poor quality of *P* and *ET* satellite data, the *P-ET* values should be interpreted as a proxy for characterising the spatial distribution of the diffuse recharge but not as absolute recharge rate. Annual precipitation and evapotranspiration averages are computed from the FEWS-Net project[3] data and the MOD16[4] product, respectively.

Range of possible diffuse recharge rate is then inspired from values measured in similar environments and its spatial dynamics is delimited with the *P-ET* vertical water balance.

3.3.1 Precipitation

The annual average precipitation map shown on Fig. 3.6 is calculated with daily images from the FEWS-Net project with a daily temporal resolution and a spatial resolution of 0.1 degree (about 10 km in this latitude). This data is based on the African Rainfall Estimation Algorithm Version 2.0, referred to later as RFE 2.0 (Laws et al., 2003)[5]. On a daily basis, uncertainty of the RFE 2.0 product is relatively high with a correlation coefficient of 0.5 between ground measurement and the RFE 2.0 product. However, Ochieng (2009) and Karimi & Bastiaanssen (2014) demonstrated that the quality of this product increases considerably over longer periods. Wide comparison of the RFE 2.0 product with rainfall ground gauging stations indicates that the correlation coefficient ranges between 0.7 and 0.9 (Ochieng, 2009) on annual average and errors range between 2 and 19% (Karimi & Bastiaanssen) on seasonal or annual periods.

---

[3] Famine Early Warning System Network, http://www.fews.net/

[4] http://www.ntsg.umt.edu/project/mod16

[5] The RFE 2.0 product combines data from two radar sensors (AMSU and SSM/I) and one infrared sensor (GPI). It is calibrated with a network of about 1000 daily rain gauge stations. Data is available on a daily basis and at a spatial resolution of 0.1 degree.

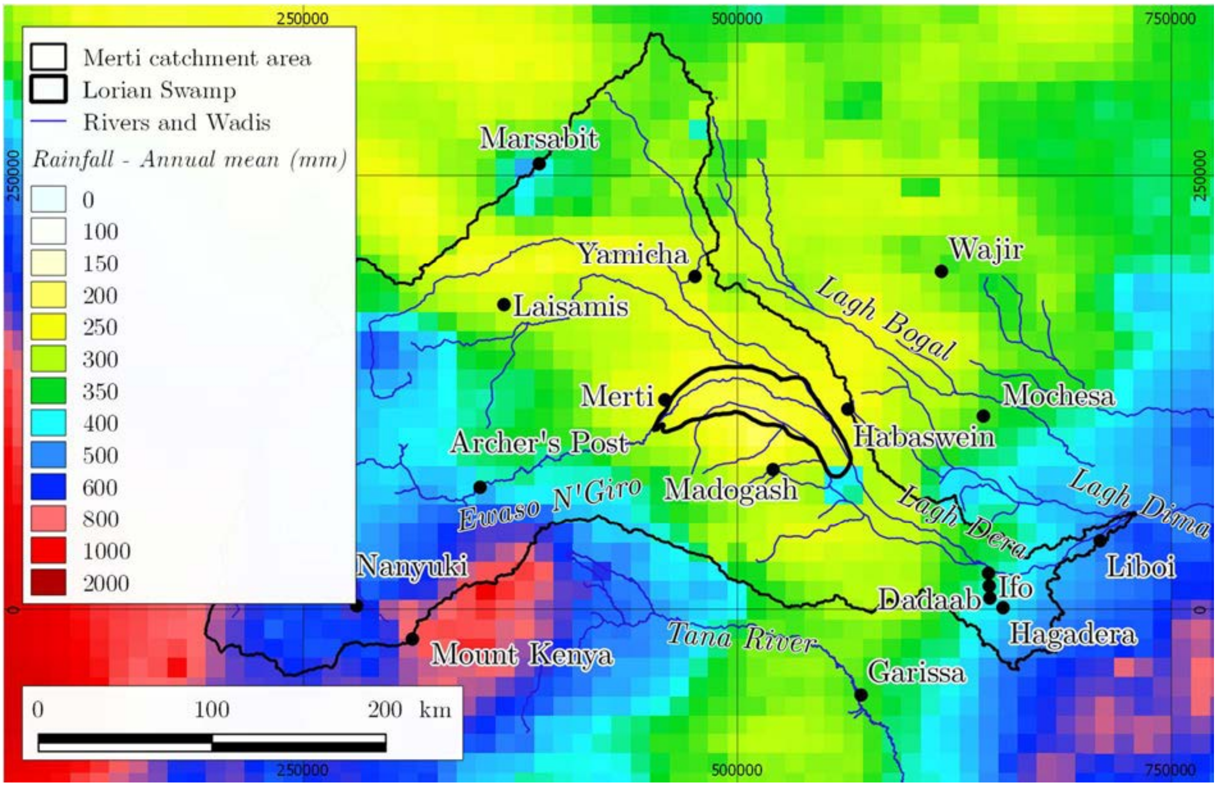

Fig. 3.6: Mean annual rainfall, calculated for the 2001-2011 period from satellite images. Source: FEWS-Net.

In order to assess the quality of the data over the Merti catchment, the FEWS-Net data of the period 2002-2013 was compared with monthly average rainfall of meteorological stations data of the Kenya Meteorological Department (KMD) for the period before 1991. Unfortunately, data from the KMD are not available after 1990 and does not allow to make a strong validation of the FEWS data with data covering the same time window.

The two sets of data show generally the same trend (Fig. 3.7), with a monthly distribution mainly controlled by seasonal cycles, characterised by two major rainy seasons (March-May and October-December). Rainfall at Laisamis, Habaswein (center of the Merti aquifer), Garissa and Wajir are characterised by low values and high variability between the two rainy seasons. Marsabit shows higher precipitations, also containing two marked seasons. Nanyuki is located in the upper Ewaso Ng'iro basin which receives more constant rainfall.

However, even these two data sets do not cover the same period, it could be observed that the FEWS-Net data is likely to underestimate the high precipitation values, especially at the Mt-Marsabit and Lamu where FEWS-Net values are about 2 times lower than the KMD values.

Based on KMD data, annual average rainfall over the Merti aquifer area ranges between 250 to 350 mm/y in the central part of the aquifer (between Merti and Dadaab) and increases progressively towards the mountains with values around 400-500 at the Mt-Marsabit (1350 m.a.s.l). Around the Mt-Kenya massif (4600 m.a.s.l), values above 1000 mm/y are measured. Close to the coast, precipitation is also considerably higher.

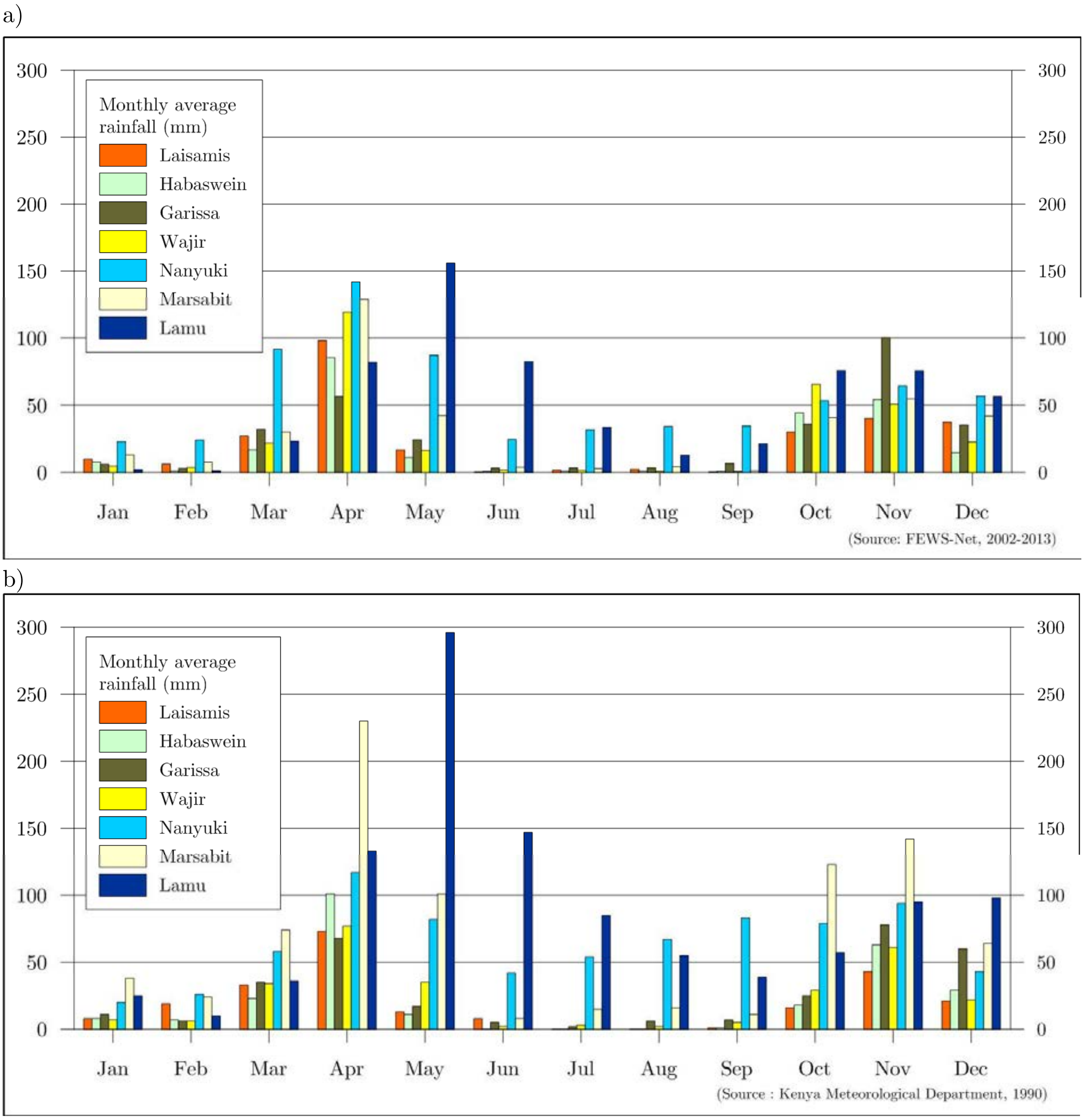

(Source: FEWS-Net, 2002-2013)

(Source : Kenya Meteorological Department, 1990)

Fig. 3.7: Monthly average rainfall (year 2001-2011) from the FEWS-Net project (a) and Kenya Meterological Departement (b) at 7 locations around the Merti aquifer. Rainfall is characterised by two rainy seasons. The Merti aquifer basin (Habaswein), characterised by low precipitation, differs from mountainous region as Nanyuki (Ng'iro basin) and Marsabit, and from coastal area (Lamu). FEWS-Net data is likely to underestimate high precipitation values.

3.3.2 Actual evapotranspiration

Actual evapotranspiration (ETa) was extracted from the MODIS satellite MOD16 product. The MOD16 product is available on an 8-day temporal basis with 1 km spatial resolution. It is calculated with the algorithm of Mu et al. (2011) which is based on the Penman-Monteith model. Quality of the MOD16 product, even on annual average, remains low. A large evaluation of this product over the United States indicates an overall uncertainty around 25% for this product. However, details for arid regions give a R^2 of 0.25 between MOD16 and eddy covariance FLUXNET sites (Velpuri et al., 2013). Other studies in Australia (King et al., 2011) and South Africa (Ramoelo et al., 2014) also revealed the high uncertainty of this data in arid regions. King *et al.* also pointed out that the seasonality of the *ETa* is poorly reproduced by this product, with a too low magnitude. In arid areas such in the Merti region, this could lead to considerable overestimation of the *ETa* because of the long dry periods. Thus, the MOD16 product may not be used to quantify precisely evapotranspiration but only qualitatively. However, this product allows to approach the spatial distribution of evapotranspiration.

The annual *ETa* spatial distribution of the MOD16 product shows trends similar to the precipitation with values between: 1) 300-400 mm/y for the plain; 2) up to 500-600 mm/y for the Mt-Marsabit; 3) and higher than 1000 mm/y for the Mt-Kenya massif (Fig. 3.8). *ETa* also increases close to the coast.

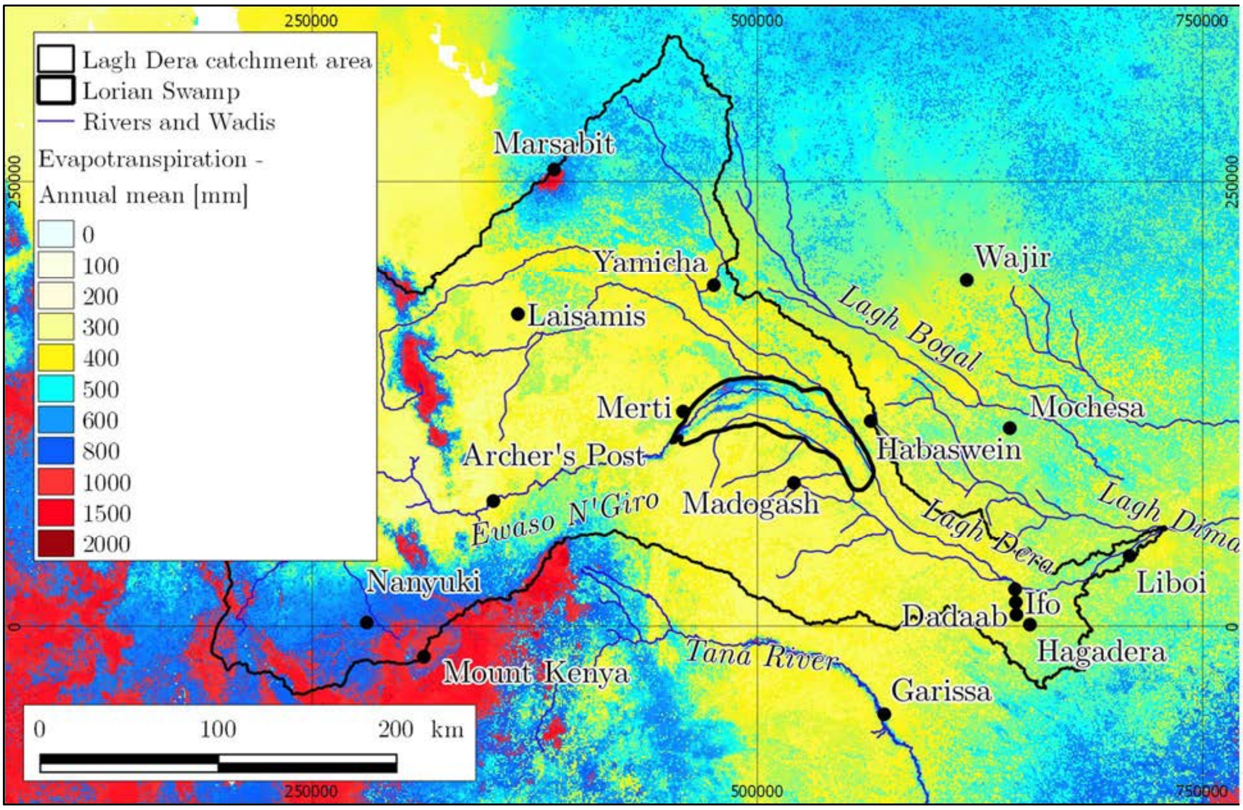

Fig. 3.8: Mean annual evapotranspiration calculated for the 2001-2011 period. Source: MOD16 product.

The *ETa* annual mean values, as shown on Fig. 3.8 reveals two interesting features. Firstly, the Lorian Swamp area shows evapotranspiration rates up to 800 mm/y that is about twice the surrounding plain. This difference is explained by the recurrent inundations which allow water to evaporate during long periods. Secondly, the basaltic plateaus indicate *ETa* values approximately 100 mm/y higher than the surrounding areas. This feature, which is particularly visible around the Merti, Yamicha and Laisamis areas (Fig. 3.9), suggests that the diffuse recharge over the basaltic plateaus is lower than over the plain. this allows to exclude the basaltic plateaus as a predominant recharge area, as it was suggested in previous studies (GIBB Ltd, 2004).

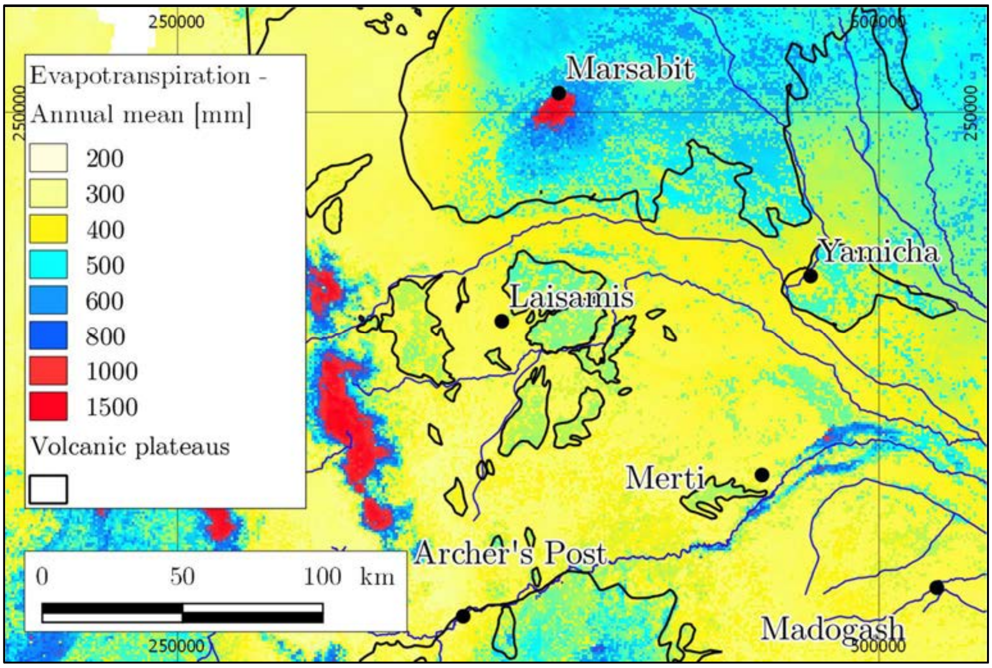

Fig. 3.9: Annual average evapotranspiration. Close up of the Merti, Yamicha and Laisamis areas with high-lighted volcanic plateaus showing higher evapotranspiraiton values (+100 mm/y).

3.3.3 *P-ET* vertical water balance

Over the Merti plain (Merti – Laisamis – Yamicha – Mochesa – Hagadera), the vertical water balance derived from the *P-ET* subtraction indicates a slight negative trend from the southwest towards the northeast (Archer's Post to Yamicha), suggesting that more water infiltrates or runs off over the southwestern area (Fig. 3.10). However, this difference of about 100 mm/y lies within the cumulated error on the rainfall and the evapotranspiration. Thus, over the Merti plain, a homogeneous diffuse recharge, or slightly decreasing toward the north-east, could be considered.

This approach, based on annual average rates allows to assess the spatial dynamics of the diffuse recharge. The local temporal dynamics of this vertical water balance is much more complex than the averaged map presented and could lead to significant temporal variability of the infiltration at the surface.

Negative *P-ET* values over the Mt-Marsabit are likely to be explained by the underestimation of the FEWS-Net precipitation data for high rates, as suggested by the comparison of FEWS-net and gauging station data (Fig. 3.7).

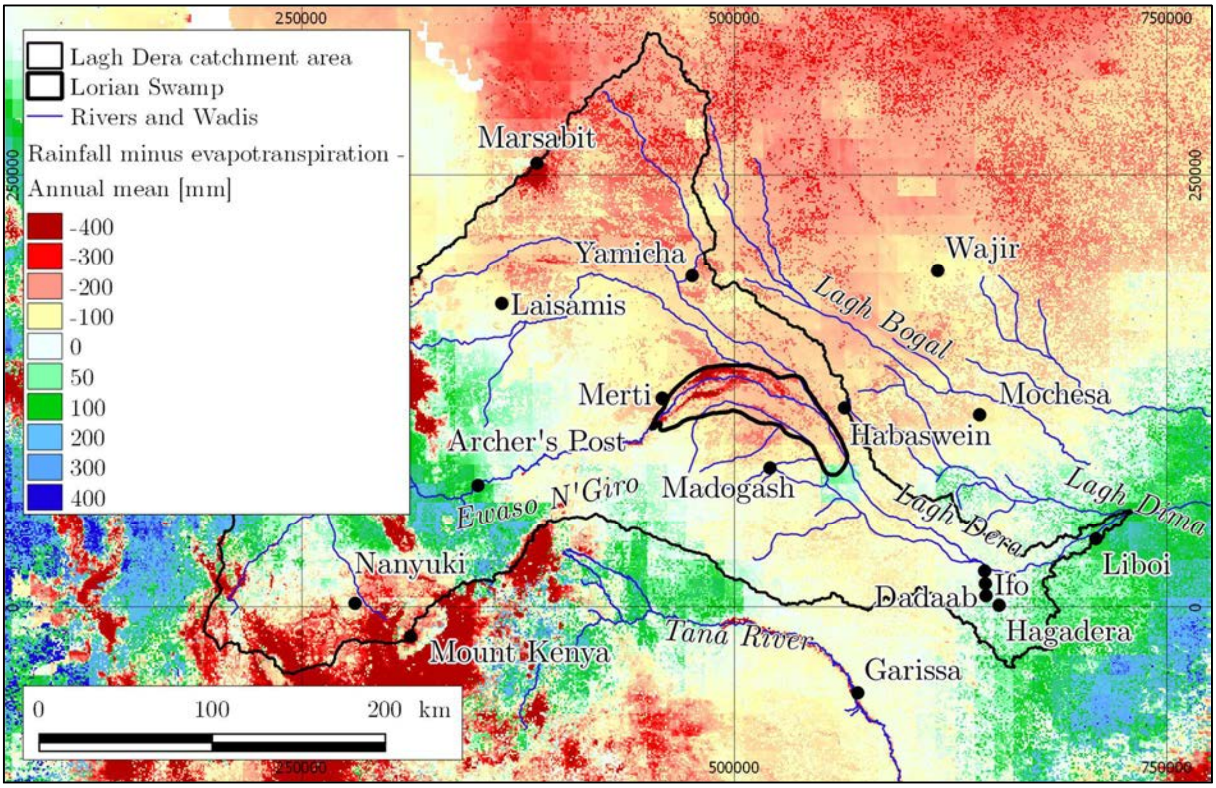

Fig. 3.10: Difference between annual mean rainfall and evapotranspiration (2001-2011). Over the Merti plain (Merti – Laisamis – Yamicha – Mochesa – Hagadera), the *P-ET* balance indicates a slight negative trend towards the northeast. However, due to the small difference (about 100 mm) diffuse recharge can be considered as homogenous over this area. The high negative values over the Lorian Swamp area is caused by the high evapotranspiration rates due to the recurrent inundations.

3.3.4 Diffuse recharge estimations in published literature

In order to complete the qualitative estimation of the diffuse recharge with a quantitative estimation, estimation of recharge in arid and semi-arid areas extracted from literature is used. Scanlon et al. (2006) propose a large synthesis of groundwater recharge in semi-arid and arid areas based on about 140 recharge studies. They found that recharge in such areas ranges between 0.2 to 35 mm/y, corresponding to 0.1 to 5% of the long term average annual precipitation. However, this large synthesis also includes concentrated recharge over inundated areas. By focusing only on diffuse recharge, in similar climatic areas (precipitation close to Merti with ~250 mm/y) and similar land use, recharge values ranging between 0.2 and 10 mm/y is found in literature (Butler and Verhagen, 2001; de Vries et al., 2000; Edmunds, 2001; Harrington et al., 2002; McMahon and Dennehy, 2003; Scanlon, 1991; Selaolo et al., 1996).

The recharge study in the Kalahari Desert (de Vries et al., 2000) is an interesting site for comparison. The Kalahari system shows similarities with the Merti aquifer: recent unconsolidated sedimentary deposits, mainly composed of sand, silt, clay and silt/clay calcrete; thick unsaturated zone of 20 to 100 meters; very low annual precipitation between 250 and 500 mm/y. Recharge rates based on chloride mass balance method yielded results of around 5 mm/y for the region where annual rainfall exceeds 400 mm and around 1 mm/y where the precipitation is lowest.

3.3.5 Conclusions of the diffuse recharge

Over the Merti aquifer area, on a long term average, evapotranspiration is very close to precipitation and the spatial distribution of the residual is fairly homogeneous. However, a smooth trend of water deficit from the southwest to the northeast was identified, but the variation of *P-ET* over this area remains smaller than the cumulated uncertainty of the rainfall and the evapotranspiration. Thus, the diffuse recharge over this area could be considered as homogeneous or with a slight trend.

The study of sites with similar climatic environment reviewed by Scanlon et al. (2006), in particular in the Kalahari desert, suggests that recharge rates are likely to range between 1 and 5 mm/y. Applied to the surface of the freshwater lens, from the Lorian swamp to the downstream area of Dadaab, (12'500 km^2), the fluxes of 1 and 5 mm/y induce a volume of 12 x 10^6 m^3/y and 62 x 10^6 m^3/y respectively. Only the diffuse recharge occurring over the freshwater surface lens is taken into account since diffuse recharge over the rest of the domain is diluted with brackish or salty water and does not contribute to exploitable fresh water. However, if the total surface of the study area (Fig. 1.4) is considered, these diffuse recharge rates yield annual diffuse recharge volumes of 136 x 10^6 m^3/y and 681 x 10^6 m^3/y respectively. The consistency of these diffuse recharge rates will be tested within the synthetic model of Chapter 4 and the regional groundwater model of Chapter 5.

3.4 Concentrated recharge – A combined approach based on remote sensing data and a fully coupled surface-groundwater model

The quantification of concentrated recharge over the Lorian Swamp during inundation events remains the key element for understanding the dynamics of the recharge of the Merti aquifer. Indeed, despite the relatively small inundation surface compared to the entire Merti aquifer, concentrated recharge is likely to play a major role because of the constant availability and the continuous infiltration during a long period under saturated conditions.

The estimation of concentrated recharge could be carried out by an analytical water-balance approach that considers that the infiltrated volume V_i (m^3) during an inundation event is equal to the river discharge $Q(t)$ (m^3/s) plus precipitation $P(t,A)$ (m^3/s), minus evapotranspiration $ET(t,A)$ (m^3/s), integrated during the flood event period (Eq 3.2). The precipitated and the evapotranspired volumes influencing the inundated surface are a function of the inundated surface itself. The infiltrated volume V_i can also be computed by a function of the inundated surface $A(t)$ (m^2) and a vertical infiltration rate I (m/s). These two relations are illustrated in Fig. 3.11. The surface outflow component can be ignored because the Ewaso Ng'Iro River never flows out of the Merti basin.

$$V_i = \int_{t_{start}}^{t_{end}} \big(Q(t) + P(t,A) - ET(t,A)\big)\, dt = \int_{t_{start}}^{t_{end}} I \cdot A(t)\, dt \qquad (3.2)$$

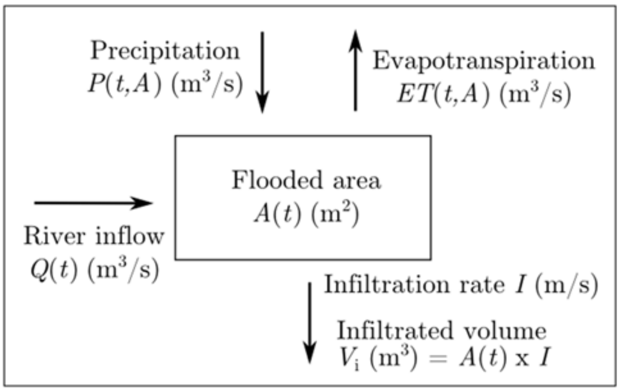

Fig. 3.11: Illustration of the quantification of the infiltrated volume during an event. Precipitation, evapotranspiration and infiltration volumes are function of the inundated surface (A), which depends on the time.

This equation is highly complex for being solved analytically because of the spatial and temporal dimensions of the problem. Indeed, the inundated surface evolves constantly during the flooding and recession phase, as well as the discharge rate, the precipitation and the evapotranspiration.

In order to solve this problem and to consider these spatial and temporal complexities, an innovative approach based on inundation satellite images and on a fully coupled surface-groundwater numerical model, based on the *HydroGeoSphere* code (*HGS*), is developed. This approach relies on the ability of the *HGS* model to simulate surface water inundation surfaces in a physically based way. The model is calibrated with satellite images showing inundation surfaces (*NDWI*) as calibration dataset, by adjusting a ground conductance (C_g) that controls the infiltration rate I, and thus the inundated surfaces $A(t)$.

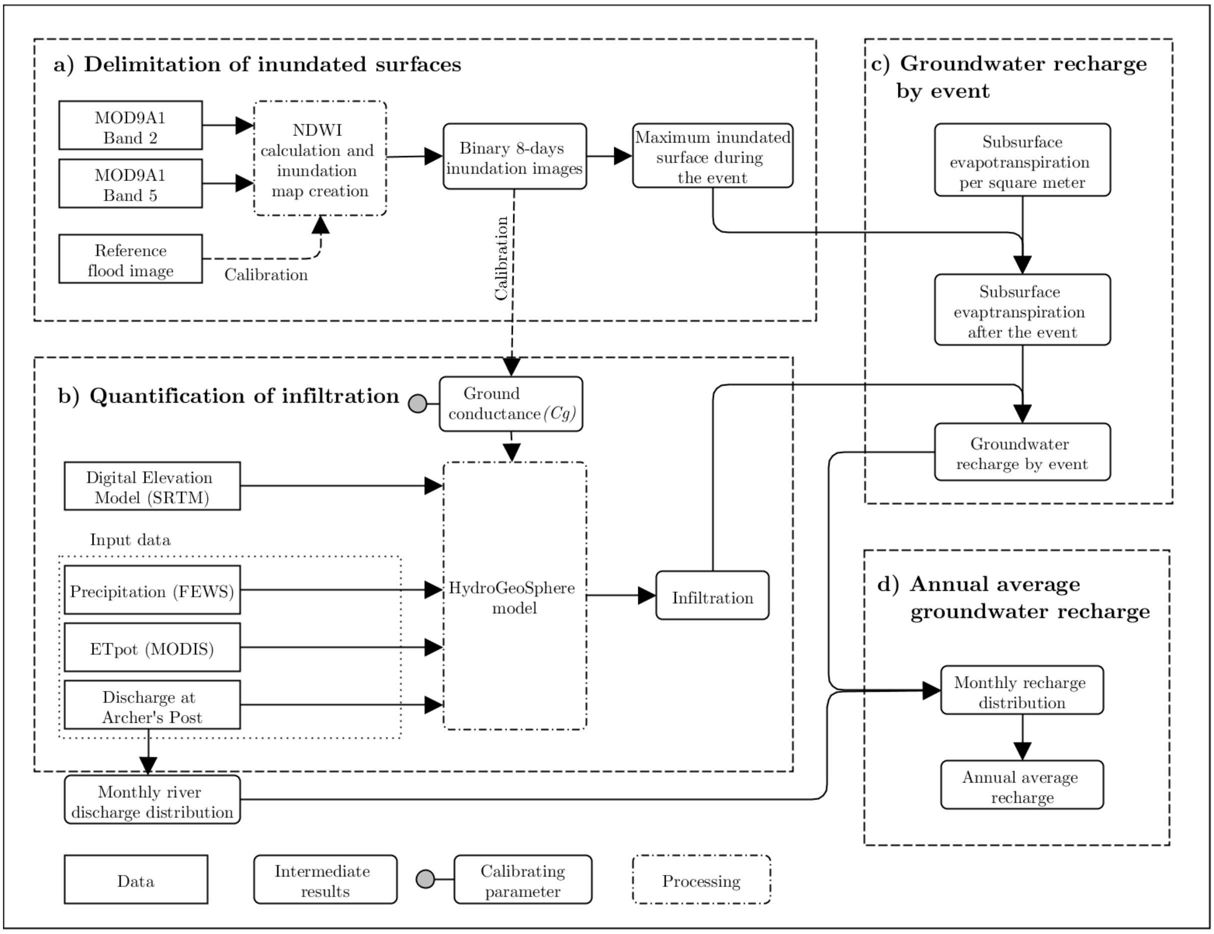

Fig. 3.12: Observed inundation surfaces, derived from MODIS 9A1 satellite product (a), serve as calibration dataset for a coupled surface-groundwater numerical model (b) which is based on the SRTM digital elevation model (resolution of 90 m), precipitation, river discharge and potential evapotranspiration. The C_g parameter (ground conductance) of the model is adjusted in order to reproduce the extent of the observed inundated surfaces. From the infiltration results, subsurface evapotranspiration is computed using further vertical numerical 1D models (c) in order to obtain the groundwater recharge for each event (d). Groundwater recharge computed for 7 separate events is then extrapolated to annual average recharge by means of long term river discharge time series.

The four main steps (Fig. 3.12) of this methodology for quantifying groundwater recharge are described in this section. The first step (Fig. 3.12a) refers to the identification of inundation surfaces images with satellites products (*NDWI*) which was already presented in section 3.2. The second step (Fig. 3.12b) consists in the quantification of infiltration with the *HGS* model. It presents the construction of the model and its calibration, as well as the results of six simulated inundation events between 2002 and 2010. In the third step (Fig. 3.12c), results of infiltration obtained with the *HGS* model are converted into recharge by subtracting the evapotranspiration of the subsurface after the inundation, that was not considered by the *HGS* model which only considers the evapotranspiration from the surface water. Finally (Fig. 3.12d), based on the relation between river discharge and recharge volume, obtained for each event in the third step, and on the river discharge time series between 1949 and 2010, a statistical recharge distribution is established. This analysis allows to establish a statistical relationship between the river discharge and the groundwater recharge.

In parallel to this method based on numerical modelling, an analytical approach was developed to quantify 1D vertical recharge based on inundation duration and soil hydraulic conductivity. This approach proposes a simple way to quantify groundwater recharge, assuming that the soil hydraulic conductivity is known.

3.4.1 Quantification of groundwater recharge by combining a coupled surface-groundwater model with remote sensing data

The following sections describe first the methodology developed and the input data used for quantifying groundwater recharge during isolated flood events (section 3.4.1.1), the model description (section 0) and the calibration method (section 3.4.1.3). Then, infiltration during six recharge events for which satellite images and river discharge data are available are quantified (section 3.4.1.4). Estimation of the evapotranspiration from the subsurface after the inundation is presented in section 3.4.1.5. Then, results of the concentrated groundwater recharge are presented in section 3.4.1.6. In section 3.4.1.7, the results of these six events are used to establish a relation between the discharge of the Ewaso Ng'Iro River and the recharge volume. Synthetic event with very high discharge rates that were not observed during the period 2002-2010 is discussed in section 3.4.1.8. Finally, uncertainty sources and their impact on the overall methodology for quantifying the groundwater recharge are listed and estimated in section 3.4.1.9.

3.4.1.1 Concept of the methodology and input data

The model is built on the SRTM digital elevation model[6] (resolution of the SRTM DEM is 90 m) and constrained by the river discharge $Q(t)$ measured at the Archer's Post[7] gauging station, the precipitation $P(t)$ from the FEWS-Net data, the potential evapotranspiration *ETp* (Table 3.1, Woodhead (1968)) and the inundated area $A(t)$ observed at specific times during a flood event (Fig. 3.13). Inundated areas are derived from MODIS satellite images by computing the *NDWI* index, as described in section 3.2.

	Jan	Feb	Mar	Apr	May	Jun	Jul	Aug	Sep	Oct	Nov	Dec
Air temp (°C)	28.8	29.6	29.8	28.9	29.2	28.0	26.7	27.3	28.0	28.7	28.2	29.5
ETp (mm/d)	7.91	9.03	8.95	8.26	8.90	9.10	8.75	9.09	9.73	9.21	6.94	6.69

Table 3.1: Air temperature and potential evapotranspiration (*ETp*) at Habaswein (centre of the Merti aquifer).

The ground conductance of the model (C_g) is adjusted so that the simulated inundated surface corresponds as much as possible to the observed inundated area. The C_g is set as constant and homogenous during an entire inundation event. In the numerical model, the C_g

---

[6] available from the U.S. Geological Survey, https://lta.cr.usgs.gov/SRTMNVF

[7] Obtained from the CETRAD (Center for training and Integrated Research In ASAL Development, www.cetrad.org)

is defined with the vertical hydraulic conductivity. Thus, the C_g is an integrative parameter that includes the real average hydraulic conductivity over the inundated surface as well as the initial conditions (e.g. the soil saturation). Since the soil properties (granulometry, porosity, hydraulic conductivity), the initial conditions and the inundated surfaces are likely to vary from an event to another, the C_g has to be adjusted for each flood event.

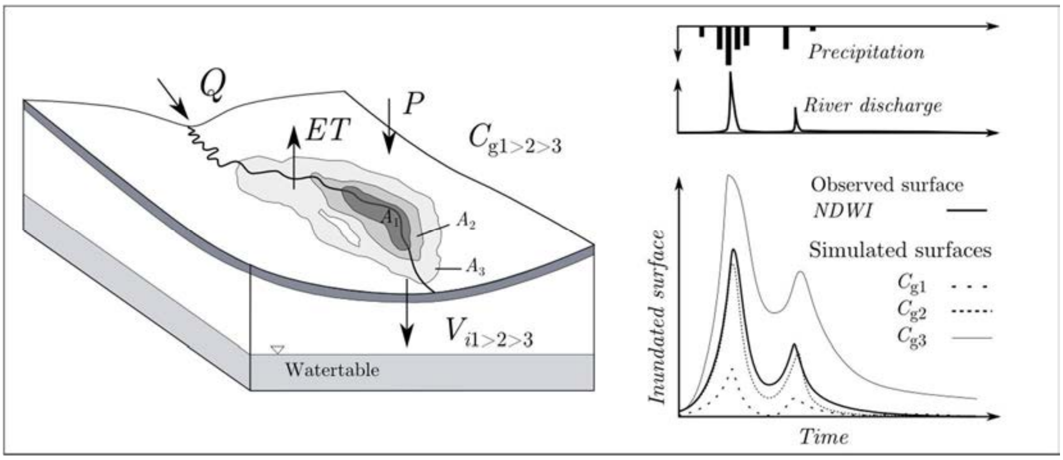

Fig. 3.13: Schematic diagram of the infiltration quantification for one event. The ground conductance value (C_g) controls the extent of the inundation. The areas A_i represent the simulated inundated surfaces at a defined time in function of the value (C_g). Reducing the C_g increases the size of the inundated area. The best C_g of each event is chosen for the simulations that best reproduce the observed inundations surfaces evolution derived from the *NDWI*.

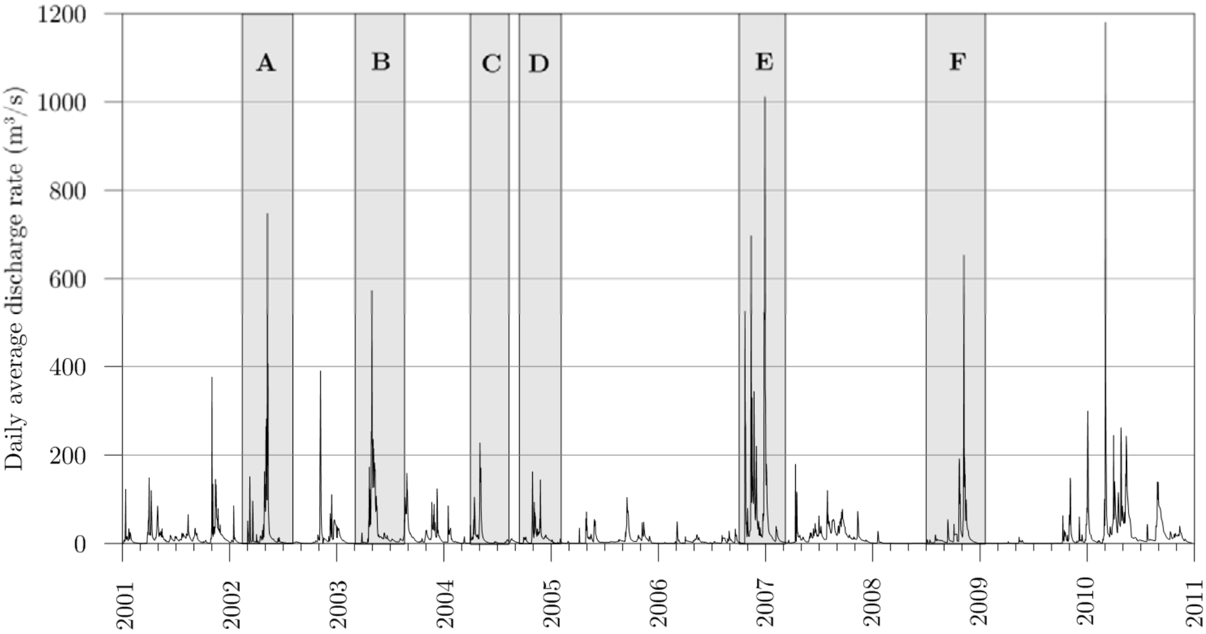

Fig. 3.14: Discharge rates of the Ewaso Ng'Iro River between 2001 and 2011 and selected flood events for the simulations. The event in 2010 was also simulated but river discharge are assumed to be corrupted and the event was not selected for the analysis. Source: CETRAD (Centre for Training and Integrated Research in Arid and Semi-arid Lands Development)

Six flood events were selected in order to cover various recharge magnitudes (Fig. 3.14). One fictitious event was also modelled in order to simulate a major event for which no inundation images are available. The water budgets computed by the model give the infiltrated volume (Vi) for each event.

3.4.1.2 Description of the model

The model was built using the physically based surface-groundwater fully-integrated *HydroGeoSphere* (*HGS*) code developed by René Therrien (2010), using the finite element approach. *HGS* solves simultaneously the variably-saturated flow and surface flow using a modified Richards' equation, the Darcy law and a simplified Saint Venant Equation.

The relation between pressure, saturation and hydraulic conductivity is defined by the Van Genuchten (1980) relation. Description of the equations and the capability of the simulation code are detailed by Therrien (2010) and Brunner and Simmons (2012).

Model domain

The model domain is chosen sufficiently large in order to cover all inundated areas, either induced by the Ewaso Ng'Iro River or by the runoff from precipitations. Historical information communicated by local people indicates that during the major flood event of 1998, the inundation was observed up to Dadaab.

The model is centred on the recurrent inundation area of the Lorian Swamp, which is located upstream of the freshwater lens. Around this area, the model was extended in order to insure that the simulated inundated surface could not reach the limit of the model (Fig. 3.15). East, this limit is fixed by the topographic ridge between Hadado, Habaswein and Liboi. Upstream (north and west), a distance of 50 to 100 km was set. The downstream limit was delimited at Liboi.

Mesh

A 2D finite element mesh is built with the Triangle algorithm developed by J.R. Shewchuck (2005). It contains 41736 elements with a resolution of about 1400 m over the entire model, except over the Lorian Swamp, the inundation area, where the resolution is around 800 m. The elevation of the model was extracted from the SRTM digital elevation model (DEM) (Fig. 3.16). The mesh is then extended to the third dimension with a thickness of 1 m in order to allow the infiltration through the soil.

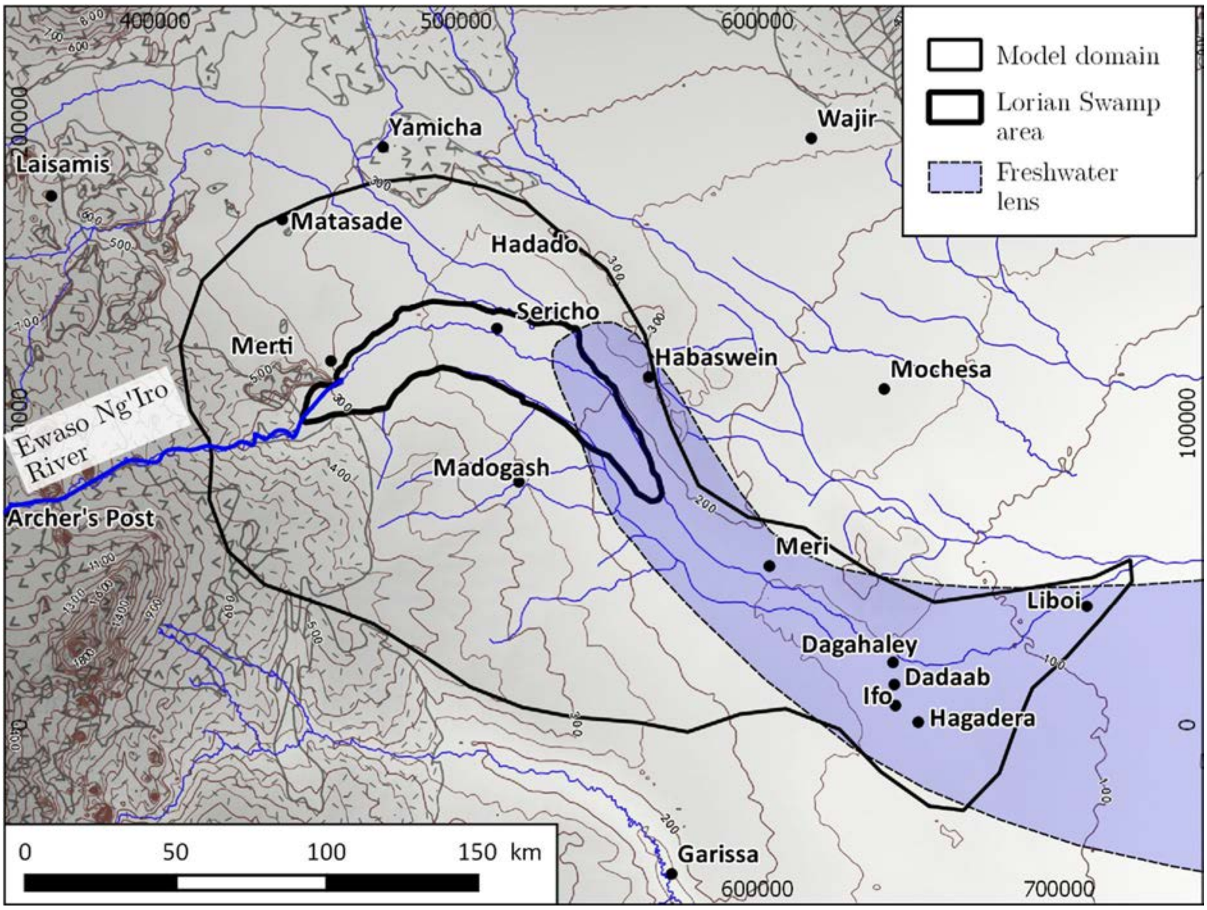

Fig. 3.15: The model domain is delimited in order that the simulated inundated surface could not reach the domain limit, based on the topography and the major historical inundation events described by local people. The freshwater lens of the Merti aquifer, which starts downstream the Lorian Swamp area and continues towards the Indian Ocean, is shown here as geographical benchmark.

Boundary conditions

The River influx Q is introduced onto the model surface with a flux-boundary condition (Neumann). Because the spatial resolution of the DEM is insufficient to reproduce adequately the channel of the Ewaso Ng'Iro River and because of the rough spatial resolution of the mesh, the injection point has to be located at the beginning of the flood plain of the Lorian Swamp, about 130 km downstream of the gauging station (Fig. 3.16), thereby assuming that no change in discharge takes place over this distance. The rainfall P is applied to the model surface with a flux boundary condition (Neumann) using daily raster extracted from the FEWS-net data. The evapotranspiration on the surface is simulated applying a potential evapotranspiration value (Table 3.1) on all the model surface faces with a flux boundary condition (Neumann).

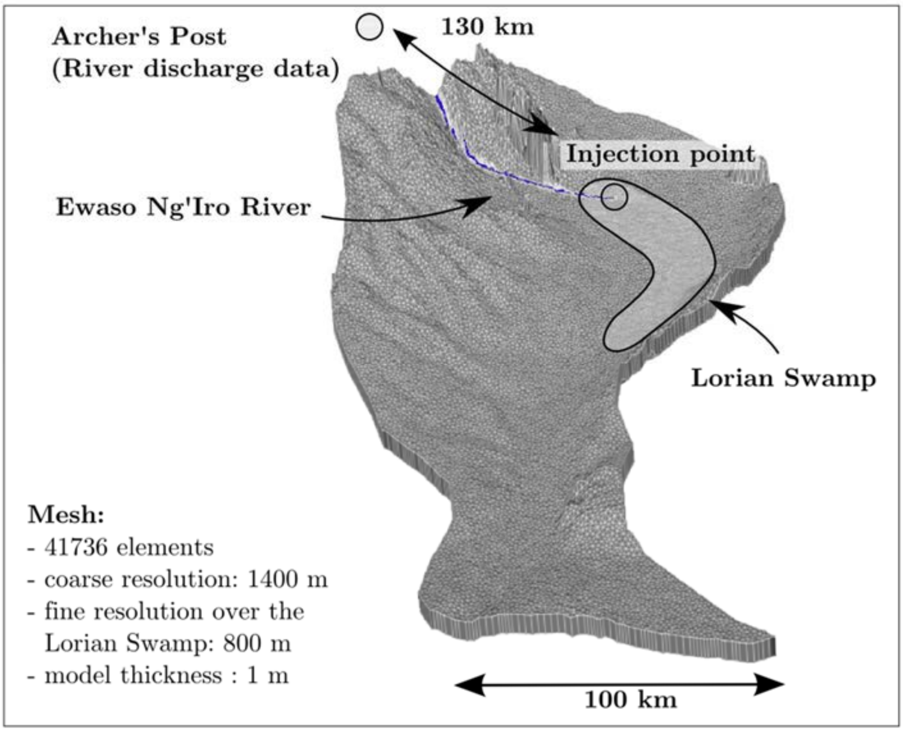

Fig. 3.16: 3D representation of the model. The injection point for the discharge is set at the beginning of the flood plain.

A head boundary condition (Dirichlet) equal to the elevation is defined at the bottom of the subsurface layer, allowing the surface water to flow towards the ground. A "*critical depth*" condition is set in order to allow surface water to flow out of the system for cases where surface water is not entirely infiltrated and could flows out of the lateral boundaries. These two boundary conditions are illustrated on the 2D vertical diagram of Fig. 3.17.

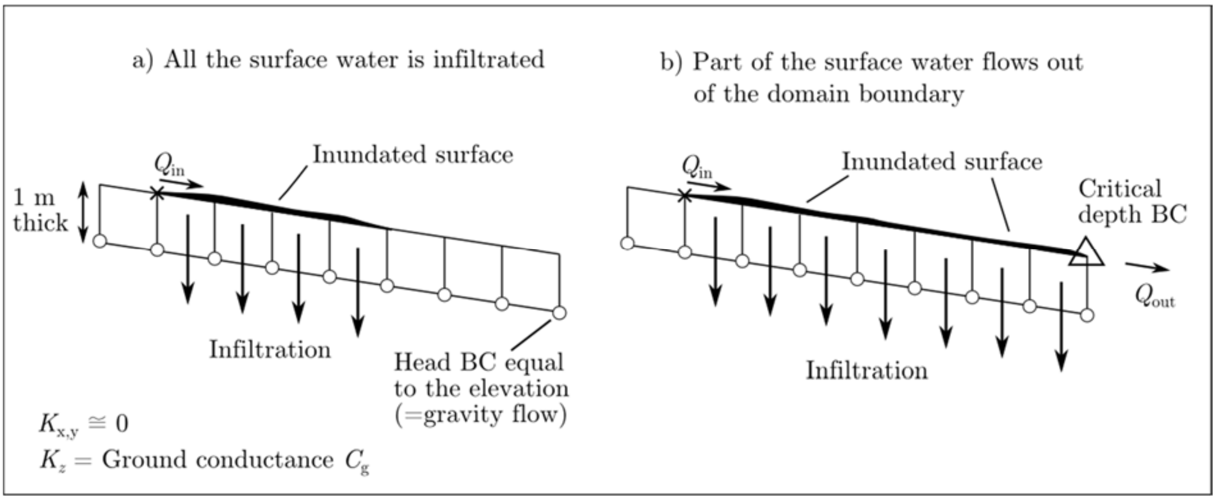

Fig. 3.17 : 2D vertical diagrams illustrating the head boundary condition (BC) and critical depth BC for a) a case where all the surface water is infiltrated and b) a case where infiltration is lower than the inflow at the discharge river (Q_{in}) at the injection point, that leads a part of the surface water to flows out of the domain boundary through the critical depth BC.

Initial conditions

In such arid climate, it is assumed that no precipitation occurs during a long period and the soil is almost dry when inundation starts. An arbitrary water depth initial condition of 0.005 m is defined at the beginning of the simulation. Then, in order to reproduce this feature, the model is run during several days before the beginning of the inundation event.

Material properties

The calibrating parameter C_g is defined in the model by modifying the vertical hydraulic conductivity. If the hydraulic conductivity is set to 0, no infiltration occurs over the domain. On the opposite, if a very high hydraulic conductivity is defined, almost all the water infiltrates into the soil and evapotranspiration is close to 0. Horizontal hydraulic conductivity (K_x and K_y) is set for each model to 5 x 10^{-10} m/d in order to avoid horizontal subsurface flow.

3.4.1.3 Calibration method

The calibration relies on the comparison of the observed inundated surfaces (*NDWI* images) with the simulated inundated surfaces obtained with the *HGS* model every 8-days, that is the temporal resolution of the *NDWI* images. The C_g is adjusted in order to produce simulated inundation surfaces as similar as possible to the observed ones over the time, as illustrated in Fig. 3.13.

In order to be compared with the *NDWI* images, the results obtained with the *HGS* model have to be converted into a binary raster having only dry and wet pixels. This delimitation is based on the water depth of the simulated surface water by applying a threshold. Surfaces below this threshold are considered as dry. Because of the microtopography of the terrain, a threshold of few centimetres has to be set in order to consider the soil as inundated. An intermediate threshold of 0.05 m was chosen. The determining of this threshold remains difficult and arbitrary, but it should reasonably ranges between 0.02 and 0.1 meters. The impact of the threshold on the resulting simulated inundated surface is significant but not crucial, as illustrated on Fig. 3.18 for various thresholds and related inundated surfaces during a same day (15th of May 2002). Between the assumed minimum (0.02 m) and maximum threshold values (0.1 m), the inundated surface varies between 331 and 257 km^2 respectively that is about 10 to 15% of a central average surface of 300 km^2. The very low threshold of 0.001 m indicates a surface 25% higher than the intermediate surface. The uncertainty related to this threshold on the infiltrated volume, as well as the other source of uncertainty of the method, will be discussed further at the end of the recharge quantification section (3.4.1.9).

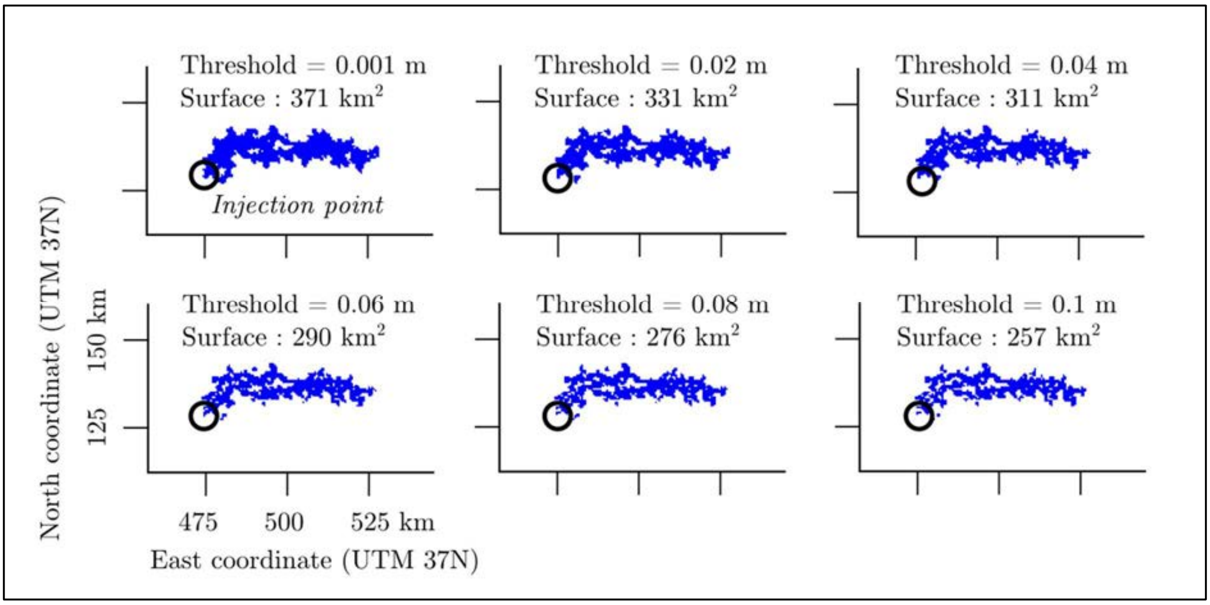

Fig. 3.18: Size of simulated inundated surfaces applying various water depth thresholds. Inundated surfaces are extracted from the *HGS* model on the 15th of May 2002.

The analysis of the simulated and observed images and their comparison was done with the *Tecplot* software and the GIS *GRASS* software. Results by event are presented in the next section.

3.4.1.4 Infiltration results by event

Infiltration of six inundation events where quantified with this method (event 'A' to 'F'). Additionally, one fictitious very large flood event ('G'), which was not observed with the satellite data, was simulated in order to discuss the impact of very high discharge and precipitation rates on the infiltration. Results on this event will be discussed separately in section 3.4.1.8.

Details of the calibration for the event 'E' are presented below. For the other events, only the inundation curves are discussed.

Four simulations were run for the event 'E', which took place between October 2006 and February 2007 (Fig. 3.19). The two simulations with the C_g values of 0.01 and 0.02 m/d reveal the difficulty to calibrate the event with a time-constant C_g value. Indeed, the *NDWI* inundation curve is characterised by two maxima, one in between the 15th of November and 1st of December 2006 (underestimated by the model) and the other one in January 2007 (over estimated by the model). The entire flood event could therefore be considered as two sub-events with two distinct C_g values. Best fit is found with a C_g value of 0.01 for the first sub-event and 0.04 m/d for the second one.

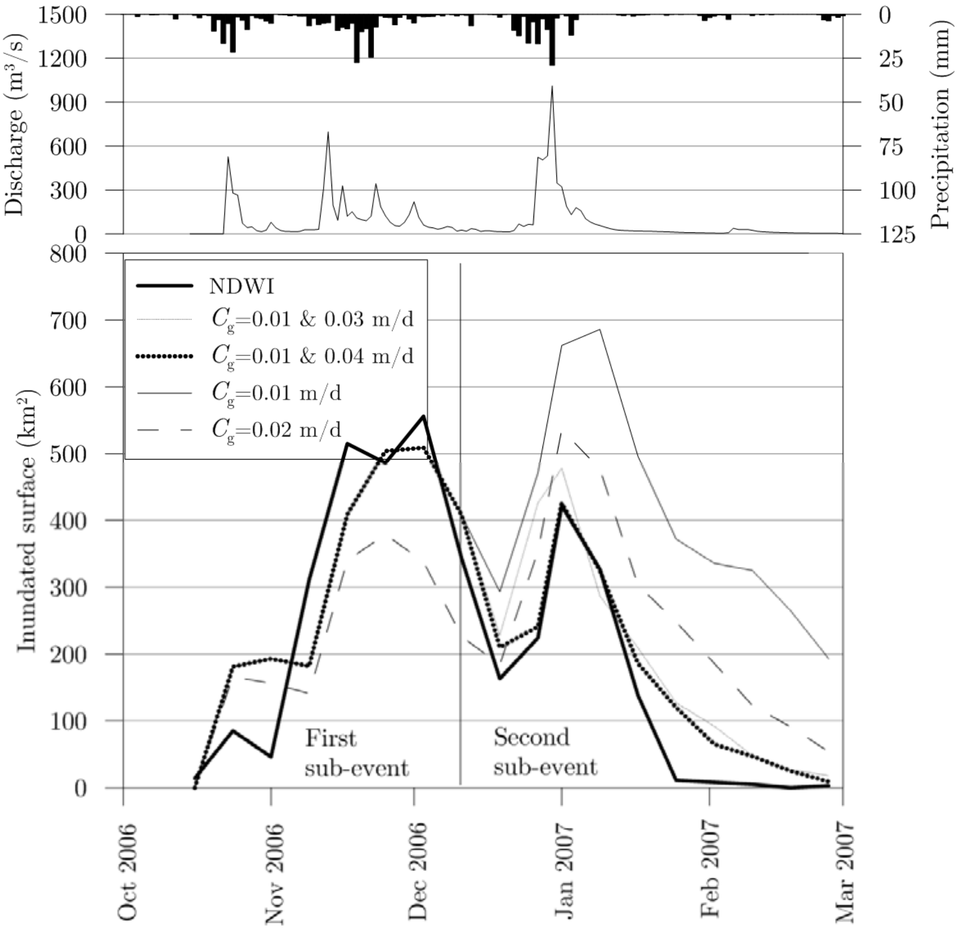

Fig. 3.19: *HGS* and *NDWI* simulations for the event E. The simulation was separated into two sub-events. Best fit is obtained with a C_g value of 0.01 for the first sub-event and 0.04 m/d for the second one.

The curves indicate that the dynamics of the flooding is well reproduced even though lower inundated surfaces below 100 km^2, at the beginning and the end of the event, are overestimated. Below this value, inundation surfaces are difficult to simulate in particular due to the unknown initial conditions and the low mesh resolution. The difficulty to reproduce perfectly the inundation dynamics also relies in the time resolution of the *NDWI* images and in the fact that the injection point of the river discharge is located about 130 km downstream from the Archer's Post gauging station. Finally, the model is based on the SRTM digital elevation model that was produced in 2000, while the morphology of the terrain and the main channel are remodelled periodically during major inundations.

A set of three images for both simulated and observed inundation surfaces during the flood event is presented in Fig. 3.20, Fig. 3.21 and Fig. 3.22. Fig. 3.20 shows the situation at the beginning of the inundation period on the 11th November 2006. On the observed inundation image (Fig. 3.20a), inundated areas are visible downstream of the injection point but also north of the Lorian Swamp area, revealing the importance of local precipitation.

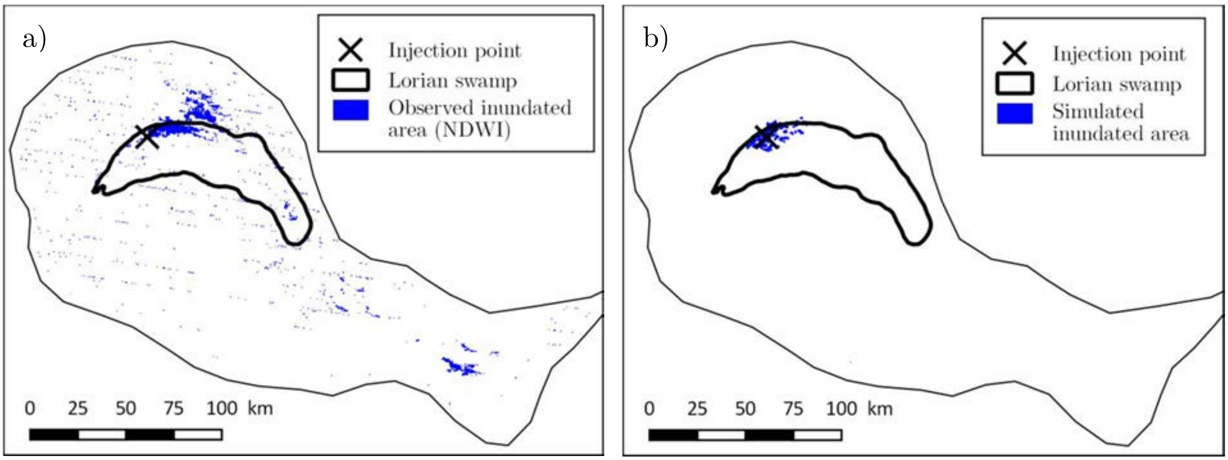

Fig. 3.20: Observed (a) and simulated (b) inundated surfaces on 11th November 2006, at the start of the flood event.

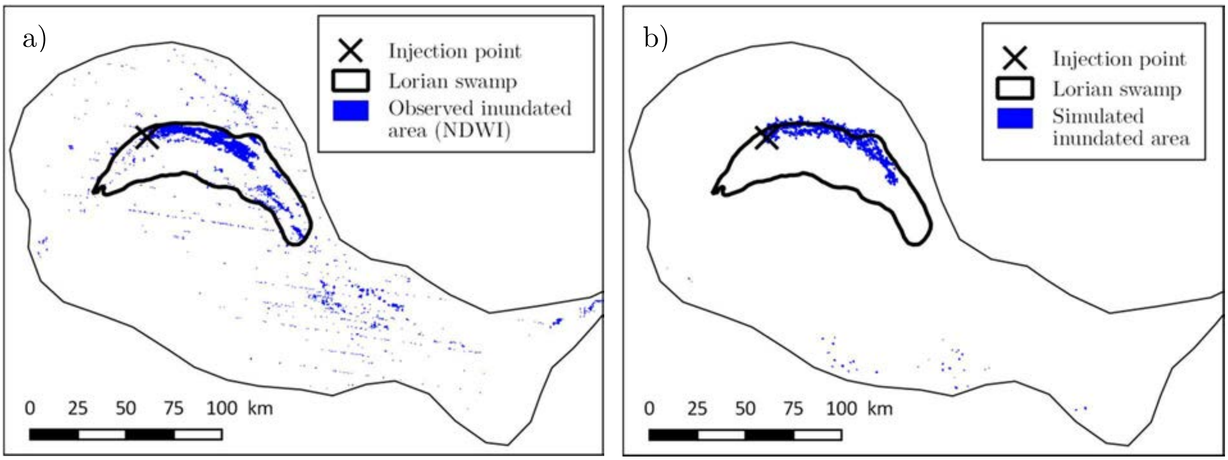

Fig. 3.21: Observed (a) and simulated (b) inundated surfaces at the maximum of the inundation (27th of November 2006).

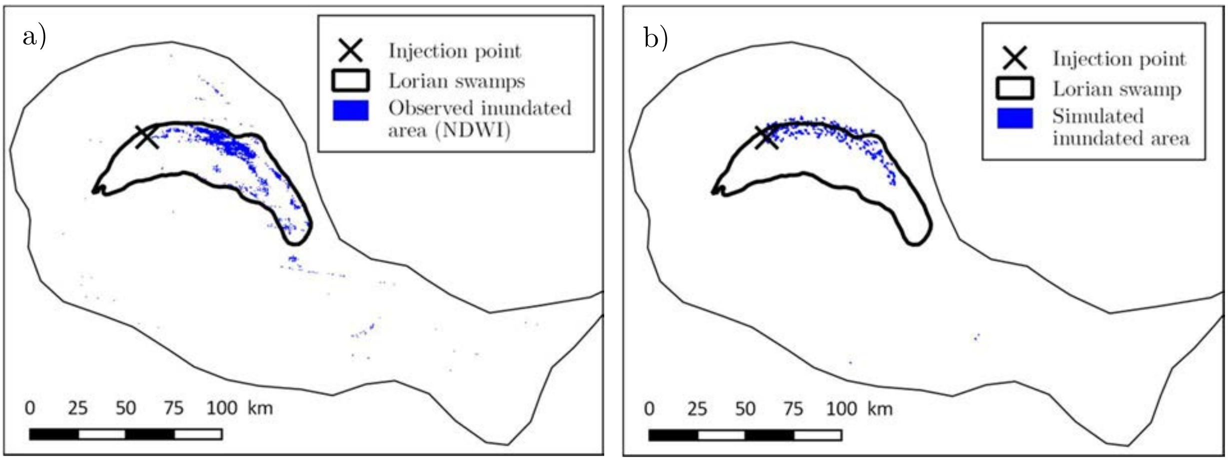

Fig. 3.22: Observed (a) and simulated (b) inundated surfaces during the recession on the 9th of January 2007. The significant difference between the two maps is explained by the slight shift between the two inundation curves (Fig. 3.19). Because the two curves are quite sharp, a small shift on the time axis induces a significant difference in resulting time-surfaces.

Still on 11th November, on the simulated inundation image (Fig. 3.20b), the inundated surface is only concentrated around the injection point, indicating the difficulty to accurately reproduce, with the numerical model, the two mechanisms leading to inundation, which are (1) the inundation from the river discharge and (2) the inundation due to runoff induced by precipitation. At the inundation maximum, inundation surface on the *NDWI* image (Fig. 3.21a) is controlled by river discharge and not any more by local precipitation. The observed inundated surfaces (Fig. 3.22a) during the recession, on the 9th of January 2007, and the simulated surfaces (Fig. 3.22b) show slight differences.

The shapes are overall similar to the simulated images despite the fact that inundated areas do not overlap perfectly. These differences are explained by the coarse resolution of the mesh as well as by the imprecision of the SRTM digital elevation model. Furthermore, differences between the simulated and observed maps could be explained by the slight shift between the two inundation curves (Fig. 3.19). Because the two rises of the two curves are quite sharp, a small shift on the time axis induces a significant difference in surface. Despite this discrepancy, the same overall geometries of the inundation surfaces are kept, explaining that even if the simulated and observed images do note perfectly overlap, inundation dynamics are well reproduced by the model.

Event 'A' and 'B' (Fig. 3.23 and Fig. 3.24) represent intermediate event magnitudes with maximum inundation surfaces between 250 and 330 km^2. Best fit is found with C_g values of 0.03 and 0.04 m/d respectively. Even though the dynamics of the two inundations is slightly different, both dynamics are well reproduced by the models: the event 'A' is characterised by a tight peak of the inundated surface while the 'B' event has a broader peak. This difference is explained by the dynamics of the discharge that increases progressively for the 'A' event before falling quickly, whereas the 'B' discharge rate has an inverse dynamic with a quick increasing followed by a progressive decrease. Furthermore, the main peak of the event 'B' is followed by a smaller one about one month and a half later which is in fact a separated minor flood event. The simulated inundation curve during the minor event overestimates the inundated surfaces, indicating that a higher C_g should be considered for this period.

Events 'C', 'D' and 'F' are representative of low discharge events (Fig. 3.25, Fig. 3.26 and Fig. 3.27), for which the C_g fitting parameter was calibrated to 0.1, 0.05 and 0.06 m/d respectively. Event 'C' has a magnitude similar to the second peak following the event 'B' discussed above. The C_g found for the event 'C' (0.1 m/d) is consistent with the higher C_g expected for the second peak of the event 'B'.

For the event 'D', the overestimation of the simulated inundation surfaces at the beginning of the inundation reveals the difficulty to simulate properly the inundation curves for small events, because of the initial conditions and the distance between the injection point of the river and the Archer's Post gauging station. Despite the peak of the river discharge at the end of October, the observed inundated surfaces remain quite low, indicating that during the beginning of the inundation, a given volume of water is used for saturating the soil between

Archer’s Post and the Lorian Swamp and limits the creation of inundated surfaces. After a short period of time, additional discharge (even lower) allows to develop larger inundation surfaces. Based on the discharge time series, the volume of water needed before starting the inundation is estimated for this event at 50 x 10^6 m^3.

For the event ‘F’, the shift between the observed and simulated curves (about one week) can again be explained by the distance between the gauging station of Archer’s Post and the river injection point in the model but also by the 8-day time resolution of the *NDWI* images.

Infiltration of each event was computed with *Tecplot* only under the inundated surfaces. Thus, infiltration related to the diffuse recharge by precipitation is not considered. All infiltration results, as well as river discharge volumes and precipitation volumes over the entire domain during the event are presented in Table 3.2. Evapotranspiration from the unsaturated zone as well as groundwater recharge and its relation with the river discharge and C_g are discussed in the next sections.

Event	Period	Best C_g (m/d)	River discharge during the event (10^6 m^3)	Precipitation during the event (10^6 m^3)	Infiltrated volume (10^6 m^3)	Max. inundated surface (km^2)	Infiltrated water height (m)
A	Mar. – Sept. 2002	0.03	385	5’600	282	2.58 x 10^2	1.1
B	Apr. – Sept. 2003	0.04	615	6’510	472	2.66 x 10^2	1.7
C	Mar. – Jul. 2004	0.1	179	3’390	137	7.80 x 10^1	1.5
D	Sept. 2004 – Jan. 2004	0.04	174	4’700	124	6.90 x 10^1	1.6
E	Oct. 2006 – Mar. 2007	0.01	967	9’650	768	5.90 x 10^2	1.5
F	Jul. 2008 – Feb. 2009	0.06	353	3’560	276	1.63 x 10^2	1.5

Table 3.2: Results of the infiltration quantification with the *HGS* model and main characteristics of each event. Precipitation is cumulated for the entire model domain during the event. The infiltrated water height (last column) corresponds of the total volume of infiltrated water normalised by the maximum inundated surface during the event.

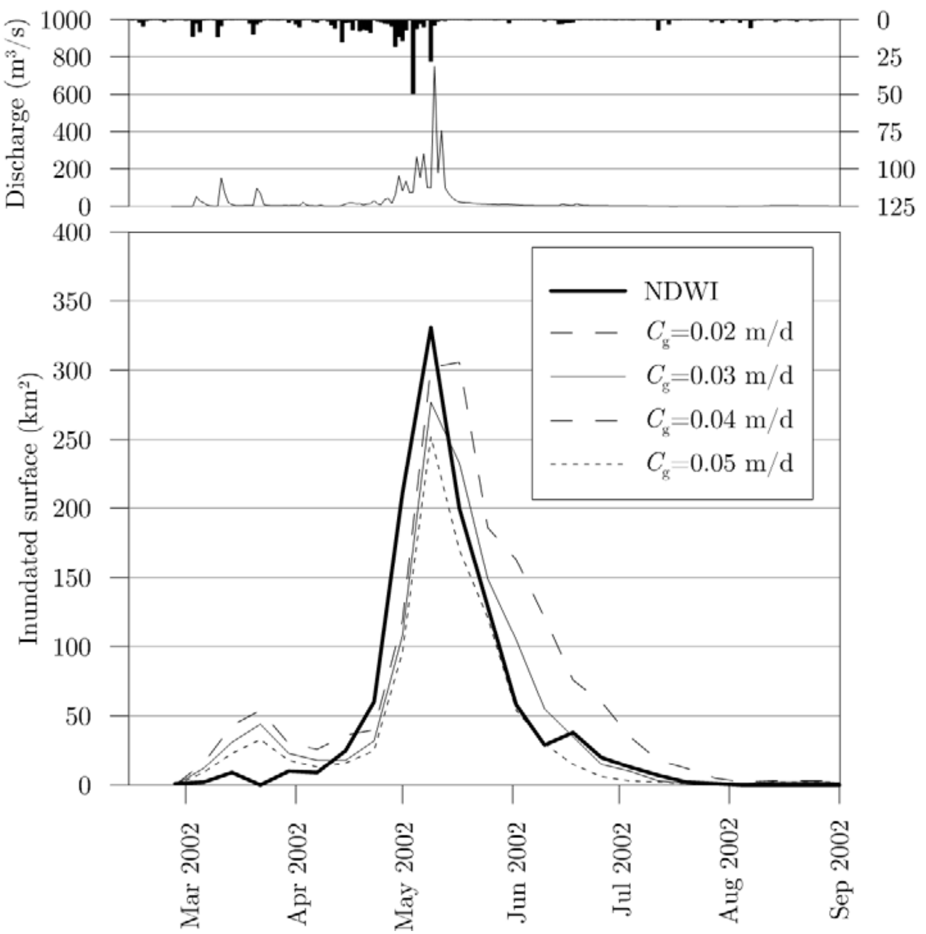

Fig. 3.23: *HGS* and *NDWI* simulations for the event 'A' between March and September 2002. The best inundation surface curve is obtained with a C_g of 0.03 m/d.

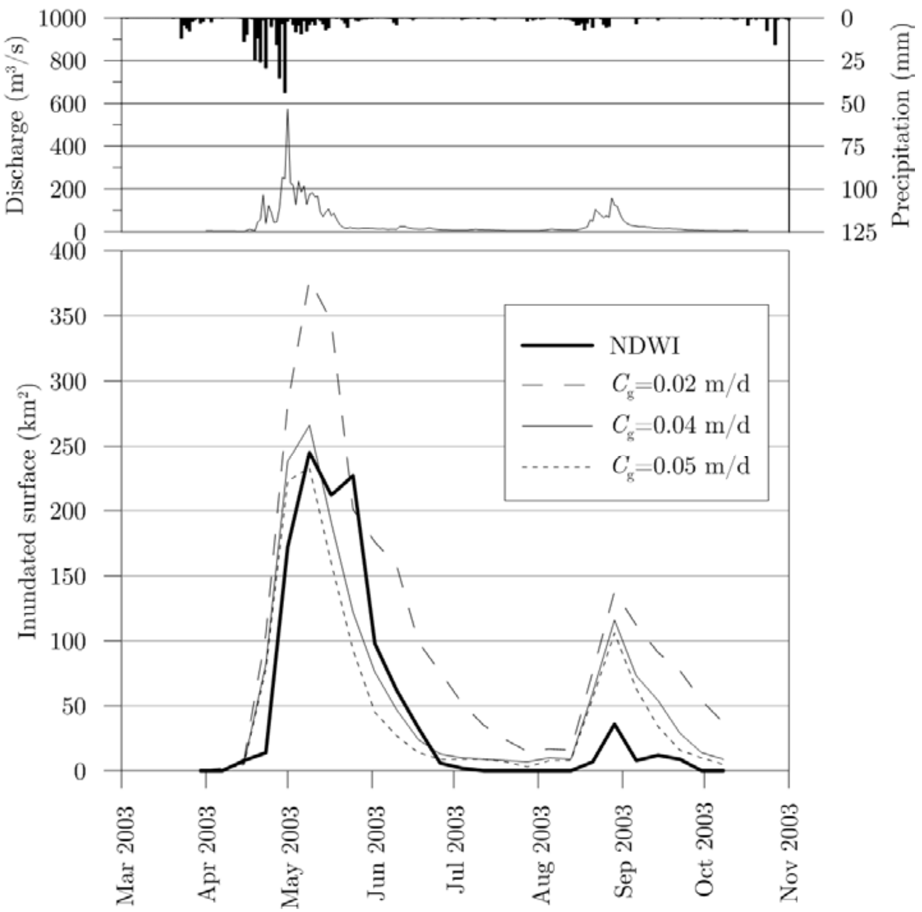

Fig. 3.24: *HGS* and *NDWI* simulations for the event 'B'. The best inundation surface curve is obtained with a C_g of 0.04 m/d.

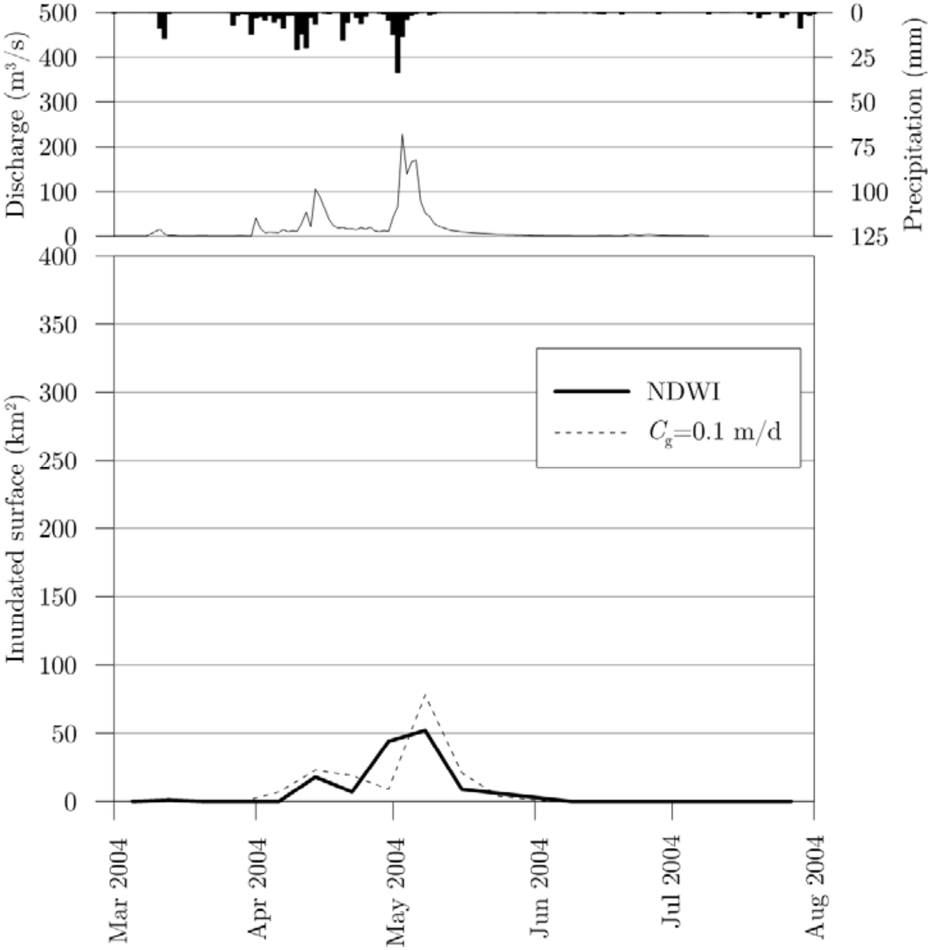

Fig. 3.25: *HGS* and *NDWI* simulations for the event 'C'. The best inundation surface curve is obtained with a C_g of 0.1 m/d.

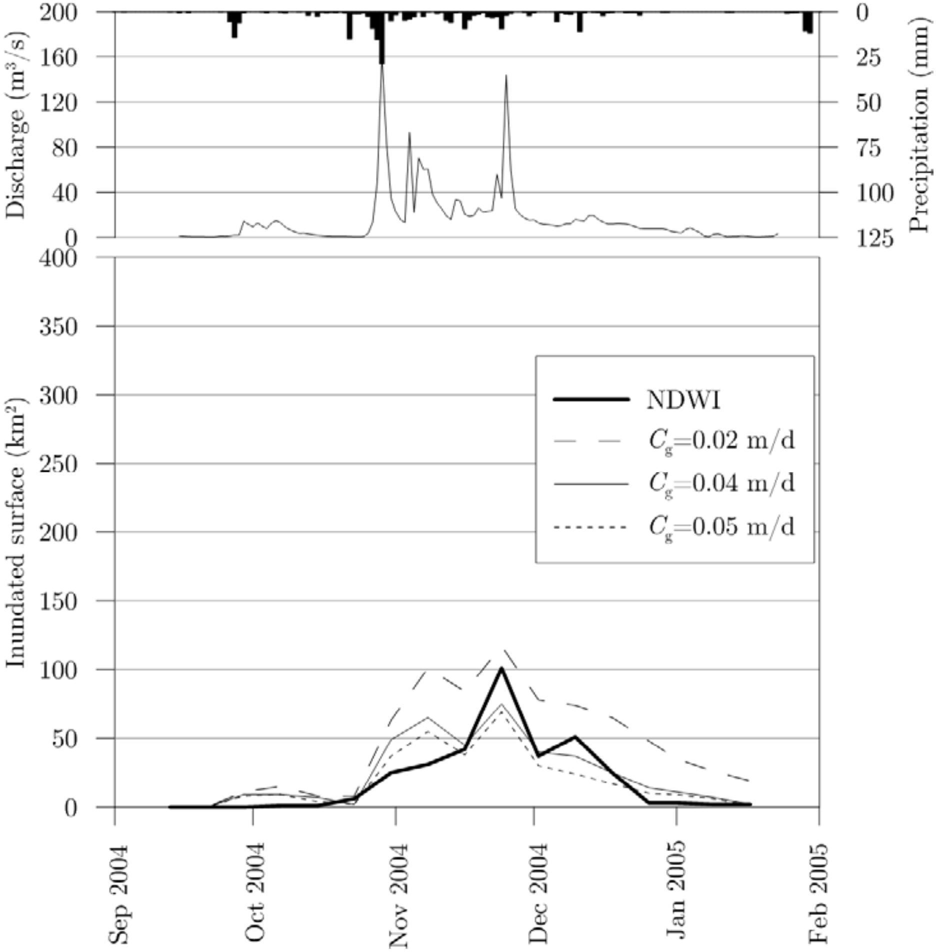

Fig. 3.26: *HGS* and *NDWI* simulations for the event 'D'. The best inundation surface curve is obtained with a C_g of 0.05 m/d.

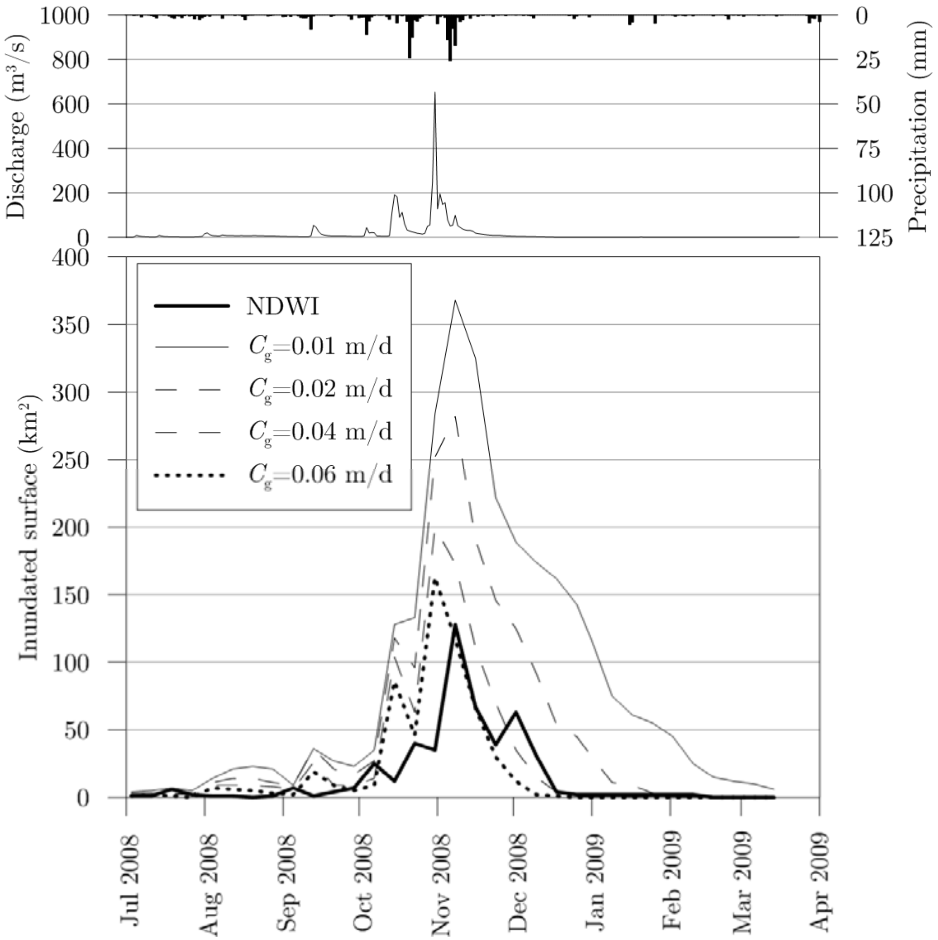

Fig. 3.27: *HGS* and *NDWI* simulations for the event 'F'. The best inundation surface curve is obtained with a C_g of 0.06 m/d.

3.4.1.5 Evapotranspiration from the subsurface

Based on the infiltration results, the groundwater recharge is computed by subtracting the evapotranspiration from the subsurface. Evapotranspiration from the subsurface is highly variable and difficult to estimate because of the material properties, the vegetation and the climatic conditions. Field measurements indicate that evapotranspiration from an unsaturated soil in arid to semi-arid areas could vary from 0.05 mm/d up to several mm/d for riparian zones, where groundwater is shallow (Bauer et al., 2004; Christoffersen et al., 2014; Nagler et al., 2007; Templeton et al., 2014; Wang et al., 2014; Yin et al., 2013). Because of the lack of field measurements on the field study, evapotranspiration is estimated with an analytical approach based on the maximum volume of water that can be evapotranspired after an inundation before the soil becomes unsaturated at the extinction depth (the depth at which no evapotranspiration can occur). This estimation is then compared with evapotranspiration rate extracted from MODIS satellite images after the inundation.

Analytical approach

This approach allows to estimate the maximum evapotranspiration height ET_h from the soil after a inundation event. This estimation is based on the volume of water that can be evapotranspired at the rate of the potential evapotranspiration before the soil is desaturated at the extinction depth L_{ext}, which is the maximum depth at which evapotranspiration occurs (Shah et al., 2006), at a time t_{ext} after the end of the inundation, as illustrated on Fig. 3.28.

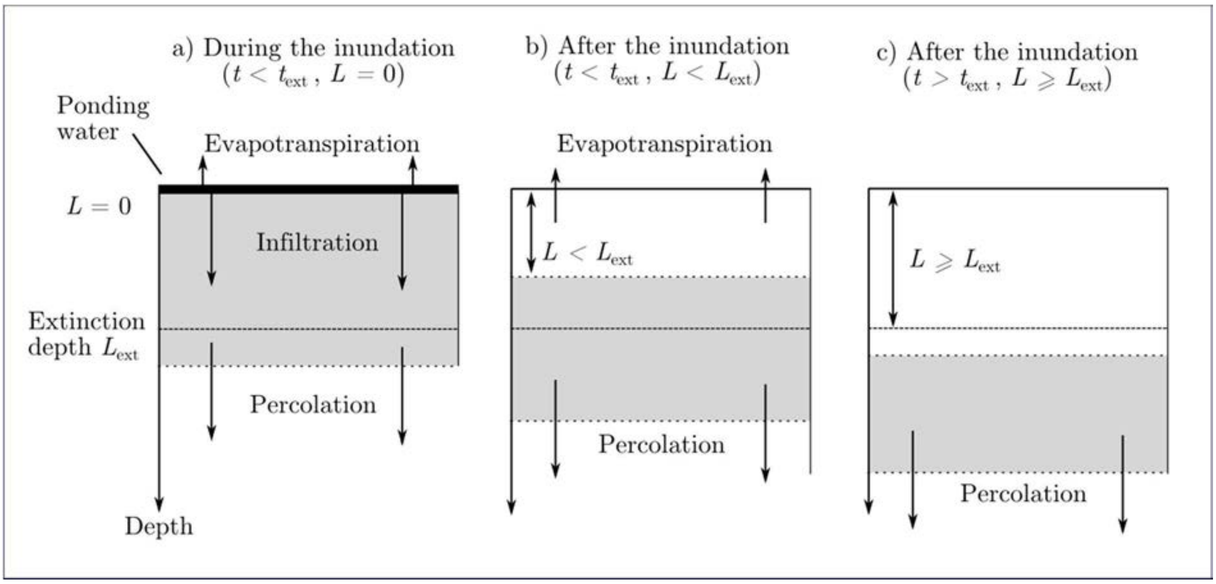

Fig. 3.28 : Location of a saturated body of water a) during the inundation, b) after the inundation and c) after the inundation once the soil at the extinction depth becomes unsaturated.

The time t_{ext} necessary to desaturate the soil up to the extinction depth L_{ext} is calculated by dividing the extinction depth L_{ext} by the percolation velocity v_p, which is the saturated hydraulic conductivity K_s divided by the effective porosity θ_e (Eq 3.3).

$$t_{ext} = \frac{L_{ext}}{v_p} = \frac{L_{ext} \times \theta_e}{K_s} \qquad (3.3)$$

In order to estimate the evapotranspired water height from the soil after the inundation, this time was computed for different typical soils and multiplied by a potential evapotranspiration rate of 9 mm/d (see Table 3.1). However, applying a constant potential evapotranspiration rate overestimates the *ET* because actual evapotranspiration ET_a quickly decreases once the upper layer of the soil becomes unsaturated. Furthermore, t_{ext} is also overestimated with this method since the evapotranspiration accelerates the descent of the desaturation front. Thus, this method is a conservative approach for estimating the evapotranspiration after the event.

Results in Table 3.3 indicate that the maximum volume of water that can be evapotranspired is mainly controlled by the saturated hydraulic conductivity K_s and in a lesser extent by the extinction depth of the soil class. Maximum computed water height that can be evapotranspired varies between less than 1 cm for sand and up to 106 cm for a silty clay.

Soil classes	Effective porosity θ_e	K_s (m/d)	Extinction depths L_{ext} (m)	t_{ext} (d)	Maximum ET_h (cm)
Sand	0.42	2.8×10^{0}	0.5	0.1	0.1
Loamy sand	0.40	7.2×10^{-1}	0.7	0.4	0.4
Sandy loam	0.41	2.6×10^{-1}	1.3	2.1	1.8
Loam	0.43	8.2×10^{-2}	2.65	14.0	12.7
silt loam	0.49	1.6×10^{-1}	4.2	12.8	11.8
Sandy clay loam	0.33	3.6×10^{-2}	2	18.3	16.5
Clay loam	0.31	2.4×10^{-2}	4.05	52.1	46.9
Silty clay loam	0.43	2.4×10^{-2}	4.5	81.0	72.9
Sandy clay	0.32	1.4×10^{-2}	2.1	48.2	42.1
Silty clay	0.42	1.2×10^{-2}	3.35	118.1	106

Table 3.3: Estimation of the maximum water height that can be evapotranspired after the inundation. The time t_{ext} indicated corresponds to the necessary time to desaturate the soil up to the extinction depth. The maximum evapotranspired water height is computed by multiplying this time with the potential evapotranspiration rate of 0.9 cm/d. Effective porosity and saturated hydraulic conductivity of typical soil are obtained from Mays (2010) extinction depth from Shah et al. (2006).

Assuming that the hydraulic conductivity of the soil is close to the ground conductance C_g obtained with the inundation simulations, soil of the most recurrently inundated (events ‘A’, ‘B’, ‘C’, ‘D’ and ‘F’) areas is likely to vary between a sandy loam (K_s=2.6 x 10^{-1} m/s) and a sandy clay loam (K_s=3.6 x 10^{-2} m/s) for the most recurrent events, leading to a maximum evapotranspiration height ET_h varying between 1.8 and 16.5 cm. Soils over the less recurrently inundated areas are likely to have a smaller hydraulic conductivity and to allow the evaporation of a higher height of water. Based on this analytical approach, the water height evaporated after each inundation events is estimated at 20 cm.

Remote sensing approach

The second way used to estimate the evapotranspiration from the unsaturated zone after the inundation is based on the measurement of the evapotranspiration at various locations after an inundation event by MODIS evapotranspiration satellite products (section 3.3.2). This analysis is carried out on the inundation event of November 2006 to January 2007 (event 'E', Fig. 3.19) and evapotranspiration values are extracted at six locations along the maximum inundated surface of the second part of the event (Fig. 3.29).

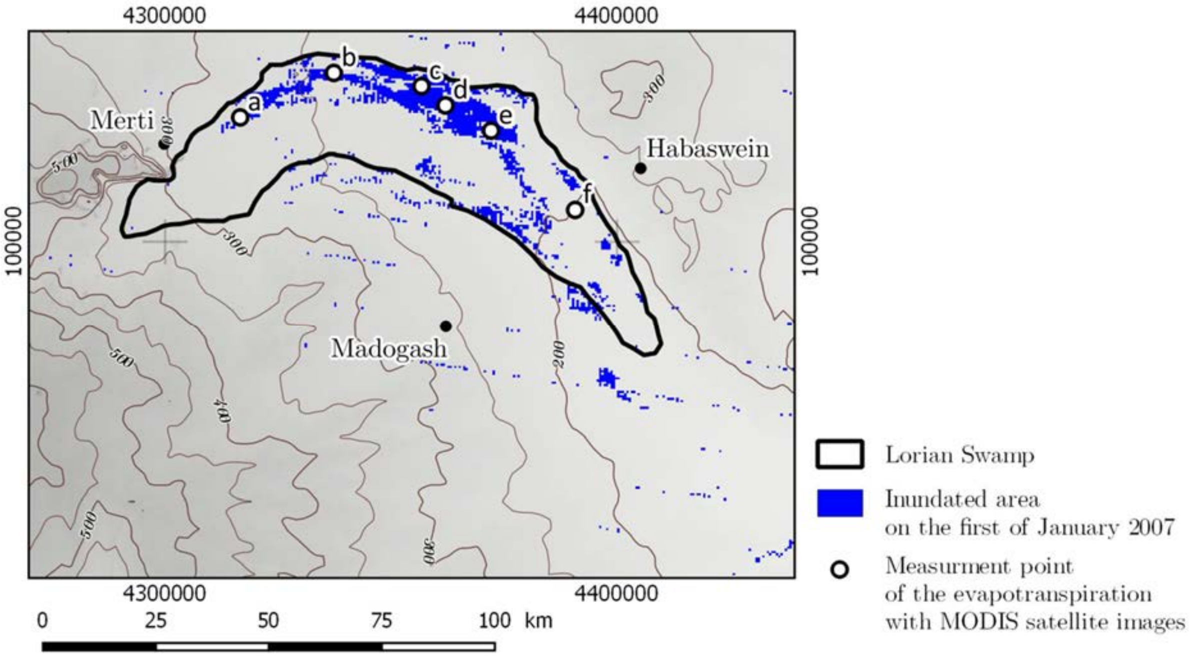

Fig. 3.29: Location of the measurement points of the evapotranspiration with MODIS satellite images and inundated surface on the 1st of January 2007.

Evapotranspired water height is computed between the end of the inundation period (shaded frame on Fig. 3.30a-f) and the next significant precipitation or the next inundation period (Fig. 3.30b and e). Daily evapotranspiration rate at the beginning of the period ranges between 0.4 and 0.15 cm/d and decreases up to less than 0.1 cm/d at the end of the evaporation period, that is similar to the evapotranspiration rate before the inundation event in October 2006. The maximum evapotranspiration rate corresponds approximately to half of the potential evapotranspiration measured by Woodhead (1968) (Table 3.1). The evapotranspired water height during this period ranges between 9.1 and 21.3 cm. After a period of three months, the impact of the evapotranspiration on the infiltrated water volume during the inundation event is assumed to become insignificant either because of the high decrease of the ET_a or because of new precipitations that humidify the soil, stopping the mechanism of deep water migration toward the surface.

These analytical and satellite-based approaches give quite converging estimations and allow to choose a rather conservative value of 20 cm as an approximation for the evapotranspired water height after an event. However, high uncertainty on this value remains due to the unknown soil composition and characteristics (hydraulic conductivity, porosity and extinction depth), for the analytical approach, and to the uncertainty on the MODIS evapotranspiration data that above 50% (3.3.2).

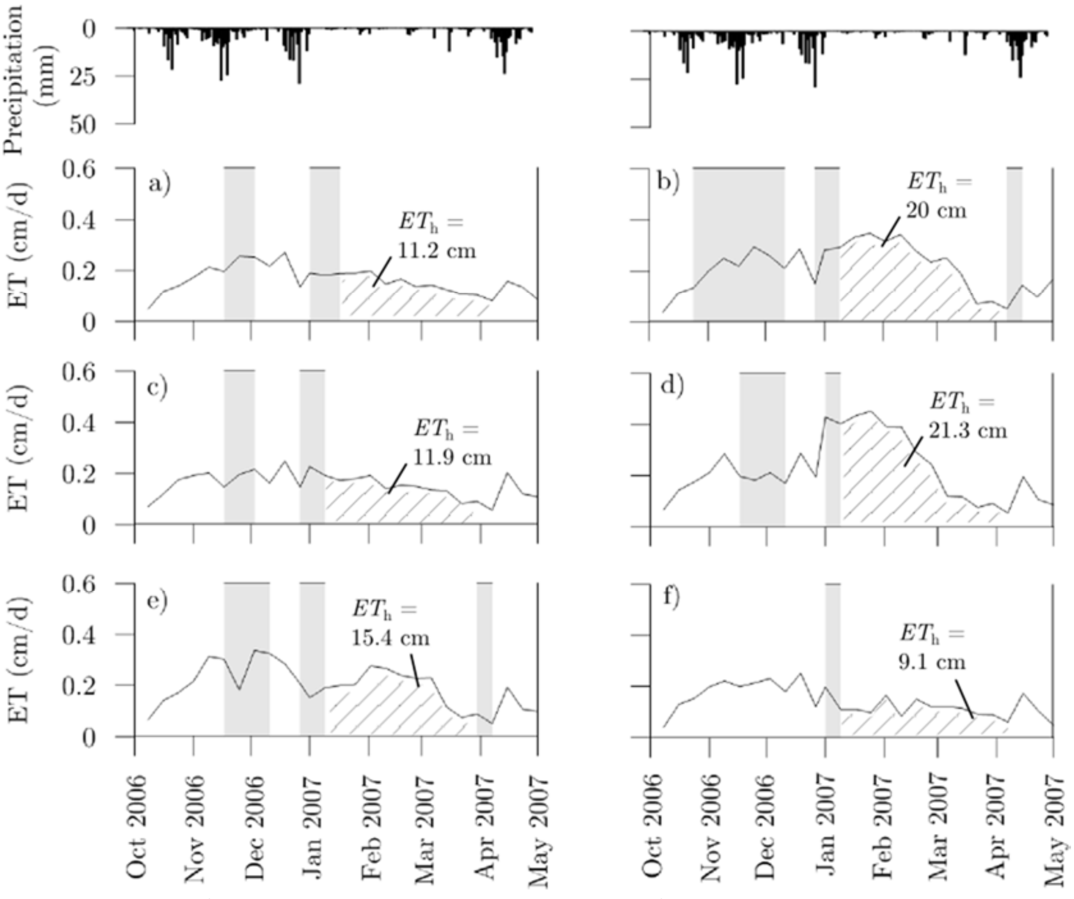

Fig. 3.30: Estimation of the evapotranspiration height ET_h after the inundation at six locations (Fig. 3.29) using MODIS evapotranspiration data. The evapotranspired height of water is calculated between the end of the inundation period (shaded frame) and the next significant precipitation (begin of April) of the event ‘E’ (Fig. 3.19).

3.4.1.6 Groundwater recharge by event

For each event, the water height of 20 cm is multiplied by the maximum inundated surface derived from the *HGS* model (Table 3.2) and subtracted to the infiltrated volume in order to obtain the groundwater recharge. This height of 20 cm amounts to between 11 and 17 % of the average infiltrated water height over the inundated areas during an event.

Among the 6 modelled events, best C_g varies between 0.03 and 0.1 m/d. Recharge varies between 94 and 688 x 10^6 m^3/y, for a total river discharge volume ranging between 174 and 967 x 10^6 m^3 (Table 3.4). Recharge ranges between 54 and 71% of the river discharge volume during the inundation. Reported to the maximum inundated surface during the event, the infiltrated volume corresponds to a water height ranging between 1.5 and 1.7 m for the event 'A' to 'F'.

The results of the fictitious event will be discussed in section 3.4.1.8.

Event	River discharge during the event (10^6 m^3)	Infiltration during the event (10^6 m^3)	Subsurface evapotranspiration (10^6 m^3)	Recharge of the event (10^6 m^3)	Recharge in % of the river discharge
A	385	269	48	221	57
B	615	461	51	410	67
C	179	117	15	102	57
D	174	107	13	94	54
E	967	785	97	688	71
F	353	244	31	213	60
G	1934	3630	2100	1530	79

Table 3.4: Results of the 6 events simulated ('A' to 'F') and the fictitious event ('G').

3.4.1.7 Relation between the ground conductance, river discharge and recharge volume by event

The modelling of flood events by means of the *HGS* model allowed to point out interesting features concerning the relation between the C_g and the inundation magnitude. Firstly, for the observed inundations, the cumulated river discharge and recharge volumes show a linear relation (Fig. 3.31). The linear regression curve crosses the discharge axis at a volume of 60 x 10^6 m^3 by event, indicating that for events with a cumulated discharge below this value at Archer's Post, no recharge occurs over the Lorian Swamp. Assuming a flood event during one month, this volume corresponds to an average river discharge of 23 m^3/s. As comparison, the average discharge at Archer's Post is 20 m^3/s (52 x 10^6 m^3/month). This threshold of 23 m^3/s is reached about three and a half months per year.

Secondly, it is observed that the homogeneous C_g that is calibrated to fit the models follows a logarithmic negative trend by increasing the recharge (Fig. 3.32). Since recharge is well correlated with the river discharge volume, it could be said that C_g diminishes by increasing the magnitude of the flood event. This could be explained by the fact that areas that are less frequently inundated are more likely to be covered by fine-grained flood deposits with lower permeabilities. The poor coefficient of determination R^2 (0.47) indicates that only half of the variation on the C_g is explained by the event magnitude and that the other half is explained by the variation of other parameters, such as the initial conditions, soil properties, changes in the river or flood plain morphology or errors in input data.

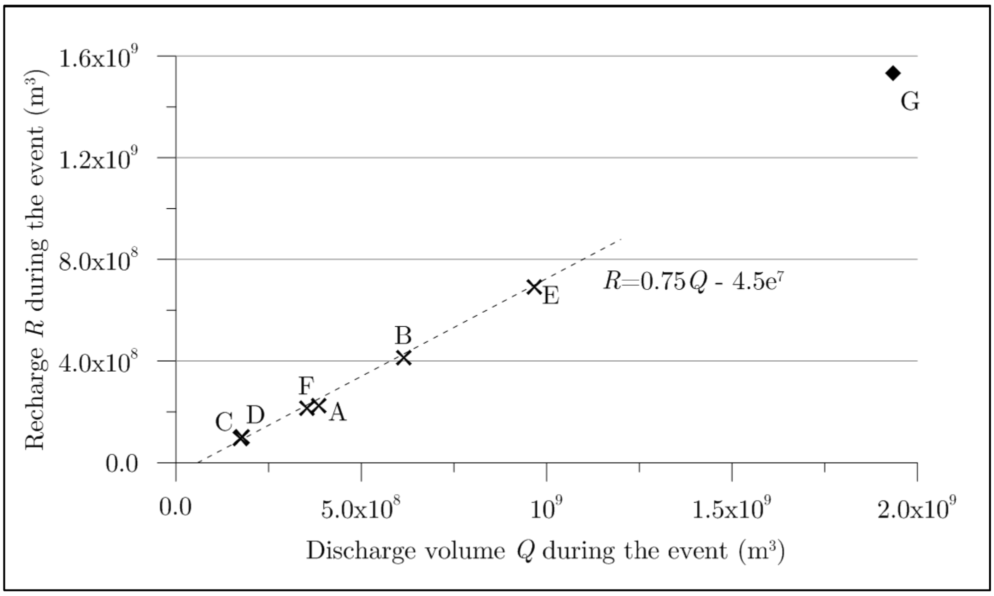

Fig. 3.31: Over the observed event magnitude domain, the relation between river discharge and recharge is linear. A fictitious simulated extreme event (‘G’) indicates that this relation can be extrapolated for higher discharge rates.

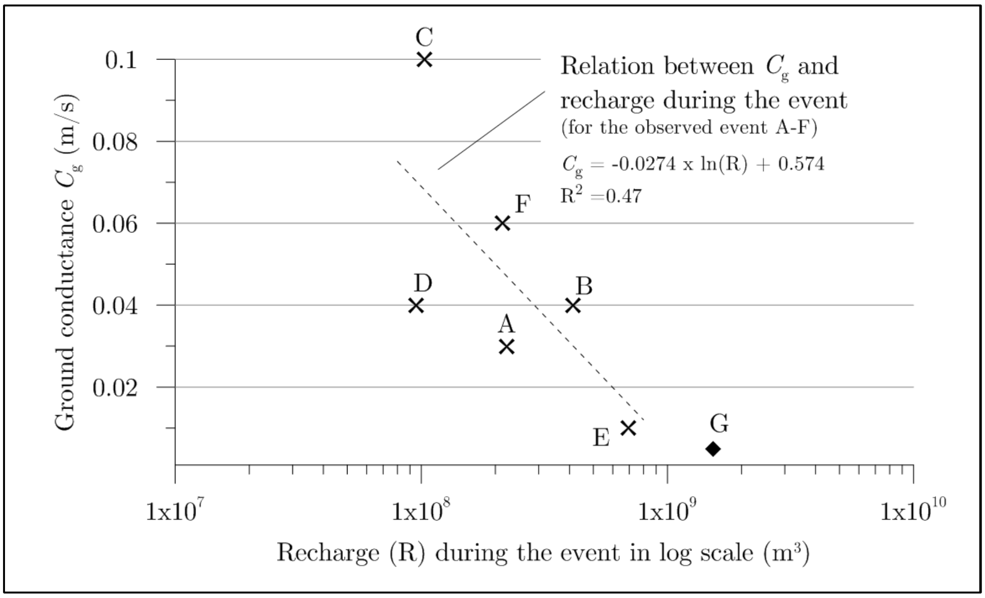

Fig. 3.32: Relation between recharge volume and C_g of the inundated area for observed events. C_g tends to diminish with increasing flood magnitude with a logarithmic relation. The poor coefficient of determination R^2 indicates that half of the C_g variation is explained by the recharge volume variation and the other half by other parameters, such as changes in initial conditions, variations of the soil properties or changes on the topography. The location of the event ‘G’ is consistent with this logarithmic relationship.

3.4.1.8 Discussion on the fictitious event ‘G’

The fictitious event ‘G’ is based on the event ‘E’ but with a doubled river discharge rate. The total discharge rate of this event corresponds approximately to the discharge rate of the major flood event in 1997, for which only monthly discharge rates are available. The impact of the precipitation (that is not known for this event) is assessed by applying, a doubled rainfalls rate, compared to the ‘E’ event. Based on the relation between C_g and recharge volume (Fig. 3.32), the C_g is set to 0.005 m/d. Inundation surfaces resulting from this C_g value are consistent with historical information from local people who reported that the inundation extended up to Dadaab. Compared to the other events, the infiltrated water height is significantly lower because of the large inundated surface and therefore the higher evapotranspired volume of water (Table 3.5).

However, the exact relation between river discharge, recharge and C_g beyond the observed inundation events remains hypothetical without precise calibration.

Event	Period	Best C_g (m/d)	River discharge during the event (10^6 m^3)	Precipitation during the event (10^6 m^3)	Infiltrated volume (10^6 m^3)	Max. inundated surface (km^2)	Infiltrated water height (m)
G	Fictitious event	0.005	1934	19’300	3630	1.93 x 10^4	0.3

Table 3.5: Ground conductance, river discharge, precipitation, infiltrated volume, maximum inundated surface and infiltrated water height of the fictitious event ‘G’.

3.4.1.9 Uncertainty on the groundwater recharge quantification

Several uncertainty sources can be identified within this approach for quantifying the concentrated groundwater recharge. These uncertainties can come from the input data, from thresholds determining used for distinguishing wet from dry pixels, from the *HGS* model and from the quantification of subsurface evapotranspiration. These uncertainties are discussed below.

River discharge

The quality of the river discharge data Q is difficult to assess, but despite the incoherent data identified within the flood event of 2010, they are assumed to be quite reliable. However, the distance between the Archer’s Post gauging station and the injection point within the model could lead to overestimation of the discharge.

An estimation of losses by evapotranspiration is carried out, based on a maximum daily evaporation rate along the channel between these two points. A daily evapotranspiration of 175’000 m^3/d was found with and *ETp* equal to 0.009 m/d (Table 3.1) and an evapotranspiration surface equal to 1.95 x 10^7 m^2 (width of the channel = 150 m, length = 130’000 m). This amount is moderate for small flood events (up to 15 % of the total discharge volume during the event) and insignificant for major ones (between 3 and 6 % of the discharge volume) (Table 3.6).

Event	River discharge during event ($10^6\,m^3$)	Event duration (d)	ET estimated before the injection point ($10^6\,m^3$)	ET estimated before the injection point	
				(% of the river discharge)	(% of the infiltrated volume)
A	385	206	36.2	9	13
B	615	199	34.9	6	8
C	179	152	26.7	15	23
D	174	130	22.8	13	21
E	967	168	29.5	3	4
F	353	266	46.7	13	19

Table 3.6: Estimation of the overestimation of the discharge rate due to evapotranspiration between the Archer's Post gauging station and the injection point for the events 'A' to 'F'. Overestimation is more significant for low flood event (up to 15 %) than for major flood events (between 3 and 6 % of the river discharge volume). Compared to the infiltrated volumes, the overestimation of the discharge rate reaches 23% for very low flood event and remains low for major flood events (between 4 and 8%).

Precipitation and evapotranspiration

As discussed in section 3.3.1, over seasonal period, the FEWS-Net data have an error between 2 and 19%. On a smaller time scale, errors could be higher. For small flood events, the contribution of precipitation to the inundation is assumed to be low. However, high precipitation could lead to surface runoff and significantly increases the inundation surfaces. Thus, uncertainty on precipitation has a higher impact on the recharge quantification for extreme climatic events.

The potential evapotranspiration was taken from field measurements and is consistent with other values in similar climates. However, an uncertainty of few percent remains possible.

NDWI images

Observed inundation surfaces obtained with the *NDWI* are derived from satellite images that are not a direct measurement, and may therefore contain uncertainty. However, this method was already used successfully by other authors for identifying inundated zone. Uncertainty on this data is assumed to be lower than 10 %.

The HGS model

The quantification of the infiltration with the *HGS* model also contains uncertainty due to the model itself. Firstly, the elevation of the *HGS* model is derived from the SRTM digital elevation model whose surface is not regular. This noise creates disconnected patches of water during the recession (Fig. 3.22). Additionally, the elevation of the model is the same for all simulations while actual topography and channel route is likely to change over the time, especially during major flood events.

Then, the ground conductance C_g of the soil is set as homogenous over the entire model, which is a simplification of the reality. Indeed, as observed on the relation between the C_g and the recharge (Fig. 3.32), the C_g is likely to be lower on less frequently inundated area. Thus, a more refined model with heterogeneous C_g could give better results.

However, despite these sources of uncertainty, the overall dynamics of the inundations is well reproduced by the model. Uncertainty related to the model is then supposed to be low (few percent).

Threshold for the distinction between wet and dry pixels

As discussed above, because of the microtopography of the soil, the choice of the threshold for distinguishing wet from dry pixels could lead to an over or underestimation of about 10% of the inundated surface (section 3.4.1.3). However, tests on models showed that a slight variation of the C_g, and thus on the inundated surface only modifies by few percent the infiltrated volume during an event.

Subsurface evapotranspiration

The probable major uncertainty related to this method is the estimation of the evaporation from the subsurface once the inundation is finished. As discussed above (section 3.3.2), evapotranspiration is very challenging to measure either with ground-based methods or remote sensing products. Additionally, this process is hard to simulate and relies on several parameters that are difficult to estimate and that could highly influence the result of the simulation (soil parameters, residual saturation of the soil, boundary conditions). Thus, the estimated infiltrated water height applied in this method may be significantly different, possibly two times higher or lower. Since evapotranspiration represents around 15% of the total infiltration (Table 3.4), an error of 100 % on the subsurface evapotranspiration can lead to a variation of 15% on the total recharge quantification. Furthermore, the method assumes a homogeneous and identic evapotranspiration height for all inundation events, while this value is likely to vary according to the climatic conditions after the inundations as well as the interval between two inundation events.

Uncertainties on these parameters and their implications on the overall method are summarised in Table 3.7. Some sources of uncertainty of parameters could be quantified between a range of percentage and other are estimated qualitatively. Their impacts on the groundwater recharge quantification are weighted by the contribution of each parameter to the overall recharge. Based on these estimations, the method has an overall uncertainty estimated between 30% and 50%.

Parameter	Uncertainty	Estimated impact on the recharge uncertainty
River discharge	3-15%	Overestimation up to 10%
Precipitation	Up to 20 %	5%
Potential evapotranspiration	Low	Low (1-5%)
NDWI images	Low	Low (1-5%)
HGS model	Low	Low (1-5%)
Threshold	20 %	1-2%
Subsurface ET	50-100%	7-15%

Table 3.7: Uncertainties on the parameters and their implications on the overall method

3.4.2 Annual groundwater recharge and return period

The simulations of flood events and the calibrations with satellite products allowed to define the relation between the discharge of the Ewaso Ng'Iro River and the recharge volume for separate events. The aim of this section is to extend this discrete quantification to the overall river discharge distribution in order to estimate the annual average recharge but also to identify the contribution of each discharge rate to the average recharge. Knowing the relation between river discharge and groundwater recharge, statistical discharge distribution is converted into a statistical recharge distribution, based on the Ewaso Ng'Iro River discharge data which is available for the period 1949-2010 on a monthly basis (Fig. 3.33). Then, based on the river discharge time series, the return period of extreme events is analysed.

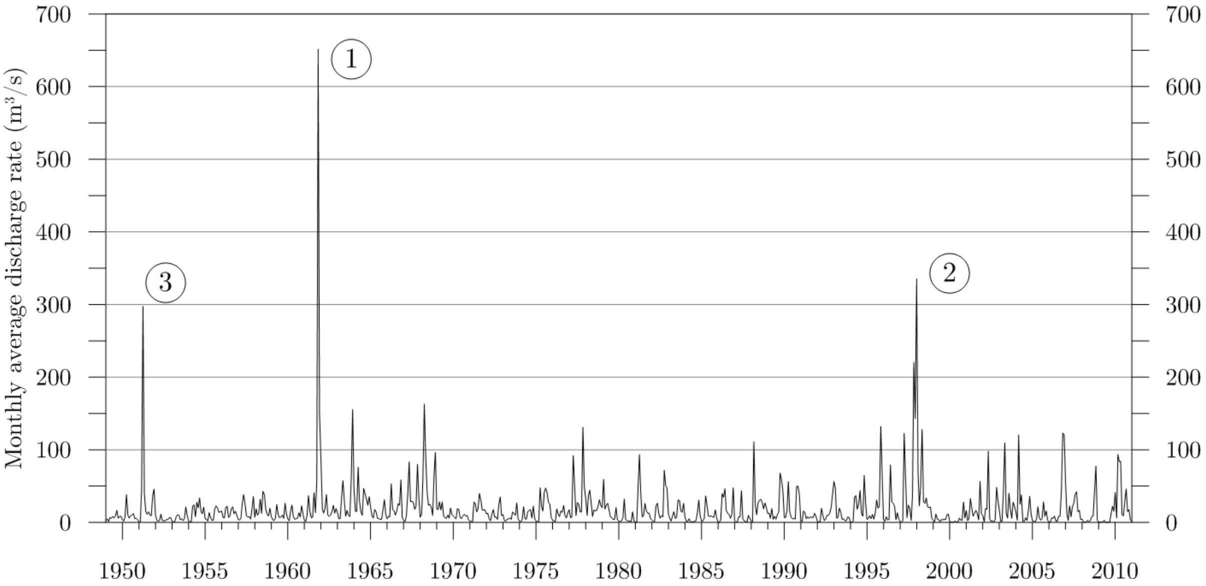

Fig. 3.33: Monthly average discharge rates at Archer's Post for the period 1949-2010 (Source : CETRAD and Swarzenski and Mundorff Study, 1977). Three major events are visible, (1) the most extreme one in 1961 with an average discharge of 652 m^3/s, followed by (2) the second in 1998 with an average discharge of 336 m^3/s and the last one (3) in 1951 with 297 m^3/s. The average annual discharge rate is 630 x 10^6 m^3/y or 20 m^3/s.

3.4.2.1 Conversion of statistical monthly river discharge distribution into monthly recharge distribution

The monthly time resolution of the discharge rate data does not allow to establish precisely the duration of each complete inundation event 1949 and 2010 and to carry out the analysis only on recharge events. Thus, in order to convert river discharge into aquifer recharge rates, each month is considered as a single event. The discharge river distribution is converted into a recharge distribution using the regression curve between the river discharge x and the recharge volumes by event y obtained in Fig. 3.31 (Eq 3.4).

$$y = -4.5 \times 10^{7} + 0.75x \qquad (3.4)$$

However, considering each month as a separate event leads to an underestimation of recharge for major and intermediate inundation events (whose duration are longer than one month) because the threshold of 60 x 10^6 m^3 derived from the linear regression curve, is subtracted from every month and not only one time by flood event. Thus, the monthly analysis based on the previously obtained regression curve is considered as minimum recharge value, and a second curve which minimises the error for the intermediate and major events will be defined in a second phase in order to consider the maximum recharge value. These minimum and maximum estimations are also a mean to consider the uncertainty related to the method discussed in section 3.4.1.9.

This statistical recharge analysis is carried out based on the statistical distribution of discharge rates $\varphi(x)$, which is converted into a recharge distribution $\varphi(y)$. The statistical model of monthly discharge distribution is fitted with the Generalized Extreme Value (GEV) distribution, which allows to reproduce well the frequency curve of the discharge rates. The GEV probability density function of discharge $\varphi(x)$ is given in Eq 3.5.

$$\varphi(x) = f(x|k,\mu,\sigma) = \frac{\left(1 + k\frac{(x-\mu)}{\sigma}\right)^{-1-\frac{1}{k}}}{\sigma} e^{-\left(1+k\frac{(x-\mu)}{\sigma}\right)^{-\frac{1}{k}}} \qquad (3.5)$$

where fitting parameters are :

k (shape parameter) = 0.57 (-)
μ (location parameter) = 7.1 (m^3/s)
σ (scale parameter) = 6.9 (m^3/s)
x = discharge rate (m^3/s)

Using the relation between the river discharge and the aquifer recharge (Eq 3.4), the discharge distribution is converted into the recharge distribution by a change of variable

(Fig. 3.34). This change of variable implies to introduce a Dirac delta function which contains all discharge frequencies below x_{min}, the threshold below which the discharge does not contribute to the recharge. This threshold point has an infinite frequency but the integral below this point is the same as the one below the discharge curve between 0 and x_{mi}.

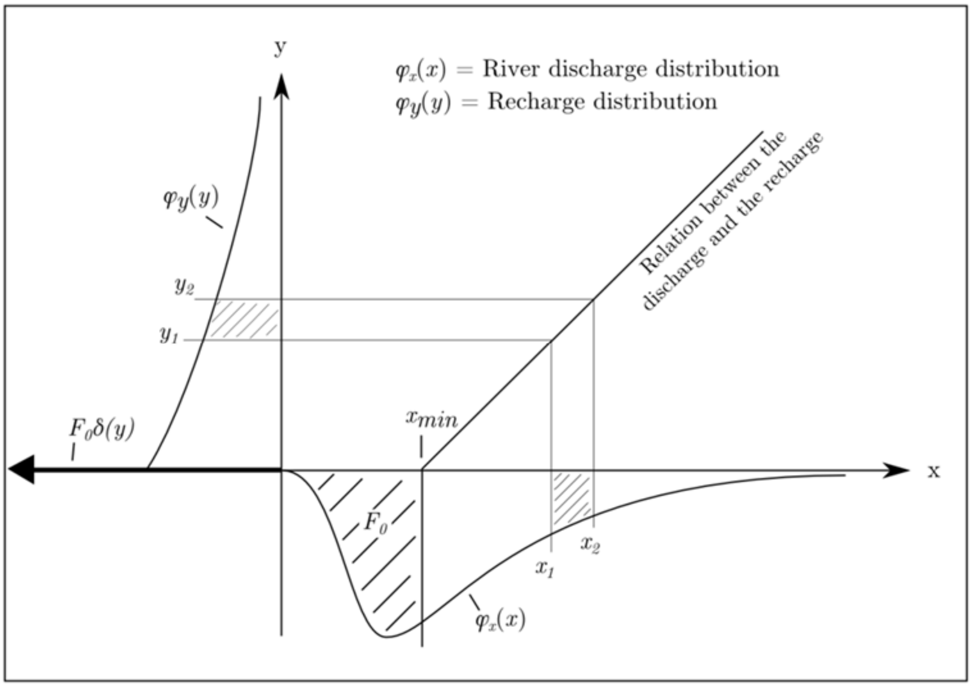

Fig. 3.34: Figure illustrating the conversion between the monthly river discharge distribution $\varphi_x(x)$ and the monthly recharge distribution $\varphi_y(y)$

The conversion is defined by

$$\varphi_y(y) = \int_0^{x_{min}} \varphi_x(x)dx\,\delta(y) + \frac{d}{dy}\int_{x_{min}}^{\frac{y-a}{b}} \varphi_x(x)dx \qquad (3.6)$$

with $x_{min} = -\frac{a}{b}$

and $\int_0^{\infty} \varphi_x(x)dx = 1$

where x and y are the discharge and recharge rates, respectively, and a and b are the constant and the slope of the linear regression of Eq 3.4. The integral of the discharge distribution approximated with the GEV distribution is 0.99.

This equation can be simplified in

$$\varphi_y(y) \;=\; F_0\delta(y) + \frac{\varphi_x\left(\frac{y-a}{b}\right)}{b} \tag{3.7}$$

$$\varphi_y(y) \;=\; F_0\delta(y) + \frac{\varphi_x(x)}{b} \tag{3.8}$$

$$F_0 \;=\int_0^{x_{min}} \varphi_x dx \tag{3.9}$$

where the Dirac function $\delta(y) = \infty$ for $y = 0$ and $\delta(y) = 0$ for $y \neq 0$.

The river discharge and recharge distributions (Fig. 3.35) show that most of the discharge frequencies (between 0 and 23 m^3/s) do not contribute to the recharge. From this threshold, the recharge distribution starts and follows then a decreasing slope.

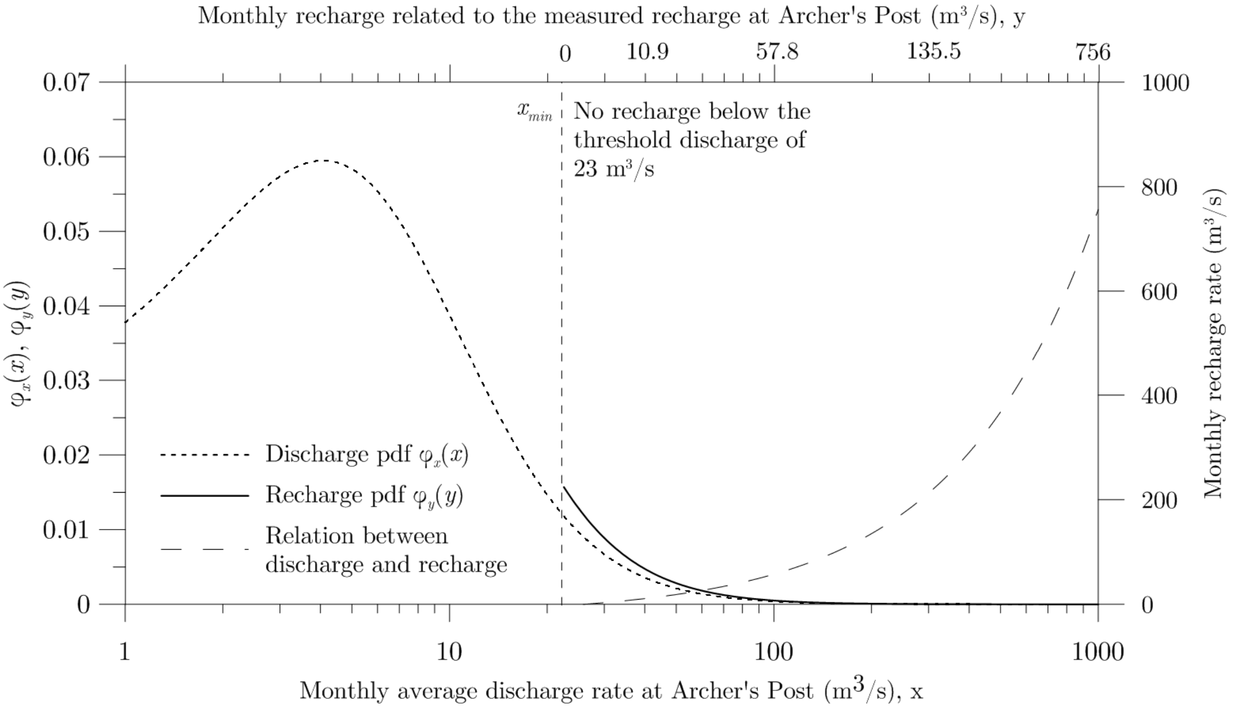

Fig. 3.35: Frequencies vs discharge and recharge rates (on logarithmic scale). The relation between recharge and discharge rate is shown on the right axis and the dashed line. No recharge occurs below a monthly average discharge rate of 23 m^3/s.

The recharge contribution of each recharge rate $\varphi'(x)$ to the total recharge is obtained by multiplying the recharge rate with its corresponding frequency (Eq 3.10). Then the integral of this function yields the annual average recharge (Eq 3.11) which is 195 x 10^6 m^3/y for the total time-series of 1949-2010. In comparison, the total annual average discharge rate (including discharge below 23 m^3/s) of the river is 630 x 10^6 m^3/y, indicating that less than a third of the long term river discharge is converted into groundwater recharge.

$$\varphi'_y = y\varphi_y(y) \tag{3.10}$$

$$\bar{y} = \int_{x_{min}}^{\infty} y\varphi_y(y)dy \tag{3.11}$$

The analysis of the distribution of discharge/recharge rates reveals that half of the recharge is controlled by major events with discharge rates exceeding 117 m^3/s (Fig. 3.36).

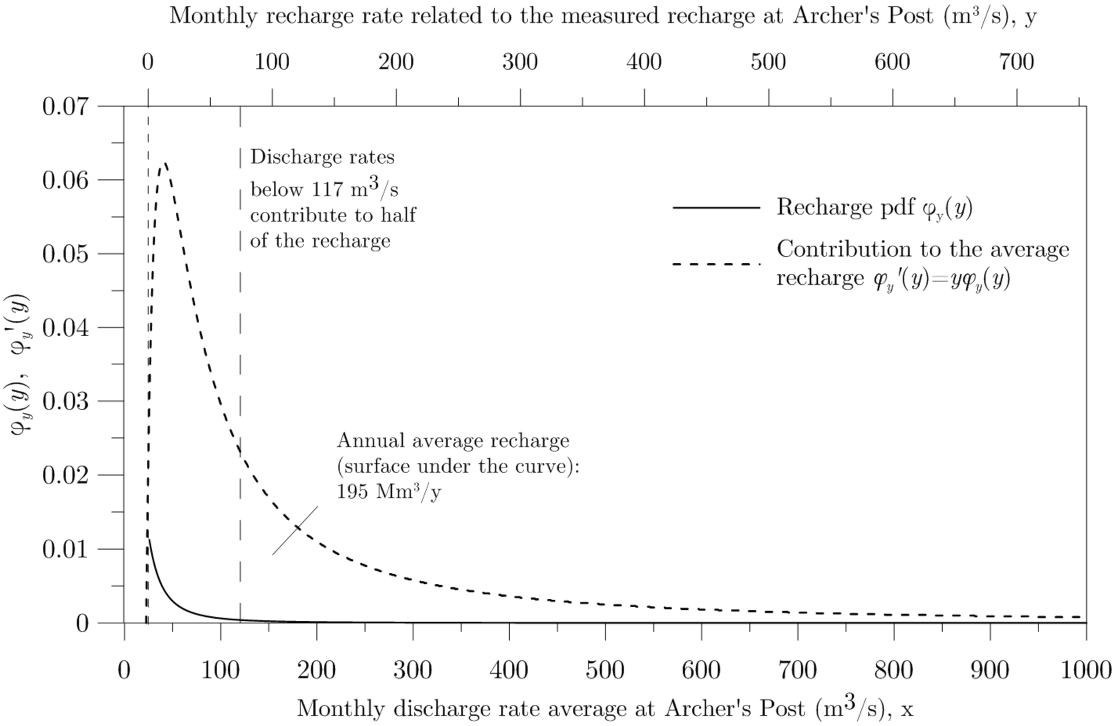

Fig. 3.36: Recharge frequency curve (black line) and curve of the contribution to the average annual recharge (dashed line) computed by multiplying the recharge frequency by the recharge rate (Eq 3.10). Annual average recharge is 195 x 10^6 m^3/y (surface under the curve, Eq 3.11) and half of the recharge occurs with river discharge rates below 117 m^3/s.

As discussed above, since this approach assumes that each month is a discrete flood event, estimation of the recharge rates is likely to be underestimated. A comparison between the simulated recharge volume by event and the computed recharge volume derived from the regression curve for the same period is given in Fig. 3.37a. This "computed recharge" is calculated by converting each monthly discharge volume into monthly recharge volume and cumulating them over the simulation period. Lower flood events are underestimated by approximately 80% and higher ones by 30%. Considering this significant bias, another discharge-recharge regression curve is fitted in order to minimise this error. It is assumed that this significant difference is caused by the distance between the gauging station and the inundation plain, thus only the constant '*a*' has to be adjusted. A better fit is found with a constant of 1 x 10^7, as shown in Fig. 3.37b.

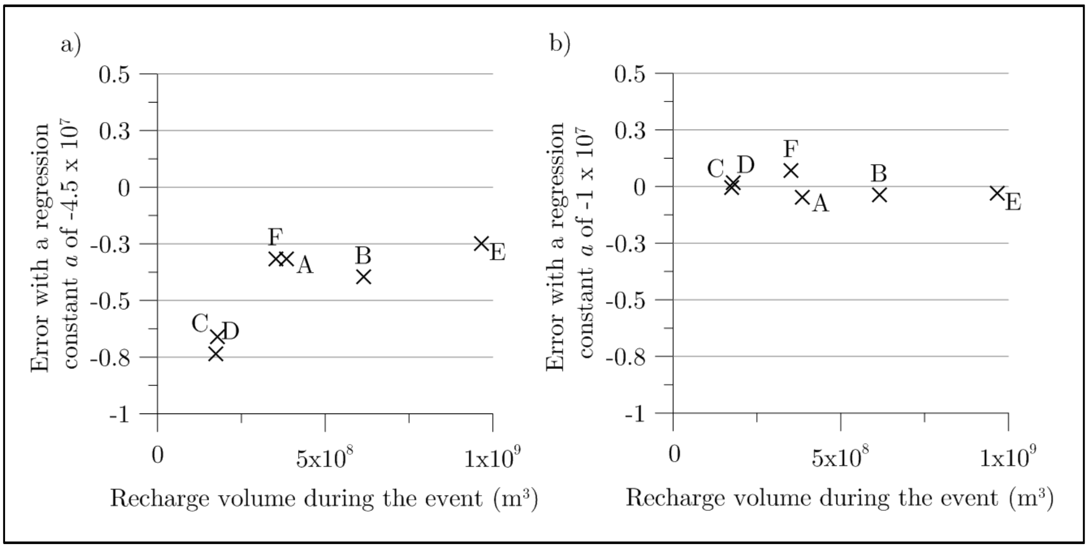

Fig. 3.37: Error between the simulated recharge during the entire flood events by the *HGS* model and the computed recharge with the regression curves: a) the regression constant a is set to -4.5 x 10^7 and b) -1.1 x 10^7.

Based on the new recharge distribution, the threshold leading to recharge is 8.5 m^3/s. Compared to the previous recharge distribution, this lower threshold gives a dramatically higher importance to lower discharge rates (Fig. 3.38). Thus, the annual average recharge increases to 329 x 10^6 m^3/y, and the discharge rate threshold explaining half of the recharge volume diminishes to 65 m^3/s. Even though this modified recharge distribution allows to minimise the error with the simulated flood episodes, it is possible that very low event (which have a high frequency) turn out to be overestimated because of a threshold being too low. Thus, this second recharge distribution should be considered as an upper limit for the recharge quantification.

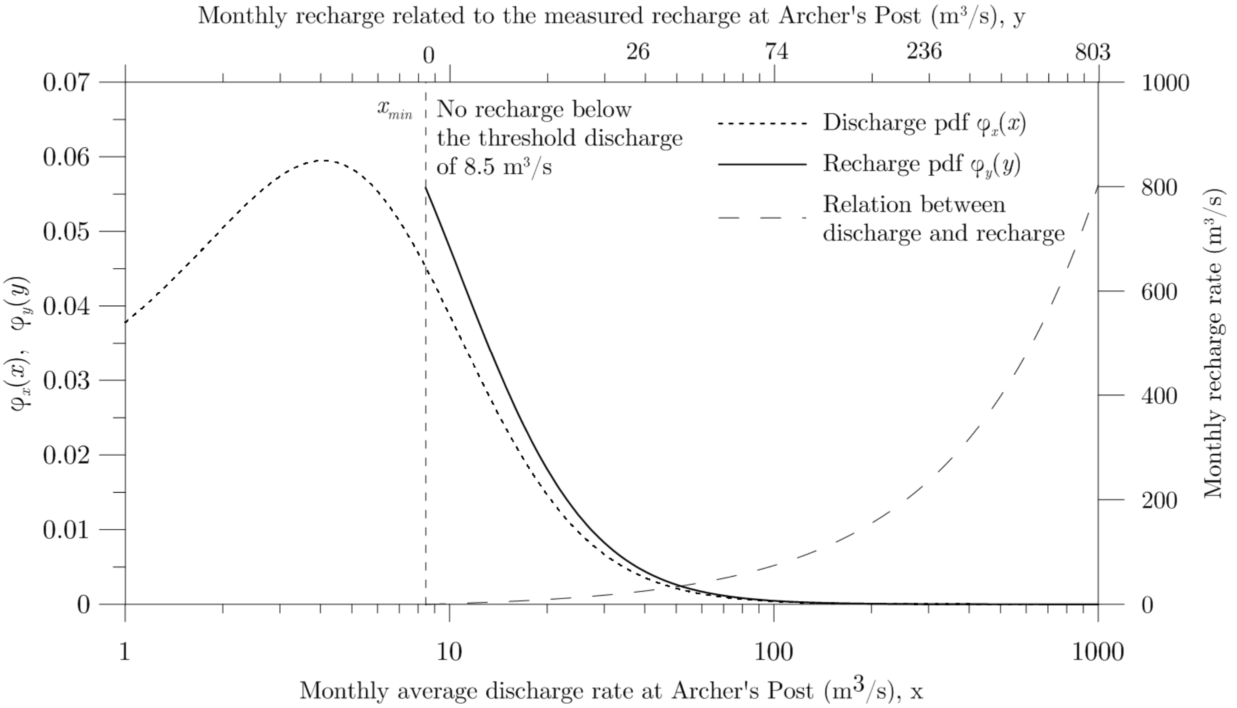

Fig. 3.38: Frequencies vs discharge and recharge rates (logarithmic scale) considering the modified discharge-recharge conversion rule. The relation between recharge and discharge rates is shown on the right axis and the dash line. No recharge occurs below a monthly average discharge rate of 8.5 m^3/s.

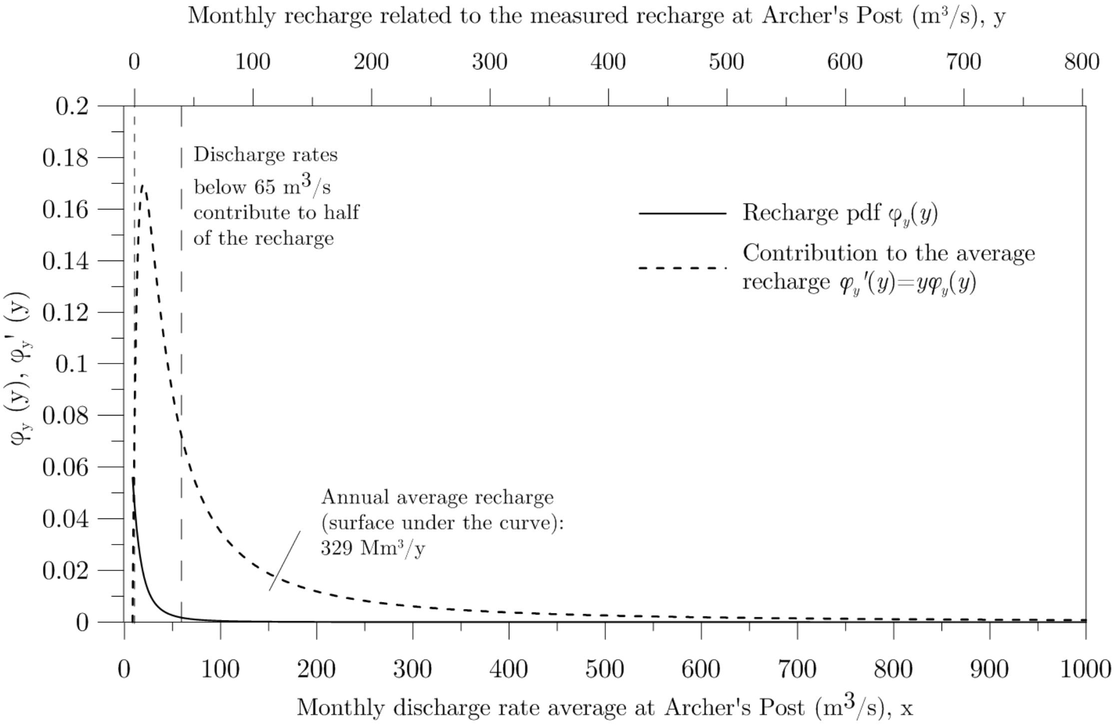

Fig. 3.39: Recharge frequency curve (black line) and curve of the contribution to the average annual recharge (dashed line) computed by multiplying the recharge frequency by the recharge rate (Eq 3.10). Annual average recharge is 329 x 10^6 m^3/y (surface under the curve, Eq 3.11) and half of the recharge occurs with river discharge rates below 65 m^3/s.

3.4.2.2 Return period of maximum annual inundation events

The return period of extreme events was computed from the GEV distribution (Eq 3.5) of the maximum monthly average discharge rate of each year. Fitting parameters of the GEV distribution are: $k = 0.61$; $\mu = 24.70$; $\sigma = 36.15$. Return period (P_r) is computed by:

$$P_r = \frac{1}{(1 - \mathrm{GEVcdf})} \qquad (3.12)$$

where GEVcdf is the cumulated distribution function of the GEV distribution.

This analysis reveals that for the discharge of the lower recharge model (Fig. 3.36), the monthly discharge average of 117 m^3/s has a return period of 6.7 years. In other words, extreme events whose return periods are 6.7 or greater contribute to half of the recharge. For the higher recharge model (Fig. 3.39), the return period for the rate of 65 m^3/s is 2.9 years. Return periods and discharge histogram of the Ewaso Ng'Iro River are shown in Fig. 3.40.

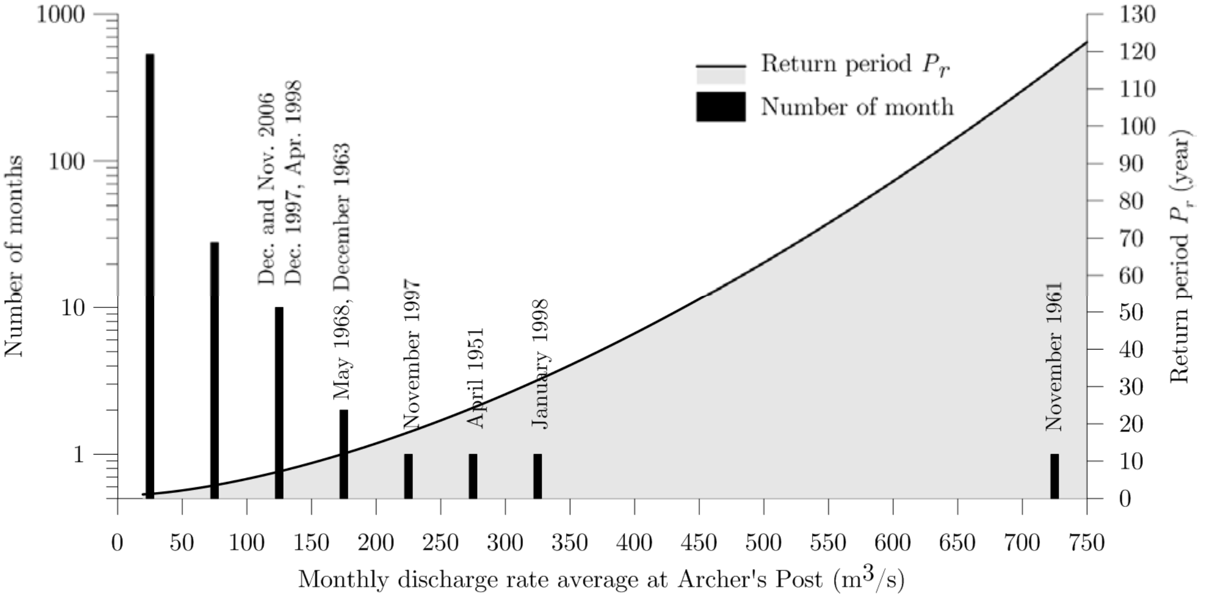

Fig. 3.40: Histogram of average monthly discharge rate and return period calculated with the General Event Value Distribution (GEV) over the period 1949-2010. The 2006 flood event investigated in this study belongs to the fifteen biggest flood events since 1949. However, it is about 6 times smaller than the 1961 event.

3.4.3 Analytical 1D vertical approach for quantifying concentrated recharge

The present section describes an analytical approach for estimating locally the groundwater recharge from inundation duration. Since the gauging station at Archer's Post stopped to record the discharge rate of the Ewaso Ng'Iro River since 2011, this analytical approach could be used to estimate the recharge during an event using inundation surfaces derived from the MODIS satellite images (3.2).

3.4.3.1 Analytical development

The approach is based on the Richard's equation and on the assumption that, over a period T, infiltration takes place periodically during a duration τ, and that the soil surface is fully saturated during, and completely dry between two inundation events (Fig. 3.41).

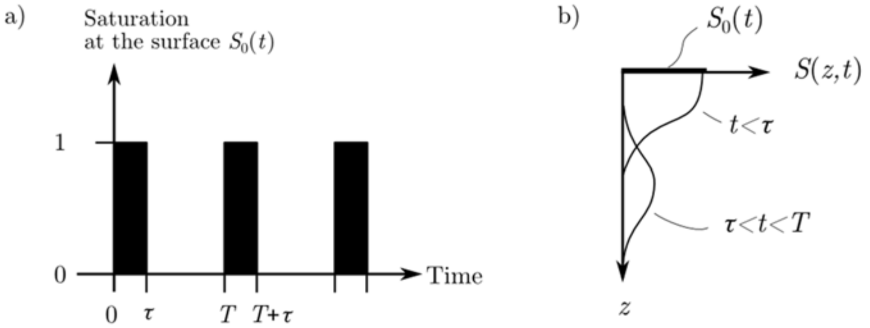

Fig. 3.41: a) Cyclical inundation events of duration τ and period T. b) The saturation front migrates down from the saturated surface ($t < \tau$). Once the surface is dry ($t < \tau < T$), part of the water is evaporated and the rest continues to flow down. The process is repeated during subsequent periods.

Consider the Richard's equation

$$\theta \frac{dS}{dt} = \frac{d}{dz}\left(K(\psi)\left(\frac{d\psi}{dz} - 1\right)\right) \qquad (3.13)$$

where θ is the porosity, ψ the suction (< 0) and S the saturation, along with the simplified exponential model,

$$K(\psi) = K_0 e^{\alpha\psi} \qquad (3.14)$$

where K_0 is the saturated hydraulic conductivity and α is a soil-texture parameter.

Assuming also that the unsaturated hydraulic conductivity linearly scales with saturation $K = K_0 S$ (Fig. 3.42.), one gets the saturation-suction relation (Fig 3)

$$S = e^{\alpha\psi} \quad , \quad \psi = \frac{1}{\alpha}\ln S \qquad (3.15)$$

yielding

$$\frac{d\psi}{dz} = \frac{d\psi}{dS}\frac{dS}{dz} = \frac{1}{\alpha S}\frac{dS}{dz} \qquad (3.16)$$

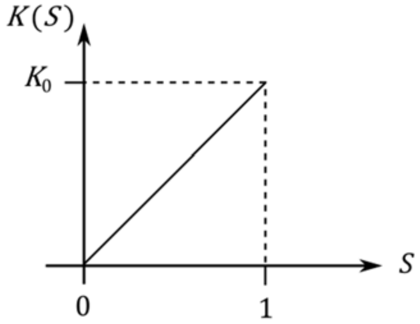

Fig. 3.42 : Linear model for the relation between the saturation S and the hydraulic conductivity $K(S)$.

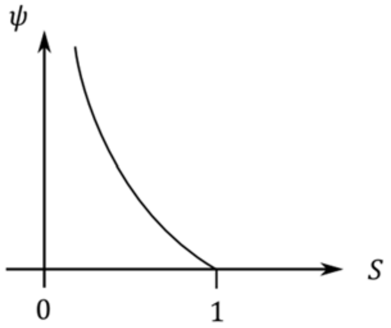

Fig. 3.43: Exponential model for the relation between the saturation S and the suction ψ.

Combining Eq 3.14 to 3.16 and substituting in Eq 3.13 results in the linearized form of Richard's equation

$$\theta\frac{dS}{dt} = -\frac{dQ}{dz} \qquad Q = K_0 S - \frac{K_0}{\alpha}\frac{dS}{dz} \tag{3.17}$$

where Q is the flux of water at depth z and time t, with an advective and a diffuse (capillary) component.

In a periodic regime, considering that the saturation profile is identical at the beginning and at the end of each period $(S(z,0) = S(z,T) = S(z,2T) = \cdots)$, the integration of both side of Eq 3.17 yields

$$\int_0^T \theta\frac{dS}{dt}dt = \theta\big(S(z,T) - S(z,0)\big) = 0 \tag{3.18}$$

and

$$-\frac{d}{dz}\int_0^T Q(z,t)\,dt = -\frac{d}{dz}V(z) \tag{3.19}$$

where $V(z)$ is the net volume of water percolating through a square meter of soil at a depth z during the period T. As indicated by Eq 3.18 and 3.19, the first derivative of this volume is zero, and, therefore, the net infiltration along the profile is a constant which can be calculated by

$$V = \int_0^T Q(z,t)\,dt = \int_0^T \left(K_0 S - \frac{K_0}{\alpha}\frac{dS}{dz}\right)dt \tag{3.20}$$

at any depth, including $z = 0$.

For a periodic inundation event of duration τ, as one of those illustrated in Fig. 3.41, the saturation of the soil surface is described by $S_0(t) = 1 - H(t-\tau)$, where $H(u)$ is the Heaviside step function ($H(u) = 0$ for $u < 0$, $H(u) = 1$ for $u > 0$). With this surface boundary condition and using the method of superposition, the solution of the linearized Eq 3.17 is

$$S(z,t) = F(z,t) - H(t-\tau)F(z,t-\tau) \qquad (3.21)$$

$$\frac{dS}{dz} = F'(z,t) - H(t-\tau)F'(z,t-\tau) \qquad (3.22)$$

where F is the response solution to a constant surface saturation ($S = 1$ at $z = 0$).

As Eq 3.20 applies at any depth, an easy way to evaluate the volume V is to set $z = 0$ in Eq 3.21 and 3.22. After substitution, Eq 3.20 results in

$$V = \int_0^T K_0 S_0(t)dt - \frac{K_0}{\alpha}\int_0^T F'(0,t)dt + \frac{K_0}{\alpha}\int_\tau^T F'(0,t-\tau)\,dt \qquad (3.23)$$

which becomes

$$V = K_0\tau - \frac{K_0}{\alpha}\int_{T-\tau}^T F'(0,t)dt \qquad (3.24)$$

Moreover, it is seen in Eq 3.24 that the remaining integral covers the end of the drought period and a relatively short time-interval during which the saturation gradient at the soil surface ($F'(0,t)$) is obviously negligible. Therefore the net volume of water infiltrated at depth as the result of periodic inundation events of duration τ is evaluated by

$$V = K_0\tau \qquad (3.25)$$

This relation indicates that the recharge volume R during an event, over an inundated area A, can be approximated by the saturated hydraulic conductivity K_0, the inundation duration τ and the inundated surface by

$$R = K_0\tau\, A = \int_0^\tau K_0 A(t)dt \qquad (3.26)$$

3.4.3.2 Application to the inundation surface of the Lorian Swamp

The relation obtained in Eq 3.26 can be used to estimate the recharge during an event, based on the inundated surface derived from satellite images, without carrying out complex numerical modelling and without knowing the river discharge. This relation is in particular useful since the gauging station stopped to record the river discharge since 2010 after damages caused by flood.

For the case of a real inundation, because the inundated surface is not constant, it should be expressed as a function of time $A(t)$.

Thus, the average saturated hydraulic conductivity of the soil K_0 is estimated by dividing the total groundwater recharge volume during an event R (m^3), which was obtained with the numerical modelling (Table 3.4), by the cumulated inundated surfaces A_{tot} (m^2 d) at each time step:

$$K_0 = \frac{R}{A_{tot}} \quad , \text{ with } \quad A_{tot} = \int_{t_{start}=0}^{t_{end}=\tau} A(t)\,dt \qquad (3.27)$$

Applied to the events A to F (Fig. 3.14), Eq 3.27 yields the results presented in Table 3.8. The estimated saturated hydraulic conductivity K_0 ranges between 0.02 to 0.08 m/d. These results are vrey close to the ground conductance C_g value obtained for each event (section 3.4.1.3), indicating that the recharge rate could be well approximated with the ground conductance. These results can be used for estimating the recharge by applying an average hydraulic conductivity K_0 of 0.05 m/d over the inundated surface during the inundation period.

Event	A_{tot} (m^2 d)	Recharge volume R by event(m^3)	Estimated hydraulic conductivity K_0 (m/d)	Best C_g (m/d)
A	9.42×10^9	2.21×10^8	0.02	0.03
B	1.17×10^{10}	4.10×10^8	0.04	0.04
C	1.31×10^9	1.02×10^8	0.08	0.1
D	2.52×10^9	9.43×10^7	0.04	0.04
E	3.15×10^{10}	6.88×10^8	0.02	0.01
F	4.21×10^9	2.13×10^8	0.05	0.06

Table 3.8: Cumulated inundated surface A_{tot}, recharge volume R and average saturated hydraulic conductivity K_0 by event. The average saturated hydraulic conductivity K_0 is close to the value of the ground conductance C_g value.

3.4.4 Conclusions of the concentrated recharge analysis

With the presented methodology based on numerical modelling, inundated surfaces derived from satellite images and statistical analysis, a range of average annual concentrated recharge between 195 and 329 x 10^6 m^3/y was found. The analysis of river discharge and recharge distribution derived from this approach does not only reveal the annual average recharge but also which flood events contribute the most to the recharge and at which return period. It indicates that recharge is equally dominated by river discharge rates below and above 117 m^3/s for the lower recharge model, which is based on the regression curve between the discharge and the recharge volumes by event, and below and above 65 m^3/s for the higher recharge model (with a corrected regression constant a).

However, as discussed in section 3.4.1.9, this method for quantifying the groundwater recharge contains various uncertainty sources that could lead to 30 to 50% of over or underestimation of the recharge volume during an event (Table 3.7). Major uncertainty sources come from the estimation of the subsurface evapotranspiration and from the distance between the Archer's Post gauging station and the injection point within the *HGS* model imposed by the poor DEM quality and the rough mesh resolution of the model. The uncertainty on the subsurface evapotranspiration has an impact on all flood event magnitudes because it is applied to the maximum inundated surface, while the overestimation of the discharge due to the injection point location affects mainly the low discharge rate. Additionally, the thresholds selected for converting inundated surfaces from satellites images and from the *HGS* model could also lead to slight over or underestimation of the groundwater recharge.

The development of two statistical recharge distributions allows to include the uncertainty of groundwater recharge by event into the average annual recharge rate uncertainty. Compared to the simulated recharge volumes, the lower statistical recharge distribution (Fig. 3.36) underestimates between 30% (for high events) and 80% (for low events) the recharge volume by event. Thus, the overestimation of river discharge rates by neglecting the losses between Archer's Post and the injection (between 3 and 15%) is largely included within this low recharge estimation. On the opposite, for the high recharge distribution (Fig. 3.39), modifying the river discharge threshold leading to recharge (i.e. the constant *a* of the regression curve) allows to better fit intermediate and higher flood episodes (events 'A' to 'F') but could lead to an overestimation of the impact of very low events which were not simulated. Thus, the values of 195 and 329 x 10^6 m^3/y should be considered as the lower and upper limit of the annual average concentrated recharge occurring over the Lorian Swamp.

Related to the Lorian Swamp surface (the recurrently inundated area, 2'700 km^2), an intermediate annual average recharge of 260 x 10^6 m^3/y represents a vertical recharge flux of 331 mm/y. On the other hand, if the recharge volume is normalised by the freshwater lens surface (12'500 km^2), the vertical flux corresponds to 21 mm/y. Normalised to the surface of the freshwater lens between the Lorian Swamp and Liboi, vertical recharge flux ranges between 16 and 26 mm/y, that is about 5 to 15 times higher than the diffuse recharge.

The statistical analysis of the Ewaso Ng'Iro River discharge rates also allowed to characterise the long-term temporal dynamics of the recharge of the Merti aquifer. It was thus observed that major flood events with return periods greater than 6.7 years (or 2.9 if the second statistical distribution is chosen) contribute to half of the groundwater recharge.

Finally, the simple analytical approach developed for estimating the recharge based on the hydraulic conductivity of the soil and the inundation duration (section 3.4.3) allows to quickly quantify the recharge of next inundation events with an accuracy similar to that resulting from complex simulations. This can be particularly useful since the gauging station at Archer's Post is out of order since 2011.

3.5 Conclusion of the recharge quantification

Previous estimations of the Merti aquifer recharge ranges between 6.8 and 32.2 x 10^6 m^3/y (Earth Water Ltd, 2012). Recharge quantification established during this study indicates considerably higher values. Diffuse recharge was estimated between 12 and 62 x 10^6 m^3/y over the freshwater lens between the Lorian Swamp and Liboi (12'500 km^2) and the concentrated recharge was estimated between 195 and 329 x 10^6 m^3/y. Based on these two estimations, the total recharge ranges between 207 and 391 x 10^6 m^3/y.

The calculation of the diffuse recharge is only considered over the surface of the freshwater lens since only this surface contributes to the freshwater recharge. Indeed, the diffuse recharge occurring over the rest of the domain could be considered as freshwater recharge since it is diluted with the brackish or saline groundwater surrounding the freshwater lens. This diffuse recharge over the rest of the domain represents volumes ranging between 125 and 623 x 10^6 m^3/y. Previous and new estimations of the recharge rates are shown in Fig. 3.44.

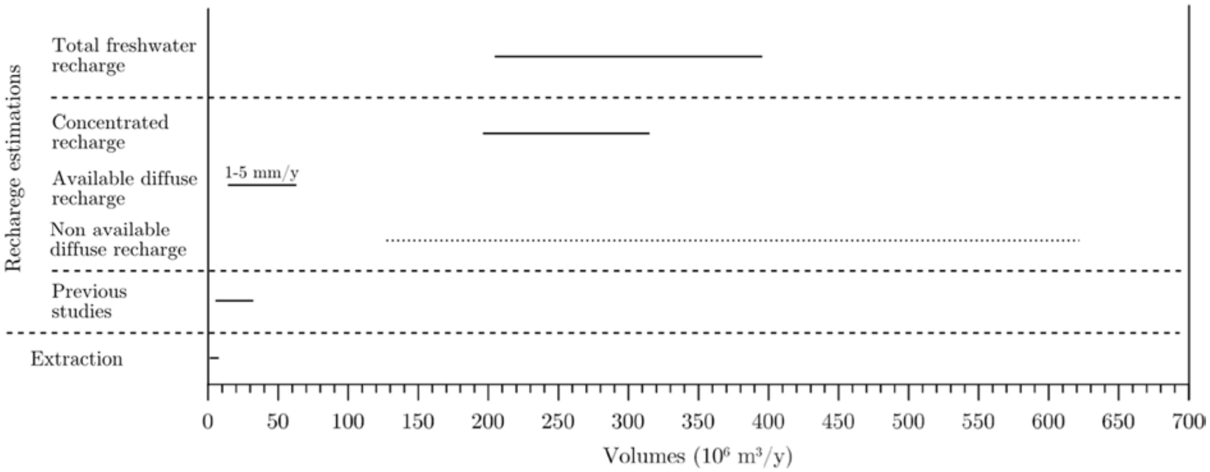

Fig. 3.44: Estimations of recharge from previous studies and from the approach developed in this study. The total freshwater recharge ranges between 207 and 391 x 10^6 m^3/y, which includes the concentrated recharge (195 to 329 x 10^6 m^3/y) and the diffuse freshwater recharge over the freshwater lens surface (i.e. the available diffuse recharge, 12 to 62 x 10^6 m^3/y, or 1 to 5 mm/y in vertical flux). The "non-available diffuse recharge" includes the diffuse recharge over the rest of the domain and which doesn't contribute to the freshwater recharge (125 to 623 x 10^6 m^3/y).

In vertical fluxes, diffuse recharge is estimated between 1 and 5 mm/y and concentrated recharge between 16 and 26 mm/y if the annual volume is normalised by the freshwater lens surface between the Lorian Swamp and Liboi.

Uncertainty about the diffuse recharge remains significant. However, without carrying out extensive field campaigns, including ground methods such as chloride mass balance, it remains challenging to assess this value more precisely from surface observations. Sensitivity between these two end members is tested by means of groundwater models in the next chapters.

This higher recharge rate is consistent with the multilayer aquifer system proposed in the previous chapter (Chapter 2). Further investigations will be carried out in the two next chapters that focus on the dynamics of the freshwater lens and the elaboration of a regional groundwater numerical model. Furthermore, compared to the extraction rates, this recharge estimation is about 2 orders of magnitude higher, indicating that, on a large scale, the recharge is more than sufficient for ensuring a sustainable exploitation of the aquifer. However, the local availability of this recharge is not known yet and should be further investigated, as well as the influence of the salinity, especially close to the limit between the fresh and brackish/saline groundwater. This concern is also the focus of the next chapter dedicated to the freshwater lens dynamics.

Chapter 4

Dynamics of continental freshwater lenses

4.1 Introduction

The second major research topic of this thesis focuses on the investigation of the dynamics of continental freshwater lenses. This analysis aims to better understand the characteristics of aquifers such as the Merti aquifer and to integrate and cross-validate the results of the recharge quantification obtained in the previous chapter.

A series of synthetic model scenarios are used to investigate the effect of hydraulic parameters (transmissivity and transmissivity heterogeneity) and groundwater recharge hypotheses (recharge rates and recharge mechanisms). These simulations are carried out by means of 2D horizontal numerical models. The sensitivity of these parameters is evaluated by the analysis of the variation in the freshwater lens surface, its geometry and the similarity with the observed Merti freshwater lens.

First (section 4.2), the synthetic model inspired from the Merti aquifer is presented, as well as the main recharge hypotheses and geometrical indicators used for the analysis. In the section 4.3, the dynamics of a large synthetic continental freshwater lens, inspired from the Merti aquifer, is investigated with steady state simulations in order to identify the control of each variable on the lens geometry by varying recharge conditions. The identification of probable recharge mechanisms and transmissivities characterising the Merti aquifer is then obtained from the similarity analysis between the synthetic lens and the real one (section 4.4). Finally, the impact of pumping on a large scale is investigated in section 4.5. A transient analysis aiming to assess the creation of a freshwater lens from a complete saline aquifer was also carried out. However, since the duration of the installation of such a freshwater lens is difficult to interpret, this analysis is presented in Appendix G.

4.2 Methodology: the Merti inspired synthetic model, varying parameters and indicators

In order to undertake a systematic investigation of freshwater lens dynamics, a series of synthetic models is elaborated. These models are inspired from the geometry of the Merti aquifer and from various recharge mechanisms that will be tested. This section includes the description of the numerical model inspired from the Merti aquifer (dimension, boundary conditions, material properties, and how the salinity is approached for the transport modelling), the various recharge conditions (mechanisms and intensities) that will be tested, and the description of the indicators that will be used to assess the dynamics of the lenses under the various conditions.

4.2.1 The Merti inspired synthetic model

The Merti aquifer is located between the Mount-Kenya and the Indian Ocean, in eastern Kenya. It extends over a length of 250 km and is up to 100 km wide (Fig. 1.1). It develops within a large sedimentary basin composed of alternating permeable coarse and fine sediments horizons. Downstream of Liboi, close to the Somali border, the freshwater lens fingers into the surrounding saline water and becomes brackish, with a very flat gradient. In its upstream part, between Habaswein and Dadaab, the hydraulic gradient is about 0.5 ‰.

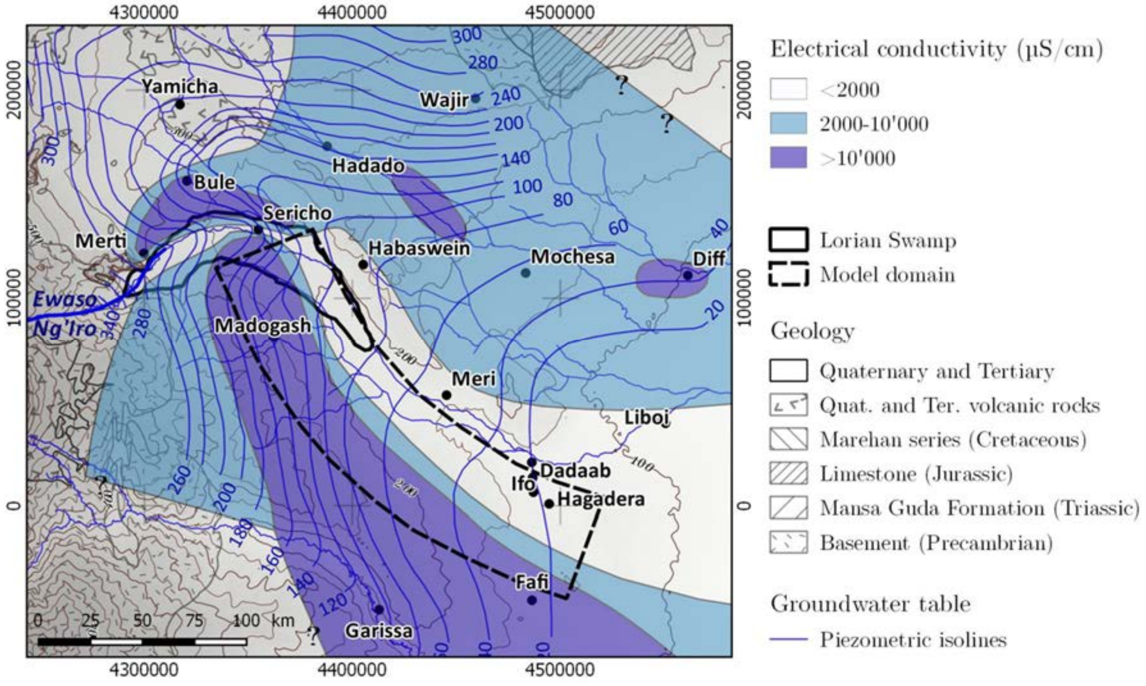

Fig. 1.1: Compiled electrical conductivity map of the Merti aquifer (Sources: GIBB 2004 and own measurements).

Regarding the groundwater salinity, GIBB (2004) suggested that the origin of salinity is trapped seawater from the period when the sea level was higher. This is supported by the Na/Cl ratio that tends towards 0.86 (modern seawater ratio) with increasing electrical conductivities, indicating that saline waters have an oceanic Na/Cl signature and origin. The presence of evaporitic rocks can be excluded over most of the Merti aquifer because of the moderate electrical conductivity values and the information from boreholes logs. Indeed, the presence of evaporitic rocks would locally lead to very high salt concentrations and thus to very high electrical conductivity beyond 45’000 µS/cm, the electrical conductivity of seawater, while the highest observed electrical conductivities range between 20’000 and 33’000 µS/cm (see section 2.3.5.) The geometry of the freshwater lens is the result of freshwater recharge that washed saline water.

To reflect the characteristics of this conceptual model, and based on the symmetry of the lens, a simplified 2D horizontal half domain (Fig. 1.2) of 200 km length and 50 km width is created. The 2D simplification is justified by the vast lateral dimension of the lens with respect to its thickness and by the fact that field observations have so far never clearly found underlying saline groundwater. The transmissivity is defined as 0.25 m^2/s. Based on pumping tests results from previous studies, the model developed is considered as confined (GIBB Ltd, 2004; Milnes, 2010; Swarzenski and Mundorff, 1977; Wanyeki, 1979).

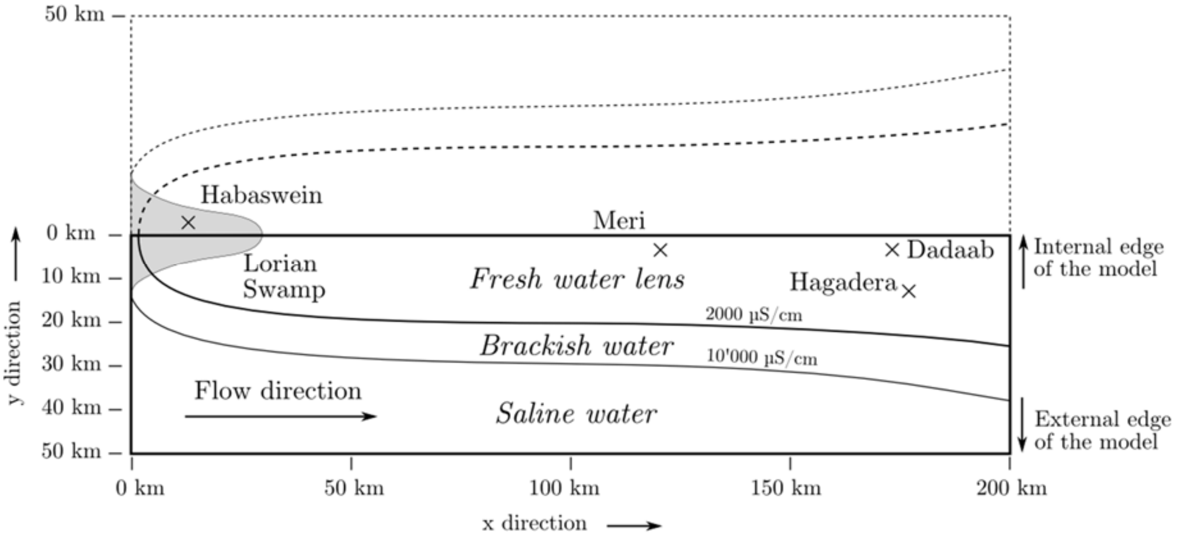

Fig. 1.2: 2D horizontal schematic illustration of the simplified half Merti freshwater lens (bold frame) whose situation is indicated in Fig. 1.1. The lens geometry is based on electrical conductivity data between the Lorian Swamp and Dadaab. The limit between fresh and brackish water is set at 2'000 μS/cm, and the limit between brackish and saline water is set at 10'000 μS/cm. The observed lens geometry was rectified into a half and symmetric model with a straight geometry.

The model is developed with the *Feflow* software, using a finite element approach (Diersch, 2014).

Mesh description

The mesh contains 40'000 quadrangular elements distributed into 400 columns and 100 lines. In the x direction, elements have a constant length of 500 m. In the y direction, in order to have a better mesh resolution within the freshwater lens and close to the main recharge mechanisms (presented below), the elements have an increasing resolution towards the internal side of the model, from 100 m to 900 m.

Recharge mechanisms and flow boundary conditions

The analysis on recharge carried out in Chapter 3 allowed to identify the two main mechanisms controlling the recharge of the Merti aquifer: concentrated recharge over the Lorian Swamp area and diffuse recharge over the rest of the domain. This section aims to test the effect of these two recharge mechanisms, as well as concentrated recharge along ephemeral rivers, on the freshwater lens geometry with a series of synthetic models combining these recharge mechanisms.

Fig. 1.3 illustrates the various tested recharge mechanisms and their implementation within the numerical models: 1) recharge by ponding, to mimic the infiltration over the Lorian Swamp (concentrated recharge); 2) recharge along ephemeral rivers (wadis) along the entire domain ; 3) or only along half the length (half river); 4) recharge by rainfall over the entire surface (diffuse recharge).

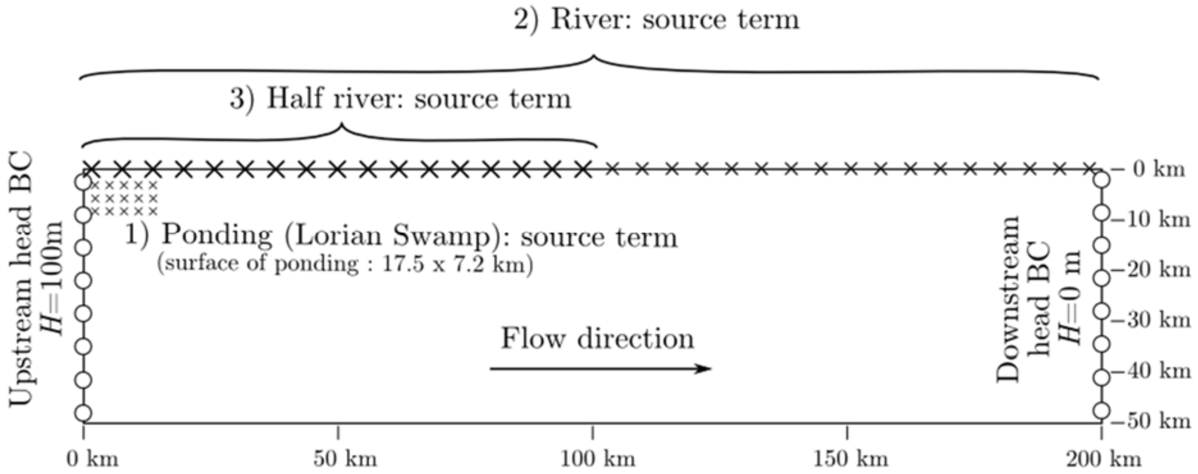

Fig. 1.3: 2D horizontal schema illustrating the recharge mechanisms and flow boundary conditions. Concentrated recharge is simulated with a fluid source term, represented with cross-symbols. The upstream model limit is defined by a head BC (H=100m) while the downstream limit is defined by a head BC of H=0m.

In the numerical model, ponding (1 in Fig. 1.3) and river recharge (2 and 3 in Fig. 1.3) are simulated with a fluid source term, represented with cross-symbols. Areal infiltration from rainfall is simulated with a fluid source term over the entire domain. The regional gradient of 0.5 ‰ is imposed with an up and downstream head-boundary condition of H=100 m and H=0 m respectively. In order to avoid outflow of water through the upper domain boundary (H=100 m) in the case of high concentrated recharge rate by ponding, a minimum flow-rate constraint of 0 m^3/s was associated to the upstream head boundary condition. Thus, the upper head boundary condition is deactivated when the head downstream the upper boundary condition is higher than 100 m.

Transport boundary conditions

For the solute transport simulations, salinity is converted into normalised concentrations between 0 and 1. The highest concentration (salty water) is defined as C=1, corresponding to values above 20'000 µS/cm in the Merti aquifer, while C=0 is used for the freshwater recharge limits. The limit defining the fresh-brackish water transition is set to 0.1, corresponding to an electrical conductivity of 2'000 µS/cm (Fig. 1.4). For the purpose of comparison with real salinities, the brackish-saline limit is defined as 0.5 (10'000 µS/cm).

The water flowing in the domain from the upstream boundary conditions (H=100 m in Fig. 1.3) is defined as saline with a mass-concentration boundary conditions of C=1. Freshwater recharge from the source term has a concentration of 0. Longitudinal dispersivity is set to 500 m (the resolution of the mesh in the flow direction) and the transverse dispersivity to 50 m. A refined mesh and a dispersivity two times lower was tested for the reference model and didn't show significant differences in the total dissolved mass (the difference of total dissolved mass was 1%) and in the local concentration over the transition zone between the fresh and brackish water surfaces. The molecular diffusion is set for all models to 1 x 10^{-9} m^2/s.

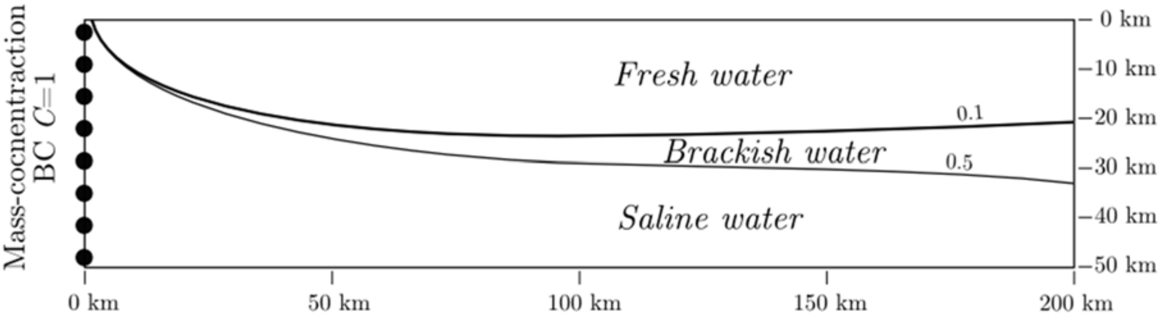

Fig. 1.4: Salinity and transport boundary conditions. Salinity is normalised with values varying from 0 to 1. Concentration between 0 and 0.1 corresponds to fresh water (0-2'000 µS/cm), concentration between 0.1 and 0.5 is brackish water (2'000-10'000 µS/cm) and saline water range between 0.5 and 1 (EC>10'000 µS/cm). Transport conditions are imposed with mass-concentration BC of C=1 at the upstream limit of the domain. Freshwater recharge imposed with the source term has a concentration of 0.

4.2.2 Recharge mechanisms and recharge ratios

Seven recharge intensities between 38 and 300 x 10^6 m^3/y are tested on the model with a transmissivity of 0.25 m^2/s in order to reproduce various freshwater lens sizes ranging between an almost complete saline to an almost complete "freshwater" aquifer. These values refer to both concentrated and diffuse recharge and apply to half the aquifer. They should be therefore be doubled in order to be compared with the actual aquifer.

Total freshwater recharge intensity R (10^6 m^3/y)	Total freshwater recharge intensity R (m^3/s)	Normalised recharge into the recharge ratio $R_r = R/T$ (m)
38	1.2	4.8
75	2.4	9.5
113	3.6	14.3
150	4.8	19.0
188	5.9	23.8
225	7.1	28.5
263	8.3	33.3
300	9.5	38.1

Table 1.1: The eight recharge intensities tested and associated recharge ratio R_r with a transmissivity T of 0.25 m^2/s. The total freshwater recharge refers to the cumulated concentrated and diffuse recharge on the half model.

The results from the recharge quantification and the uncertainty on the transmissivity of the aquifer require to adopt an approach based on the measured transmissivities and on the recharge. Thus, recharge scenarios and their impact on the lens geometry will be discussed based on the recharge ratio R_r (m) defined as the total freshwater recharge intensity R (m^3/s) normalised by the transmissivity T (m^2/s) (Table 1.1). Based on this ratio, results obtained with the seven initial recharge intensities can be further interpreted for other couples of recharge intensities and transmissivities, as for instance for a model with lower transmissivity as obtained from pumping tests, by multiplying them by the same factor. This extrapolation is only valid for steady state simulation without pumping.

The effect of recharge mechanisms on lens geometry is tested by four "uncombined" recharge mechanisms models that are: river, half river, ponding and rainfall, as illustrated in Fig. 1.3. Then, these distinct recharge mechanisms are combined together (Table 1.2). For the combined models, each mechanism contributes to recharge with an equivalent amount of fresh water.

Recharge mechanisms scenarios and their relative contribution to fresh water (in %)			
Uncombined mechanisms		Combined mechanisms	
A	River (100%)	*E*	River and ponding (50% / 50%)
B	Half river (100%)	*F*	Half river and ponding (50% / 50%)
C	Ponding (100%)	*G*	Ponding and rainfall (50% / 50%)
D	Rainfall (100%)	*H*	Half river, ponding and rainfall (33% / 33% / 33%)
		I	River, ponding and rainfall (33% / 33% / 33%)

Table 1.2: The four uncombined and five combined recharge tested conditions and the relative contribution of each mechanisms to the total recharge intensity.

As illustrated in Fig. 1.5, the combination of recharge intensities and recharge mechanisms lead to various geometries. Besides the fact that the freshwater lens size is directly related to the recharge rate, it should be noticed that the recharge mechanism has a significant impact on the lens geometry: recharge along a continuous river along the central axis of the lens (model *A*) creates a continuous increase of the lens width, while concentrated recharge on ponding area (model *C*) produces a lens geometry with a high freshwater width progression in the very upstream of the lens, but then the lens width slightly diminishes. The half-river model *B* produces intermediate lens geometries between the *A* and *C* model geometries.

These simulations also reveal that the variation of recharge has a much greater impact on the lens geometry for concentrated recharge in the upper part of the domain (ponding model *C*) than for distributed recharge along lateral boundary of the model (river *A* and half-river *B* models). This is explained by the high hydraulic head induced by concentrated recharge that diminishes the gradient in the very upper part of the domain, diminishing, or avoiding the inflow of saline water from the upper model boundary.

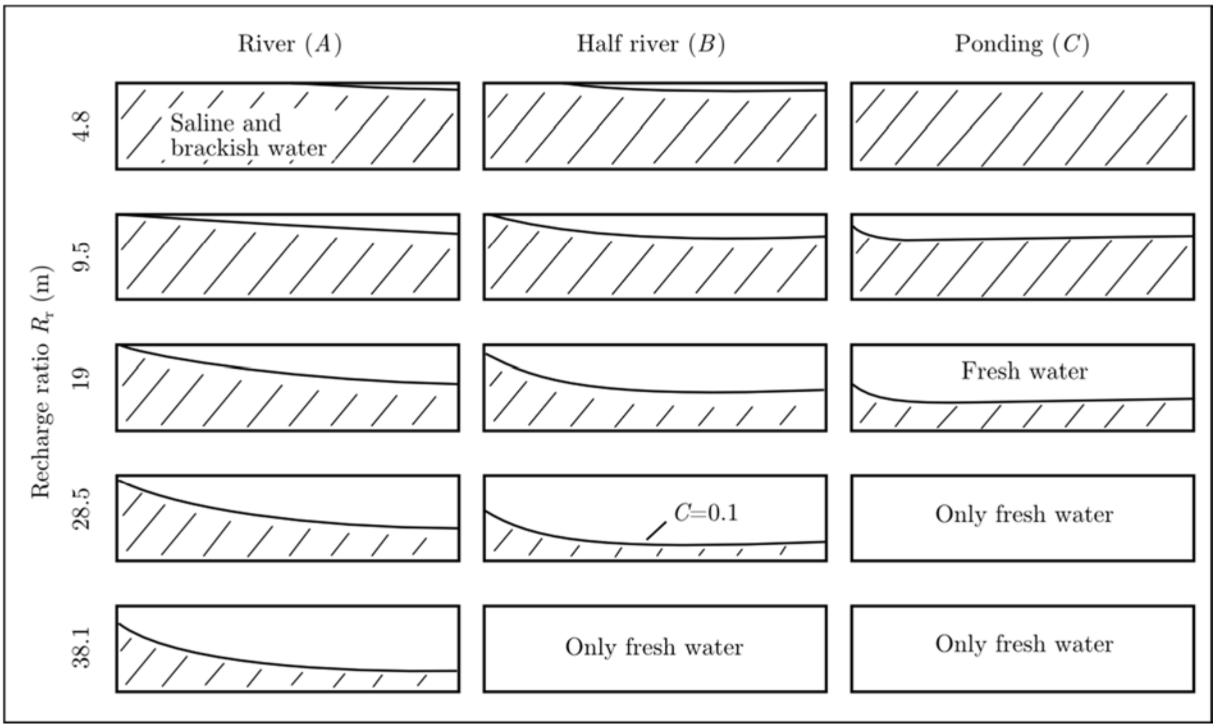

Fig. 1.5: Top-view diagrams of freshwater lens shapes resulting from the main recharge mechanisms and recharge ratios R_r models. Saline and brackish water is represented with the shaded area and derived from the concentration iso-contour C=0.1.

4.2.3 Geometrical ratios

In order to quantify the relations between the geometries and the recharge conditions identified above, indicators were developed. These indicators are based on geometrical measures: the freshwater lens surface A_F and the freshwater lens width L_i at three positions of the lens (at one-tenth x_{10}, one-half x_{50} and at the end of the lens x_{100}), as illustrated in Fig. 1.6.

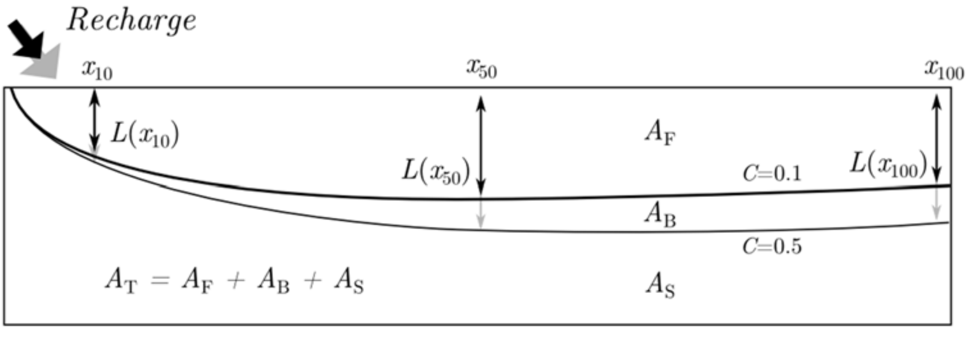

Fig. 1.6: Geometrical measures used to calculate indicators of the freshwater lens dynamics: freshwater surface A_F; with freshwater lens widths at one-tenth $L(x_{10})$, one-half $L(x_{50})$ and at the end of the lens $L(x_{100})$. A_T is the total surface of the domain.

The *Freshwater Surface Ratio* F_{SR} is a normalised surface obtained by dividing the freshwater surface by the total surface of the domain A_T (Eq 1.1).

$$F_{SR} = \frac{A_F}{A_T} \qquad (1.1)$$

The width indexes describe the development of the lens width along the flow direction. They are computed by normalising the difference between the lens width at an upstream and downstream position.

Two width indexes are used: one between the beginning (x_{10}) and the half (x_{50}) of the lens $WI\ (x_{50-10})$ (Eq 1.2) and the other one between the half (x_{50}) and the end (x_{100}) of the lens $WI\ (x_{100-50})$ (Eq 1.3).

$$WI\ (x_{50-10}) = \frac{L(x_{50}) - L(x_{10})}{L(x_{50}) + L(x_{10})} \qquad (1.2)$$

$$WI\ (x_{100-50}) = \frac{L(x_{100}) - L(x_{50})}{L(x_{100}) + L(x_{50})} \qquad (1.3)$$

For both indexes, a zero value indicates that the lens width remains constant and is parallel to the flow direction. Positive values indicate an increase of the shape (curve *a* and *c* in Fig. 1.7) and negative values indicate that the lens width reduces (curve *b* between x_{50} and x_{100} in Fig. 1.7).

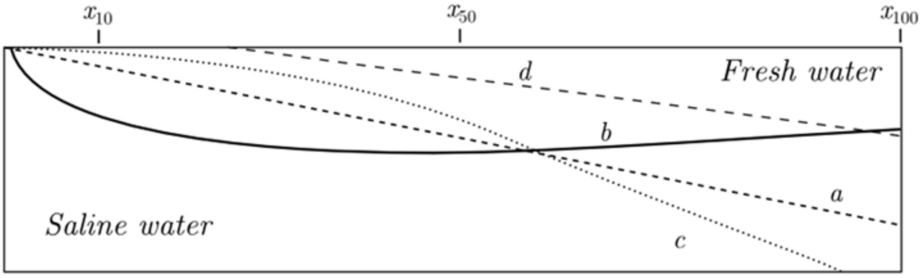

Fig. 1.7: Freshwater lenses with similar surface ratios but different geometries and width indexes. The lens *a* has a linear progression with a $WI\ (x_{50-10})$ of 0.67. Lens *b* has a $WI\ (x_{50-10})$ smaller than 0.67, while the lens *c* is close to 1. The curve *d* shows a lens starting after the x_{10} distance.

For the $WI\ (x_{50-10})$, that characterises the progression between the beginning of the lens and the half of the lens, a width index of 0.67 indicates a linear progression (curve *a* in Fig. 1.7, $L(x_{50})$ is equal to 5 times $L(x_{10})$, then $WI\ (x_{50-10})$ is equal to 4/6). Values below 0.67 (curve *b*) indicates a greater progression of the lens width before x_{10} than between x_{50} and x_{100}, while values between 0.67 and 1 indicate a slower progression before x_{10} (curve *c*). Ratio of 1 indicates that the lens starts after the x_{10} distance (curve *d*, $L(x_{10}) = 0$). For the downstream half of the model, a linear progression of the lens is characterised by a $WI\ (x_{100-50})$ of 0.33.

These three indicators offer the advantage of describing the geometry of a freshwater lens without knowing the flux and the recharge rates.

4.3 Characterisation of freshwater lens dynamics

Based on the model and using the indicators presented previously, this section focuses on the characterisation of a synthetic freshwater lens, through a sensitivity analysis described below.

The geometry of a freshwater lens similar to the Merti aquifer is characterised under steady state conditions by varying the recharge mechanisms and intensities. This analysis allows to identify the control of the recharge mechanisms and the intensities on the freshwater size and shape. Additionally, the effect of lateral heterogeneous transmissivity on the lens geometry is assessed.

This steady state approach includes the following four points that are investigated in this section:

a) the effect of recharge intensity on the freshwater lens size. This investigation is carried out by the analysis of the freshwater ratio, in function of the recharge ratio;

b) the impact of the recharge intensities and recharge mechanisms on the lens size and geometry, that is done by the analysis of the freshwater ratio versus width indices plotted for various recharge rate;

c) the effect of rainfall proportion (related to the total freshwater recharge) on the freshwater and brackish surface ratio;

d) the effect of lateral transmissivity heterogeneity on the lens size;

4.3.1 Effect of recharge on freshwater lens surface

The impact of the recharge on the lens surface is assessed with the freshwater surface ratio F_{SR} (Eq 1.1) for the eight recharge ratios R_r and for the nine recharge mechanisms listed in Table 1.1 and Table 1.2 respectively. Fig. 1.8 shows a compilation of all simulation results.

The main observation is that a R_r variation lower than one order of magnitude (between 4.8 and 38.1 m) induces considerable variations of the freshwater lens extension, with minimum freshwater surface extension ranging between 0 and 5% and maximum surface between 60 and 100% of the total domain surface, except for the rainfall mechanism that will be discussed further below.

The simulations also show that the evolution of the freshwater surface with increasing R_r is not identical for the different recharge mechanisms. A general observation is that mechanisms with a more concentrated recharge over the upper part of the domain lead to higher freshwater surface ratios and also higher progression of this surface when increasing the recharge.

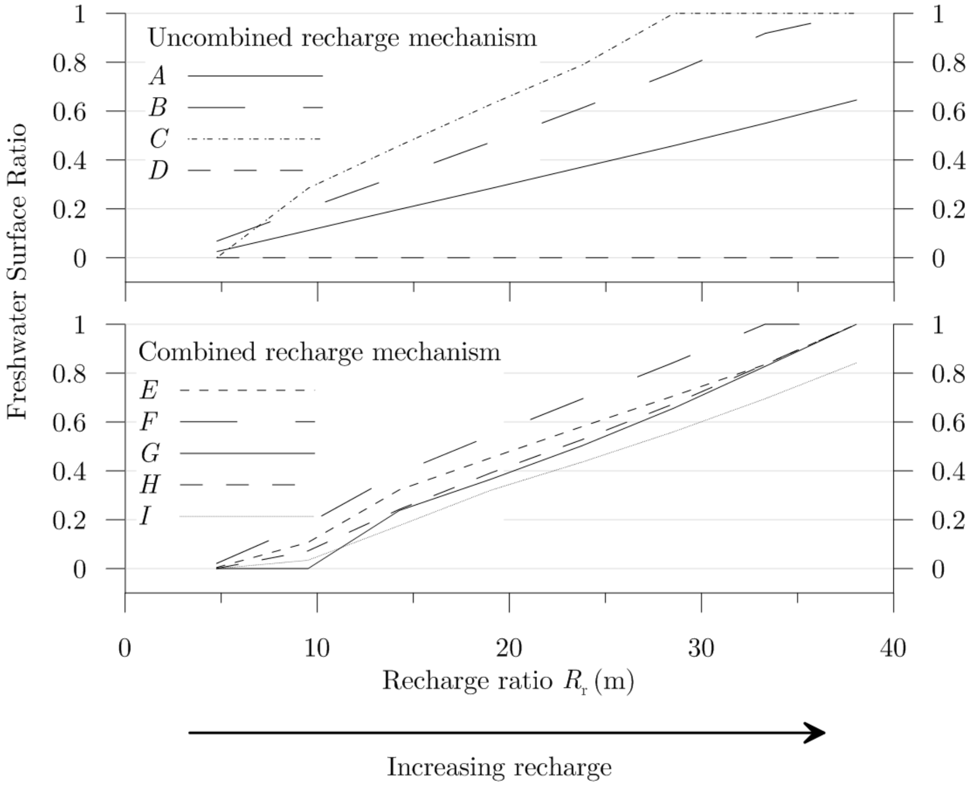

Fig. 1.8 : Freshwater surface ratio vs recharge ratio R_r for different recharge scenarios (see Table 1.2). Four uncombined recharge mechanisms (upper graph, *A*: River, *B*: Half-river, *C*: Ponding, *D*: Rainfall) and four combined mechanisms (lower graph, E: River and ponding, *F*: Half-river and ponding, *G*: Ponding and rainfall, *H*: Half-river, ponding and rainfall, *I:* River, ponding and rainfall) are tested with eight R_r (1.8, 9.5, 14.3, 19, 23.8, 28.5, 33.3 and 38.1 m)

As an example, the ponding model (curve *C*), has the biggest freshwater surface increase and allows to fill the entire aquifer with freshwater for the maximum R_r, while the whole river model (curve *A*) begins with a close freshwater surface as the half-river model but then, its freshwater surface follows a smaller increase. The half-river recharge model (curve *B* in Fig. 1.8), has a dynamics intermediate between the *C* and *A* model.

These differences have two reasons. Firstly, concentrating the recharge in the upstream half of the model slightly increases the hydraulic heads within this area and therefore reduces the gradient at the upstream boundary of the model and the inflow of saline water from this same boundary as well. Secondly, the more freshwater recharge is located downstream, the less it can contribute to the development of a freshwater lens.

The freshwater surface resulting for rainfall recharge follows a different dynamics. The freshwater area develops from the downstream area of the aquifer due to increasing dilution with fresh water but does not strictly form a lens.

Combining recharge processes leads to more homogeneous curves. The curve with the highest freshwater surfaces (curve *F* in Fig. 1.8) is the one combining ponding and the half-river mechanisms. When combining these two recharge mechanisms with rainfall (curve *H*), the curve decreases by only a few per cent. Replacing half of the concentrated recharge by diffuse recharge (rainfall), as simulated with the experiment *G*, the freshwater surface diminishes in a small proportion. These observations suggest that even if a significant part of the recharge (up to 30%) occurs by rainfall over the entire surface domain, the lens size does not vary drastically.

4.3.2 Width ratio analysis

The relation between the lens geometry and the recharge mechanisms is investigated with the width index (Eq 1.2 and Eq 1.3) for the same scenarios investigated in the previous section. Results are displayed by plotting the width indexes vs the freshwater water surface ratio (Fig. 1.9). Four main observations can be done:

- The resulting lens geometry varies more for low recharge ratios R_r and is more homogenous for high R_r. For a R_r of 9.5 m (Fig. 1.9a), $WI\ (x_{50-10})$ varies between -0.02 and 1 while it only varies between 0.01 and 0.38 with a R_r of 28.5 m (Fig. 1.9e). This same observation is noticeable for the $WI\ (x_{100-50})$ with values ranging between -0.7 and 0.45 for the low R_r (Fig. 1.9b) and between -0.02 and 0.09 with a R_r of 28.5 m (Fig. 1.9f). This homogenisation of the lens geometry is an effect of the model size that constrains the development of the freshwater lens for high recharge ratios, and therefore its geometry.
- Freshwater lens with concentrated recharge (ponding mechanism *C*) develops in the very beginning of the lens and then remains constant between x_{10} and x_{50} ($WI\ (x_{50-10})$ is close to 0, Fig. 1.9a and c) and slightly decreases in the second half of the domain ($WI\ (x_{100-50})$ is negative, Fig. 1.9b and d). On the opposite, more equally distributed recharge along the domain side (river mechanism *A*) induces a more constant progression of the freshwater lens due to the continuous contribution of fresh water along the internal model edge (the *A* mechanism has the higher width ratio in Fig. 1.9c, d, e and f). Intermediate mechanisms between the river and the ponding mechanisms, such as the half-river *B*, the river/ponding *E* and the half-river/ponding *F* mechanisms show intermediate width ratios (Fig. 1.9a, b, c and d). For the high recharge ratio with the ponding mechanism, the domain is entirely filled with fresh water and width indexes are equal to 0.

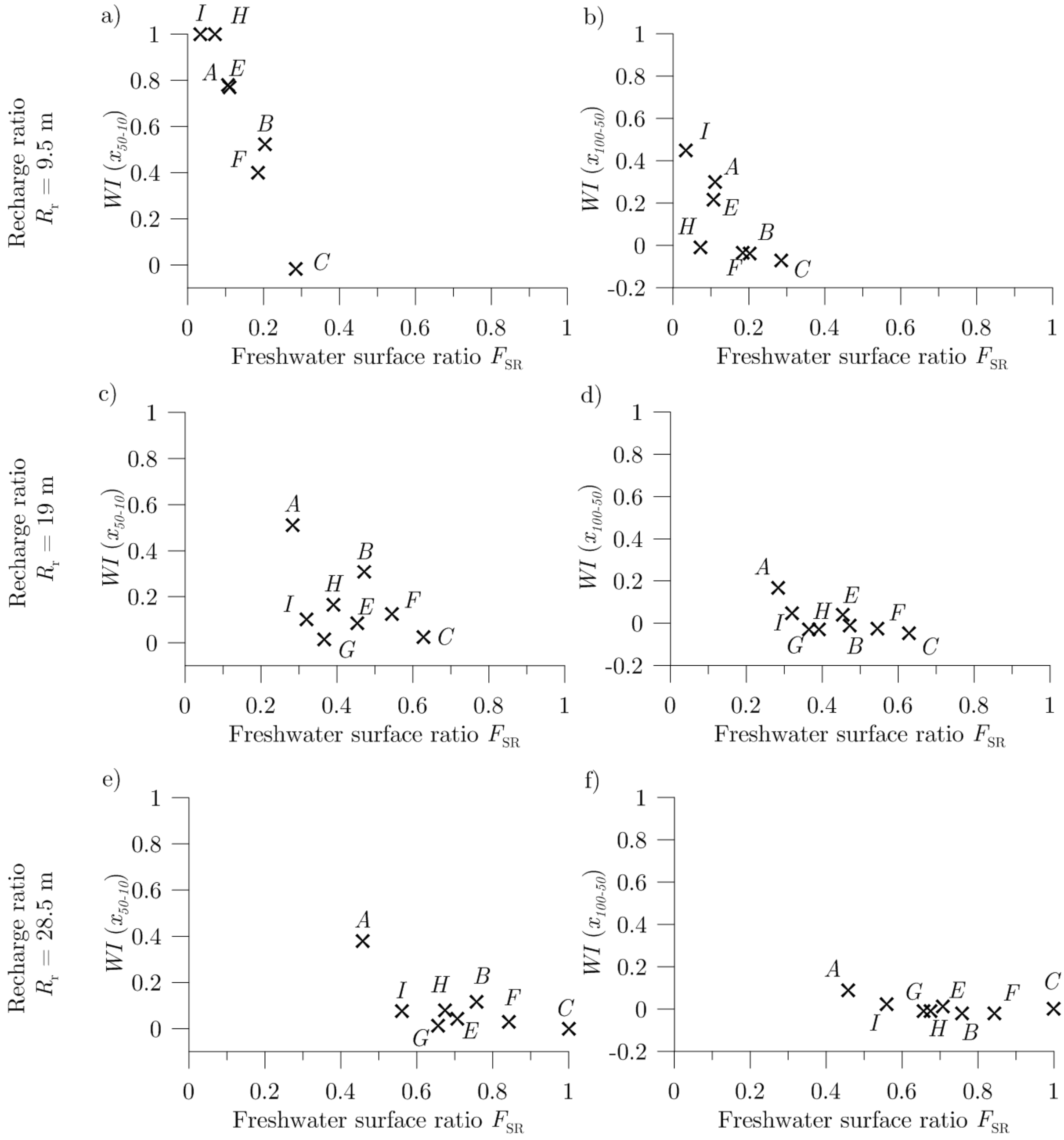

Fig. 1.9 : $\mathrm{WI}\ (x_{50-10})$ (a, c and e) and $\mathrm{WI}\ (x_{100-50})$ (b, d and f) width indexes vs freshwater surface ratio F_{SR} with a R_r of 9.5 x 10^3 m (a and b), 19 m (c and d) and 28.5 x 10^3 m (e and f).

- For low recharge ratios, mechanisms with more equally distributed recharge are not sufficient to create a lens from the beginning of the model (experiment *A* and *E*) and lead to $WI\ (x_{50-10})$ higher than 0.67 or equal to 1 if the lens starts after the x_{10} distance (experiment *H* and *I*, Fig. 1.9a, b), as illustrated in Fig. 1.7 with the curve *d*. This explains why the experiment *I* in Fig. 1.9a and b and the experiment *H* in Fig. 1.9b has width indexes higher than the river experiment *A*. The combined ponding and rainfall mechanism (experiment *G*) creates a too diluted lens that has a concentrations above 0.1, thus no freshwater lens is present with recharge ratio of 9.5 m.

- The rainfall end-member is not shown on these graphics because no longitudinal lens develops with this recharge mechanism. For combined mechanism with rainfall (experience *G*, *H* and *I*), the effect of rainfall is to diminish the lens sizes, but it has little influence on the width indexes. In Fig. 1.9c, d, e and f, experiences *G*, *H* and *I* have width ratios close to the corresponding experiences mechanisms without rainfall (*C* corresponds to *G*, *E* to *I* and *F* to *H*), but with a lower freshwater surface ratio. For the low recharge ratio R_r of 9.5 m, the fact that the freshwater lens do not develop from the beginning of the domain for the experiments *I* and *H* (as discussed above) modifies the width ratios compared to the recharge mechanisms without rainfall.

4.3.3 Effect of rainfall on lens geometry

The effect of rainfall on the lens geometry and saline water dilution is investigated more specifically by varying the part of rainfall of the total recharge between a 100% ponding recharge mechanism and a 100% rainfall recharge mechanism. Analysis is carried out for four R_r (9.5, 19, 28.5 and 38.1 m). Results are presented with top-view diagrams in Fig. 1.10 and in graphics displaying the freshwater (Fig. 1.11a) and brackish (Fig. 1.11b) water surface ratios in function of the rainfall contribution for various recharge ratios.

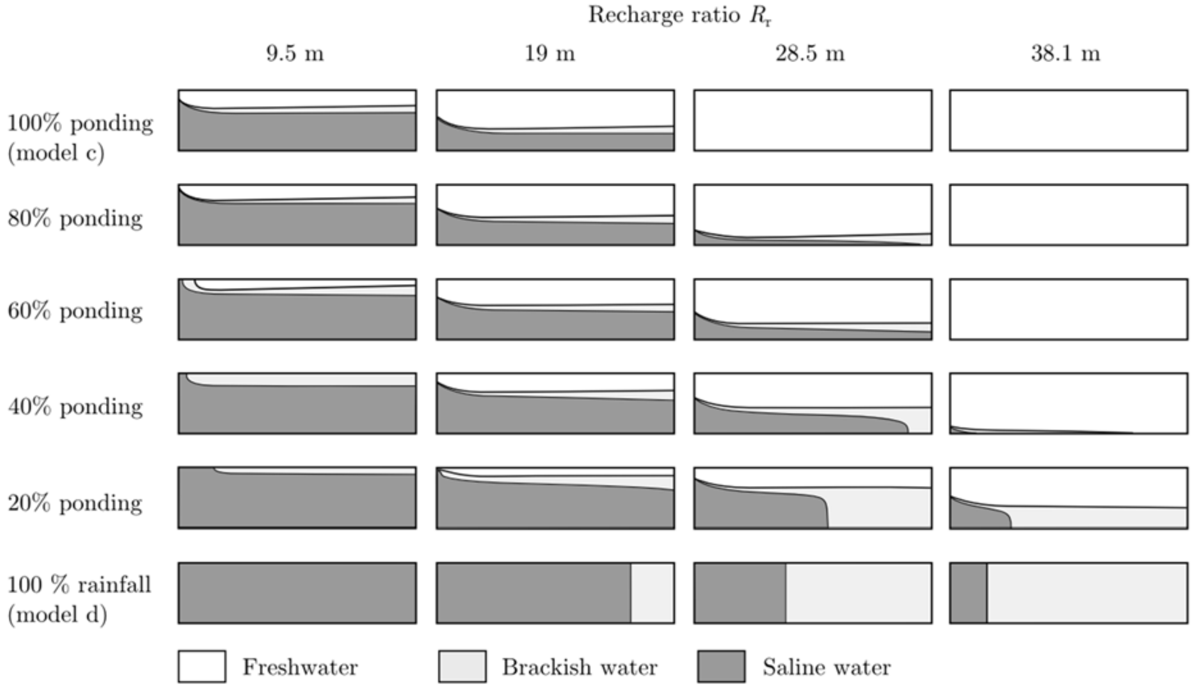

Fig. 1.10 : Fresh water, brackish water and saline water surfaces as function of the proportion of rainfall recharge for four recharge ratios (9.5, 19, 28.5 and 38.1 m). The effect of rainfall is to increase the brackish water surface due to saline water dilution.

The main effect of rainfall is to dilute the saline water and to create a more progressive transition between the freshwater lens and the saline water. This effect is particularly noticeable for high R_r, while differences with low R_r are less significant (Fig. 1.10).

The freshwater surface ratio of models between a 100% ponding and a 100% rainfall mechanism shows that the freshwater surface diminishes progressively until reaching 0 for a recharge composed of 100% of rainfall. The variation of the freshwater lens surface according to the proportion of rainfall is not linear. The diminishing of the freshwater lens size by increasing the proportion of rainfall is lower for low rainfall proportion than for higher ones.

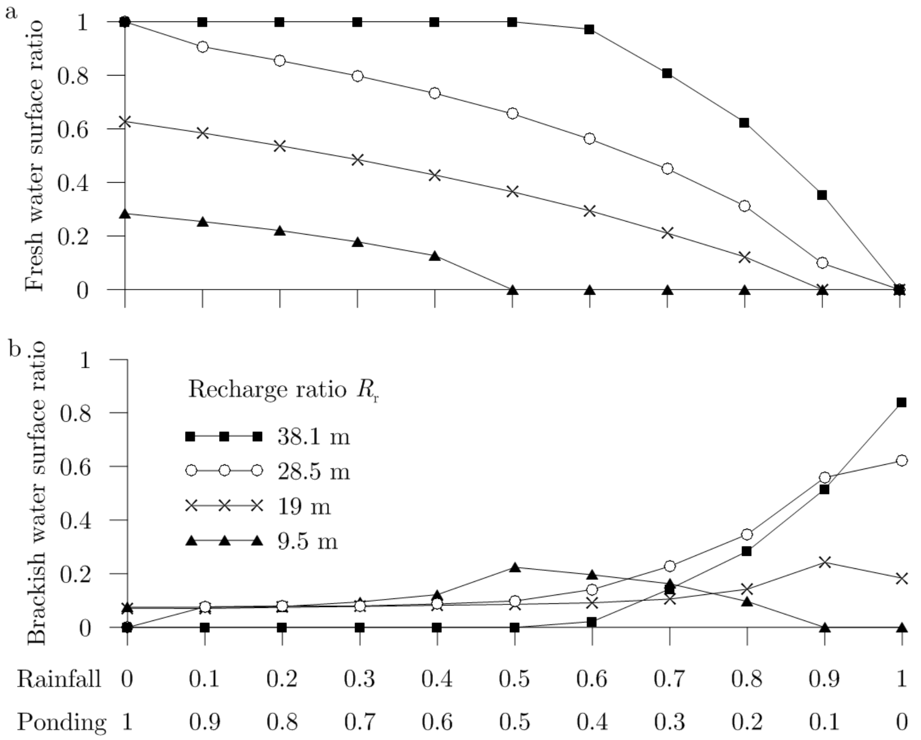

Fig. 1.11 : Effect of rainfall on freshwater surface (a) and brackish water surface (b). Four recharge intensities have been tested by varying the part of rainfall recharge between a 100% ponding pole and a 100% rainfall pole.

The diffuse recharge starts differently to have an impact on the brackish surface according to each recharge ratio curves (Fig. 1.11b). The brackish surface ratio curve of the lower recharge ratio (9.5 m) remains constant (0.08) up to a rainfall proportion of 30% and then increases up to 0.22 at 50% of rainfall proportion, before decreasing up to 0 at 90% of rainfall. The peak of 0.22 at 50% is explained by the fact that the concentrated recharge is not sufficient to maintain a freshwater lens (the 9.5 curve of Fig. 1.11a stops at 50% of rainfall). Thus, the freshwater lens is replaced by a brackish water lens. Increasing more the rainfall proportion reduces the size of this brackish lens because of the lower dilution of the saline water with fresh water.

Similar observations are visible with the 19 m R_r curve but the brackish surface ratio begins to increase from a proportion of rainfall of 70% and the peak is reached at a proportion of rainfall of 90%, which also corresponds to the proportion of rainfall for which the freshwater lens is not maintained (90%, Fig. 1.11a). For the 28.5 and 38.1 m R_r curves, the maximum brackish water surface is obtained when the recharge is only composed of rainfall and the brackish surface ratio curves increase from 60% of rainfall proportion. The fact that the 38.1 m curve remains below the 28.5 m curve up to the rainfall end-member is explained by the domain size that avoids the complete development of the brackish zone.

Based on a visual evaluation of the salinity maps of Fig. 1.10 and the curves of the saline and brackish surface ratios of Fig. 1.11, it could be postulated that the diffuse recharge starts to have a significant impact on the freshwater lens dynamics from a contribution of 50%.

4.3.4 Effect of longitudinal transmissivity heterogeneity on lens geometry

The previous experiments investigated lens geometries with the hypothesis of a homogeneous transmissivity field, which may not reflect the situation of a real aquifer. The formation of freshwater lens may not only be constrained by recharge mechanisms and intensity but also by heterogeneity.

In this section, the hypothesis of the Merti aquifer developing along a more transmissive section is tested. The impact of longitudinal heterogeneity is tested by assigning a width-variable band of lower transmissivity at the external side of the model (Fig. 1.12), corresponding to a possible heterogeneity in the Merti aquifer. Simulations are carried out for two ranges of recharge ratios R_r (9.5 and 19 m) for the half-river recharge mechanism (experiment B). Results are shown in Fig. 1.13.

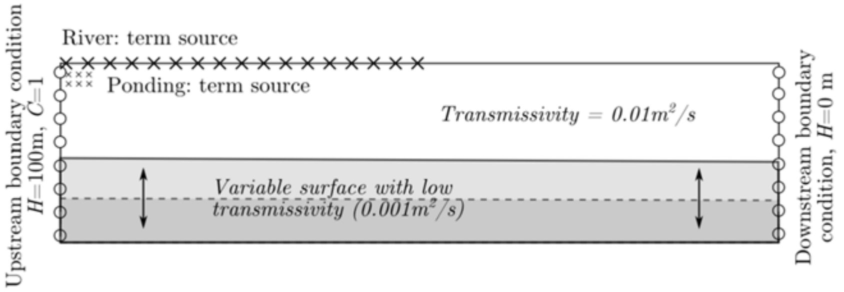

Fig. 1.12: Model showing the longitudinal transmissivity heterogeneity. Various simulations are run with different bands widths of lower transmissivity on the external side of the model.

These two series of simulations reveal that the freshwater lens surfaces are not influenced by the lower transmissivity zone as long as this low transmissivity zone does not reach the freshwater lens (dashed line on Fig. 1.13 a and b). Once the lower transmissivity zone exceeds the saline water zone, the size of the freshwater lens increases dramatically. Furthermore, the quantity of saline water entering the domain from the upstream boundary condition decreases constantly up to this same limit, up to an inflow of 0.

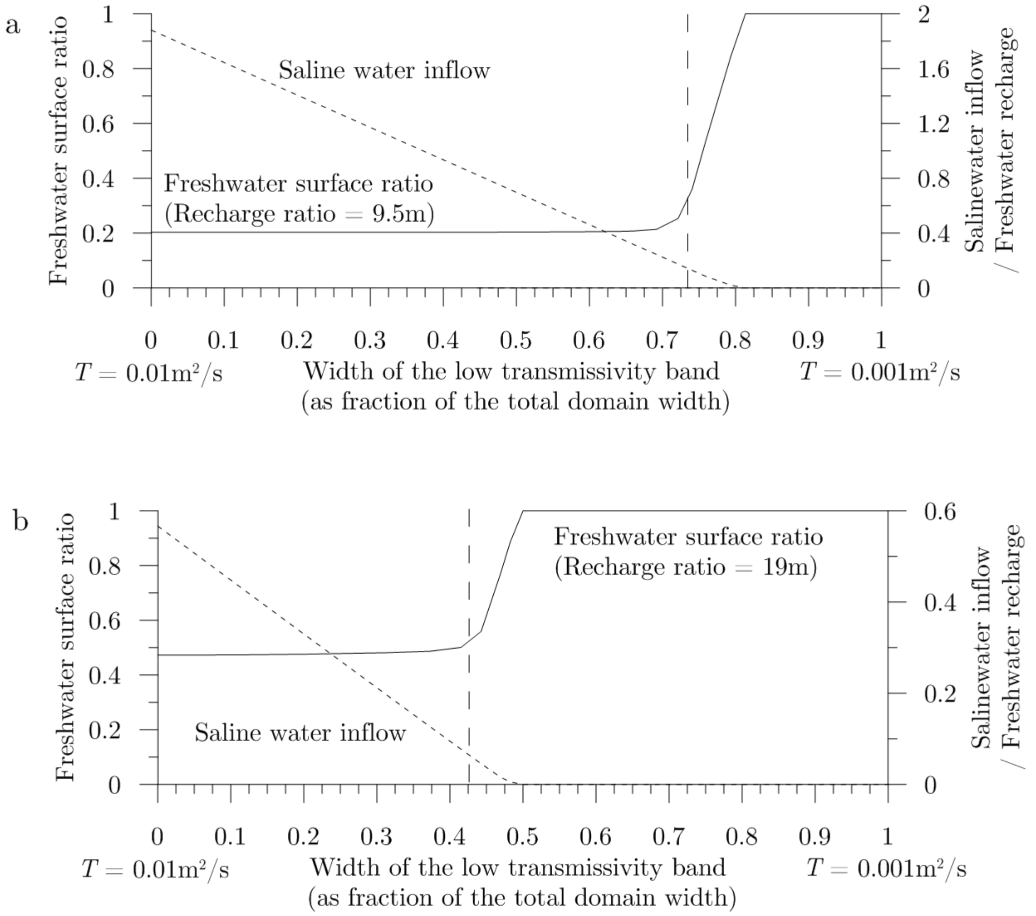

Fig. 1.13: Freshwater surface ratio (solid line) and saline water inflow (dashed line) vs low transmissivity surface proportion. Simulations are carried out with two recharge ratios: (a) 9.5 m and (b) 19 m. The vertical dashed line indicates the width of the freshwater lens without low transmissivity.

4.3.5 Conclusion of the steady state analysis

The steady state simulations allowed to characterise the impact of recharge mechanisms and recharge ratios R_r on the lens size and its geometry. The first observation is that the lens size is mainly controlled by the freshwater recharge ratio, but also partly by the recharge mechanism, in particular for high recharge ratios (Fig. 1.8 and Fig. 1.9). Secondly, the proportion of rainfall in the recharge plays a significant role on the lens size, in particular when rainfall proportion becomes higher than 30% (Fig. 1.11).

Then, the effect of longitudinal transmissivity heterogeneity was assessed. This analysis revealed that, as long as the lower transmissivity zone does not overlap the freshwater lens zone, this lower transmissivity does not significantly alter the geometry and the size of the lens.

4.4 Comparison with the Merti freshwater lens geometry

This section focuses on the comparison between the synthetic model analyses and the Merti aquifer in order to define a range of recharge mechanisms and recharge ratio R_r that could be considered as valid for the Merti aquifer. This approach also aims to define possible relation between the diffuse and concentrated recharge, which is not quantified in the previous chapter. Based on the obtained surface ratio, pairs of recharge and transmissivity giving the best geometries are selected and compared with the field measured transmissivities and possible recharge values.

4.4.1 Similarity surface ratio

This approach is based on a similarity surface ratio S_R, which compares the surface of the Merti aquifer freshwater surface and the simulated freshwater surfaces. This ratio is calculated by dividing the difference between the joint surface S_J and the overestimated surface S_O by the Merti freshwater surface S_M (Fig. 1.14 and Eq 1.4). Thus, if the simulated freshwater surface tends to the Merti one, the ratio tends to 1. The underestimated surface (Fig. 1.14) is included within the joint surface S_J with $S_M - S_u = S_J$.

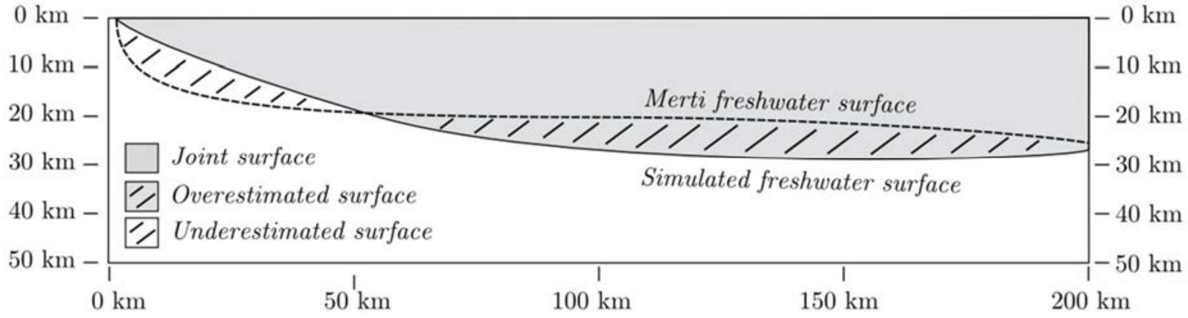

Fig. 1.14 : Illustration of the comparison between the Merti (observed) freshwater surface and the simulated freshwater surface.

$$S_R = \frac{(S_J - S_O)}{S_M} \qquad (1.4)$$

With :
S_R = Similarity ratio
S_J = Joint surface
S_O = Overestimated surface
S_M = Merti freshwater surface

Similarity ratios S_R are calculated for seven recharge ratios R_R (9.5, 14.3, 16.7, 19, 21.4, 23.8 and 28.5 m) and the nine recharge mechanisms (Table 1.2). Similarity ratios S_R higher than 0.9 (shaded squares, Table 1.3) are obtained with a R_R ranging between 14.3 and 21.4 m for the models *E* (river/ponding mechanisms), *F* (half-river/ponding), *H* (half-river/ponding/rainfall) and *G* (river/ponding/rainfall).

Other recharge mechanisms, or combinations of recharge mechanisms, as well as higher ratios also show satisfactory results. The uncombined recharge mechanisms *B* and *C* (half-river and ponding) have results ranging between 0.80 and 0.85 for recharge ratios between 14.3 and 16.7 m (in bold in Table 1.3). The combined river and ponding mechanism (experiment *E*) also show acceptable results with recharge ratios of 14.3 and 19 m, as well as the models with rainfall (experiment *G*, *H* and *I*) with recharge ratios between 5.2 and 7.5 m.

This suggests that the recharge of the Merti aquifer, if the transmissivity is homogeneous, is likely to be controlled by a combination of concentrated recharge over the Lorian Swamp and the Lagh Dera wadi (lateral side of the model) and also possibly by diffuse recharge related to rainfall. Compared to the models without rainfall, models including the rainfall recharge mechanism (experiment *G*, *H* and *I*) produces better results with higher recharge ratios. This observation indicates that, for a same concentrated recharge rate, adding between a half or a third of diffuse recharge lead to close similarity surface ratios, but with a total higher recharge rate. This observation is consistent with the width ratio analysis (section 4.3.2) that revealed that the rainfall has as effect to vary the size of the freshwater lens without modifying significantly its geometry, compared to recharge models without rainfall.

Worst results are obtained with the rainfall mechanism, which do not allow to produce freshwater lens with the tested recharge ratio (Fig. 1.10) and with the river mechanism (experiment *B*). Generally, low recharge ratios (9.5 m) and higher recharge ratios (28.5 m) also produce poor results.

Recharge ratio (m)	Similarity ratio by recharge mechanism								
	A	*B*	*C*	*D*	*E*	*F*	*G*	*H*	*I*
9.5	0.28	0.51	0.70	0.00	0.27	0.47	0.00	0.18	0.09
14.3	0.50	**0.84**	**0.80**	0.00	**0.81**	**0.93**	0.57	0.61	0.44
16.7	0.61	**0.85**	0.63	0.00	**0.96**	0.82	0.74	**0.80**	0.64
19	0.71	0.78	0.42	0.00	**0.86**	0.63	**0.88**	**0.95**	0.78
21.4	0.78	0.63	0.21	0.00	0.70	0.44	**0.86**	**0.84**	**0.93**
23.8	0.79	0.46	0.01	0.00	0.53	0.25	0.73	0.67	**0.89**
28.5	0.76	0.09	-0.52	0.00	0.22	-0.12	0.35	0.30	0.59

Table 1.3: Similarity surface for various recharge ratios R_R and various sets of recharge mechanisms (*A*: River, *B*: Half river ,*C*: Ponding, *D*: Rainfall, *E*: River and ponding, *F*: Half river and ponding, *G*: Ponding and rainfall, *H*: Half river, ponding and rainfall, *I*: River, ponding and rainfall). Best results are obtained with a recharge ratio R_R between of 14.3 and 21.4 m and for recharge mechanisms combining the river or half-river mechanisms with ponding (experiment *E* and *F*) and rainfall (experiment *H* and *I*).

4.4.2 Pairs of transmissivity and recharge

The pair transmissivity-recharge implies that various pairs of transmissivities and recharges can produce the same geometry as the models identified with the similarity surface analysis. In this section, pairs of recharges and transmissivities leading to the same geometries are computed and compared with well tests transmissivity estimations and with recharge estimations from previous studies and from the results of the recharge analysis presented in the Chapter 3 dedicated to the recharge.

This analysis is carried out based on a recharge ratio of 18 m. This value is an intermediate result between the *I* and *H* models and the *E* and *F* models, with recharge ratio of 21.4, 19, 16.7 and 14.3 m respectively. As discussed in Chapter 3, even though its high uncertainty, the diffuse recharge is likely to contribute only in a lesser extent than the concentrated recharge, justifying to select a recharge ratio closer to the *E* and *F* model (without rainfall recharge mechanism), than to the *H* and *I* models (with rainfall).

Maximum transmissivity values measured within the Merti aquifer range between 10^{-3} and 10^{-2} m^2/s (section 2.3.4) and minimum transmissivity values are around 2.5 x 10^{-4} m^2/s. Corresponding freshwater recharge for these two extremes range between 11.4 and 0.3 x 10^6 m^3/y respectively.

Transmissivity (m^2/s)	*0.00025*	*0.0025*	*0.01*	*0.025*	*0.18*	*0.34*
Merti aquifer transmissivity estimation (*T*)	*Minimum measured T*		*Maximum measured T with well tests*			
Recharge estimated (10^6 m^3/y)	*0.3*	*2.8*	*11.4*	*28.4*	*200*	*390*
Merti recharge estimation (*R*)		*Min. estimated R in previous studies*		*Max. estimated R in prev. studies*	*Min. estimated R in this study*	*Max. estimated R in this study*

Table 1.4: Pairs of transmissivity and annual average recharge *R* giving a similar geometry to the Merti freshwater lens, derived from a recharge ratio of 18 m. Pairs are calculated for minimum and maximum measured transmissivities over the Merti aquifer and for minimum and maximum recharge estimations. Recharge is considered on the entire lens (i.e. the double of recharge calculated for a half-lens, 20'000 km^2) and includes the concentrated and diffuse recharge.

Extrapolation with the recharge obtained in Chapter 3 leads to transmissivities values between 0.18 and 0.34 m^2/s, that is about 18 to 34 times higher than the maximum measured transmissivity deduced from pumping tests. However, it should be considered that transmissivities evaluated with well tests do not entirely reflect the reality. Indeed, transmissivities measured in boreholes are likely to be underestimated because boreholes do not cross the entire aquifer and also due to well-losses (quadratic head-losses), as already discussed in section 2.3.4.

4.4.3 Conclusion of the comparison with the Merti aquifer

The comparison between synthetic lens geometries and the Merti freshwater lens geometry reveal an incompatibility between the field measured transmissivities and the recharge rate obtained with the remote sensing analysis in previous chapter. The analysis of recharge-transmissivity pairs indicates that the actual transmissivity of the Merti aquifer should be about 18 to 34 times higher than the maximum transmissivities measured by well tests. On one hand, assuming a hypothetical homogenous hydraulic conductivity of 1 x 10^{-3} m/s (well sorted gravels), a transmissivity of 0.2 m^2/s implies an aquifer thickness of 200 m, instead of the 50 m currently considered. On the other hand, a lower hydraulic conductivity of and 1 x 10^{-4} (well sorted sands) would lead to an aquifer thickness of 2'000 m.

Considering the transmissivities obtained from well tests, the comparison with the Merti aquifer lens geometry indicates that recharge should be around 11 x 10^6 m^3/y, that is more consistent with previous recharge estimations (GIBB 2004).

Additionally, if the aquifer transmissivity is homogeneous, this comparative analysis indicates that the total freshwater recharge is mainly composed of concentrated recharge taking place over inundated areas and along an ephemeral river crossing partly or entirely the domain. The diffuse recharge (rainfall mechanism) over the entire domain is likely to play a lesser significant role (up to a third).

4.5 Effect of pumping on the lens geometry

Influence of water extraction on freshwater lens geometry is tested on a transient model with a recharge of 6 x 10^6 m^3/y divided between the half-river, ponding and rainfall recharge mechanisms (experiment *H*). This recharge volume is selected because it represents the lower estimation of the recharge (derived from the pumping tests) and thus a conservative approach. Two abstraction models are simulated: one with an abstraction rate of 2 x 10^6 m^3/y and the other one with an abstraction of 3 x 10^6 m^3/y. The evolution of the lens geometry from the undisturbed lens before pumping up to a new equilibrium is evaluated with the freshwater surface ratio (Fig. 1.15).

This analysis reveals a high inertia of the system, with needed time of 20'000 years before reaching the steady state.

The final geometries of the lenses indicate that the shape of the freshwater lens changes significantly in the vicinity of the extraction point (Fig. 1.16). However, the freshwater surface as a whole does not alter significantly. Similar groundwater extractions simulated on models with a higher recharge rate, but with an identical recharge ratio R_R (i.e. by increasing the transmissivity with the same factor that the recharge), will lead to an intermediate lens geometry, between the undisturbed one and the simulated ones shown in Fig. 1.16.

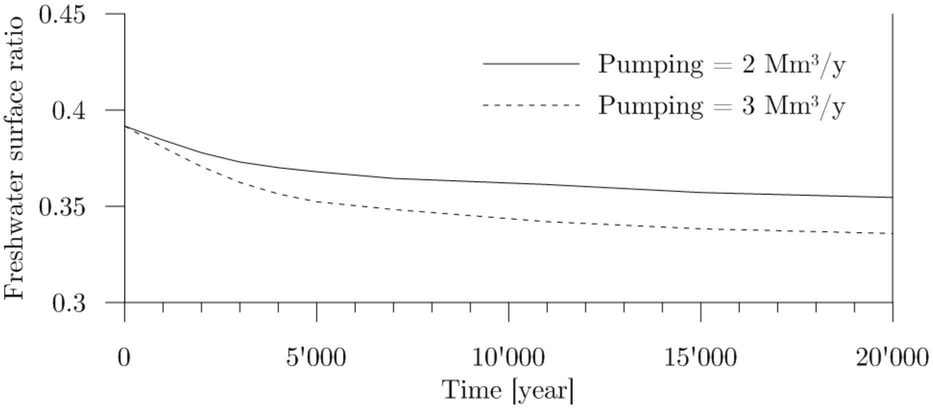

Fig. 1.15 : Evolution of a freshwater lens under pumping rates of 2 and 3 x 10^6 m^3/y respectively. Recharge of 6 x 10^6 m^3/y is divided between the half-river, ponding and rainfall (experiment *H*).

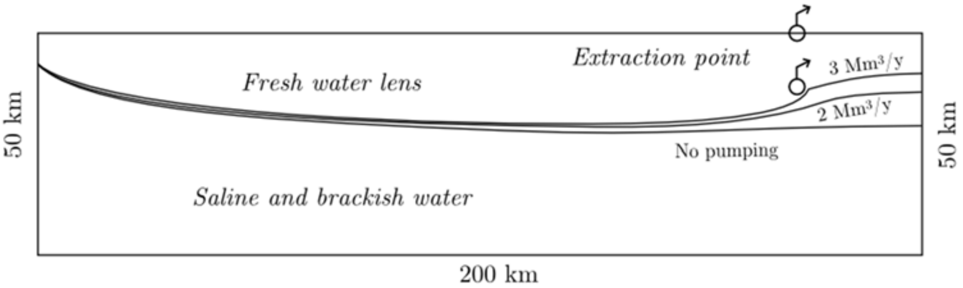

Fig. 1.16 : Freshwater surfaces in steady state flow without pumping and with pumping of two different abstraction rates (2 x 10^6 m^3/y and with 3 x 10^6 m^3/y). Freshwater surfaces of the "pumping models" are shown after reaching a pseudo steady state.

These simulations indicate that the risk of salinisation from the saline/brackish water zone is limited within the camps on the regional scale and may only occur after a very long period of pumping, revealing by the way the very high inertia of the aquifer (several thousands of years are needed to reach a steady state). However, this 2D horizontal approach does not consider possible upconing of saline/brackish water from underlying layers. As discussed in Chapter 2, dedicated to the hydrogeological characterisation of the aquifer, and especially in the sections 2.3.3 and 2.3.6, these risks of salinisation by upconing remain possible but, based on the short and mid-term data, no signs of dramatic increase of salinity were identified.

Furthermore, if a recharge ranging between 207 and 392 x 10^6 m^3/y is considered, as quantified in Chapter 3, the risk of salinisation from the lateral saline/brackish water zones becomes almost insignificant and the risk of upconing is significantly lowered because of the freshwater water contained in the underlying layers of the aquifer system. Indeed, this underlying freshwater acts as a buffer between the exploited freshwater of the Merti beds and the saline/brackish water located in much higher depth. However, as no deep water-prospection boreholes were drilled below the first layer of the aquifer system (the Merti beds), the exact transition between the fresh and brackish/salty water is not known and thus, the effect of upconing from this deep brackish/salty water could not be assessed.

4.6 Conclusions of the freshwater lens dynamics

The analysis of the freshwater lens dynamics allowed to point out the following observations.

The steady state analysis revealed that the size of a freshwater lens is mainly controlled by the couple recharge/transmissivity (integrated into the recharge ratio R_r for steady state simulations) while the recharge mechanism mainly influences the lens geometry (characterised with the width ratios $WI\ (x_{50-10})$ and $WI\ (x_{100-50})$) and in a lesser extent the lens size (Fig. 1.9). However, for high recharge rates leading to large freshwater lenses, the effect of the recharge mechanism on the lens geometry decreases and plays a more significant role for the lens size.

Up to a proportion of 30-50%, the rainfall mechanism does not significantly modify the geometry of the freshwater lens and affect its size of about 20%. Beyond this proportion, rainfall starts to have a major impact on the freshwater lens size and the proportion of brackish water (Fig. 1.10 and Fig. 1.11).

Comparison with the Merti aquifer carried out using a similarity ratio (Table 1.3) indicated that the freshwater lens of the Merti aquifer is likely to be created by a combination of concentrated recharge over the Lorian Swamp area and partly along the Lagh Dera wadi. Diffuse recharge could contribute to the recharge, increasing the total freshwater recharge rate up to 30%.

Pairs of transmissivities and recharges, leading to the same geometry, revealed a discrepancy between the estimation of recharge carried out in this study (Chapter 3) and the field measurements of transmissivities. Indeed, higher transmissivities obtained from field well tests indicate maximum values of 0.01 m^2/s, while the transmissivity necessary to accommodate a recharge between 200 and 390 x 10^6 m^3/y ranges between 0.18 and 0.34 m^2/s, which is 18 to 34 times higher than the measured transmissivity in the Merti aquifer.

This discrepancy leads to two hypotheses. Firstly, the Merti aquifer does not receive the entire recharge. This implies others aquifer systems in the vicinity of the Merti aquifer, for instance through the possible karstified limestones identified at the Matasade Horse, north of Merti. However, as discussed in the characterisation of the Merti aquifer (section 2.2), based on the geology analysis, no evidence of such a connection was found. The second hypothesis is to consider a higher aquifer transmissivity, which could be either explained by a higher hydraulic conductivity or a higher aquifer thickness.

This second hypothesis is supported by two possibilities. Firstly, as previously discussed in section 2.3.4, it is likely that the transmissivity was underestimated within the tested aquifer thickness because of well losses that diminishes the measured transmissivity compared to the actual one. Furthermore, as discussed in previous chapters, it is suggested that the entire Merti aquifer has not been entirely drilled by existing boreholes and has a thickness significantly higher than the one considered up to now. Whereas the lateral extension of the freshwater lens is well identified, its exact depth remains unknown: hydrogeological prospections with boreholes were confined to the so-called Merti beds, probably for budget reasons but also because this formation has always been providing sufficient water.

Thus it remains possible that deeper water-productive horizons could be found, leading to consider the Merti aquifer as a "multi-layer aquifer system". This assumption is also supported by the very large extension of the Merti aquifer and its geology. Actually, given the extension of about 50 km by 250 km and the several superimposed layers of sediment that constitute the aquifer, it would be unlikely to find fresh water only over 50 m of thickness, while other horizons similar to the Merti beds are described in deeper boreholes logs (Bosworth and Morley, 1994) unfortunately, without description of the groundwater availability and quality. These hypotheses will be further investigated in the chapter dedicated to the regional model of the Merti aquifer.

It was also observed that the freshwater lens is not affected by lateral lower transmissivities as long as this lower transmissivity zone does not overlap the freshwater zone.

Then, based on the analysis of the effect of rainfall on the lens geometry (section 4.3.3) and the similarity ratio (section 4.4), the diffuse recharge is likely to constitute up to a third of the total recharge, according to the geometry of the synthetic model. As for the previous chapter dedicated to the recharge quantification, the diffuse recharge volumes are here only considered for the freshwater surface. Diffuse groundwater recharge over the brackish and saline zones of the model is thus not considered as "freshwater recharge". According to the synthetic model, the freshwater lens surface (4'000 km^2) represents 40% of the entire model surface. Thus, according to the dynamics between the fresh and brackish water, the freshwater recharge may represent up 40% of a third of the concentrated recharge. Related to the results of the concentrated recharge quantification (between 195 and 329 x 10^6 m^3/y, see Chapter 3), the diffuse recharge may range between a maximum of 26 and 43 x 10^6 m^3/y (2.1 to 3.5 mm/y in vertical rate). Based on this approach, the minimum diffuse recharge could theoretically be 0. Total freshwater recharge ranges thus between 195 and 372 x 10^6 m^3/y (Fig. 1.17).

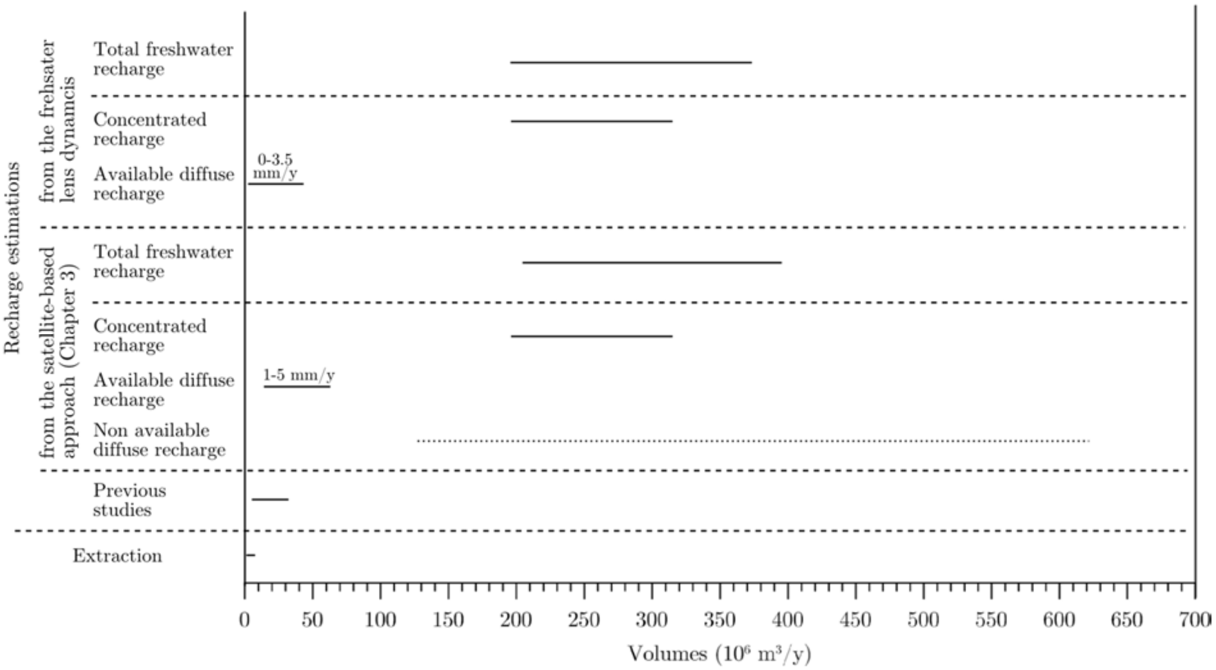

Fig. 1.17 : Estimations of recharge from the satellite-based approach (Chapter 3) and the freshwater lens dynamics (this chapter).

Finally, transient simulations investigating the effect of pumping on the lens size revealed the low risk of salinisation from the lateral saline/brackish water and the high inertia of the aquifer. However, this analysis carried out with 2D horizontal simulations does not consider the risk of salinisation from underlying layer (upconing), which possibly contain saline water. Based on the mid and short term electrical conductivity data discussed in Chapter 2, this risk is assumed to be low. Furthermore, as discussed above, the higher recharge rates obtained in Chapter 3 implies to consider an aquifer system composed of several water-productive layers. Thus, possible underlying layers below the Merti beds horizon may act as “buffer” between the Merti beds (the exploited layer) and deeper underlying saline/brackish waters.

Chapter 5

Conceptual and numerical regional models of the Merti aquifer

5.1 Introduction

The aim of this chapter is to synthetize, into a comprehensive regional numerical groundwater flow model, the main results obtained from the field data investigation (Chapter 2), the recharge quantification (Chapter 3) and from the freshwater lens analysis (Chapter 4).

In the first section of this chapter, based on the analyses and interpretations from previous chapters, a conceptual model of the aquifer is established. Then, in the second section, a series of models is developed in order to test various hypotheses on recharge volumes and concentrated recharge location.

In a first step calibration is done in steady state. In a second step, transient simulations are carried out in order to simulate the formation of a fresh water lens from a saline aquifer. The shape of the created freshwater lens and the relation between the salinity of the freshwater lens zone and the surrounding zones is used for additional calibration.

These models serve in particular to discuss the discrepancy between the transmissivities measured on the field and the recharge rates computed in Chapter 3. Indeed, as discussed before in section 0, the results from the groundwater recharge quantification are in contradiction with the transmissivity values obtained from pumping tests, suggesting a lower underflow and thus a recharge that is significantly lower.

5.2 Conceptual model

The development of the conceptual model is based on the synthetic model discussed in Fig. 2.23 (page 47) that summarises the geological and hydrogeological characteristics of the Merti aquifer investigated in Chapter 2. The three main aquifer zones of the central channel of the Merti aquifer are used for the elaboration of the conceptual model (Fig. 5.1): the lower Merti aquifer with a very high transmissivity, the central Merti aquifer with a high transmissivity and the upper Merti aquifer with an intermediate transmissivity. Since, the exact values of transmissivity are not known for the entire thickness of the Merti aquifer, transmissivity is discussed qualitatively.

The very high transmissivity of the lower Merti aquifer (zone 1, Fig. 5.1) becomes evident due to the dramatic break of the hydraulic gradient from Liboi towards the ocean (Fig. 2.7) and is explained by the presence of karstified limestones below the unconsolidated cover (Fig. 2.5 and Fig. 2.6). Transmissivities and extent of the upper and central Merti aquifer (zone 2 and 3, Fig. 5.1) are derived from well test data (Table 2.1) and from the geological interpretations discussed in section 2.2.

Laterally to the main aquifer zones, decreasing transmissivities are observed from well test data. These lower transmissivities are consistent with the higher water levels and higher electrical conductivity measured within these areas. From the border of the central transmissive channel, specific capacity values (Fig. 2.18) suggest that the transmissivity decreases progressively towards the limit of the Anza Graben. Over the shoulder of the Graben, transmissivity is assumed to be constant.

The area downstream of Merti (zone 4 in Fig. 5.1), around the Lorian Swamp, is considered separately from the rest of the lateral zone of the aquifer because of the specific hydrologic regime related to the Ewaso Ng'Iro River that could lead to the deposition of coarser sediments and the presence of higher transmissivity. This hypothesis is supported by the higher specific capacity values identified over this area, compared to the surrounding regions.

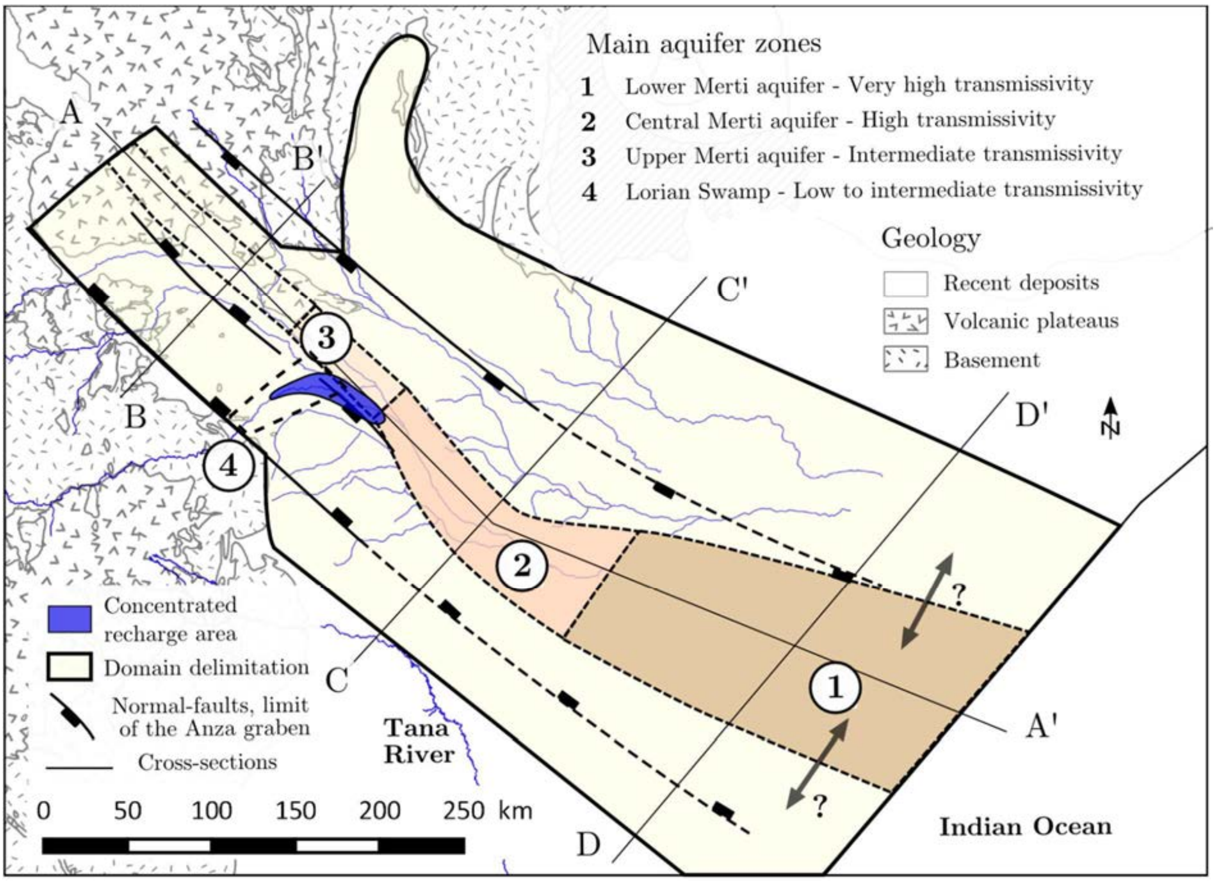

Fig. 5.1: Conceptual model of the Merti aquifer. Main aquifer zones are derived from well tests, hydraulic gradient and shape of the freshwater lens. The location of the main aquifer zones are constrained by the lateral down-faults. Within the lower Merti aquifer, the width of the aquifer is uncertain. The domain is defined in the upper part by the basement, at the downstream boundary by the Indian Ocean. Diffuse recharge is considered as homogenous over the entire system, except at the Lorian Swamp where significant concentrated recharge occurs periodically.

Upstream, the domain is delimited by the piezometric ridge of the Mt-Marsabit and the downstream limit of the domain is the Indian Ocean. Up to 200 km downstream of Mt-Marsabit, both sides of the domain are delimited by the basement. Further downstream, the lateral limits of the domain are not defined by clear geological features. These limits are based on the significant decrease of the observed transmissivity and specific capacity values. South-southwest, measurements indicate very high electrical conductivity in the ground and low transmissivities, showing that the Tana River is disconnected from groundwater.

The lateral and longitudinal relative variation of the transmissivity is illustrated in Fig. 5.2 below.

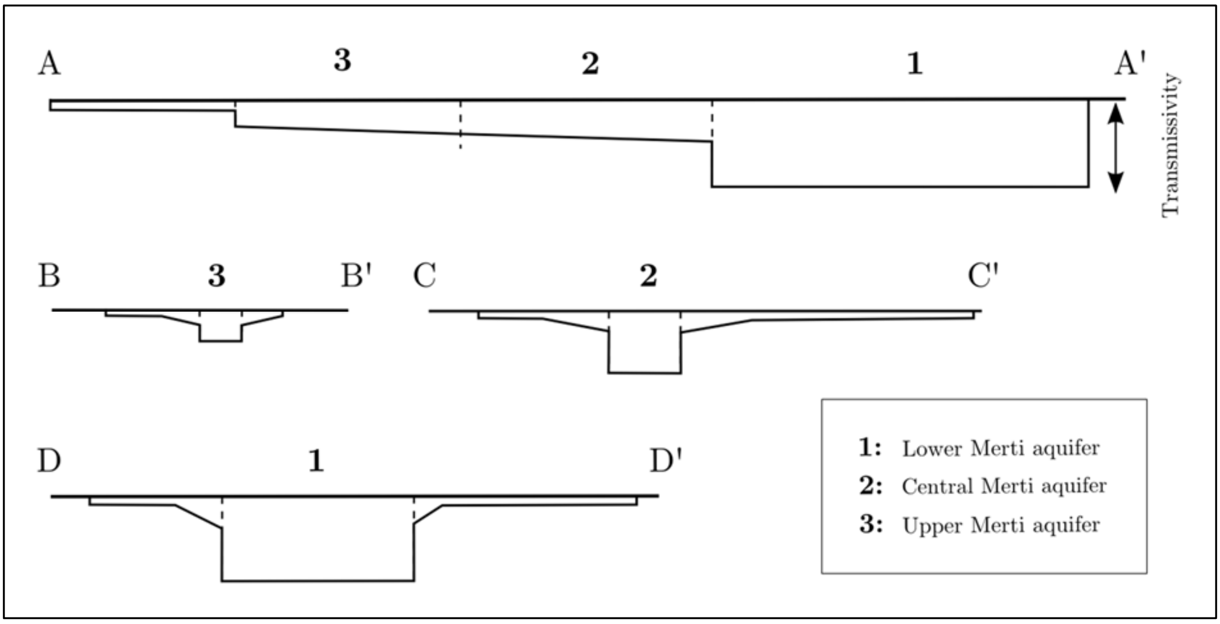

Fig. 5.2: Cross-sections showing the lateral and longitudinal variation of the transmissivity. Cross-sections locations are displayed on Fig. 5.1.

Based on the results of the recharge investigations of Chapter 3 and of the freshwater lens dynamics of Chapter 4, the recharge of the aquifer is divided into two mechanisms. Diffuse recharge is equally distributed over the entire domain, while concentrated recharge is located over the Lorian Swamp area. The diffuse recharge rate is estimated between 1 and 5 mm/y, while concentrated recharge volume is estimated between 195 and 329 x 10^6 m^3/y.

Precise locations of the recharge area, distribution of the transmissivity and transient parameterisation of the model are further discussed within the model description in the next section.

5.3 Regional numerical model

The regional numerical model is based on the conceptual model presented above. Firstly, a reference model is developed with the average diffuse and concentrated recharge rates obtained in Chapter 3. Secondly, from this reference model, a series of models are derived in order to test the various hypotheses on the diffuse recharge rates and concentrated recharge locations: a) models with two and five times lower and higher recharge rates will be tested in order to assess the possible range of diffuse recharge contribution to the total recharge; b) models with different concentrated recharge locations and inter-aquifer recharge will also be tested.

The reference model and its derived versions are established for steady state flow. This simplification is justified by the observation that static water levels only fell by a few decimetres since the beginning of intensive aquifer exploitation about 20 years ago (see section 2.3.2). The observed decrease is in fact much lower than the uncertainty about the groundwater depths and borehole elevations (section 2.3.1).

Because of the significant uncertainty on absolute recharge and transmissivity values, as well as on their spatial distributions, the model is little constrained, allowing a high flexibility for the calibration. In order to avoid an over-calibration of the model (i.e. to create a degree of precision higher than the available data), the models are developed keeping simple hypotheses, in particular for the definition of the transmissivity and the recharge zones.

All models are developed with the finite-element *Feflow* software. The *Feflow* model is described in detail in the next section on the reference model.

5.3.1 Reference model

This section starts with the description of the model (domain limits, the boundary conditions, recharge mechanisms, the mesh and the observation points). Then the calibration of the model is discussed. This calibration is done in two steps. In the first step (section 5.3.1.2), the model is calibrated in steady state without pumping. In the second step (section 5.3.1.3), mass-transport and transient simulation of the formation of the freshwater lens from an entire saline aquifer serves to adjust the calibration by comparison of the observed salinity of the aquifer with the simulated one.

5.3.1.1 Model description

The model description includes the following points: model domain, hydrostratigraphic units and transmissivity, boundary conditions and recharge conditions, transient parameterisation and finally the observations points used for the calibration.

Model domain

The developed model (Fig. 5.3) follows the geometry of the domain illustrated in Fig. 5.1 and discussed in section 5.2. The upstream limit is defined by the topographic limit of Mt-Marsabit. The downstream limit is defined at the Indian Ocean. Lateral limits are defined in the upstream part by the contact between the Quaternary and Miocene deposits of the Anza Graben and the surrounding basement rocks. Downstream, the limit is assumed to follow a line up to the Ocean, being defined by the line of decrease of transmissivity. This limit remains relatively uncertain due to progressive transition of the transmissivity from the center of the aquifer up to the lateral limit of the basin.

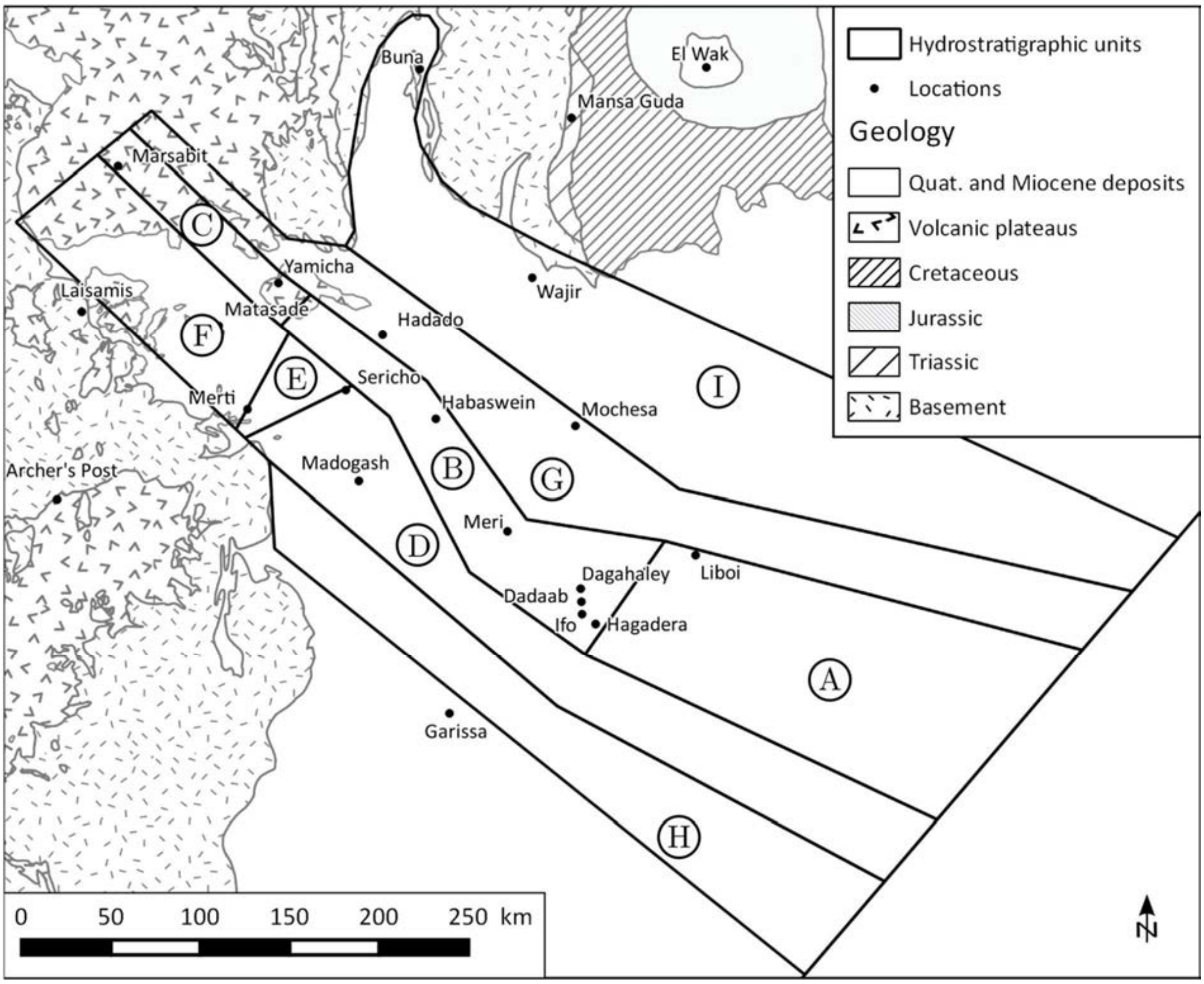

Fig. 5.3: Model domain and delimitation of the hydrostratigraphic units that will be used for the calibration of the numerical model by adjusting the transmissivity.

Mesh

The mesh was generated with the Triangle Mesh Generator developed by J.R. Shewchuk (2005). It contains about 19'000 elements with a resolution of about 4 km. The mesh is refined over the Lorian Swamp (the concentrated recharge area), with a resolution of about 1.1 km.

Hydrostratigraphic units and transmissivity

The main hydrostratigraphic units of the aquifer are derived from the conceptual model of Fig. 5.1. The upper, central and lower aquifer zones (zones 1 to 3 in Fig. 5.1) constitute the main aquifer (zones A and B on Fig. 5.3). Zones 2 and 3 on Fig. 5.1 are defined in the numerical model as one hydrostratigraphic zone with a decreasing transmissivity from the lower Merti aquifer (Fig. 5.3, zone A) to the upper part of the aquifer, as illustrated in Fig.

5.2. The zone A is defined separately because of higher required transmissivity, as discussed in the conceptual model. This zone is considered to have a homogeneous transmissivity. Zones C, D, F and G represent the transition from high and very high transmissivities to the lower transmissivities present on the edges of the aquifer (zones I and H). Zone E, which is located under the Lorian Swamp area, represents a zone of intermediate to low transmissivity compared to the central channel of the Merti aquifer, but higher than the adjacent transmissivity of the zones D and F.

These zones are used for calibration of the model by adjusting their transmissivity values. Zones D, F and G are defined with a progressive transmissivity from the central aquifer to the edge of the model, while zones I and H are defined as homogenous with a low transmissivity, as illustrated in Fig. 5.2.

Boundary conditions and recharge

A first kind boundary condition (Dirichlet) is defined at the downstream boundary of the model (the Indian Ocean) with a constant head $H = 0$ m. Both, diffuse and concentrated recharge, are defined within the model as a source term with a material *source-term* parameter. For the reference model, the diffuse recharge rate is fixed at 2.3 mm/y, corresponding to an annual average diffuse recharge volume of 286 x 10^6 m^3/y, while the average annual concentrated recharge is fixed at 260 x 10^6 m^3/y, for a total annual recharge of 575 x 10^6 m^3/y over the entire model (Table 5.1). These recharges correspond to the average recharge volumes established in Chapter 3. Concentrated recharge is located over the recurrent inundated areas derived from the MODIS images with the *NDWI* ratio (Fig. 3.5) Other recharge rates and locations of concentrated recharge will be tested in further models modified from this reference model.

	Concentrated recharge	Diffuse recharge over the freshwater lens	Diffuse recharge over the rest of the domain	Total recharge
Recharge volumes (10^6 m^3/y)	260	29	286	575

Table 5.1: Recharge volumes and vertical recharge rates for the concentrated and diffuse recharge volumes of the reference model.

Compared to the synthetic models of Chapter 4, the diffuse recharge volume is significantly higher because of the greater extent of the model and the fact that the regional flow within this model is induced by the diffuse recharge while it is created by a first head boundary condition in the synthetic model.

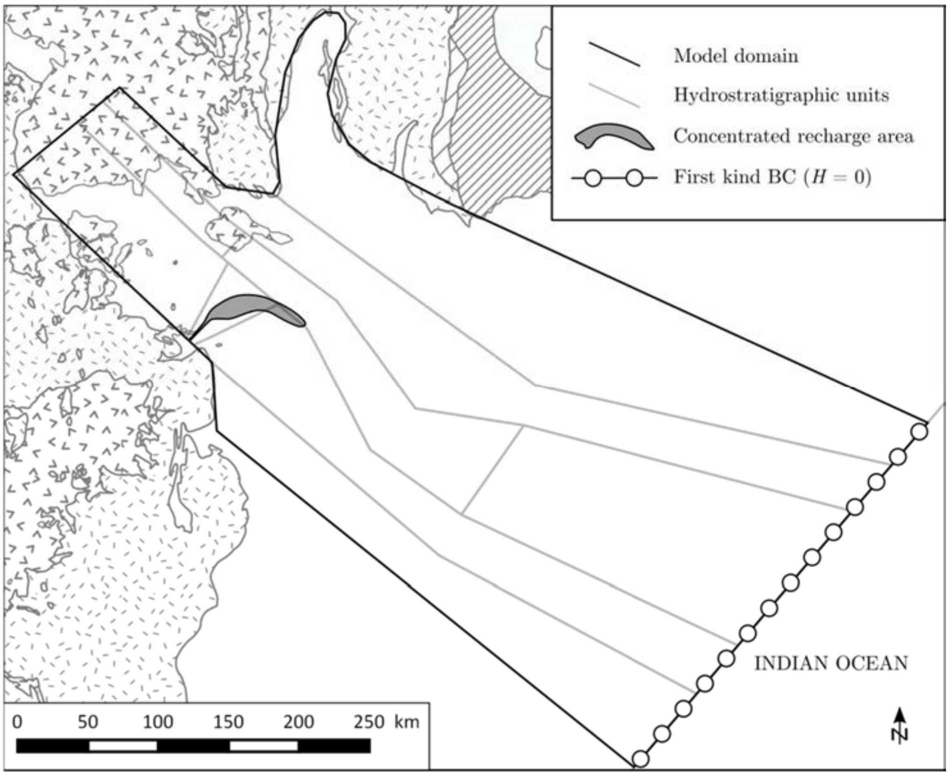

Fig. 5.4: Concentrated recharge area and first kind boundary condition (Dirichlet).

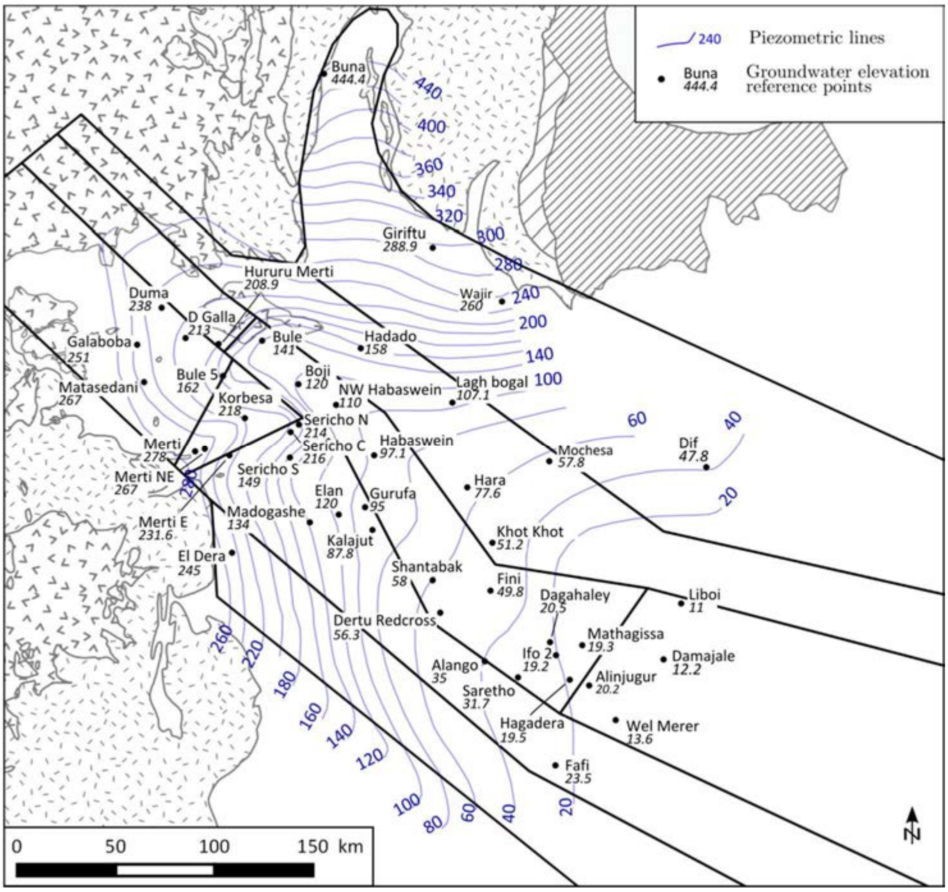

Fig. 5.5: Piezometric lines and the 45 groundwater observation points used for the calibration.

Transient parameterisation

For the transient simulations, the porosity is set to 0.3 and the longitudinal and transverse dispersivity are set to 2'000 and 200 m respectively. The thickness is defined to 200 m. A refined mesh and a dispersivity two times lower was tested for the reference model and didn't show significant differences in the total dissolved mass (maximum 0.2%) and in local concentration over the transition zone between the fresh and brackish water surfaces. Thus, the model with the rough mesh resolution was kept in order to optimise the computational time.

Observation points

Forty-five observation points are selected from the points used for the elaboration of the piezometric map (Fig. 2.7) in order to calibrate the model. All elevations are, or are assumed to be, static water levels. The list of the observation points with coordinates and elevations can be found in Appendix H.

5.3.1.2 Steady state calibration of the reference model

Following the assumptions described in Fig. 5.1 and Fig. 5.2, transmissivity is defined to the hydrostratigraphic zones of Fig. 5.3. Transmissivity of the reference model is shown in Fig. 5.6. Within the reference model, the lower Merti aquifer (unit A in Fig. 5.3) has a homogeneous transmissivity of 2.4 m^2/s. Towards the upstream part of the Merti aquifer (unit B in Fig. 5.3), the transmissivity decreases linearly up to 0.23 m^2/s. From this central high transmissivity zones, transmissivity progressively decreases down to 0.002 m^2/s towards the edges of the model (zones D, F and G). The hydrostratigraphic unit of the Lorian Swamp is defined with a transmissivity linearly decreasing from 0.04 m^2/s at the central boundary to 0.001 m^2/s at the external boundary.

The results of the calibration for the reference model are shown on the scatter in Fig. 5.7 and on the maps of the observed and simulated hydraulic heads Fig. 5.8 and Fig. 5.9. The error between the observed and simulated hydraulic heads is shown on the map of Fig. 5.10.

Calibration over the main aquifer zones and the Lorian Swamp

This model reproduces partially the overall trend of the observed hydraulic heads (Fig. 5.7 and Fig. 5.10), with an average error of 14.9 m and a root mean square of 21.7 m. Hydraulic heads over the central Merti aquifer (zones 2 in Fig. 5.1) is overall well reproduced while the differences between the observed and the simulated heads are more variable along the border of the model and around the Lorian Swamp.

The high complexity of the piezometry around the recharge area of the Lorian Swamp and the increasing hydraulic gradient between Sericho N and Merti explain the difficulty in reproducing the hydraulic heads over this area. The upstream part of the model (northwest of Bule) is also difficult to calibrate because this area highly depends on the recharge and hydraulic characteristics over the Lorian Swamp.

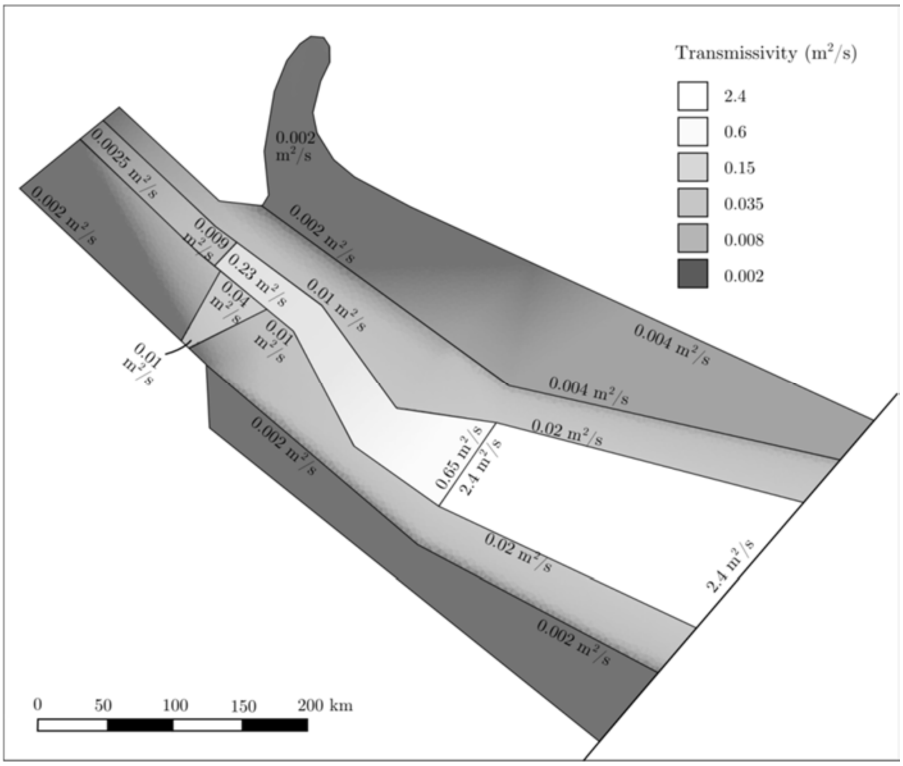

Fig. 5.6: Transmissivity map of the reference model.

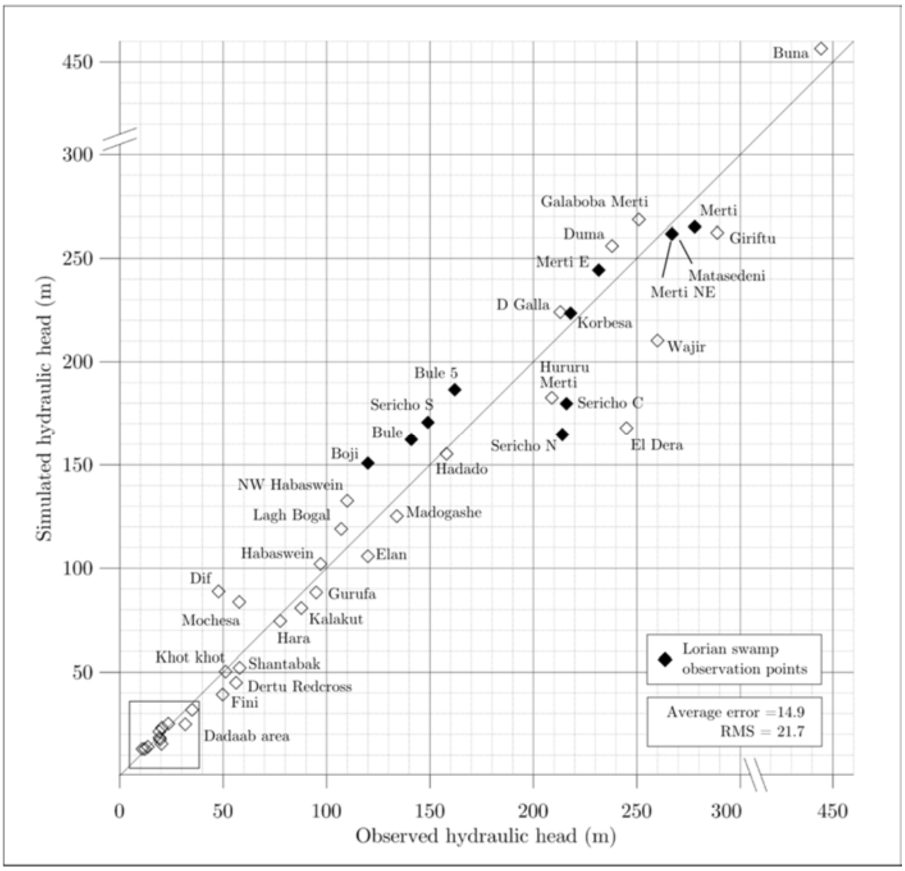

Fig. 5.7: Scatter plot between the observed and simulated hydraulic head for the reference model.

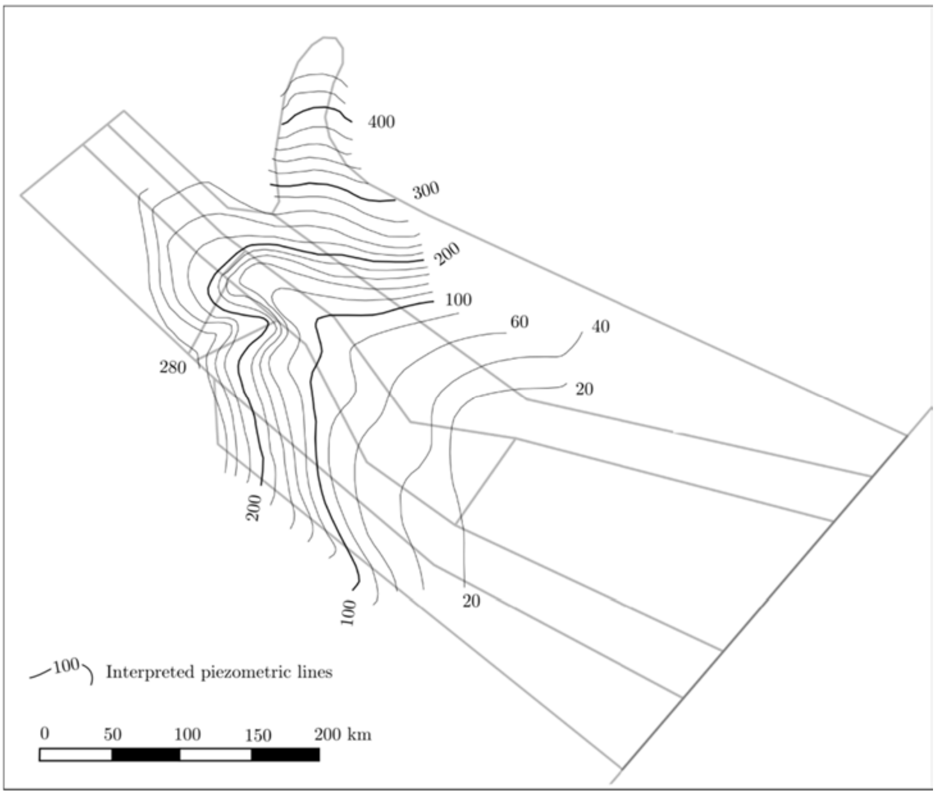

Fig. 5.8: Interpreted piezometric map.

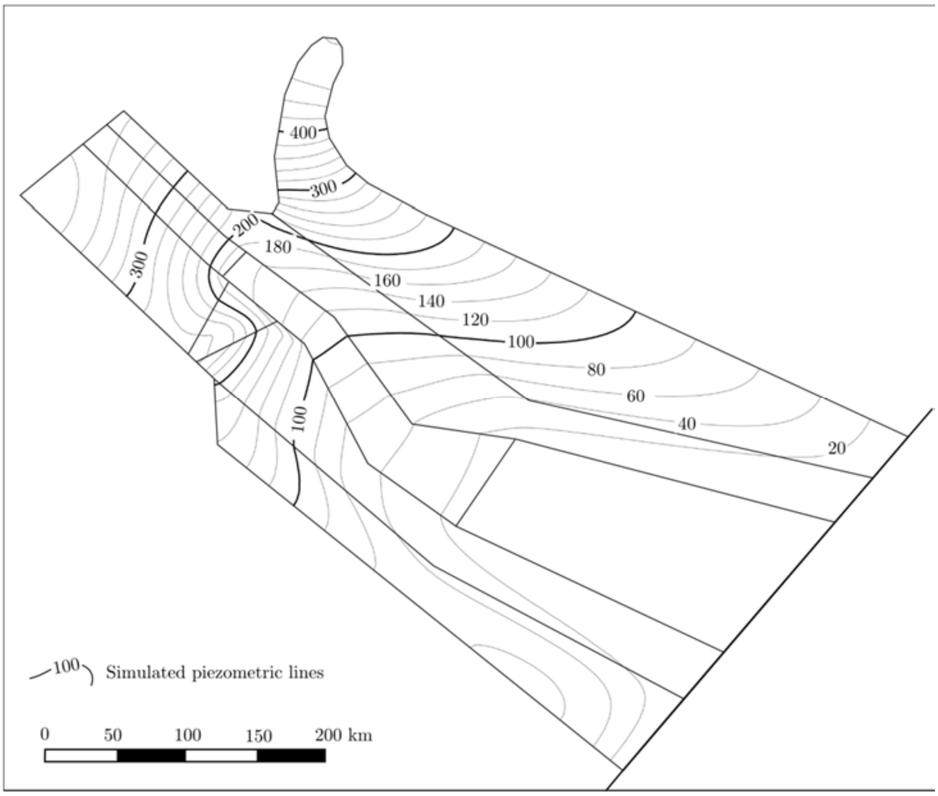

Fig. 5.9: Simulated piezometric map.

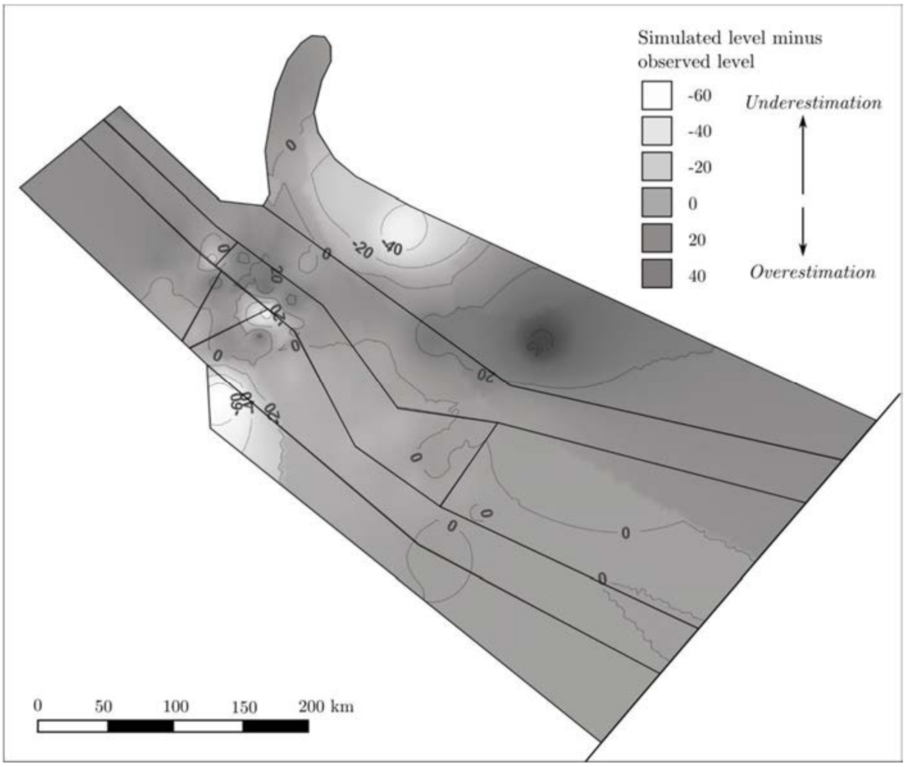

Fig. 5.10: Error between the observed and simulated groundwater level.

Thus, the observation points of Sericho C, Sericho N, Sericho S, Bule 5, Bule and Boji are not fully satisfied. Better calibration would require introducing higher recharge heterogeneity and transmissivity heterogeneity around this area, but without solid evidence to justify it. For these reasons, preference is given to a model imperfectly calibrated but with simple and consistent assumptions rather than to models that are better calibrated but rely on hypotheses, which lack strong support from measurements.

Calibration of the lateral zones of the model

As discussed in the model description and according to the conceptual model (section 5.2), transmissivity over the edge of the Anza Basin (zones H and I in Fig. 5.3) is supposed to be very low and quite homogeneous. For this reason, the model is calibrated with a homogeneous transmissivity of 0.02 m^2/s over these zones. Only the area northeast of Mochesa has a transmissivity two times higher in order to lower the simulated hydraulic head at Dif and Mochesa. Despite this small adjustment of transmissivity, error of simulated hydraulic heads remains significant at multiple observation points over the zones H and I, such as at Dif, Mochesa and Wajir at the northern edge, and at El Dera on the southern edge.

On the one hand, the lower transmissivity defined northeast of Mochesa allows adjusting the simulated hydraulic head in this part of the model, but on the other hand, it diminishes the water level at Wajir, which is already too low, compared to the reference hydraulic head. The other water levels over these zones (Giriftu and Buna) are quite well reproduced with this value. On the other side of the model, at El Dera, the hydraulic head is clearly too low. A better calibration could be obtained either with lower transmissivity values over this zone (H in Fig. 5.3), higher diffuse recharge or with lateral recharge justified by possible inter-aquifer recharge. This latter hypothesis will be discussed further in section 5.3.3.2. As for the calibration around the Lorian Swamp, it was preferred to keep imperfect calibration over the edge of the basin instead of over-calibrating the model by modifying arbitrarily the model parameters without sufficient evidence.

Discussion

Compared to the maximum measured field transmissivities (0.007 m^2/s, see section 2.3.4), the transmissivity of this reference model around Dadaab are about 86 times higher than those obtained with pumping tests. This discrepancy was already pointed out in the chapter dedicated to the freshwater lens dynamics (Chapter 4), but to a lesser extent. This higher difference between the model and measured transmissivity at Dadaab is explained by the fact that the section with the higher transmissivity is shorter in the regional model than in the one considered in the synthetic model of Chapter 4, but also by the higher contribution of diffuse recharge in the regional model because of the greater model extent.

A model with a transmissivity 85 times lower (the transmissivity of the exploited horizon) would lead to an annual average concentrated recharge of 3×10^6 m^3/y and a diffuse recharge of 0.026 mm/y. These recharge rates would imply that the concentrated recharge quantification methodology developed in section 3.4 is significantly inaccurate, but also that the diffuse recharge obtained with this model is about ten times lower than the minimum possible diffuse recharge previously defined from literature review (section 3.3.4).

In order to assess the impact of the diffuse recharge on the transmissivity calibration, four models will be tested with two and five times higher and lower diffuse recharge rates (section 5.3.2).

5.3.1.3 Transient analysis - Formation of the freshwater lens

From this steady state model, a further model including transient transport is developed. In this model, the development of a freshwater lens in a completely saline aquifer is simulated with freshwater recharge. Like for the experiments carried out in Chapter 4, the concentration was normalised between 0 for freshwater water and 1 for saline water. Assuming that the initial salt concentration of the water is close to the sea water concentration, the maximum electrical conductivity corresponding to a normalised concentration of 1 is defined at 50’000 µS/cm.

The transient analysis indicates that the model, assuming an initially completely saline aquifer, reproduces partly the development of the freshwater lens. The overall shape of the freshwater lens along the central Merti aquifer is well reproduced from a simulation period of

3’000 years but the freshwater area around the recharge area of the Lorian Swamp (Fig. 5.4) develops too largely during this period. This could be explained either by a too low transmissivity over the recharge area or because concentrated recharge is not well distributed in space and may therefore be more present in the downstream part of the Lorian Swamp (i.e. at the beginning of the freshwater lens). This hypothesis will be tested further in section 5.3.3.

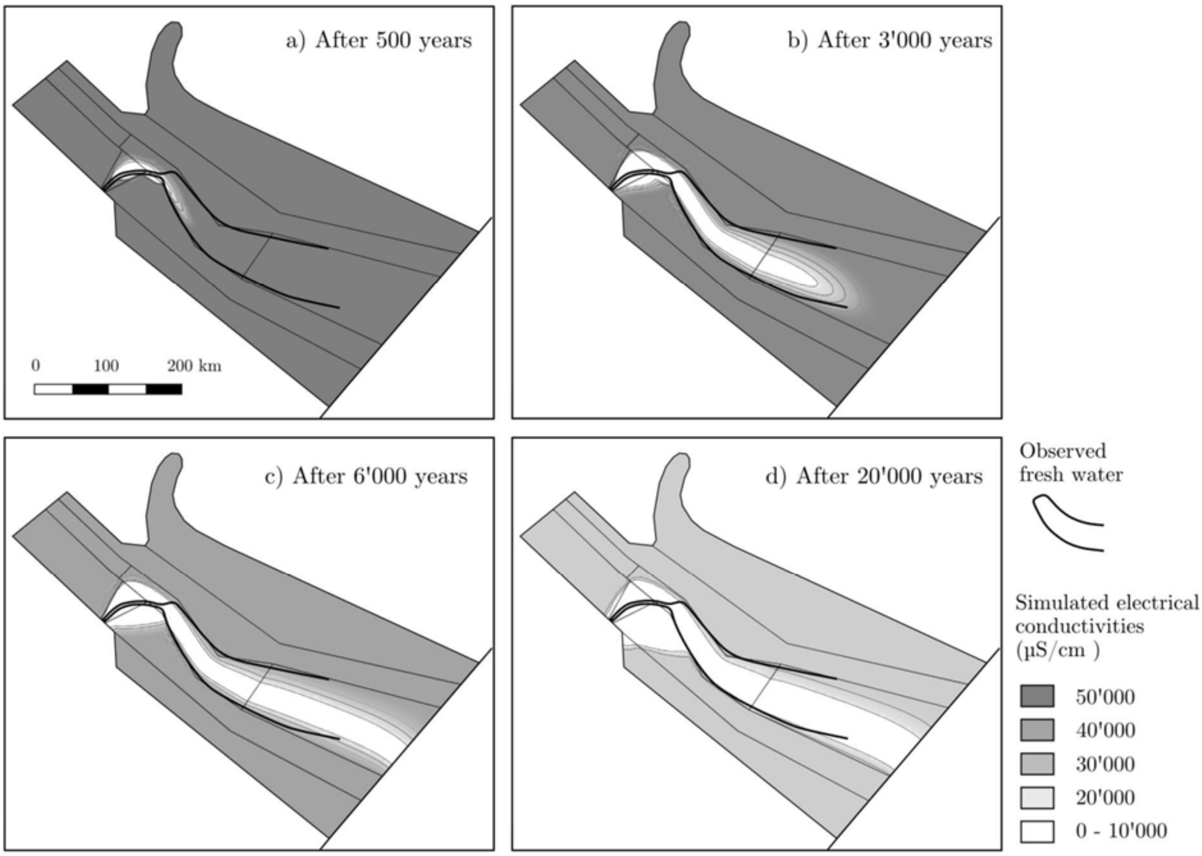

Fig. 5.11 : Formation of the freshwater lens from a complete saline aquifer. Salinity is normalised with values between 1 (saline water) and 0 (fresh water). Salinities are shown for four time steps at a) 500 years, b) 3’000 years), c) 6’000 years and d) 20’000 years. The observed limit between the fresh and brackish water is highlighted with the bold line.

5.3.2 Sensitivity analysis on the diffuse recharge

From the reference model, four different diffuse recharge rates are tested: 2 and 5 times lower and 2 and 5 times higher. Diffuse recharge rates of these models vary between 0.46 and 11.2 mm/y and the total recharge (diffuse and concentrated recharge) ranges between 322 and 1’850 x 10^6 m^3/y (Table 5.2).

	Diffuse recharge (rate mm/y)	Diffuse recharge (annual volume) (10^6 m^3/y)	Total recharge (10^6 m^3/y)	Recharge divided by the reference model recharge
Very low diffuse recharge	0.46	63	323	0.55
Low diffuse recharge	1.15	158	417	0.72
Reference model	*2.3*	*315*	*575*	1
High diffuse recharge	4.6	630	890	1.54
Very high diffuse recharge	11.5	1575	1’835	3.19

Table 5.2: Models with different of diffuse recharge combined with a constant concentrated recharge rate.

Steady state calibration

The calibration of these models is done by adjusting the transmissivity over the hydrostratigraphic zones described in Fig. 5.3. The transmissivity maps as well as the scatter plots between the observed and simulated hydraulic heads of these next models are available in Appendix I. The ratio of transmissivity for the different hydrostratigraphic zones between the various scenarios and the reference model is shown in Table 5.3 below.

Hydrostratigraphic zones	Ratio of transmissivity with the reference model			
	Very low diffuse recharge model (0.2)	Low diffuse recharge model (0.5)	High diffuse recharge model (2)	Very high diffuse recharge model (5)
A	0.54	0.81	1.21	2.64
B	0.73	0.74	1.21	2.28
C	0.37	0.82	1.21	3.07
D, F, G	0.50	0.93	2.35	4.23
E	1.03	1.03	0.98	0.43
H, I	0.07	0.18	0.98	2.15

Table 5.3: Ratio of the transmissivity per zone between the reference model and models with higher and lower diffuser recharge rate. The number in bracket in the first line indicates the proportion of recharge compared to the reference model.

These simulations indicate that the transmissivity of each hydrostratigraphic zone are not adjusted in the same way. In particular, it should be noticed that the zone around the Lorian Swamp (zone E) follows an opposite trend than the other zones. In other words, it means that the transmissivity of this zone should be lowered when the diffuse recharge increases. However, the transmissivity of this zone does not need to be increased for diffuse recharge rates lower than half of the reference model (value remains at 1.03). This overall observation is explained by the fact that, when higher transmissivity are present around zone E, drainage of zone E from the surroundings is higher and needs to be counterbalanced by lower transmissivity in order to maintain the hydraulic heads within this area. For very low diffuse recharge rate, diffuse recharge becomes insignificant and only the concentrated recharge controls the transmissivity of the zone E.

In absolute values (see the transmissivity maps in Appendix I), very high diffuse recharge rates require assigning a transmissivity to zone E that has a lower value than the surrounding lateral zones D and F; this is contradictory to the measured specific capacity and transmissivities (Fig. 2.18). This finding allows dismissing the hypothesis of a diffuse recharge being about 5 times higher than the concentrated recharge

The calibration quality with these transmissivities remains close to the reference model with errors ranging between 15.7 and 17.4 m. As for the reference model, the main difficulty for the model calibration remains around the area of the Lorian Swamp and over the edge of the models, specifically at Buna, El Dera, Dif and Mochesa (see the scatter plot in Appendix I for more details about the calibration of these models).

Compared to the maximum transmissivity measured around Dadaab, these models have transmissivity values 62.7, 63.5, 104 and 197 times higher (very low diffuse recharge to very high diffuse recharge models).

Transient analysis

The transient analysis (the development of the freshwater lens from a complete saline aquifer), shows very close results to the reference model for the scenarios with diffuse recharge two times lower and higher. For these two scenarios, slight changes in concentration out of the freshwater zone are noticeable but these changes do not allow drawing conclusions for the calibration of the model.

The scenarios with diffuse recharge five times higher and lower show significant differences (Fig. 5.12 Fig. 5.13). Firstly, for the five-times higher diffuse recharge scenario, it is noticeable that within the time needed for establishing the freshwater lens, the brackish zone around the freshwater zone becomes almost entirely washed away by the diffuse recharge; that makes this scenario incompatible with the observed concentrations.

Secondly, it could be observed that higher diffuse recharge leads to narrower freshwater lens while the model with low or very low diffuse recharge leads to a broader freshwater lens. This observation is explained by the fact that a high diffuse recharge rate induces significant flow from the lateral zones of the model towards the transmissive zone of the aquifer, limiting the development of the freshwater lens. These observations give additional reasons for dismissing a scenario with high diffuse recharge rates compared to the concentrated one.

However, one should keep in mind that the interpretation of salinity in a 2D model is difficult because the vertical distribution and heterogeneity of concentration could not be considered in such a model.

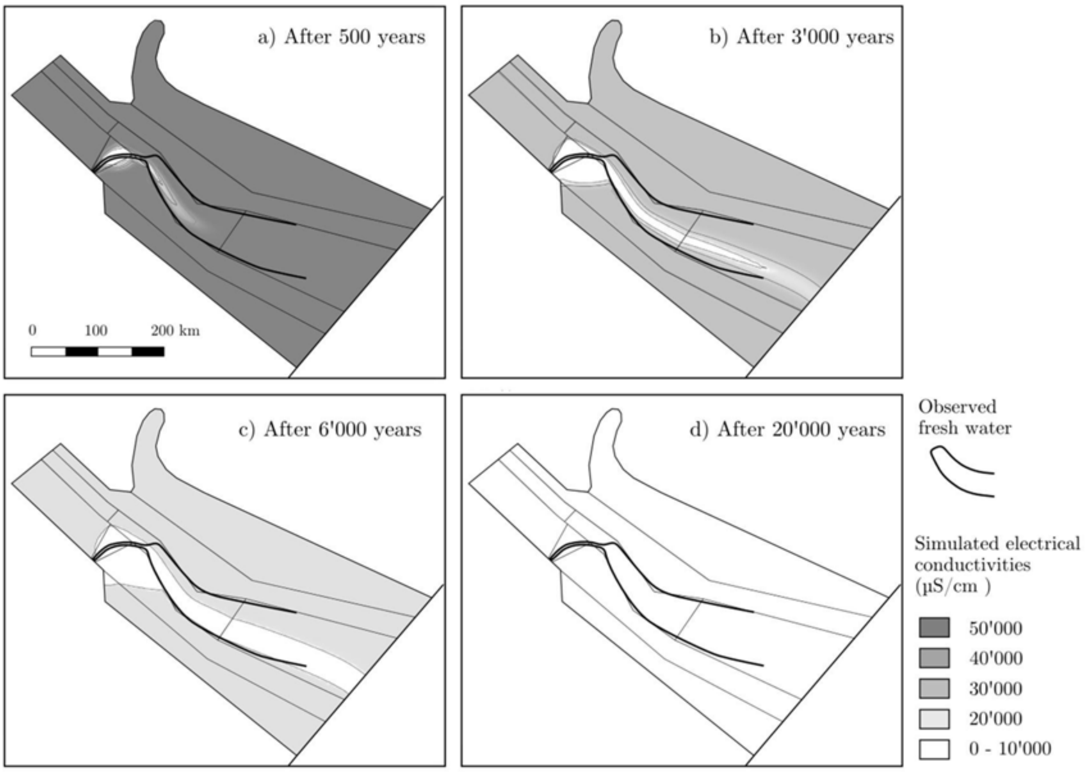

Fig. 5.12: Development of a freshwater lens from a complete saline aquifer. The diffuse recharge rate is five times higher than in the reference model. Salinities are shown for four time steps at a) 500 years, b) 3’000 years), c) 6’000 years and d) 20’000 years.

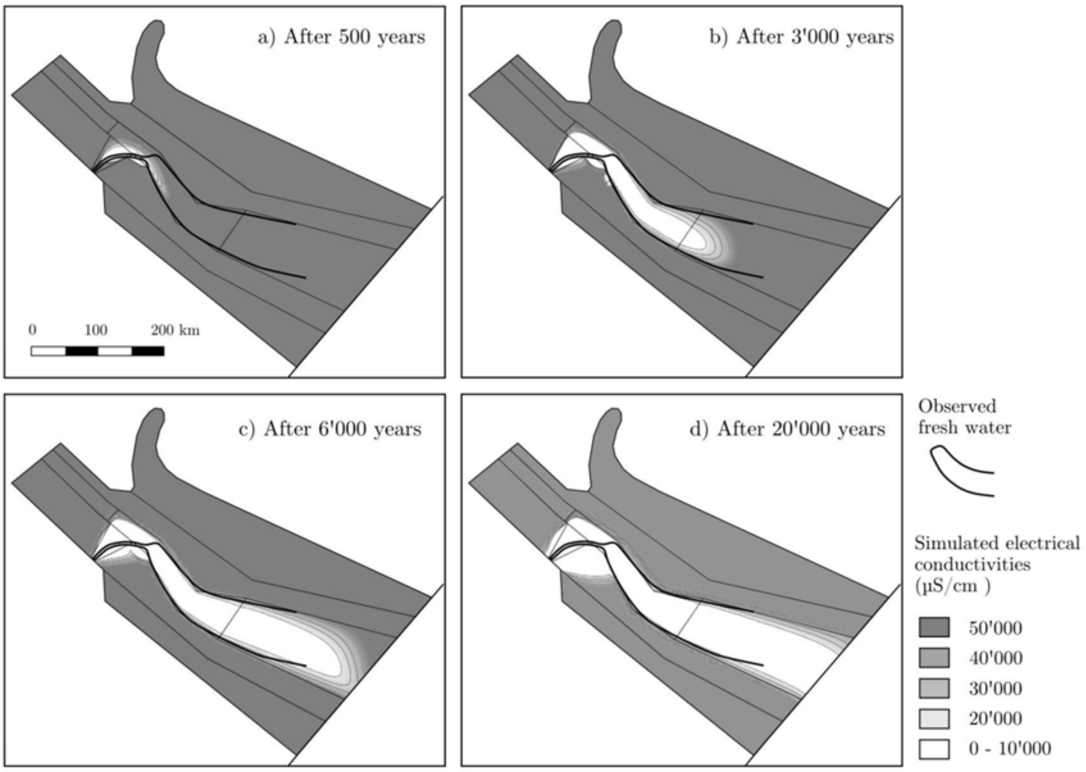

Fig. 5.13: Development of a freshwater lens from a complete saline aquifer. The diffuse recharge rate is five times lower than in the reference model. Salinities are shown for four time steps at a) 500 years, b) 3’000 years), c) 6’000 years and d) 20’000 years.

5.3.3 Sensitivity analysis on the recharge location

As observed above for the transient analysis of the reference model, the freshwater water zones over the Lorian Swamp develop too extensively upstream of the freshwater lens, possibly because of the location of the concentrated recharge and also because of the groundwater gradient north of the Lorian Swamp, which is too much south directed.

This section tests the effect of a different concentrated recharge location and the effect of inter-aquifer recharge west of the Lorian Swamp.

5.3.3.1 Sensitivity analysis on the spatial distribution of concentrated recharge

This model tests a spatial distribution of concentrated recharge, which gives more importance of concentrated recharge to the lower part of the Lorian Swamp, as illustrated in Fig. 5.14.

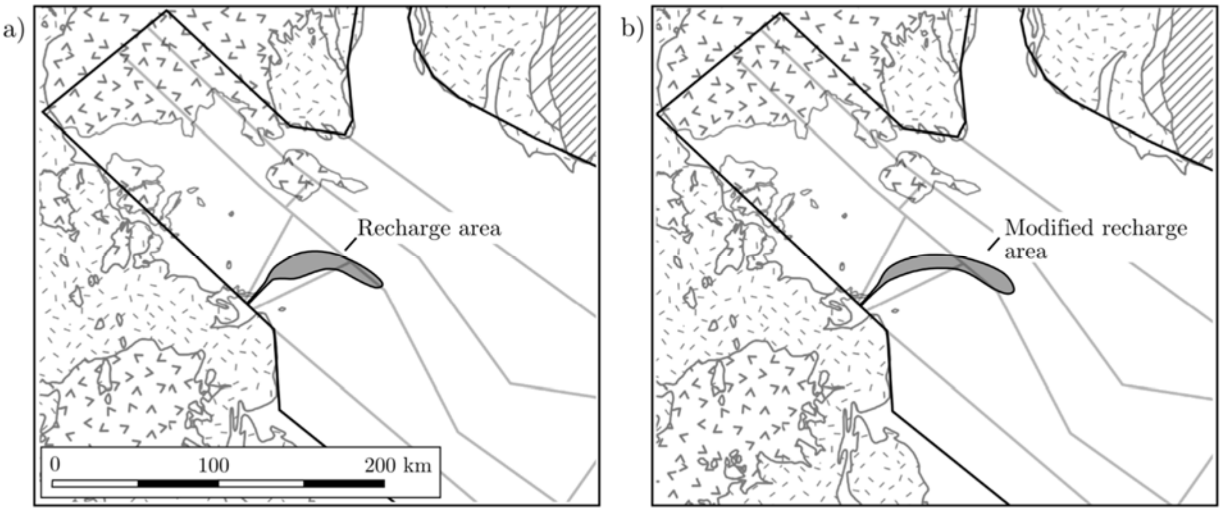

Fig. 5.14: Concentrated recharge area of the reference model (a) and modified concentrated recharge area (b). The modified concentrated recharge give more impact of the concentrated recharge in the lower part of the Lorian Swamp, in order to minimise the development of a freshwater zone around the Lorian Swamp.

This model is calibrated with identical transmissivities along the main aquifer zones (zones A, B and C in Fig. 5.3) as the reference model. However, transmissivities around the main aquifer zones are 20% lower within the lateral zones D, F, G, H and I, and the transmissivity of unit E about 15% lower than the reference model. Compared to the reference model, most of the observation points have similar simulated hydraulic heads (Appendix I), except the points located on the northern border of the domain (unit I in Fig. 5.3), which indicates a higher hydraulic head, due to the lower transmissivity.

For the transient analysis (Fig. 5.15), the evolution of the freshwater lens is very similar to the reference model. This indicates that a small variation of the concentrated recharge location has almost no influence on the development of the freshwater lens.

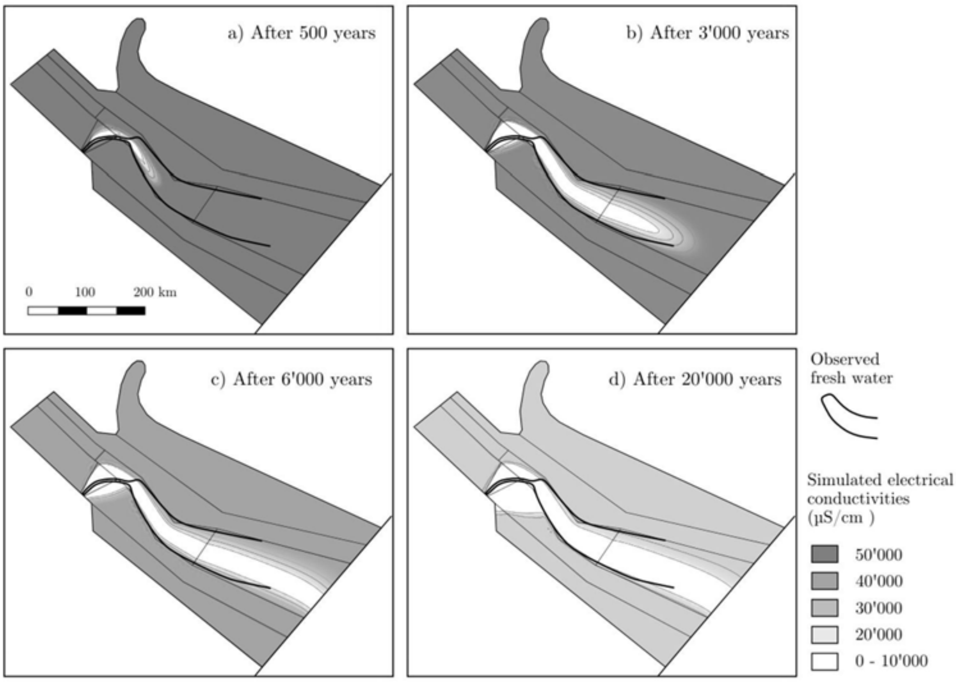

Fig. 5.15: Formation of the freshwater lens from a complete saline aquifer for a model with a modified concentrated recharge spatial distribution, compared to the reference model (see Fig. 5.14). Salinities are shown for four time steps at a) 500 years, b) 3’000 years), c) 6’000 years and d) 20’000 years.

This model indicates that a model with recharge concentrated over the lower part of the Lorian Swamp is possible. This scenario would give more importance to major and rare flood events inundating large surfaces beyond the recurrent inundation surface identified within the concentrated recharge analysis of Chapter 3. In order to satisfy the shape of the freshwater channel over the Lorian Swamp, the concentrated recharge would have to be more located downstream, which is in contradiction with the observation of Chapter 3.

5.3.3.2 Lateral recharge model

In this model, a lateral recharge coming from the surrounding mountains (Fig. 5.16) is tested in order to evaluate the impact of a possible inter-aquifer recharge on the hydraulic heads and on the formation of the freshwater lens. This recharge hypothesis is supported by the high hydraulic head observed at El Dera, which is underestimated in the reference model. This recharge mechanism hypothesis could be explained by the presence of the mountains east of El Dera, which could induce underground water flux toward the Merti aquifer.

Concentrated and diffuse recharge rate of this model are the same as for the reference model, i.e. 260 and 320 x 10^6 m^3/y. The lateral recharge represents an annual recharge rate of 16 x 10^6 m^3/y. The model is calibrated with the same transmissivities as for the reference model (Fig. 5.6). This model yields very similar simulated hydraulic heads as the reference model, except for the El Dera and Madogashe observation points, which are better calibrated than in the reference model (scatter plot is printed in Appendix I).

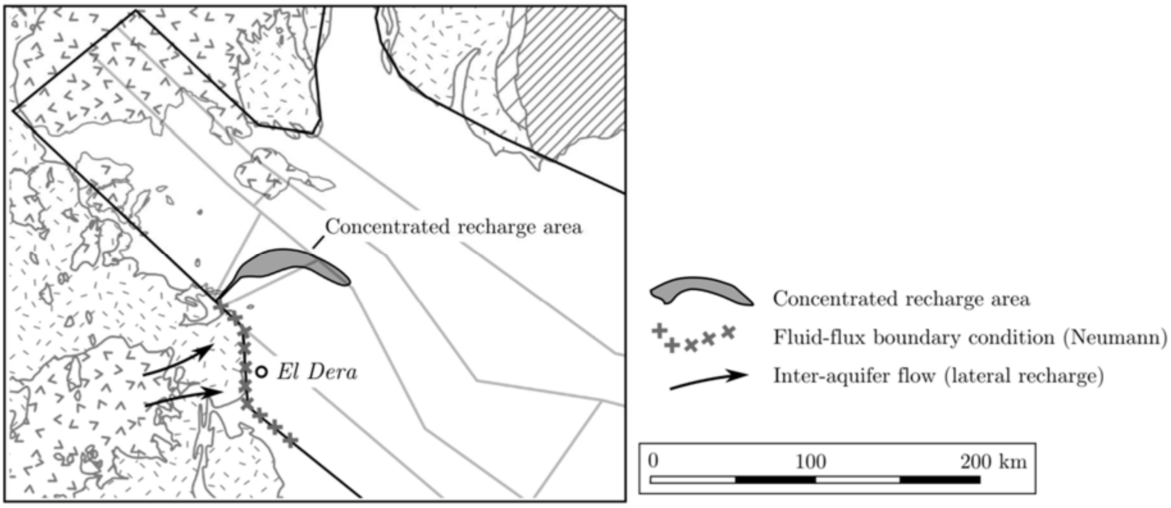

Fig. 5.16: Lateral recharge is simulated with a fluid-flux boundary condition along the western boundary of the model, between the Lorian Swamp and south of El Dera.

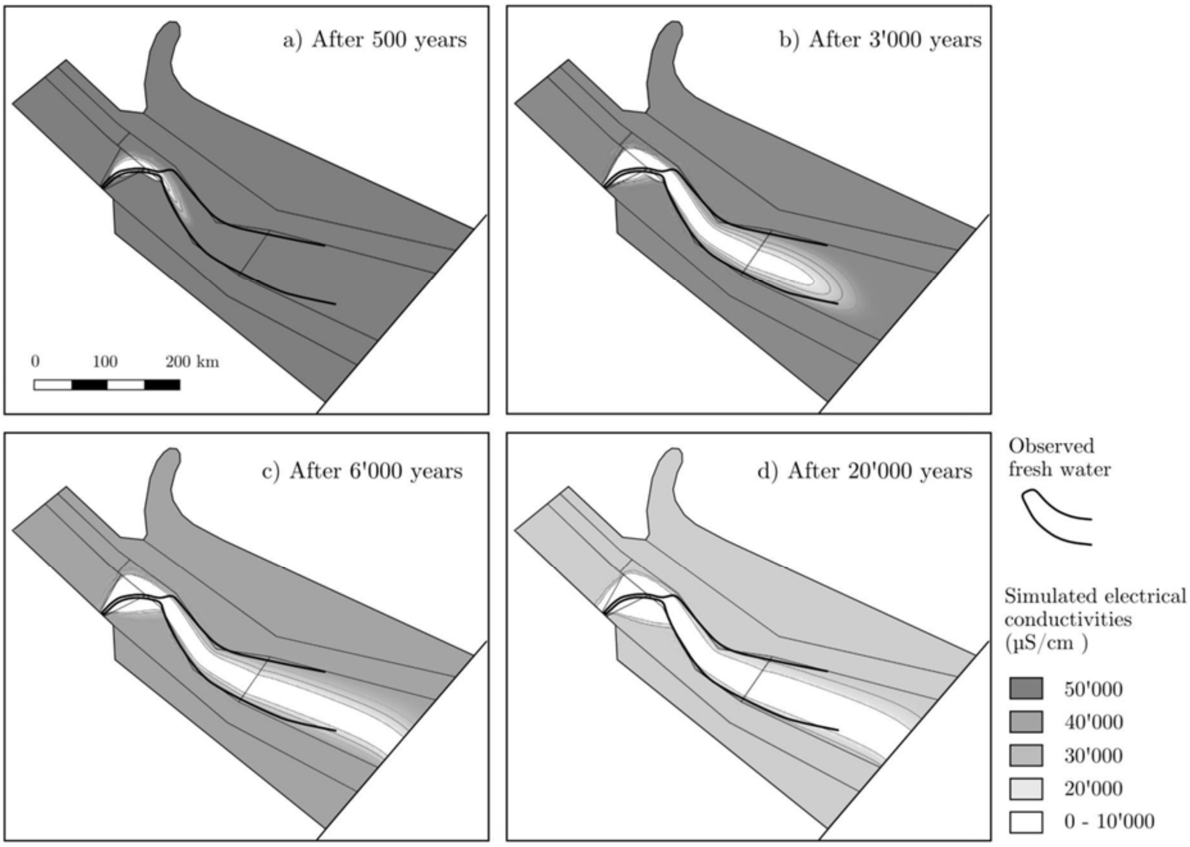

Fig. 5.17: Formation of the freshwater lens from a complete saline aquifer for a model with a lateral recharge (inter-aquifer recharge). Salinities are shown for four time steps at a) 500 years, b) 3'000 years, c) 6'000 years and d) 20'000 years.

The transient analysis of the formation of the freshwater lens from a saline aquifer indicates that this recharge model allows to better constrain the development of the freshwater zone above the freshwater lens (marked with the bold line in Fig. 5.17). Indeed, the better calibration of the hydraulic head at El Dera and at Madogashe (higher hydraulic head compared to the reference model) also modify the hydraulic gradient between the Lorian Swamp and Madogashe, redirecting the groundwater flows towards the main aquifer zone, as illustrated on the piezometric map in Fig. 5.5. This redirection of the flows towards the center of the aquifer allows limiting the propagation of the freshwater zone within the border of the model.

5.4 Conclusion of the regional numerical model

The development of this regional numerical model allowed refining the hypotheses on the Merti aquifer recharge, its location and the relation between the diffuse and concentrated recharge.

The model reproduces the overall groundwater flow of the Merti aquifer. Groundwater levels are mostly well reproduced, except for few observation points on the lateral units of the domain and close to the concentrated recharge area, the Lorian Swamp. For the transient simulation, the concentrated recharge over the Lorian Swamp allows to fairly well reproduce the geometry of the freshwater lens. However, around the Lorian Swamp, a too broad freshwater zone is observed compared to the geometry of the actual groundwater salinity. This feature could be explained by 1) the dispersivity of the model which is too high due to the mesh resolution of the model, which results itself from the large size of the model and 2) by the "rough" parametrisation of the transmissivity zones of the model. As discussed in the description of the model (section 5.3.1.1), because of the lack of precise information of the transmissivity distribution, preference was given to simple assumptions and units geometries in order to avoid an overcalibration of the model.

Other conclusions can be made concerning the study:

The first conclusion is that the diffuse recharge is likely to contribute half (or less) of the total recharge. Despite the conceptual differences between this approach and the synthetic approach of Chapter 4, this observation is consistent with the results of the synthetic model that indicates that the diffuse recharge by precipitation is likely to be lower than 30% of the total recharge. It is interesting to note that, despite the simplifications made within the synthetic model (homogeneous transmissivity, simplified geometry of the aquifer, regional saline flow imposed by boundary conditions), this simplified approach allows to produce consistent results compared to a more complex model as the regional one elaborated in this chapter.

The above analysis was carried out with an average concentrated recharge rate derived from the recharge quantification of Chapter 3 (260 x 10^6 m^3/y) and therefore high transmissivity values compared to those obtained with pumping tests. For such high concentrated recharge rates, the possible diffuse recharge rates range between 0.5 and 4.6 mm/y. Lower diffuse recharge rates are theoretically possible but it remains unlikely compared to diffuse recharge measured in a similar context, as reviewed in section 3.3. Higher diffuse recharge can be excluded because of the dynamics between the freshwater lens and the surrounding water (Fig. 5.12). This range of diffuse recharge rate is consistent with the diffuse recharge rates estimated in Chapter 3 (1 and 5 mm/y)

The second conclusion relates to the difference of transmissivity defined for the model with high concentrated recharge volume and the transmissivity measured in the field. Indeed, for the reference model transmissivity are about 86 times higher than the measured transmissivity. If a lower diffuse recharge rate is considered (1.15 mm/y instead of 2.3 mm/y), the ratio between the measured and simulated transmissivity around Dadaab diminishes to 63 (this ratio does not diminish significantly more for further a lowering of diffuse recharge).

Thus, by extrapolation from the reference model, models calibrated with transmissivity values derived directly from field measurements would imply concentrated and diffuse recharge rates about 86 to 60 times lower, i.e. concentrated recharge between 3.1 and 4.2 x 10^6 m^3/y and diffuse recharge between 0.014 and 0.019 mm/y. These diffuse recharge rates are also evidently too low in comparison to diffuse recharge measured in a similar context (section 3.3).

These observations suggest that the aquifer is thicker than the currently exploited horizon. This hypothesis is supported by the geological description of deep boreholes which indicate a succession of coarse and fine sediments layers (section 2.2), but also by pumping test data interpretation which allowed characterising the currently exploited layer as a leaky aquifer with thick underlying aquifer horizon(s) (Fig. 2.19). However, the thicknesses and the hydraulic conductivities of these underlying layers are not documented and do not allow to define a precise complete transmissivity of the aquifer.

Thirdly, possible inter-aquifer recharge from the mountains west of the Lorian Swamp was pointed out. Even though this inter-aquifer recharge may not be significant compared to the total recharge, it allows to better calibrate the El Dera and Madogashe simulated hydraulic heads, but also to slightly better reproduce the development of the freshwater lens.

Fourthly, this numerical modelling approach highlighted the difficulty to calibrate “a unique” model because of the high uncertainty on the transmissivity values and their spatial distribution, in particular around the Lorian Swamp area. This uncertainty gives a high flexibility to calibration, which is well illustrated by the fact that all the different models derived from the reference model could be calibrated with a quality close to the reference model. The model with a modification of the concentrated recharge location revealed in particular this flexibility and the fact that other locations for concentrated recharge remain possible.

Fifthly, this model also allows to complete the estimation of recharge elaborated during the previous chapters of this study (Fig. 5.18). Based on an average concentrated recharge of 260 x 10^6 m^3/y, the total diffuse recharge over the entire domain is estimated to range between 63 and 630 x 10^6 m^3/y. However, as discussed in previous chapters, the freshwater diffuse recharge should only be considered on the freshwater zones. The diffuse recharge over the rest of the domain is assumed to contribute to the general flow of the aquifer but not as freshwater recharge. Thus, the range of diffuse recharge to be considered diminishes to 5.8 and 58 x 10^6 m^3/y (respectively 0.46 and 4.6 mm/y). If the complete range of concentrated recharge is considered (195 to 329 x 10^6 m^3/y), the range of diffuse recharge is extended to 4.3 to 43 x 10^6 m^3/y for a concentrated recharge of 195 x 10^6 m^3/y and to 7.3 to 73 x 10^6 m^3/y for a concentrated recharge of 329 x 10^6 m^3/y, leading to a total freshwater recharge ranging between 199 and 402. With this same approach, the diffuse recharge over the rest of the domain is extrapolated between 43 and 725 x 10^6 m^3/y.

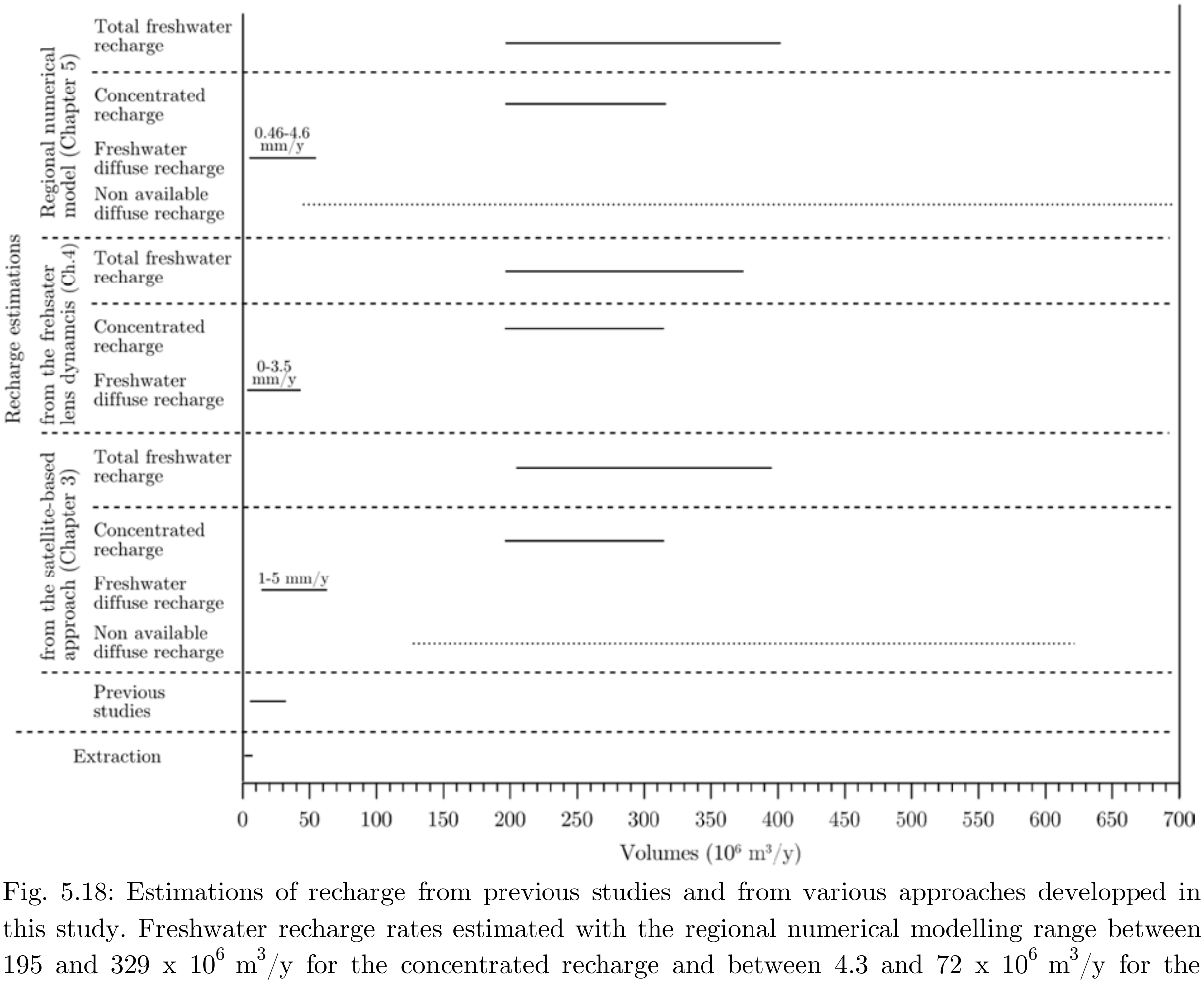

Fig. 5.18: Estimations of recharge from previous studies and from various approaches developped in this study. Freshwater recharge rates estimated with the regional numerical modelling range between 195 and 329 x 10^6 m^3/y for the concentrated recharge and between 4.3 and 72 x 10^6 m^3/y for the diffuse recharge (0.46 to 4.6 in vertical rate). Total freshwater recharge ranges between 199 and 402 x 10^6 m^3/y. The diffuse recharge out of the freshwater lens region amounts to 43 and 725 x 10^6 m^3/y.

These results of recharge are within the ranges of recharge quantified in Chapter 3 and Chapter 4. The estimation of 1 to 5 mm/y defined in Chapter 3 is a central estimation leading to diffuse recharge estimation ranging between 12 and 62 x 10^6 m^3/y. Thus, an intermediate total freshwater recharge is estimated between 207 and 391 x 10^6 m^3/y.

Finally, as already discussed in previous chapters, these volumes require adopting a model with a multi-layer aquifer as illustrated in Fig. 2.19 and to consider that most of the groundwater recharge does not flow through the exploited horizon (the Merti beds) but in underlying layers which are difficult to exploit and whose salinity is not documented.

These conclusions and hypothesis are summarised in the Fig. 5.19 below.

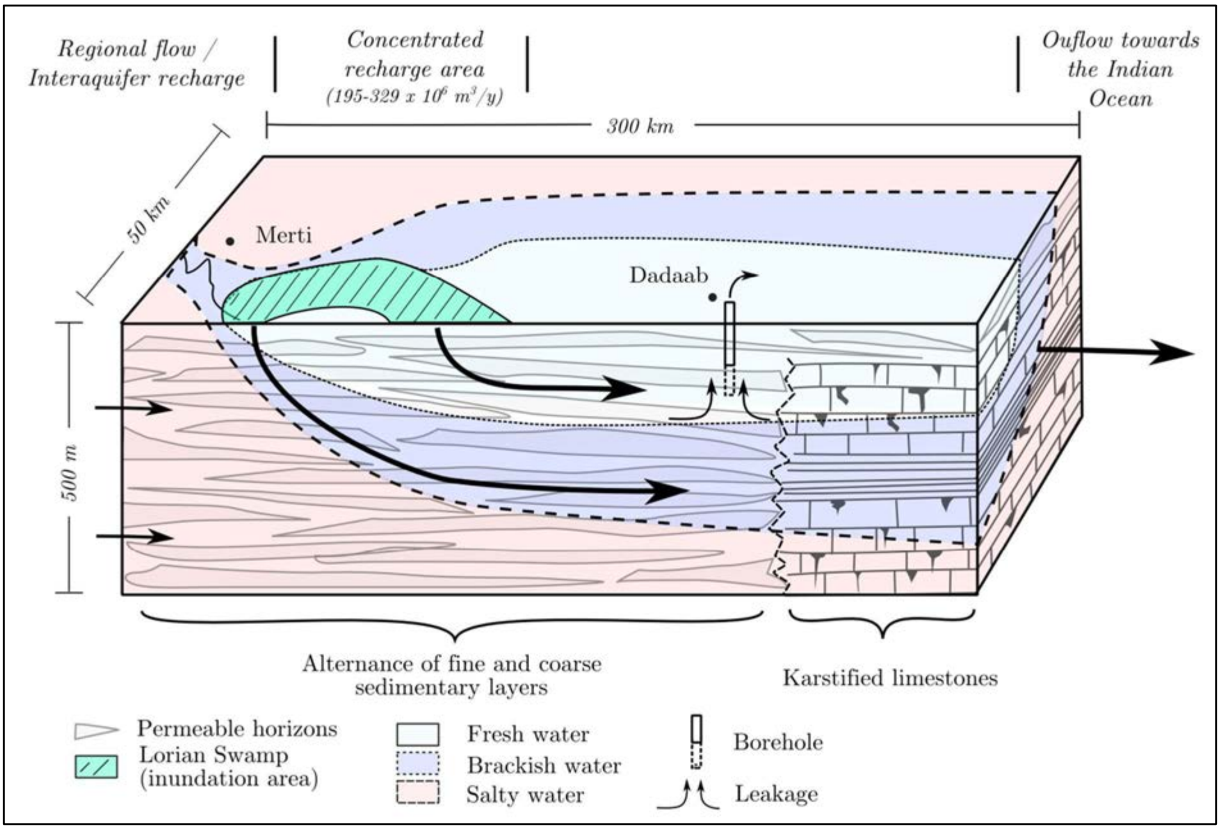

Fig. 5.19: Conceptual model of the Merti aquifer system. The Merti aquifer consists in a succession of fine and coarse sedimentary layers, where the Merti beds are only the upstream horizon. Freshwater recharge occurs mainly as concentrated recharge over the Lorian Swamp area (between 195 and 329 x 10^6 m^3/y). From this location, the freshwater lens develops in width and thickness. Part of this freshwater recharge is diluted with the surrounding brackish and salty water. Regional flow is induced by diffuse recharge over the entire domain (1 to 5 mm/y, corresponding to 136 to 681 x 10^6 m^3/y) and possible inter-aquifer recharge. The diffuse recharge contributing to the freshwater lens is estimated between 12 and 62 x 10^6 m^3/y. Close to the Indian Ocean, the karstified limestones reduce considerably the hydraulic gradient between Dadaab and the Ocean (0.1‰).

This figure also illustrates the limitation of the risk of upconing of saline water because of the "buffer" effect of the freshwater contained in the underlying layers. Indeed, as previously discussed, the recharge estimation carried out within this study suggests that fresh water could be found in deeper horizons than the Merti beds and that brackish/saline water is not directly present below the Merti beds. However, this hypothesis needs to be confirmed by deeper boreholes in order to ensure the low risk of upconing.

Chapter 6

Conclusions, perspectives and recommendations

6.1 Main results

This thesis followed three main objectives. The central objective was related to the humanitarian situation of the Dadaab refugee camp. It aims to assess the sustainability of the Merti aquifer under the increasing groundwater extraction related to the development of the camp. This implies avoiding a groundwater level depletion and an increase of the salinity by upconing from the saline water surrounding the freshwater lens. The two secondary objectives result from the particular characteristics of the Merti aquifer: the development of a comprehensive approach for the quantification of recharge of mega-aquifers in semi-arid to arid regions; and a better understanding of the dynamics of freshwater lenses in a continental context. These two second objectives aimed to better understand the Merti aquifer and could also be applied to other aquifers in similar contexts.

The work carried out during this study allowed to conclude that, under the current exploitation regime, the risks of groundwater salinisation by upconing and water level depletion are limited on the regional scale. This conclusion is based, on one hand, on the quantification of the groundwater recharge volumes which have been estimated being between 50 to 100 times higher than the extraction rates. On the other hand, the aquifer revealed to have a very great inertia that led to very small changes in water levels (less than 1 m since 1994) and water quality since the beginning of the intensive exploitation due to the establishment of the Dadaab refugee camp.

However, on the smaller scale, risk of salinisation of boreholes remains critical due to the presence of brackish/saline water around and below the freshwater lens. Thus, effort should be maintained in monitoring, particular at the camps located close to the brackish water transition (e.g. Hagadera).

These results were obtained by developing new approaches for quantifying the concentrated groundwater recharge and by characterising the dynamics of continental freshwater lenses with numerical modelling. In parallel, a network of twenty groundwater monitoring devices was successfully installed and used in order to monitor continuously the water levels and electrical conductivities of the Merti aquifer since September 2013. This network served to observe the dynamics of the aquifer and to cross-validate the results of numerical modelling.

Quantification of recharge

The methodology developed in this study for quantifying the groundwater recharge relied on the combination of inundation surfaces derived from satellite images and coupled surface/groundwater flow numerical modelling. This methodology allowed to establish that most of the groundwater recharge occurs by ponding over the Lorian Swamp, during periodical inundations events generated by the intermittent Ewaso Ng'Iro River. This concentrated recharge was quantified between 195 and 329 x 10^6 m^3/y, corresponding to about 20 mm/y over the entire freshwater lens.

In contrast to this, the diffuse recharge occurring over the rest of the domain was estimated between 1 and 5 mm/y (up to 20 % of the total recharge). Cumulated over the freshwater lens surface, these diffuse recharge rates correspond to an annual freshwater recharge volume ranging between 12 and 62 x 10^6 m^3/y. Thus the total average annual recharge of the Merti aquifer ranges between 207 and 391 x 10^6 m^3/y, while the groundwater abstraction is estimated around 4.8 x 10^6 m^3/y.

This analysis also allowed to characterise the temporal dynamics of the recharge and its statistical distribution. It was especially observed that the groundwater recharge by event follows a linear relation with the discharge volume of the Ewaso Ng'Iro River during the inundation events. Furthermore, the statistical analysis of the river discharge rate revealed that flood events which are responsible for half of the groundwater recharge have, according to the chosen statistical models, a return period greater than 2.9 and 6.7 years, respectively.

Characterisation of a multi-layer aquifer

However, the groundwater recharge volume obtained with this approach revealed a great discrepancy when compared with the measured transmissivity over the Merti aquifer. Indeed, the transmissivity required to accommodate an average concentrated recharge of 260 x 10^6 m^3/y and an average total diffuse recharge of 29 x 10^6 m^3/y (2.3 mm/y) is 2.4 m^2/s while the maximum transmissivities measured in the Merti beds are about 80 times lower.

This observation led to the conclusion that the Merti aquifer is an aquifer system not only composed of the currently exploited horizon of the Merti beds but most likely a multi-layer aquifer composed of several productive layers. This hypothesis is supported by the analysis of the geology that indicates a succession of several fine and coarse layers of sediments (section 2.2) deposited within the Anza graben. Pumping test analyses carried out at the Dagahaley BH 3 borehole-old (section 2.3.5) also suggests the presence of underlying productive layers leaking into the exploited horizon during pumping (leakage).

Electrical conductivity and groundwater levels time series also revealed the very high inertia of the system and the rather low impact of pumping on the groundwater quality and levels since the 1990s, beginning of the intensive exploitation of the aquifer. Finally, from a geometrical point of view, the great length and width of the aquifer suggests that, due to the effect of dispersion and diffusion, the freshwater layer should be thicker than 40 m in order to remain fresh over a distance of 200 km.

Furthermore, even though this study suggests a thicker aquifer system, its exact thickness and the distribution of the salinity below the exploited horizon remain unknown.

Freshwater lens dynamics and groundwater monitoring

The investigations on the freshwater lens dynamics allowed to better understand the relation between the freshwater lens geometry and the recharge mechanisms. In particular, the analysis with synthetic models supports the observation obtained with the remote sensing approach of concentrated recharge mainly located over the beginning of the freshwater lens and partly along the axis of the lens (section 4.4). The transient analysis carried out with the synthetic model after initiating a pumping allowed to reveal the very high inertia of the aquifer. The numerical approach for quantifying the freshwater lens dynamics of the Merti aquifer gave a consistent proportion of diffuse vs concentrated recharge compared to the remote sensing approach, with a proportion of diffuse recharge up to 20 %.

The operational aspects of this study confirmed the high importance to record reliable, precise and long term groundwater observations. Despite the challenging installation and maintenance conditions, the network of twenty monitoring devices installed over the central part of the Merti aquifer at the beginning of this study gave very valuable information. It allowed in particular to characterise on a multi time-scale (daily and annual) the dynamics of the aquifer, confirming the very high inertia of the system. This type of monitoring network also gives unavoidable information for the day-to-day and long term management of the groundwater, in particular by allowing to foresee groundwater quality changes or groundwater level depletion.

6.2 Sustainability of the management of the Merti aquifer

On the scale of the Merti aquifer, the difference between the extraction and the recharge estimation (about 2 orders of magnitude) suggests that the current exploitation of the groundwater resource of the Merti aquifer is sustainable. However, the vertical structure of the aquifer system, composed of several supposed superimposed water-productive layers and the presence of saline and brackish water surrounding the freshwater, requires to consider with care the availability of the groundwater. Indeed, only the first level of the aquifer system, the so-called Merti beds, is clearly identified and documented with hydrodynamic and groundwater quality (salinity) characteristics. Thus, as long as a better hydrodynamic and water quality characterisation of the entire aquifer system is not conducted, only the flow within the Merti beds should be considered as available. This flow is estimated between 5 and 8 x 10^6 m^3/y, which could be critical compared to the extraction of 4.8 x 10^6 m^3/y.

This concern is confirmed by the evolution of the electrical conductivity at the boreholes. Even though the water levels and electrical conductivities observed through the monitoring network show a general high stability on the aquifer scale (see section 2.3.7), some significant increase of the salinity (for instance between 50 and 100 µS/cm at Hagadera) imply that risks of salinisation from the underlying layers of the aquifer system (upconing) remain possible.

Thus, despite the "buffer" effect of the probable underlying freshwater, the uncertainty on the depth of the vertical transition between the fresh and the brackish water requires to adopt a precautionary approach for the groundwater exploitation in order to avoid a well salinisation by upconing. Furthermore, it is recommended to maintain the monitoring of the groundwater in order to observe the evolution of the groundwater quality and level, as well to serve as early alert system.

In order to limit these risks, it is suggested to adopt the following recommendations:

- Encourage the exploitation of the aquifer toward the center instead of the limit of the freshwater lens. Thus, from a hydrogeological point of view, any development of the camp should be oriented toward the north and not toward Hagadera (limit of the freshwater lens).
- Drill groundwater prospection boreholes below the currently exploited level (up to 300-350 m) in order to estimate the quality of deeper groundwaters and the hydraulic conductivity of underlying productive beds. Such boreholes may be exploited if the electrical conductivity is close to the values of the upper exploited horizon.
- Electrical conductivity should be monitored on the sensible boreholes (close to the brackish transition or deep boreholes) in order to identify any risk of well salinisation. If such risks are observed at a borehole (significant increase of the electrical conductivity by several 100 µS/cm and acceleration of this increase), pumping should be stopped.

6.3 Perspectives for further research

This research work allowed to quantify and better understand the recharge and the dynamics of the Merti aquifer. However, some parts of this work need further investigations in order to reduce the uncertainties. This work also opens further perspectives that are discussed below.

Firstly, the uncertainty on the quantification of the concentrated recharge could be improved with the following suggestions:

- A refining of the digital elevation model in order to make possible the "injection" of the river discharge at the gauging station of Archer's Post.
- As observed with the analysis of the flood events (section 3.4.1.7), central zones of the inundation surfaces are likely to be more permeable then areas less frequently

inundated. This observation may allow to build a model with a spatial permeability heterogeneity, instead of adjusting the ground conductance (C_g) for each event.

- A validation of the delimitation of the inundated surface derived from MODIS products with other remote or ground-based methods (radar, multispectral embarked camera on drones, ground observations).

Secondly, a cross-validation of the groundwater recharge quantification with other methods would allow to validate this new methodology. This cross-validation could be carried out by using this same methodology on similar sites where the groundwater recharge is known or could be easily estimated, or on the Merti aquifer site itself.

Cross-validation of the groundwater recharge of the Merti aquifer can be made by applying classical groundwater recharge methods as reviewed by Scanlon et al. (2002) but also by defining more precisely the transmissivity of the aquifer and its underflow. This could be done by drilling deeper exploration boreholes (about 300-400 m deep) at few places, for instance at Dadaab and Habaswein, and by carrying out pumping tests in order to obtain the transmissivity.

Additionally to deeper boreholes drilling, but less expensive, state-of-the-art pumping tests carried out during a long period (several days) and the interpretation of the data with advanced analytical tools could allow to confirm, and possibly better characterise, this postulated multi-layer aquifer system.

Another way to quantify the recharge of the Merti aquifer would be to install high time-resolution monitoring devices in locations very close to the recharge areas in order to measure directly the change of groundwater level after inundation events. Locations around Sericho would be well suited because it is the centre of the recurrent inundated areas and also because this region has a thinner unsaturated zone, about 20 m thick.

Thirdly, the future evolution of the groundwater recharge of the Merti aquifer system could be better characterised, considering: 1) the impact of climate change over the Merti aquifer region and over the Ewaso Ng'Iro catchment; 2) the effect of increasing surface water extraction in the Ewaso Ng'Iro catchement due to irrigation and population increase.

At first, as identified by de Leeuw *et al.* (2012), the increase of surface water extraction in the Ewaso Ng'Iro catchment led to a dramatic increase of the number of days per year with very low discharge rate at Archer's Post. However, as identified within this study, the recharge of the Merti aquifer depends on the frequency of intermediate to extreme inundation events which seem not to be, or almost not, perturbed by surface water use so far. Nevertheless, the impact of increasing water consumption by the population and irrigation in this basin need to be confirmed in order to define the best water use policy.

Then, the understanding of the future evolution of the Merti aquifer also needs to consider the climate change over the area that could have impact on both diffuse and concentrated recharge. Pulido-Velazquez *et al.* (2015) and Taylor *et al.* (2013) discussed the effect of climate change and El Niño Southern Oscillation (ENSO) on groundwater recharge in arid and semi-arid regions. They pointed out that for the same average annual rainfall, climate change is likely to increase the groundwater recharge because of the higher variability in rainfall, leading to more numerous extreme events. However, predictions are difficult to elaborate because of the uncertainty on the local climate evolution.

Finally, the water of the Merti aquifer have been coveted recently for the supply of the city of Wajir, which would imply drilling new boreholes within the area of Habaswein. Before starting large groundwater extraction projects, such as the Wajir-project, or possible large-scale irrigation projects, it is strongly recommended to better characterise the aquifer as proposed above, especially by investigating the aquifer thickness. In parallel to this, it is also highly recommended to maintain the groundwater monitoring system used for this research, but also to reinforce the monitoring of the rainfall over the area in order to have precise data of this parameter that could be compared with the FEWS-Net data. As basic information needed for the understanding of the Lorian Swamp hydrology and the Merti aquifer, it is also crucial to rehabilitate the gauging station of the Ewaso Ng'Iro at Archer's Post.

Chapter 7

References

Anderson, E.K., Brakenridge, G.R., 2006. DFO Event # 2006-203 Kenya and Somalia - Lach Dera River - Rapid response inundation Map 5 [WWW Document]. URL http://www.dartmouth.edu/~floods/2006210and203.html

Arnold, R.T., 1952. Lorian Swamp Ground Water Investigation. Nairobi, Kenya.

Bauer, P., Held, R.J., Zimmermann, S., Linn, F., Kinzelbach, W., 2006. Coupled flow and salinity transport modelling in semi-arid environments: The Shashe River Valley, Botswana. J. Hydrol. 316, 163–183. doi:10.1016/j.jhydrol.2005.04.018

Bauer, P., Thabeng, G., Stauffer, F., Kinzelbach, W., 2004. Estimation of the evapotranspiration rate from diurnal groundwater level fluctuations in the Okavango Delta, Botswana. J. Hydrol. 288, 344–355. doi:10.1016/j.jhydrol.2003.10.011

Bosworth, W., Morley, C.K., 1994. Structural and stratigraphic evolution of the Anza rift, Kenya. Tectonophysics 236, 93–115. doi:10.1016/0040-1951(94)90171-6

Brotzu, P., Morbidelli, L., Nicoletti, M., Piccirillo, E., Traversa, G., 1984. Miocene to Quaternary volcanism in eastern Kenya: sequence and geochronology. Tectonophysics 101, 75–86.

Brunner, P., Cook, P.G., Simmons, C.T., 2011. Disconnected surface water and groundwater: from theory to practice. Ground Water 49, 8. doi:10.1111/j.1745-6584.2010.00752.x

Brunner, P., Franssen, H.J.H., Kgotlhang, L., Bauer-Gottwein, P., Kinzelbach, W., 2007. How can remote sensing contribute in groundwater modeling? Hydrogeol. J. 15, 5–18. doi:DOI 10.1007/s10040-006-0127-z

Brunner, P., Simmons, C.T., 2012. HydroGeoSphere: A Fully Integrated, Physically Based Hydrological Model. Ground Water 50, 170–176. doi:10.1111/j.1745-6584.2011.00882.x

Butler, M.J., Verhagen, B.T., 2001. Isotope studies of a thick unsaturated zone in a semi-arid area of Southern Africa.

Campos, J.C., Sillero, N., Brito, J.C., 2012. Normalized difference water indexes have dissimilar performances in detecting seasonal and permanent water in the Sahara–Sahel transition zone. J. Hydrol. 464-465, 438–446. doi:10.1016/j.jhydrol.2012.07.042

Carbonneau, P., Piégay, H., 2012. Fluvial remote sensing for science and management. John Wiley & Sons, Chichester, West Sussex. doi:10.1002/9781119940791

Cartwright, I., Weaver, T.R., Simmons, C.T., Fifield, L.K., Lawrence, C.R., Chisari, R., Varley, S., 2010. Physical hydrogeology and environmental isotopes to constrain the age, origins, and stability of a low-salinity groundwater lens formed by periodic river recharge: Murray Basin, Australia. J. Hydrol. 380, 203–221. doi:10.1016/j.jhydrol.2009.11.001

Cendón, D.I., Larsen, J.R., Jones, B.G., Nanson, G.C., Rickleman, D., Hankin, S.I., Pueyo, J.J., Maroulis, J., 2010. Freshwater recharge into a shallow saline groundwater system, Cooper Creek floodplain, Queensland, Australia. J. Hydrol. 392, 150–163. doi:10.1016/j.jhydrol.2010.08.003

Cheng, A., 2004. Coastal aquifer management monitoring, modeling, and case studies.

Christoffersen, B.O., Restrepo-Coupe, N., Arain, M.A., Baker, I.T., Cestaro, B.P., Ciais, P., Fisher, J.B., Galbraith, D., Guan, X., Gulden, L., van den Hurk, B., Ichii, K., Imbuzeiro, H., Jain, A., Levine, N., Miguez-Macho, G., Poulter, B., Roberti, D.R., Sakaguchi, K., Sahoo, A., Schaefer, K., Shi, M., Verbeeck, H., Yang, Z.-L., Araújo, A.C., Kruijt, B., Manzi, A.O., da Rocha, H.R., von Randow, C., Muza, M.N., Borak, J., Costa, M.H., Gonçalves de Gonçalves, L.G., Zeng, X., Saleska, S.R., 2014. Mechanisms of water supply and vegetation demand govern the seasonality and magnitude of evapotranspiration in Amazonia and Cerrado. Agric. For. Meteorol. 191, 33–50. doi:10.1016/j.agrformet.2014.02.008

De Leeuw, J., Said, M., Kifugo, S., Musyimi, Z., Mutiga, J., Peden, D., 2012. Benefits of Riverine Water Discharge into the Lorian Swamp, Kenya. Water 4, 1009–1024. doi:10.3390/w4041009

De Vries, J.J., Selaolo, E.T., Beekman, H.E., 2000. Groundwater recharge in the Kalahari, with reference to paleo-hydrologic conditions. J. Hydrol. 238, 110–123. doi:10.1016/S0022-1694(00)00325-5

Diersch, H.-J. g., 2014. FEFLOW: Finite Element Modeling of Flow, Mass and Heat Transport in Porous and Fractured Media » E-books PDF, 1st ed. Springer-Verlag Berlin Heidelberg. doi:10.1007/978-3-642-38739-5

Earth Water Ltd, 2012. Merti Aquifer Study, Northern Kenya - Aquifer investigation. Kenya.

Edmunds, W., 2001. Investigation of the unsaturated zone in semi-arid regions using isotopic and chemical methods and applications to water resource problems. Isot. Assess. Groundw. Renew. ....

Edmunds, W.M., 2010. Conceptual models for recharge sequences in arid and semi-arid regions using isotopic and geochemical methods, in: Wheater, H.S., Mathias, S.A., Li, X. (Eds.), Groundwater Modelling in Arid and Semi-Arid Areas. Cambridge University Press, Cambridge, pp. 21–38. doi:10.1017/CBO9780511760280

Essaid, H.I., 1990. A multilayered sharp interface model of coupled freshwater and saltwater flow in coastal systems: Model development and application. Water Resour. Res. 26, 1431–1454. doi:10.1029/WR026i007p01431

Essink, G.H.P.O., 2001. Salt Water Intrusion in a Three-dimensional Groundwater System in The Netherlands: A Numerical Study. Transp. Porous Media 43, 137–158. doi:10.1023/A:1010625913251

Gachanja, A., Tole, M., 2002. Management of Ground Water Resources of The Merti Aquifer Preliminary report. Nairobi.

Gao, B., 1996. NDWI—A normalized difference water index for remote sensing of vegetation liquid water from space. Remote Sens. Environ. 58, 257–266. doi:10.1016/S0034-4257(96)00067-3

Gheith, H., Sultan, M., 2002. Construction of a hydrologic model for estimating Wadi runoff and groundwater recharge in the Eastern Desert, Egypt. J. Hydrol. 263, 36–55.

GIBB Ltd, 2004. Study of the Merti aquifer, Final report. Unicef, Shell/BP Hause, Harambee Avenue.

Greene, L.C., Richards, D.R., Johnson, R.A., 1991. Crustal structure and tectonic evolution of the anza rift, northern Kenya. Tectonophysics 197, 203–211. doi:10.1016/0040-1951(91)90041-P

Hantush, M.S., Jacob, C.E., 1955. Non-steady radial flow in an infinite leaky aquifer. Trans. Am. Geophys. Union 36, 95. doi:10.1029/TR036i001p00095

Harrington, G., Cook, P., Herczeg, A., 2002. Spatial and temporal variability of ground water recharge in central Australia: a tracer approach. Groundwater.

Healy, R., Cook, P., 2002. Using groundwater levels to estimate recharge. Hydrogeol. J. Volume 10, pp 91–109. doi:10.1007/s10040-001-0178-0

Healy, R.W., 2010. Estimating Groundwater Recharge. Cambridge University Press, Cambridge.

Hendrie, D.B., Kusznir, N.J., Morley, C.K., Ebinger, C.J., 1994. Cenozoic extension in northern Kenya: a quantitative model of rift basin development in the Turkana region. Tectonophysics 236, 409–438. doi:10.1016/0040-1951(94)90187-2

Ingraham, N.L., Matthews, R.A., 1988. Fog drip as a source of groundwater recharge in northern Kenya. Water Resour. Res. 24, 1406–1410. doi:10.1029/WR024i008p01406

Jackson, T., 2002. Remote sensing of soil moisture: implications for groundwater recharge. Hydrogeol. J. 10, 40–51. doi:10.1007/s10040-001-0168-2

Jordan, P.R., 1977. Streamflow Transmission Losses In Western Kansas. J. Hydraul. Div. 103, 905–919.

Karimi, P., Bastiaanssen, W.G.M., 2014. Spatial evapotranspiration, rainfall and land use data in water accounting – Part 1: Review of the accuracy of the remote sensing data. Hydrol. Earth Syst. Sci. Discuss. 11, 1073–1123.

Key, R., Rop, B., Rundle, C., 1987. The development of Late Cenozoic alkali basaltic Marsabit Shield Volcano, northern Kenya. J. African Earth Sci. 6, 475–491.

King, E.A., Niel, T.G. van, Kijk, A.I.J.. van, Wang, Z., Paget, M.J., Raupach, T., Gueschman, J., Haverd, V., McVicar, T.R., Miltenburg, I., Raupach, M.R., Renzullo, L.J., Zhang, Y., 2011. Actual Evapotranspiraiton Estimates for Australia Inter-comparison and Evaluation.

Lane, I., 1995. A Preliminary Assessment of the Hydrogeology and Hydrochemistry of the Merti Aquifer (North Eastern Province, Kenya: and Lower Juba. Somalia.

Laws, K., Janowiak, J., Huffman, G., 2003. Verification of rainfall estimates over Africa using RFE, NASA MPA-RT, and CMORPH. AGU Fall Meet.

Lerner, D.N., 1997. Groundwater Recharge, in: Saether, O., de Caritat, P. (Eds.), Geochemical Processes, Weathering and Groundwater Recharge in Catchments. AA Balkema, Rotterdam, pp. 109–150.

Lerner, D.N., Issar, A., Simmers, I., 1990. Groundwater Recharge: A Guide to Understanding and Estimating Natural Recharge. Heise.

Matgen, P., Schumann, G., Henry, J.-B., Hoffmann, L., Pfister, L., 2007. Integration of SAR-derived river inundation areas, high-precision topographic data and a river flow model toward near real-time flood management. Int. J. Appl. Earth Obs. Geoinf. 9, 247–263. doi:10.1016/j.jag.2006.03.003

Mays, L.W., 2010. Water Resources Engineering, 2 edition. ed. Wiley.

Mc Feeters, S.K., 1996. The use of the Normalized Difference Water Index (NDWI) in the delineation of open water features. Int. J. Remote Sens. 17, 1425–1432. doi:10.1080/01431169608948714

McMahon, P., Dennehy, K., 2003. Water movement through thick unsaturated zones overlying the central High Plains aquifer, southwestern Kansas, 2000-2001.

Milnes, E., 2010. Hydrogeological field mission in the Dadaab refugee camps (north eastern Kenya). CHYN, Neuchâtel.

Milnes, E., Meilhac, C., Yeo, D., Renard, P., Hunkeler, D., Schnegg, P., Bourret, F., 2006. Hydrogeochemical and hydrogeological investigation in the Akrotiri aquifer: identification of multiple salinisation processes and implementation criteria for monitoring networks, in: Proceeding of the 1st SWIM-SWICA Conference. Cagliary, pp. 229–238.

Milnes, E., Renard, P., 2004. The problem of salt recycling and seawater intrusion in coastal irrigated plains: an example from the Kiti aquifer (Southern Cyprus). J. Hydrol. 288, 327–343. doi:10.1016/j.jhydrol.2003.10.010

Morin, E., Grodek, T., Dahan, O., Benito, G., Kulls, C., Jacoby, Y., Langenhove, G. Van, Seely, M., Enzel, Y., 2009. Flood routing and alluvial aquifer recharge along the ephemeral arid Kuiseb River, Namibia. J. Hydrol. 368, 262–275. doi:10.1016/j.jhydrol.2009.02.015

Mu, Q.Z., Zhao, M.S., Running, S.W., 2011. Improvements to a MODIS global terrestrial evapotranspiration algorithm. Remote Sens. Environ. 115, 1781–1800. doi:DOI 10.1016/j.rse.2011.02.019

Mundorff, M.J., Swarzenski, W.V., 1970. Report on drilling in the North Eastern Province by the 521st Specialist team, R.E. Phase II,.

Nagler, P.L., Glenn, E.P., Kim, H., Emmerich, W., Scott, R.L., Huxman, T.E., Huete, A.R., 2007. Relationship between evapotranspiration and precipitation pulses in a semiarid rangeland estimated by moisture flux towers and MODIS vegetation indices. J. Arid Environ. 70, 443–462. doi:10.1016/j.jaridenv.2006.12.026

Neuman, S.P., Witherspoon, P.A., 1969. Applicability of Current Theories of Flow in Leaky Aquifers. Water Resour. Res. 5, 817–829. doi:10.1029/WR005i004p00817

Nyagah, K., 1995. Stratigraphy, Depositional History and Environments of Deposition of Cretaceous through Tertiary Strata in the Lamu Basin, Southeast Kenya and Implications for Reservoirs for Hydrocarbon Exploration. Sediment. Geol. 96, 43–71.

Ochieng, W.O., 2009. Comparative study of performance of satellite derived rainfall estimates. University of Dar es Salaam.

Ordoyne, C., Friedl, M.A., 2008. Using MODIS data to characterize seasonal inundation patterns in the Florida Everglades. Remote Sens. Environ. 112, 4107–4119. doi:10.1016/j.rse.2007.08.027

Pearson, F.J., Swarzenski, W. V, 1974. Carbon-14 evidence for the origin of arid region ground water, in: ISOTOPE TECHNIQUES IN GROUNDWATER HYDROLOGY Vol. II, IAEA/SM-182-22. pp. 95–110.

Pulido-Velazquez, D., García-Aróstegui, J.L., Molina, J.-L., Pulido-Velazquez, M., 2015. Assessment of future groundwater recharge in semi-arid regions under climate change scenarios (Serral-Salinas aquifer, SE Spain). Could increased rainfall variability increase the recharge rate? Hydrol. Process. 29, 828–844. doi:10.1002/hyp.10191

Ramoelo, A., Majozi, N., Mathieu, R., Jovanovic, N., Nickless, A., Dzikiti, S., 2014. Validation of Global Evapotranspiration Product (MOD16) using Flux Tower Data in the African Savanna, South Africa. Remote Sens. 6, 7406–7423. doi:10.3390/rs6087406

Reeves, C. V., Karanja, F.M., Macleod, I.N., 1987. Geophysical evidence for a failed Jurassic rift and triple junction in Kenya. Earth Planet. Sci. Lett. 81, 299–311.

Renard, P., Glenz, D., Mejias, M., 2009. Understanding diagnostic plots for well-test interpretation. Hydrogeol. J.

Rop, B.K., 2011. Petroleum potential of NW-Kenya Rift Basins : A synopsis of evidence and issues [WWW Document]. Pet. Geol. Forum.

Salama, R.B., Tapley, I., Ishii, T., Hawkes, G., 1994. Identification of areas of recharge and discharge using Landsat-TM satellite imagery and aerial photography mapping techniques. J. Hydrol. 162, 119–141.

Scanlon, B., 1991. Evaluation of moisture flux from chloride data in desert soils. J. Hydrol.

Scanlon, B.R., Healy, R.W., Cook, P.G., 2002. Choosing appropriate techniques for quantifying groundwater recharge (vol 10, pg 18, 2002). Hydrogeol. J. 10, 347. doi:DOI 10.1007/s10040-002-0200-1

Scanlon, B.R., Keese, K.E., Flint, A.L., Flint, L.E., Gaye, C.B., Edmunds, W.M., Simmers, I., 2006. Global synthesis of groundwater recharge in semiarid and arid regions. Hydrogeol. J. 3370, 3335– 3370. doi:10.1002/hyp

Selaolo, E., Beekman, H., Gieske, A., Vries, J. De, 1996. Multiple tracer profiling in Botswana–GRES findings, in: Xu, Y., Hans E. Beekman (Eds.), Groundwater Recharge Estimation in Southern Africa. UNESCO, Cape Town, pp. 33–47.

Shah, N., Nachabe, M., Ross, M., 2006. Extinction depth and evapotranspiration from ground water under selected land covers. Ground Water 45, 329–38. doi:10.1111/j.1745-6584.2007.00302.x

Shanafield, M., Cook, P.G., 2014. Transmission losses, infiltration and groundwater recharge through ephemeral and intermittent streambeds: A review of applied methods. J. Hydrol. 511, 518–529. doi:10.1016/j.jhydrol.2014.01.068

Sklash, M.G., Mwangi, M.P., 1991. An Isotopic Study of Groundwater Supplies in the Eastern Province of Kenya. J. Hydrol. 128, 257–275.

Sophocleous, M., Ma, T., 1998. A decision support model to assess vulnerability to salt water intrusion in the great bend prairie aquifer of Kansas. Ground Water 36, 476–483.

Sorman, A. u., Abdulrazzak, M.J., 1993. Infiltration-recharge through wadi beds in arid regions. Hydrol. Sci. J. 38, 173–186. doi:10.1080/02626669309492661

Soti, V., Tran, A., Bailly, J.-S., Puech, C., Seen, D. Lo, Bégué, A., 2009. Assessing optical earth observation systems for mapping and monitoring temporary ponds in arid areas. Int. J. Appl. Earth Obs. Geoinf. 11, 344–351. doi:10.1016/j.jag.2009.05.005

Steyl, G., Dennis, I., 2010. Review of coastal-area aquifers in Africa. Hydrogeol. J. 18, 217–225. doi:DOI 10.1007/s10040-009-0545-9

Swarzenski, W. V, Mundorff, M.J., 1977. Geohydrology of North Eastern Province, Kenya, Geological Survey water-supply paper. U.S. Agency for International Developments, Washington.

Taylor, R.G., Todd, M.C., Kongola, L., Maurice, L., Nahozya, E., Sanga, H., MacDonald, A.M., 2013. Evidence of the dependence of groundwater resources on extreme rainfall in East Africa. Nat. Clim. Chang. doi:10.1038/nclimate1731 <http://dx.doi.org/10.1038/nclimate1731>

Templeton, R.C., Vivoni, E.R., Méndez-Barroso, L.A., Pierini, N.A., Anderson, C.A., Rango, A., Laliberte, A.S., Scott, R.L., 2014. High-resolution characterization of a semiarid watershed: Implications on evapotranspiration estimates. J. Hydrol. 509, 306–319. doi:10.1016/j.jhydrol.2013.11.047

Therrien, R., Mclaren, R.G., Sudicky, E.., Panday, S., 2010. HydroGeoSphere: A Three-dimensional Numerical Model Describing Fully-integrated Subsurface and Surface Flow and Solute Transport.

Thorne, R., Hoxley, G., Chaplin, H., 1990. Nyah to the South Australian Border Hydrogeological Project. Investigations Branch, Rural Water Commission of Victoria.

Van Genuchten, M.T., 1980. A Closed-form Equation for Predicting the Hydraulic Conductivity of Unsaturated Soils1. Soil Sci. Soc. Am. J. doi:10.2136/sssaj1980.03615995004400050002x

Van Weert, F., van der Gun, J., Reckman, J., 2009. Global Overview of Saline Groundwater Occurrence and Genesis. Utrecht.

Velpuri, N.M., Senay, G.B., Singh, R.K., Bohms, S., Verdin, J.P., 2013. A comprehensive evaluation of two MODIS evapotranspiration products over the conterminous United States: Using point and gridded FLUXNET and water balance ET. Remote Sens. Environ. 139, 35–49. doi:10.1016/j.rse.2013.07.013

Vengosh, A., Rosenthal, E., 1994. Saline groundwater in Israel: its bearing on the water crisis in the country. J. Hydrol. 156, 389–430. doi:10.1016/0022-1694(94)90087-6

Wang, H., Guan, H., Gutiérrez-Jurado, H.A., Simmons, C.T., 2014. Examination of water budget using satellite products over Australia. J. Hydrol. 511, 546–554. doi:10.1016/j.jhydrol.2014.01.076

Wanyeki, S., 1979. Well Field Design for the Merti Beds Aquifer, North Eastern Province, Kenya. Ohio University, USA.

Werner, A.D., 2009. A review of seawater intrusion and its management in Australia. Hydrogeol. J. 18, 281–285. doi:10.1007/s10040-009-0465-8

Wheater, H.S., A., M.S., Xin, L., 2010. Groundwater Modelling in Arid and Semi-Arid Areas. Cambridge University Press.

Winn, R.D.J., Steinmetz, J.C., Kerekgyarto, W.L., 1993. Stratigraphy and rifting history of the Mesozoic-Cenozoic Anza rift, Kenya. Am. Assoc. Pet. Geol. Bull. 77, 1989–2005.

Woodhead, T., 1968. Studies of potential evaporation in Kenya. Ministry of natural resources, Nairobi.

WRAP, 1991. Water Resources Assessment Study: ISIOLO. Water Resources Asessment Section/TNO-Institute of Applied Geosciences, Delft., Nairobi, Kenya.

Yin, L., Zhou, Y., Ge, S., Wen, D., Zhang, E., Dong, J., 2013. Comparison and modification of methods for estimating evapotranspiration using diurnal groundwater level fluctuations in arid and semiarid regions. J. Hydrol. 496, 9–16. doi:10.1016/j.jhydrol.2013.05.016

Young, M.E., Macumber, P.G., Donald Watts, M., Al-Toqy, N., 2004. Electromagnetic detection of deep freshwater lenses in a hyper-arid limestone terrain. J. Appl. Geophys. 57, 43–61. doi:10.1016/j.jappgeo.2004.09.002

Appendix A

Synthesis of groundwater levels

No.	Location	Long. (WGS 84)	Lat. (WGS 84)	Elevation	Year	Borehole depth (m)	DWL (m)	SWL (m)	Hydraulic head (m.a.s.l)	Q (m^3/h)	Source
69	Liboi	40.973	0.422	98	1941	90.9	88.4	86	12	1.8	Swarzenski 1977
96	El Dera	38.831	0.591	354	1940	124.4		108.3	245.7	3.3	Swarzenski 1977
1758	SE Logo Logo	38.082	1.918	414		85.3	69.8	66.3	347.7	8	Swarzenski 1977
2485	Dadaab	40.304	0.058	130	1955	128.4	105.2	103.1	26.9	4.6	Swarzenski 1977
2643	Dif	40.991	0.982	153	1956	122	112.8	105.2	47.8	3.9	Swarzenski 1977
2685	Liboi	40.876	0.357	102	1957	93.9	91.2	91.2	10.8	3.9	Swarzenski 1977
2686	Alunjugul	40.456	-0.029	130	1957	111	108	108	22	2.7	Swarzenski 1977
2687	Garissa	39.667	-0.473	146	1957	54.9	42.7	42.7	103.3	1.4	Swarzenski 1977
2718	Kolbio	41.076	-1.151	65	1957	78.1	70.1	70.1	-5.1	3.9	Swarzenski 1977
2719	Kolbio	41.157	-1.151	55	1957	79.3	61.9	61.9	-6.9	3.9	Swarzenski 1977
3033	Fafi	40.303	-0.384	135	1960	137.2	111.3	111.3	23.7	2.3	Swarzenski 1977
3038	Galma Galla	40.809	-1.182	84	1960	106.7		70.4	13.6	1.7	Swarzenski 1977
3041	Lagh Bogal	39.846	1.291	226	1960	175.4	155.5	118.9	107.1	5.7	Swarzenski 1977
3085	Wel Merer	40.58	-0.174	129	1960	128.1		115.3	13.7	2.3	Swarzenski 1977
3155	Wajir: 8/63	40.091	1.742	265	1964	186.4	126.4	13.7	251.3	1	Swarzenski 1977
3218	Habaswein	39.477	1.038	221	1963	143.9	132.7	126.3	94.7	5.1	Swarzenski 1977
3240	Darken	40.436	0.133	128	1963	140.3		108.3	19.7	1.8	Swarzenski 1977
3306	Wajir	40.091	1.782	265	1964	263	170.7	14.6	250.4	1.3	Swarzenski 1977
3411	Kurdi	40.673	-0.738	124	1966	140.3		132.7	-8.7	2.2	Swarzenski 1977
3540	Giriftu	39.742	1.991	302	1968	55.8	11.6	14.9	287.1		Swarzenski 1977
3591	Garissa E	39.821	-0.376	210	1968	231.8		136.6	73.4	0.6	Swarzenski 1977
3592	Garissa E	39.821	-0.376	210	1968	231.8		151	59	1.6	Swarzenski 1977
3628	Kolbio	41.076	-1.151	55	1969	73.2	60.4	60.4	-5.4	0.8	Swarzenski 1977
3654	Habaswein	39.477	1.038	220	1970	134.5	126.6	122.9	97.1	6.8	Swarzenski 1977
3655	Habaswein	39.432	1.061	204	1970	120.2		105.5	98.5	6.8	Swarzenski 1977

No.	Location	Long. (WGS 84)	Lat. (WGS 84)	Elevation	Year	Borehole depth (m)	DWL (m)	SWL (m)	Hydraulic head (m.a.s.l)	Q (m^3/h)	Source
3656	Giriftu	39.742	1.991	302	1970	20.4	13.1	13.1	288.9	0.4	Swarzenski 1977
3667	Liboi	40.876	0.357	101	1970	99.7	90.3	90.3	10.7	10.2	Swarzenski 1977
3684	Kulan	40.641	0.215	119	1970	119.2	108.3	102.8	16.2	9.6	Swarzenski 1977
3685	Dilmanyale	39.604	0.811	191	1970	108.3	88.1	87.2	103.8	6.8	Swarzenski 1977
3687	Meri	39.925	0.482	153	1970	122	105.2	100	53	2.2	Swarzenski 1977
3695	Ifo 0	40.305	0.109	128	1970	131.1	116.5	106.7	21.3	9.1	Swarzenski 1977
3695	Dadaab	40.308	0.058	128	1970	130.8	116.5	106.7	21.3	9.1	Swarzenski 1977
3697	W Meri	39.824	0.382	156	1970	130.8	116.5	106.7	49.3	9.1	Swarzenski 1977
3715	SW Meri	39.847	0.495	159	1971	136.9	103.7	100.6	58.4	5.3	Swarzenski 1977
3726	Khot Khot	40.018	0.636	157	1971	140	110.1	105.8	51.2	10.7	Swarzenski 1977
3751	Shantabak	39.741	0.464	160	1971	133.6	110.7	101.9	58.1	6.8	Swarzenski 1977
3752	NW Meri	39.557	0.636	174	1971	151.6	108.6	92.1	81.9	7.3	Swarzenski 1977
3753	Lorian Swamp	39.432	0.865	188	1971	113.7	94.5	91.2	96.8	4.6	Swarzenski 1977
3769	Hara khot Khot	39.901	0.891	177	1971	132.1	103.7	99.4	77.6	7.7	Swarzenski 1977
3770	W Dadaab	39.977	-0.034	171	1971	165.3	145.8	137.5	33.5	3.7	Swarzenski 1977
3781	Lorian Swamp	39.437	0.8	189	1972	122.9	94.9	93.6	95.4	6.4	Swarzenski 1977
3788	Fini	40.013	0.416	148	1972	119.5	101.5	98.2	49.8	5.6	Swarzenski 1977
3792	Kalalut	39.639	0.754	189	1972	112.8	100.6	96.1	92.9	4.6	Swarzenski 1977
3804	W Kalakut	39.471	0.694	186	1972	158.6	114.4	98.2	87.8	5	Swarzenski 1977
3805	Sericho	39.099	1.146	239	1972	91.5	50.3	22.3	216.7		Swarzenski 1977
3814	Sericho	39.099	1.146	236	1972	51.8	15.2	26.5	209.5		Swarzenski 1977
3819	Gudas	38.291	2.077	360	1973	125.6	106.4	85.9	274.1	8.2	Swarzenski 1977
3820	Sabuli	40.111	0.351	143	1972	128.7	96.1	93.6	49.4	8.1	Swarzenski 1977
3821	Dagahaley N	40.369	0.229	139	1972	147.9	146.4	125	14	4.5	Swarzenski 1977
3822	Sericho	39.094	1.028	229	1972	125	100.6	79.9	149.1	3	Swarzenski 1977

No.	Location	Long. (WGS 84)	Lat. (WGS 84)	Elevation	Year	Borehole depth (m)	DWL (m)	SWL (m)	Hydraulic head (m.a.s.l)	Q (m^3/h)	Source
3830	NW Habaswein	39.234	1.208	216	1972	129	118.9	107.3	108.7	10.9	Swarzenski 1977
3831	Alunjugul	40.456	-0.029	130	1972	134.8	112	108.3	21.7	4.3	Swarzenski 1977
3852	Hag 0	40.373	0.006	127	1992	146.7	108.5	107.6	19.4	8	Lane 1995
3853	Merti	38.663	1.056	293	1972	67.1	33.8	21.7	271.3		Swarzenski 1977
3860	S Meri	39.969	0.347	151	1972	134.8	99.1	97.6	53.4	4.7	Swarzenski 1977
3864	Merti	38.663	1.056	290	1972	30.8	18.3	12.5	277.5	13.6	Wanyeki 1979
3877	Kumahumato	40.08	0.316	135	1973	132	97	94.8	40.2	8.1	Swarzenski 1977
3878	NW Sabule	40.144	0.287	144	1973	137.2	96.1	94.5	49.5		Swarzenski 1977
3902	Liboi	40.872	0.356	102	1973	103.7	91.5	90.9	11.1	9.1	Swarzenski 1977
3915	Hadado	39.419	1.532	262	1973	176.8	106.1	102.2	159.8	7.5	Swarzenski 1977
4341	Rhowa	40.782	-0.472	110	1977	144.8	134.1	112.1	-2.1	6	Lane 1995?
4425	Korbesa E	38.889	1.211	248	1979	180	54	30	218		Lane 1995
4475	Malka Daka	38.471	0.84	358	1978	147	82	14	344	5	Lane 1995
4514	Merti E	38.817	1.039	266	1978	160	34	34.4	231.6	7.2	Lane 1995
4524	Biamathow	40.40817	0.61344	128	1978	143.5	113	109.6	18.4	5	Lane 1995
4561	Merti NE	38.706	1.068	285			26	17.5	267.5	4.6	Lane 1995
4586	Boji 3	39.133	1.365	237	1979	150.4	130	117	120	12	Wanyeki 1979
4587	Bule	38.968	1.566	264	1979	164	120.5	123	141	12	Lane 1995
4588	Bule 5 ?	38.792	1.404	265	1979	200.7	127.5	103	162		Lane 1995
4643	Hururu Merti	38.769	1.551	282	1979	180	110	73.1	208.9	3.5	Lane 1995
4645	D Galla	38.619	1.577	297	1979	200	80	84	213		Lane 1995
4677	Matasadeni	38.429	1.375	327	1980	150	66	60	267		Lane 1995
4681	Galobaba Merti	38.397	1.548	341	1980	176	96	90	251	1	Lane 1995
4826	Iresa Buru	38.893	1.145	254	1980	76	58	15.6	238.4	4	Lane 1995
5012	Habaswein	39.487	0.994	223	1982	140	127.5	123.3	99.7	3.1	Lane 1995

No.	Location	Long. (WGS 84)	Lat. (WGS 84)	Elevation	Year	Borehole depth (m)	DWL (m)	SWL (m)	Hydraulic head (m.a.s.l)	Q (m^3/h)	Source
5506	Hadado	39.42	1.529	262	1984	176	159	104.5	157.5	4.2	Lane 1995
5795	Habaswein	39.487	0.994	221	1985	153.6	130	112.3	108.7	6.3	Lane 1995
6712	Wajir Giris	40.064	1.734	265	1986	57.5	7	4.9	260.1	2.1	Lane 1995
6738	Leheley	40.018	1.618	260	1981	126	64	56.3	203.7	3	Lane 1995
7325	Sericho	39.133	1.181	226	1987	21	19.5	11.4	214.6	3.3	Lane 1995
7329	Sericho	39.123	1.169	226	1987	24	18.5	11.7	214.3	9.2	Lane 1995
9009	Liboi	40.876	0.357	102	1991	123	91	88.1	13.9	9	Lane 1995
9380	Merti	38.663	1.056	293			30	15	278	21	GIBB 2004
9384	NW Habaswein	39.304	1.272	222			109	112	110	4.5	GIBB 2004
9740	Ifo 1	40.306	0.105	128	1991	141	110	108.4	19.6	6.6	Lane 1995
9749	Ifo 2	40.305	0.121	128	1991	141	110	108.8	19.2	6.9	Lane 1995
9758	Liboi	40.878	0.357	102	1992	130.5	93.8	91.4	10.6	11.7	Lane 1995
9760	Hag 1	40.373	0.004	127	1992	150.1	110.1	107.5	19.5	4.9	Lane 1995
9761	Hag 2	40.374	0.008	127	1992	151	120.6	107.7	19.3	7.8	Lane 1995
9848	Ifo 3	40.321	0.11	127	1991	140.4	118	108	19	8.8	Lane 1995
9849	Ifo 4	40.318	0.109	128	1991	140	119	108.4	19.6	8.8	Lane 1995
9999	Ifo 5	40.316	0.115	128	1992	140	124	109	19	8.8	Lane 1995
10011	Ifo 6	40.313	0.123	128	1992	141	120	108.4	19.6	8.8	Lane 1995
10094	Dag 1	40.285	0.191	129	1992	153.5	104	111.1	17.9	5.6	Lane 1995
10095	Dag 2	40.279	0.195	130	1992	147	117	111.3	18.7	9.6	Lane 1995
10096	Dag 3	40.3	0.19	128	1992	143.5	114	109.6	18.4	18.3	Lane 1995
10098	Hag 4	40.357	0	135	1992	150	110	115.2	19.8	16.8	Lane 1995
10099	Dag 4	40.276	0.193	129	1992	150	124	111	18		Lane 1995
10417	Liboi	40.872	0.356	102	1993	140.9	87	91.5	10.5	24	Lane 1995
10418	Dadaab	40.308	0.058	130	1993	150.9	105.7	106.4	23.6	24	Lane 1995

No.	Location	Long. (WGS 84)	Lat. (WGS 84)	Elevation	Year	Borehole depth (m)	DWL (m)	SWL (m)	Hydraulic head (m.a.s.l)	Q (m^3/h)	Source
10419	Dag 5	40.284	0.176	129	1993	150	125	111.1	17.9	20	Lane 1995
10420	Alunjugul	40.456	-0.029	130	1993	150	112	108.6	21.4	24	Lane 1995
10421	Hag 5	40.35	0.004	134	1993	154	112	113.6	20.4	28.8	Lane 1995
10422	Shantabaq	39.74	0.464	160	1993	142.3	95.8	102	58	24	Lane 1995
10436	Liboi Mon	40.874	0.356	102	1993	125.2	92.5	91	11		Lane 1995
10437	Liboi L/S	40.864	0.352	104	1993	127	92	91.5	12.5	6.6	Lane 1995
13313	Elan	39.319	0.767	235	2001	148	120	114.28	120.72	0.4	GIBB 2004
13331	Kumahumato	40.08	0.316	150	2001	158	120.2	93.3	56.7	19.6	GIBB 2004
13332	Gurufa	39.464	0.804	180	2001	135.1	92	93.57	86.43	8.2	GIBB 2004
13387	Welmerer	40.58	-0.177	129	2001	182.7	117	115.4	13.6	17.8	GIBB 2004
13777	Damajale	40.797	0.104	126	2003	164	125	113.8	12.2	19.4	GIBB 2004
9761B	Hag 6	40.374	0.008	127	2000	135	104	106.3	20.7	13	GIBB 2004
Duma	Duma BH	38.508	1.718	328			100	90	238	6.5	GIBB 2004
3866	Tuli Roba	39.04428	2.72289	509	1972	152.4		54.9	454.1	0.36	Swarzenski 1977
3849	Buna	39.21967	2.79461	483	1972	139.3		38.7	444.3	0.36	Swarzenski 1977
	Dagahaley 6	40.28276	0.19517	127	2013	180	124.5	113.3	13.7	34	Earthwater 2013
	Alango Arba New	39.98782	0.09132	177	2013	160		141.56	35.44	0.12	Earthwater 2013
	Gurufa WVK	39.46417	0.80347	190	2013			95.4	94.6		Earthwater 2013
	Mathagisse New JICA	40.42697	0.16578	124	2013			104.7	19.3		Earthwater 2013
	Mochesa 2	40.27436	1.0083	183	2013			125.2	57.8		Earthwater 2013
	Kambioos BH 2	40.39253	0.05102	144	2013	147	-	121.8	22.2		Earthwater 2013
	Gurufa BGP BH	39.42537	0.81445	192	2013		101.1	100.78	91.22		Earthwater 2013
	Dagahaley BH 9(old)	40.2788	0.18013	134	2013		.	113.52	20.48		Earthwater 2013
	Dagahaley BH 3 (old)	40.29972	0.19003	125	2013		.	113.7	11.3		Earthwater 2013
	Dadaab Redcross BH	40.31044	0.04089	138	2013		115.1	112.6	25.4	16	Earthwater 2013

No.	Location	Long. (WGS 84)	Lat. (WGS 84)	Elevation	Year	Borehole depth (m)	DWL (m)	SWL (m)	Hydraulic head (m.a.s.l)	Q (m^3/h)	Source
	Ifo BH 7	40.32724	0.11567	127	2013			100.8	26.2	53	Earthwater 2013
	Saretho BH 2	40.13295	0.0209	169	2013	210	139.3	137.3	31.7	16	Earthwater 2013
	Dertu Redcross BH 1	39.7809	0.31643	172	2013		116.8	115.7	56.3	30	Earthwater 2013
	Sabule Oxfam BH	40.11899	0.34705	149	2013		99.1	95.2	53.8	40	Earthwater 2013
	Madogashe Hospital BH	39.18519	0.73537	276	2013	262	145.9	141.8	134.2	1	Earthwater 2013
	Habaswein Hospital BH	39.5092	1.02901	220	2013		109.8	107.94	112.06	8	Earthwater 2013
	Habaswein Kibilay NIB BH	39.47927	1.01055	205	2013		108	106	99	10	Earthwater 2013
	Alinjugur Faida (new) BH	40.45647	-0.01818	132	2013		112	111.8	20.2	20	Earthwater 2013
	Skanska Redcross BH 1	39.31859	0.90706	210	2013		114.7	109.2	100.8	36	Earthwater 2013
	Ifo 2 West BH 1	40.29906	0.15209	138	2013		118.5	115.64	22.36	56	Earthwater 2013

Appendix B

Water level monitoring within the Dadaab refugee camp (1993-2003)

Reprinted from GIBB (2004)

Dagahaley 1 (C-100094)

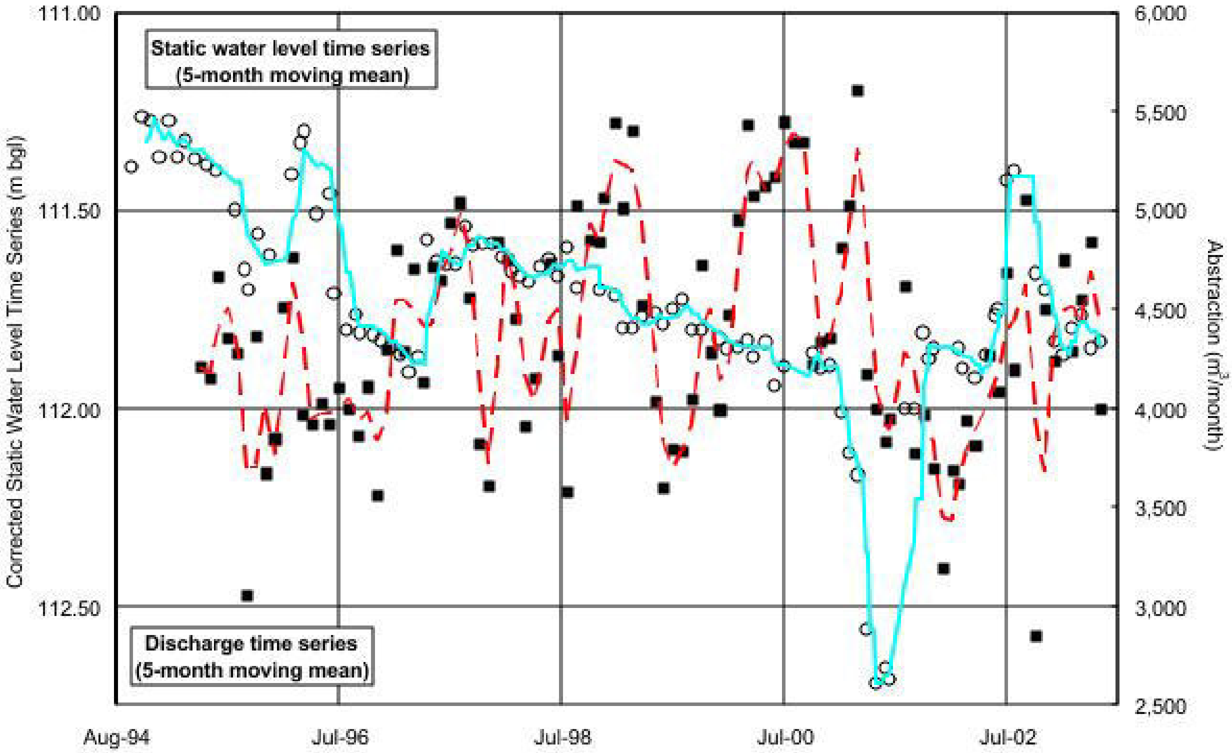

Dagahaley 2 (C-100095)

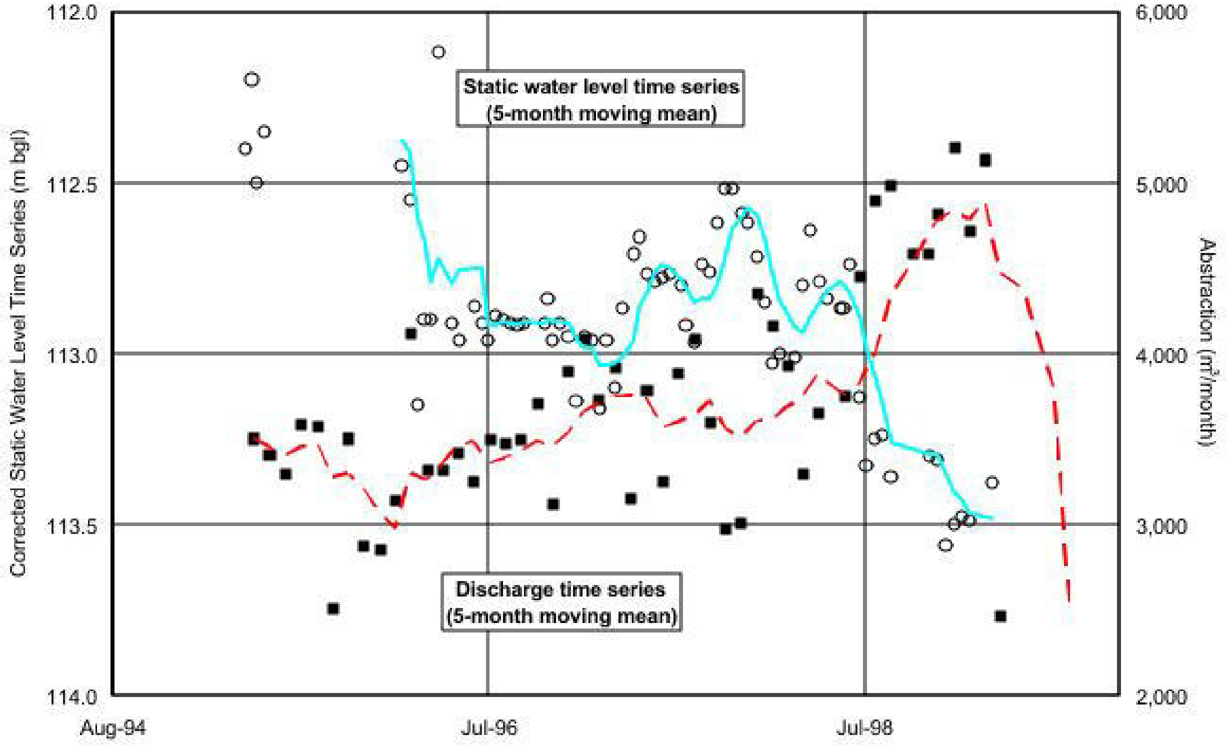

Dagahaley 3 (C-100096)

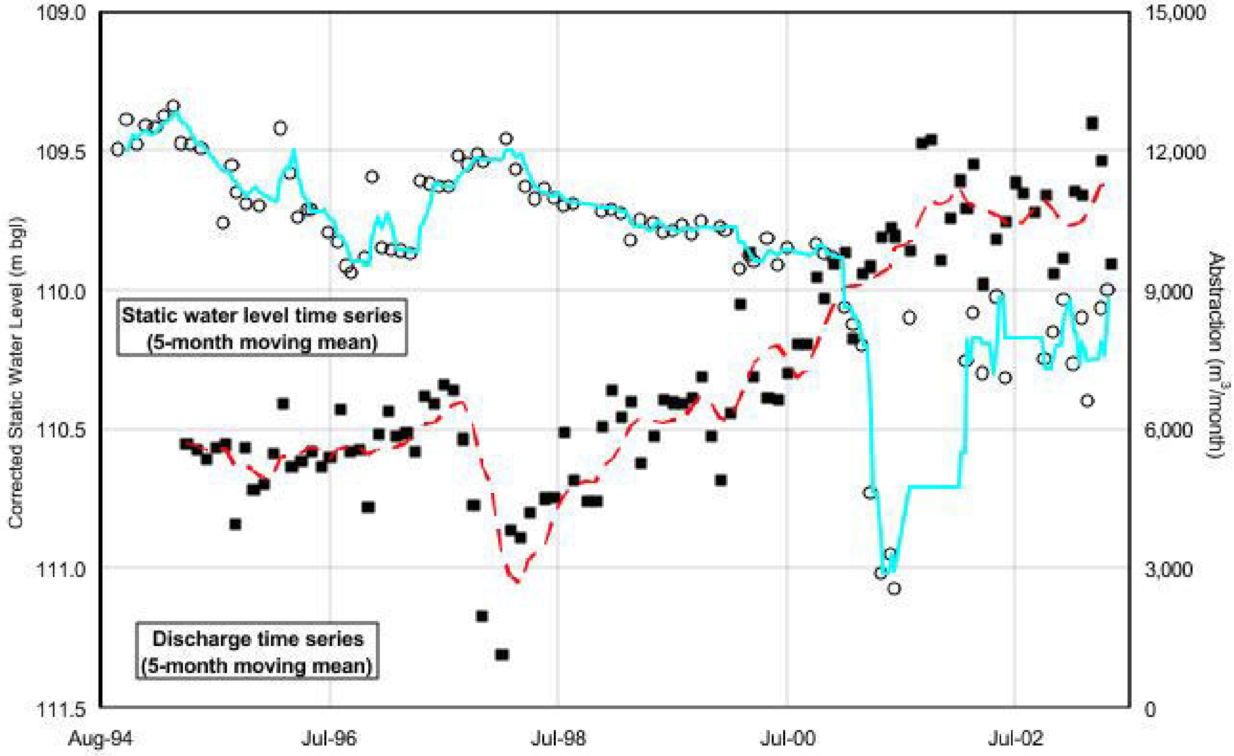

Dagahaley 4 (C-100099)

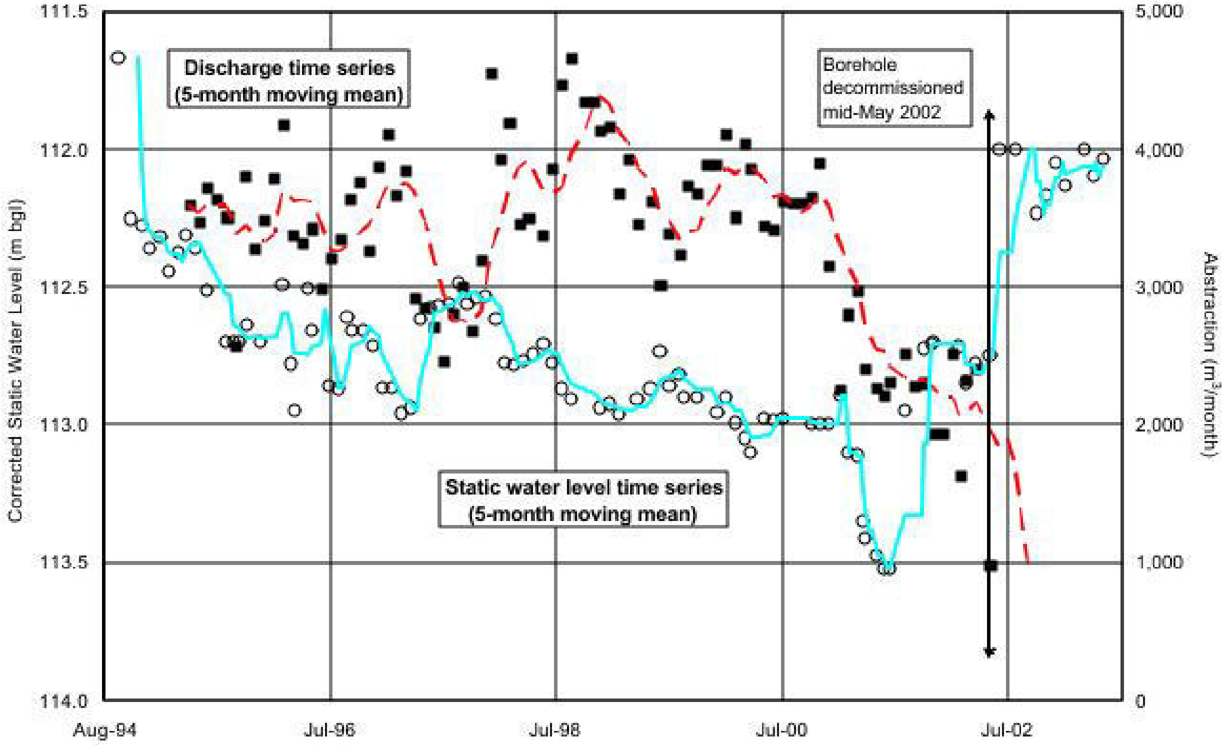

Dagahaley 6

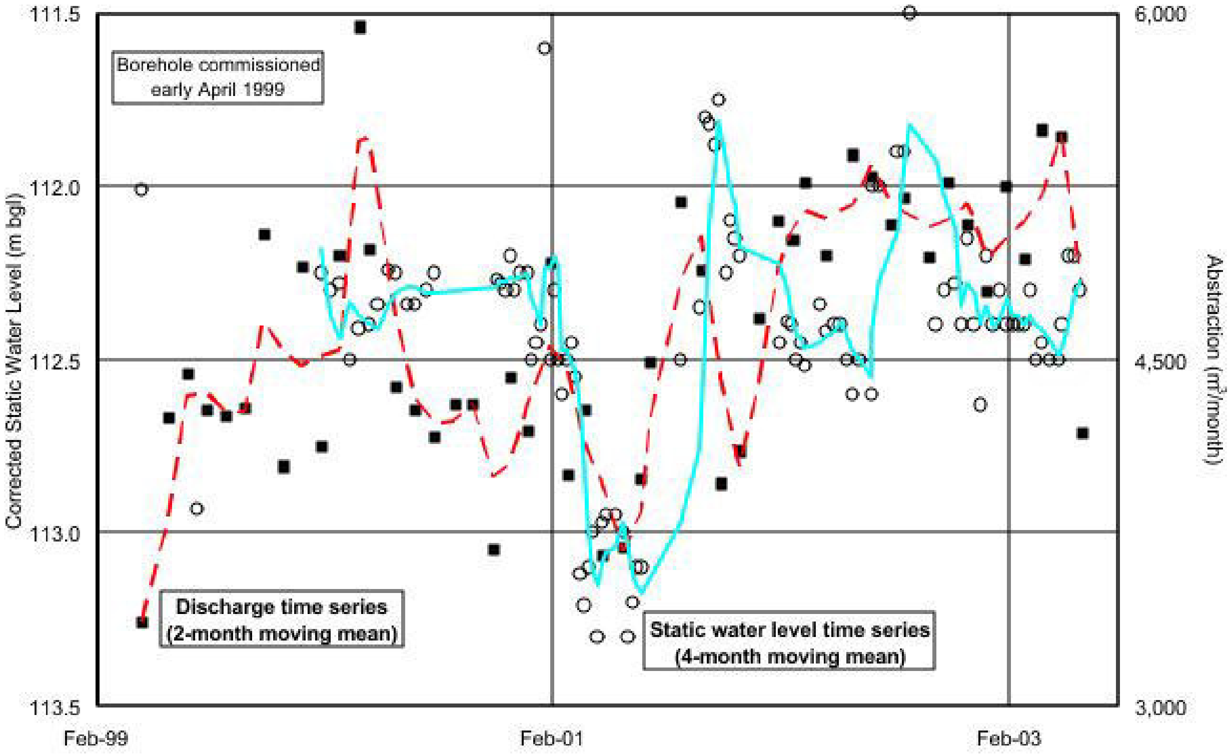

Ifo 1 (C-9740)

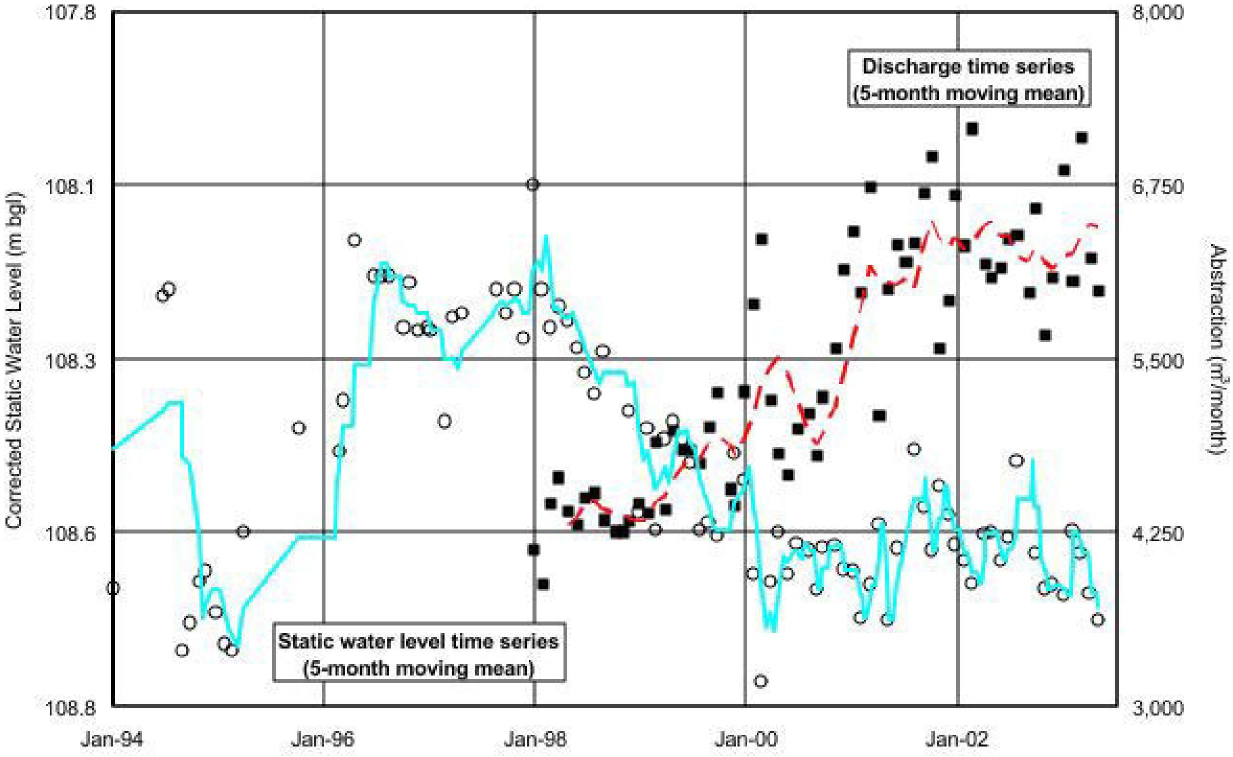

Ifo 2 (C-9749)

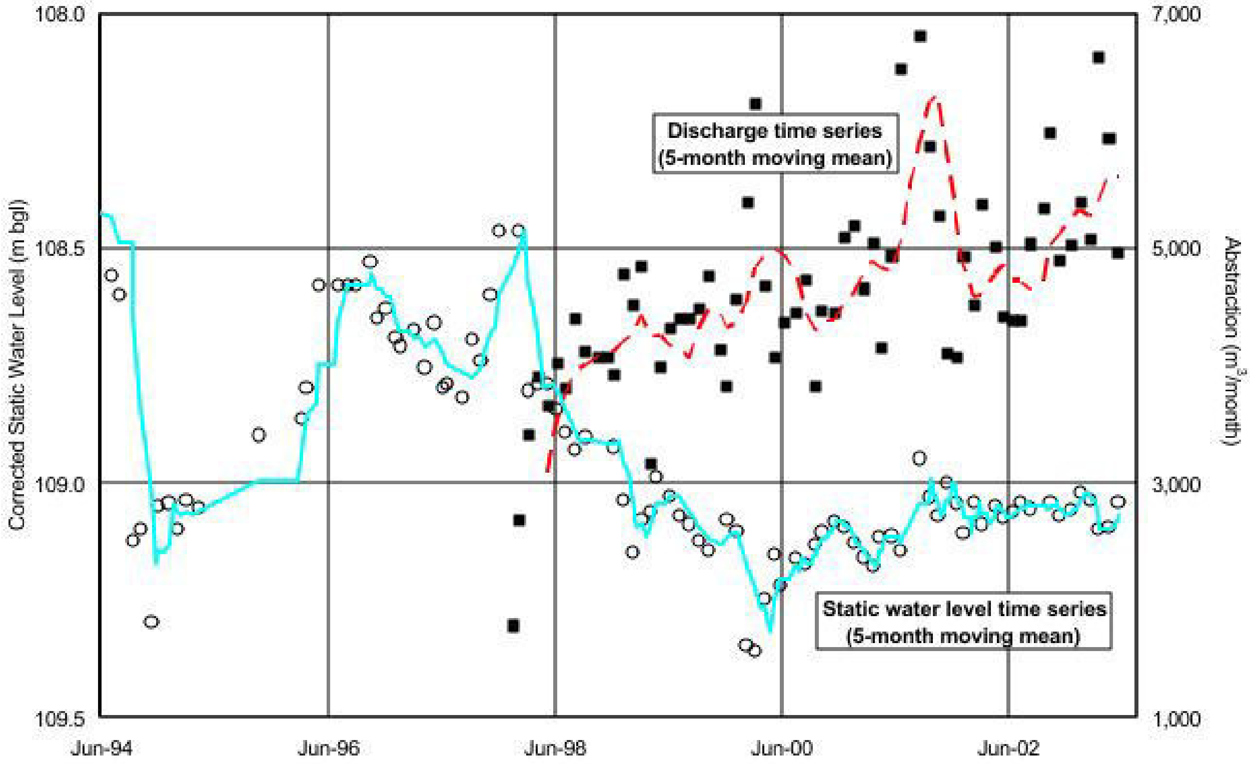

Ifo 4 (C-9849)

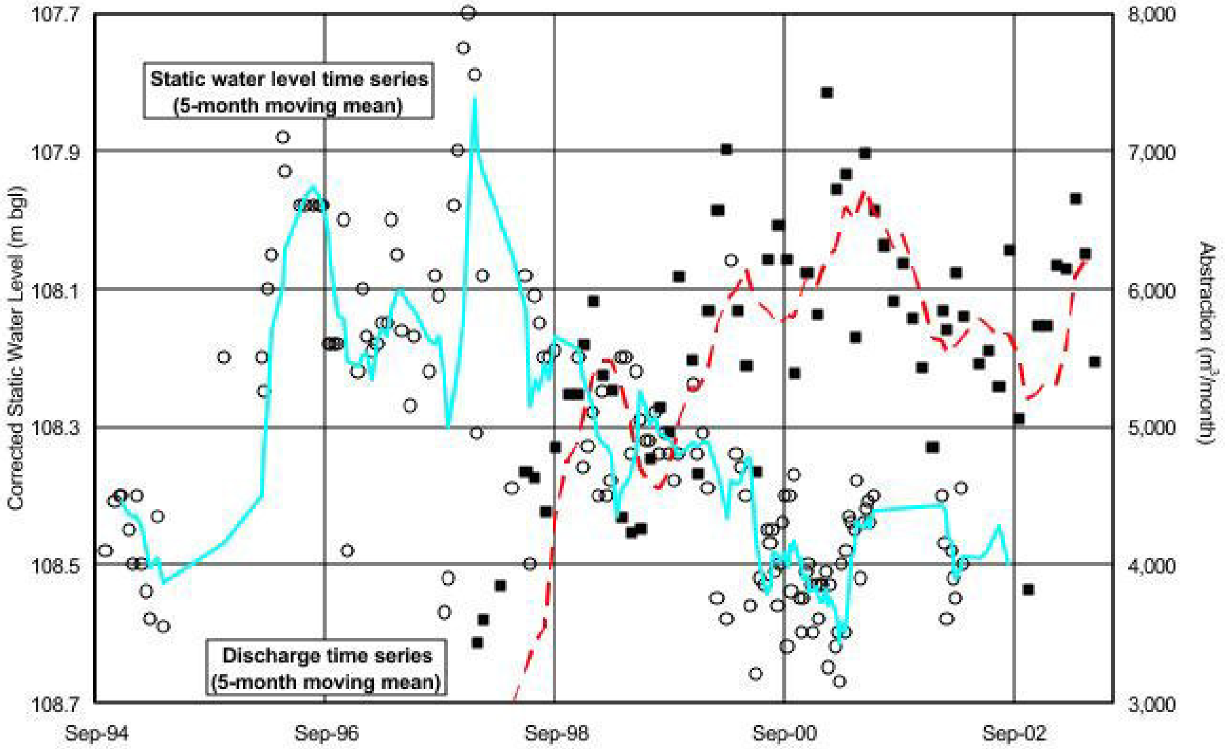

Ifo 5 (C-9999)

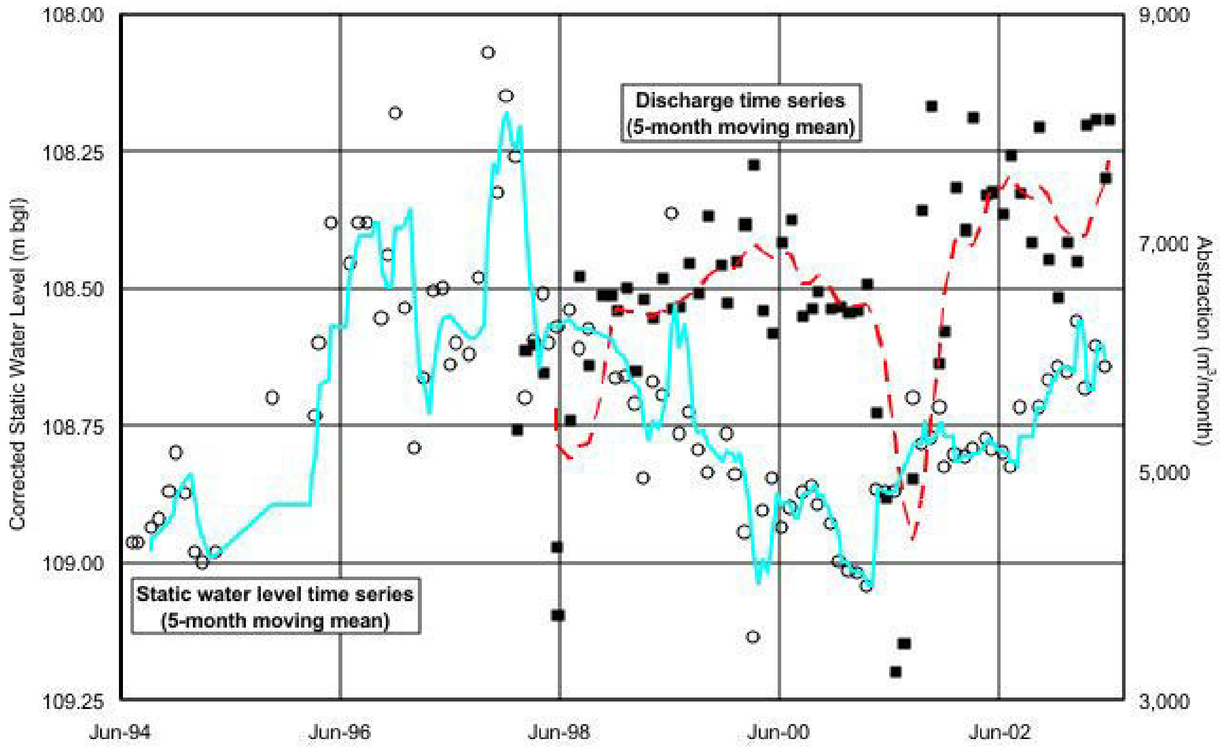

Ifo 4 (C-10011)

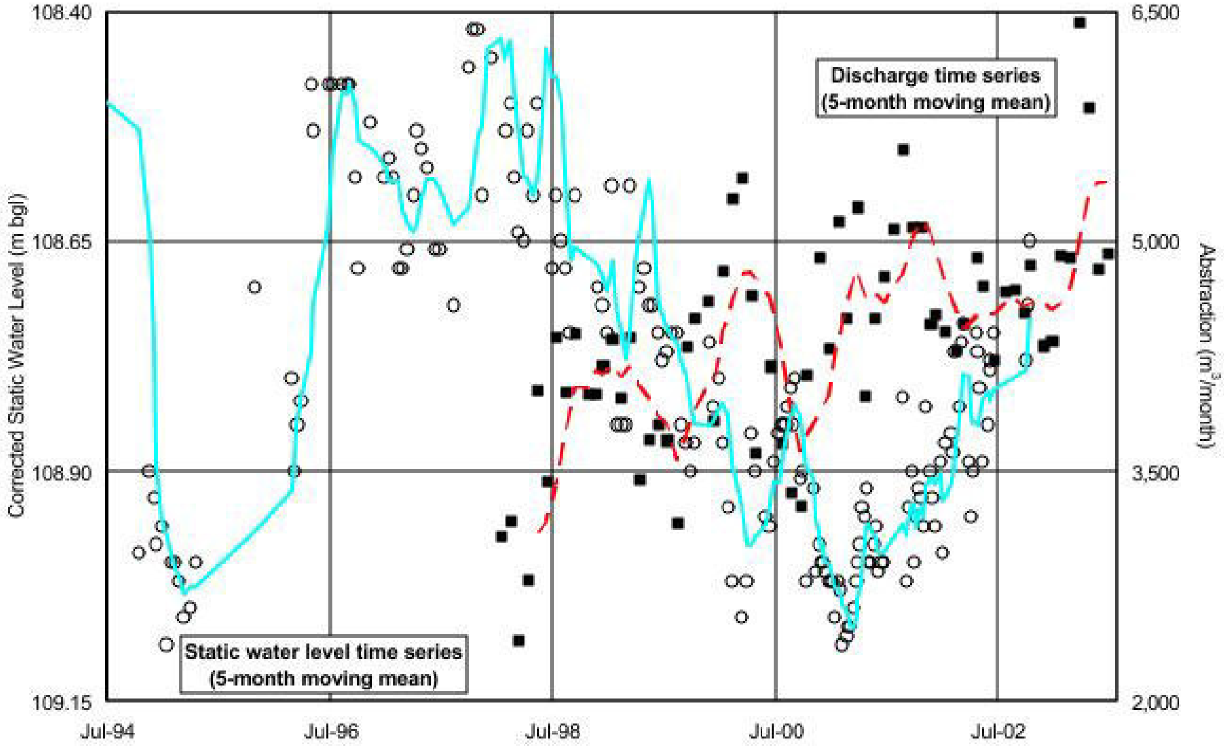

Hagadera 1 (C-9760)

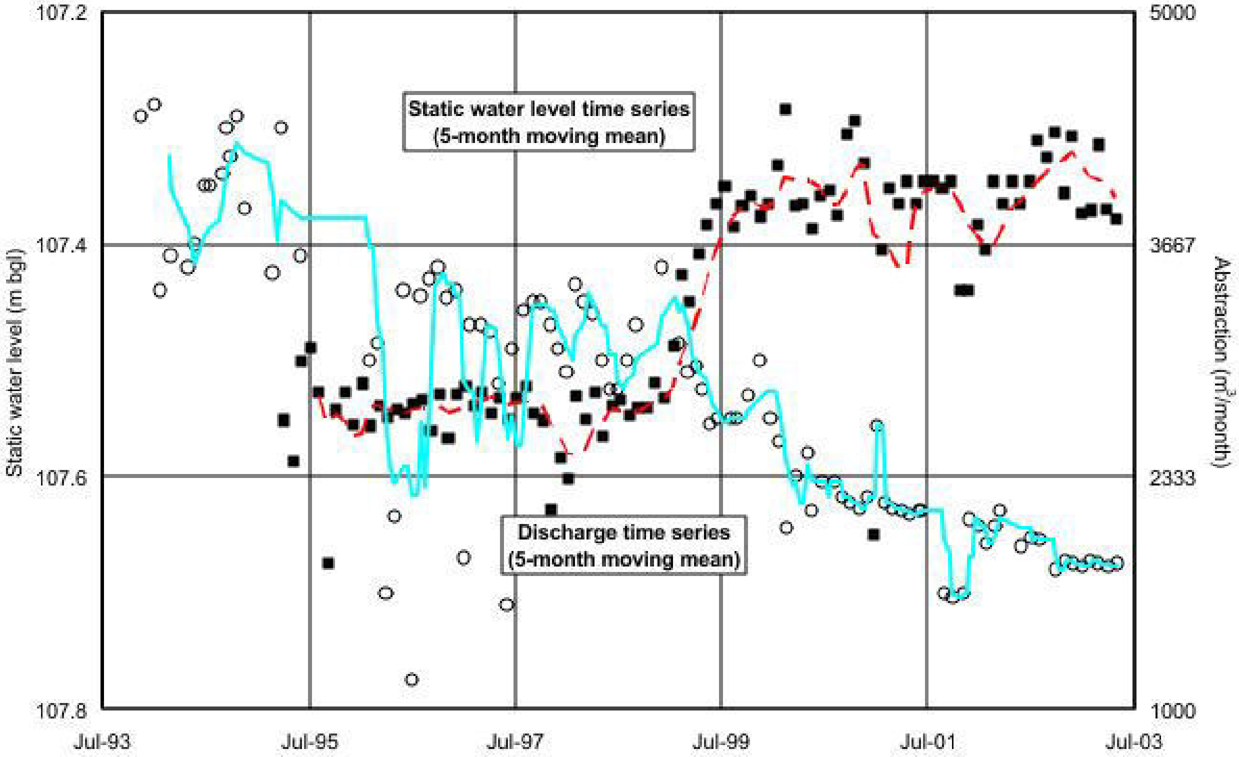

Hagadera 2 (C-9761)

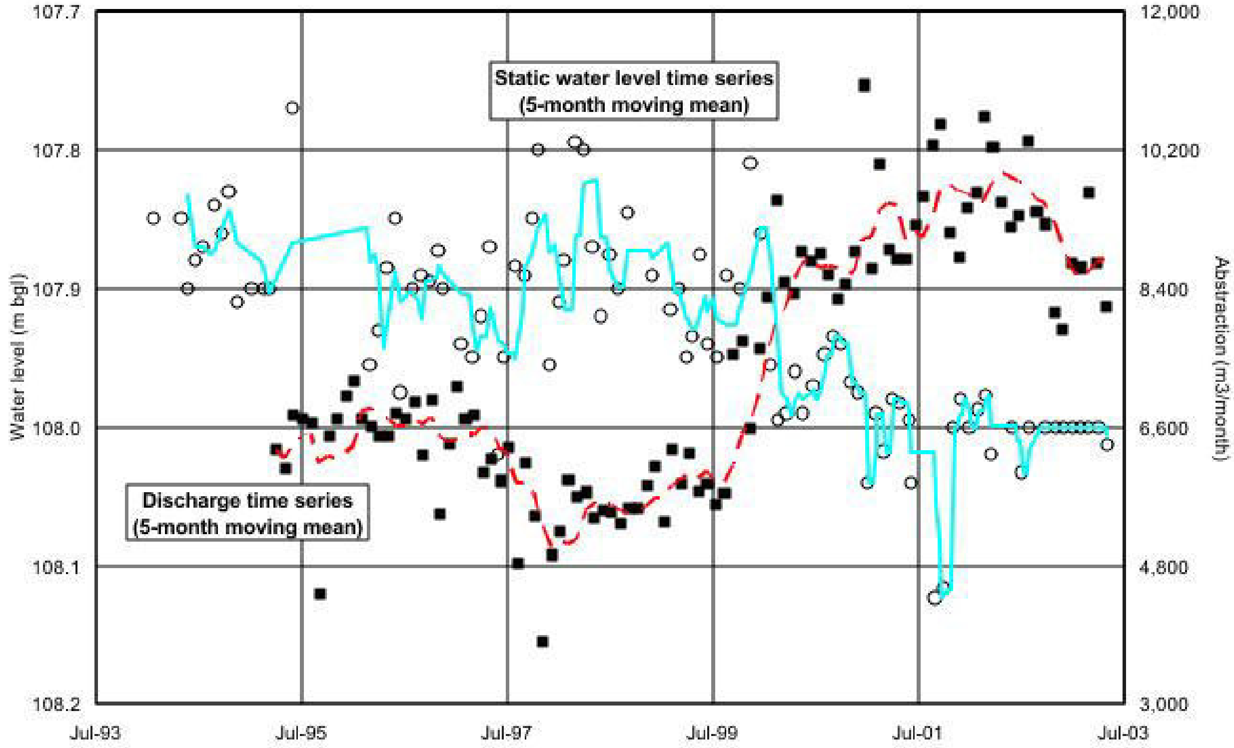

Hagadera 3 (C-10097)

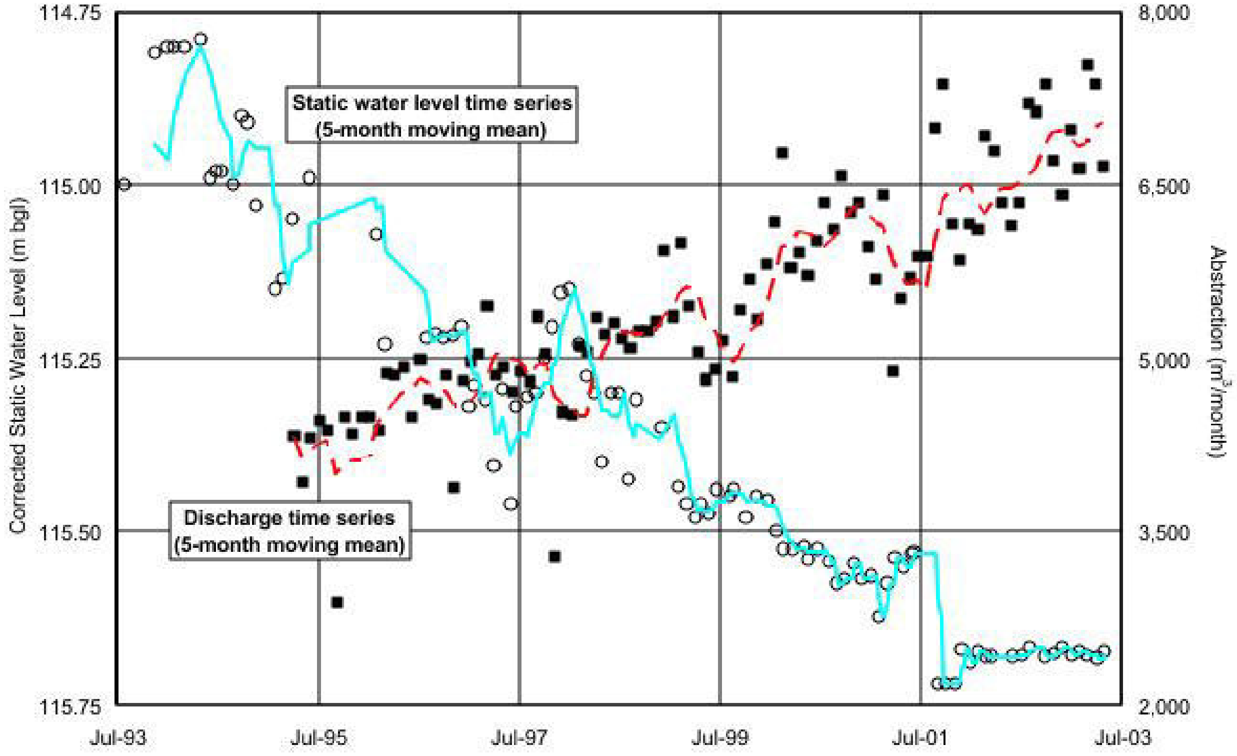

Hagadera 5 (C-10098)

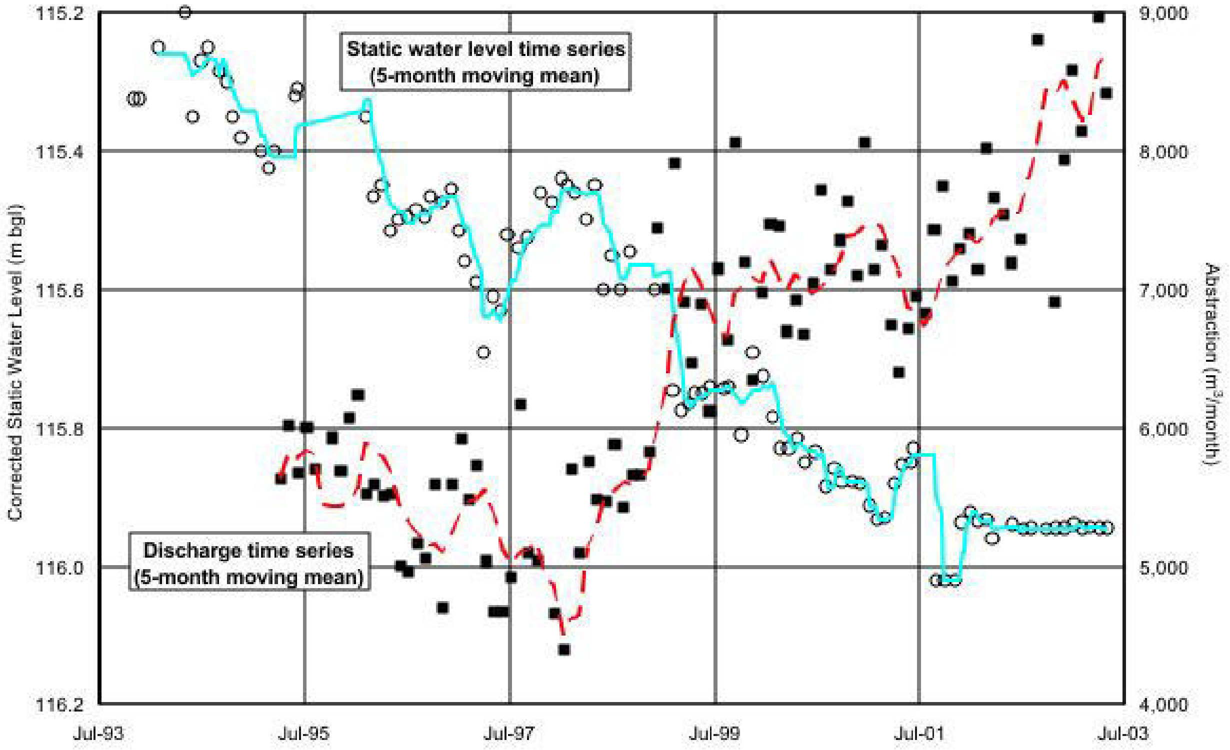

Appendix C

High temporal resolution monitoring of the groundwater levels and electrical conductivities

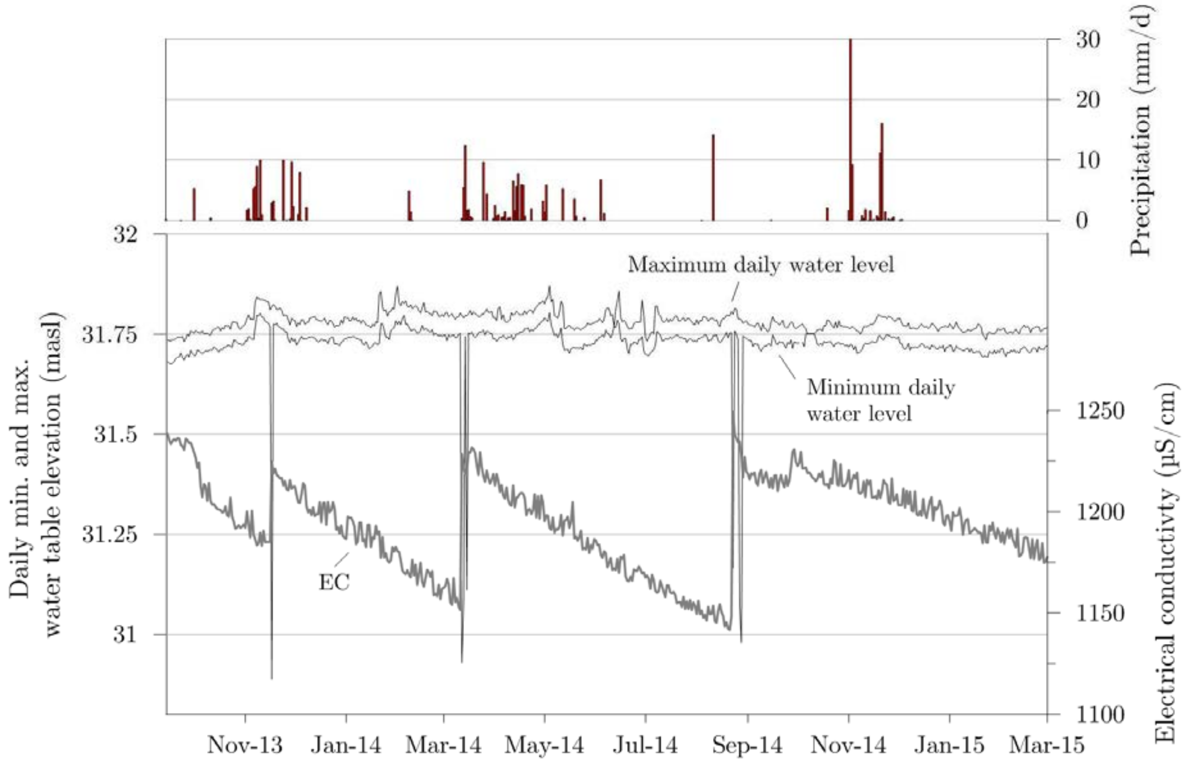

Alinjugur Faida (20m^3/h)

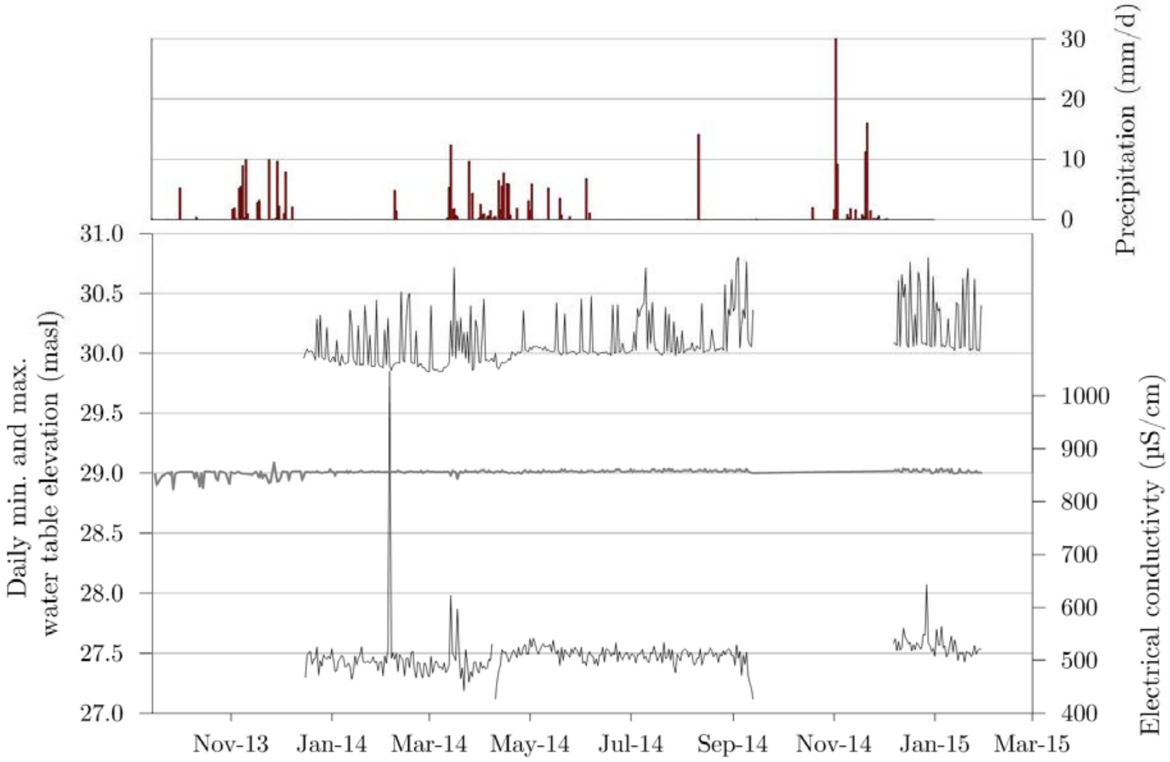

Dadaab Redcross (16m^3/h)

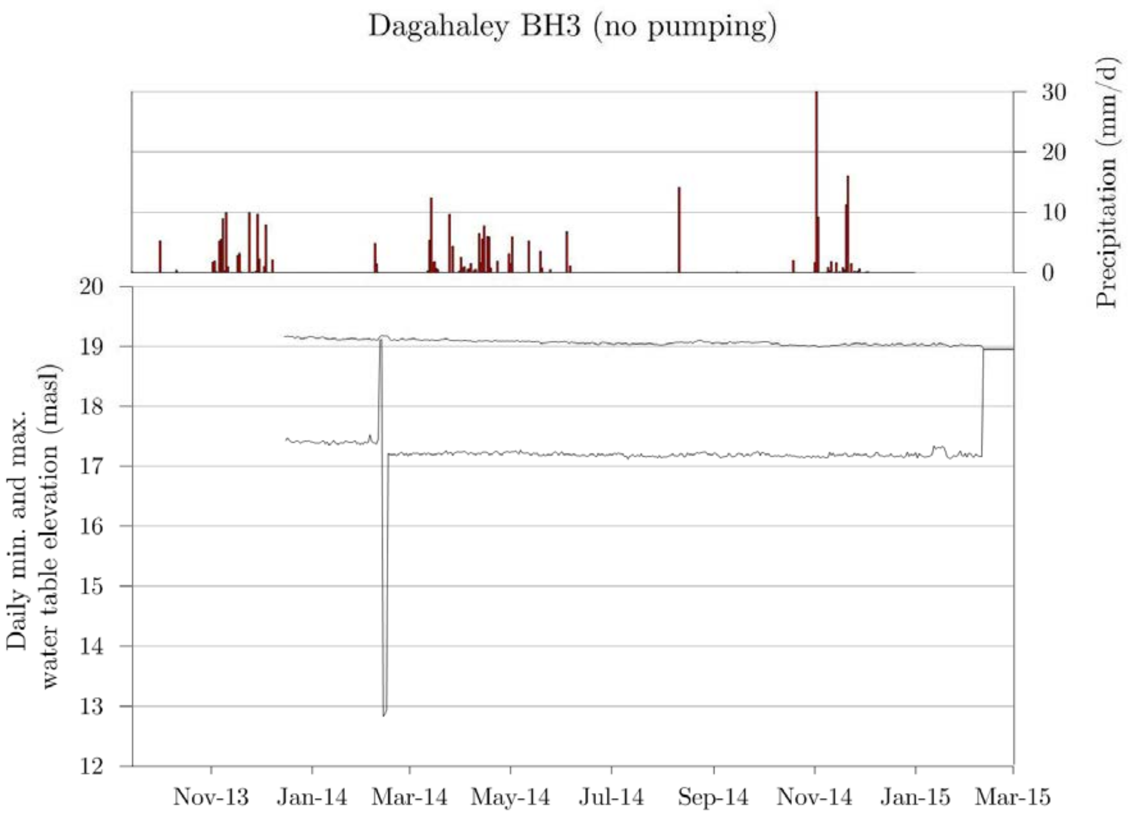
Dagahaley BH3 (no pumping)

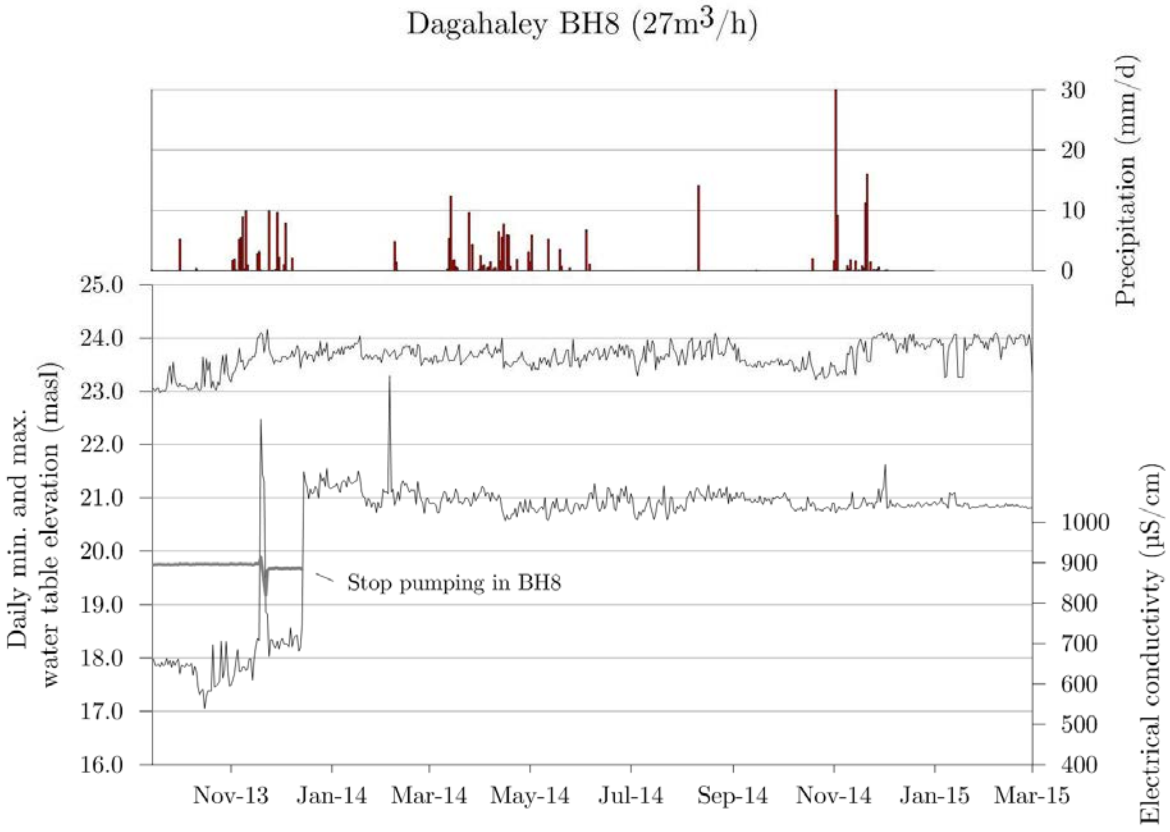
Dagahaley BH8 (27m^3/h)

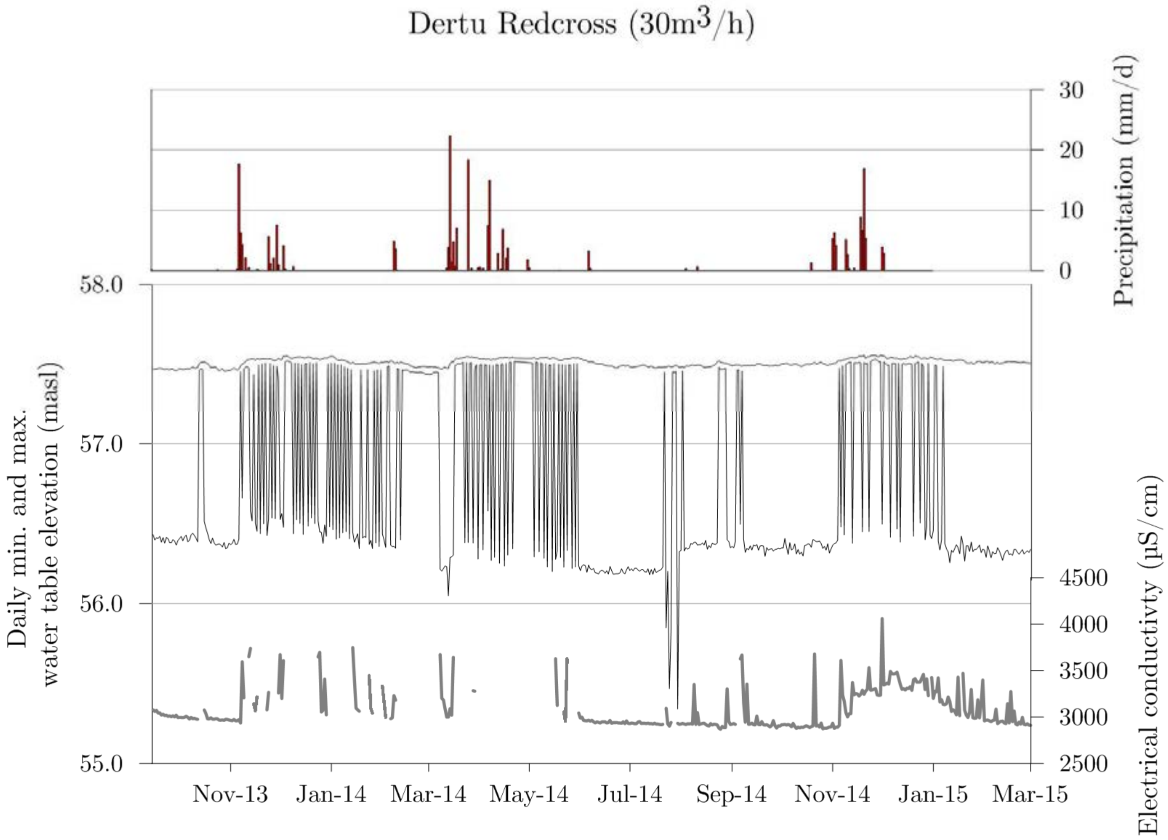
Dertu Redcross (30m3/h)
Precipitation (mm/d)
30
20
10
0
Daily min. and max. water table elevation (masl)
58.0
57.0
56.0
55.0
Electrical conductivty (µS/cm)
4500
4000
3500
3000
2500
Nov-13
Jan-14
Mar-14
May-14
Jul-14
Sep-14
Nov-14
Jan-15
Mar-15

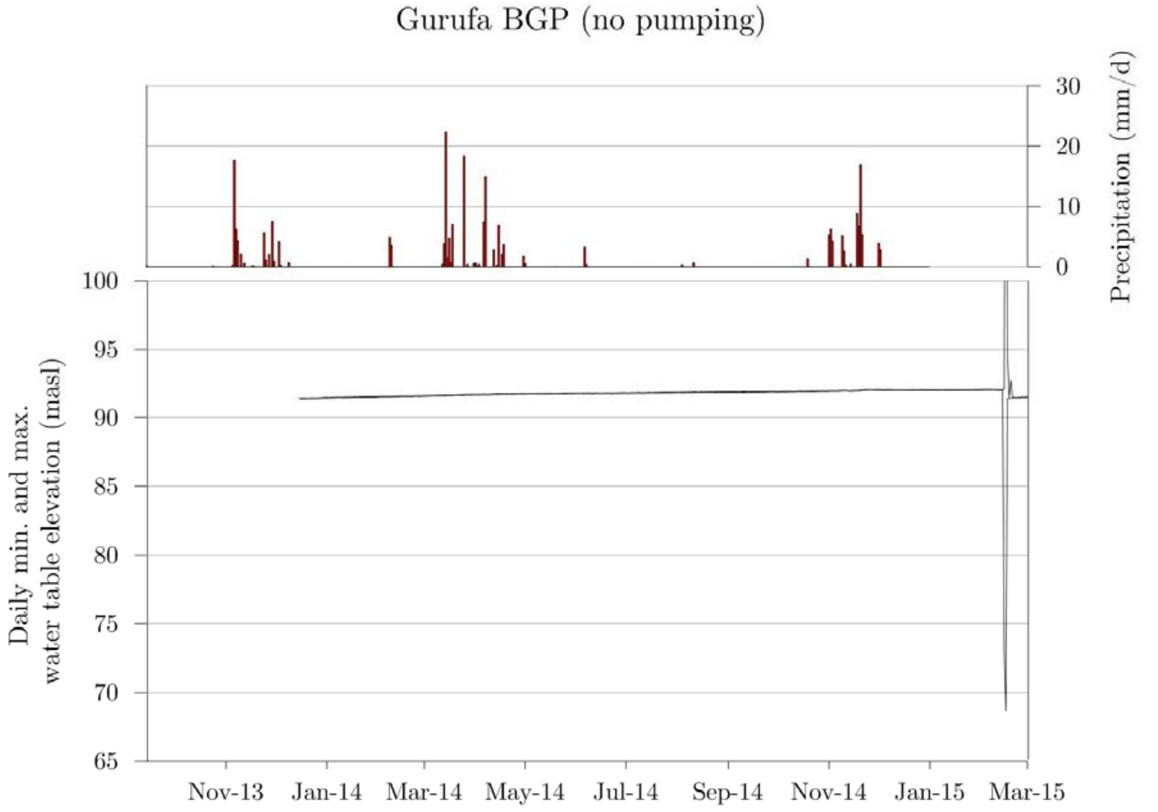
Gurufa BGP (no pumping)
Precipitation (mm/d)
30
20
10
0
Daily min. and max. water table elevation (masl)
100
95
90
85
80
75
70
65
Nov-13
Jan-14
Mar-14
May-14
Jul-14
Sep-14
Nov-14
Jan-15
Mar-15

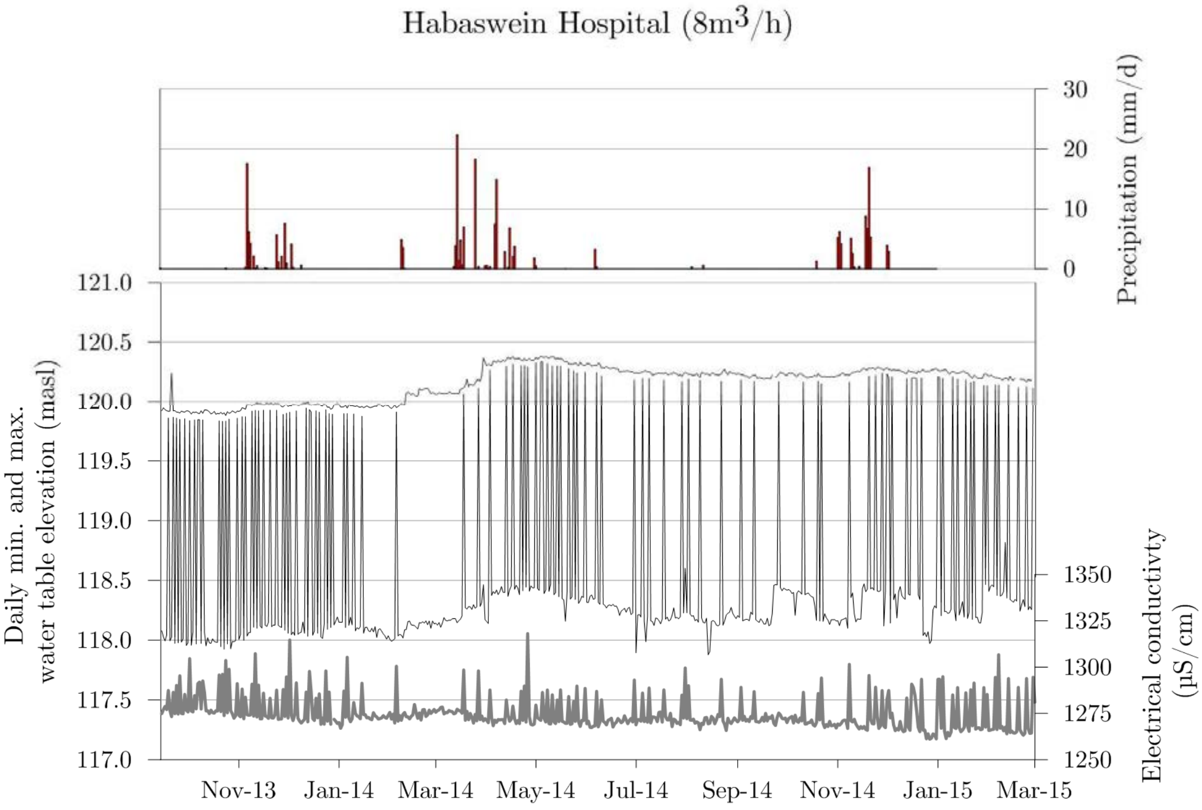
Habaswein Hospital (8m³/h)
Precipitation (mm/d)
30
20
10
0
Daily min. and max. water table elevation (masl)
121.0
120.5
120.0
119.5
119.0
118.5
118.0
117.5
117.0
Electrical conductivty (µS/cm)
1350
1325
1300
1275
1250
Nov-13
Jan-14
Mar-14
May-14
Jul-14
Sep-14
Nov-14
Jan-15
Mar-15

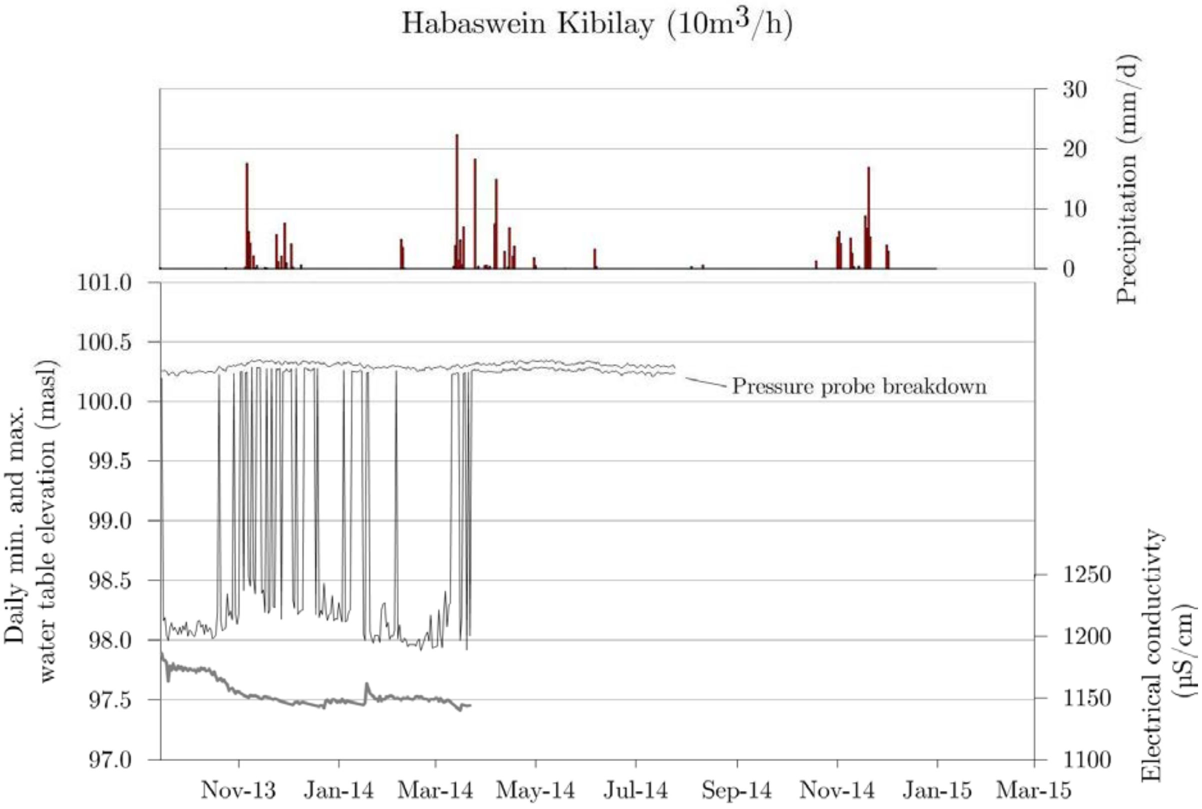
Habaswein Kibilay (10m³/h)
Precipitation (mm/d)
30
20
10
0
Daily min. and max. water table elevation (masl)
101.0
100.5
100.0
99.5
99.0
98.5
98.0
97.5
97.0
Pressure probe breakdown
Electrical conductivty (µS/cm)
1250
1200
1150
1100
Nov-13
Jan-14
Mar-14
May-14
Jul-14
Sep-14
Nov-14
Jan-15
Mar-15

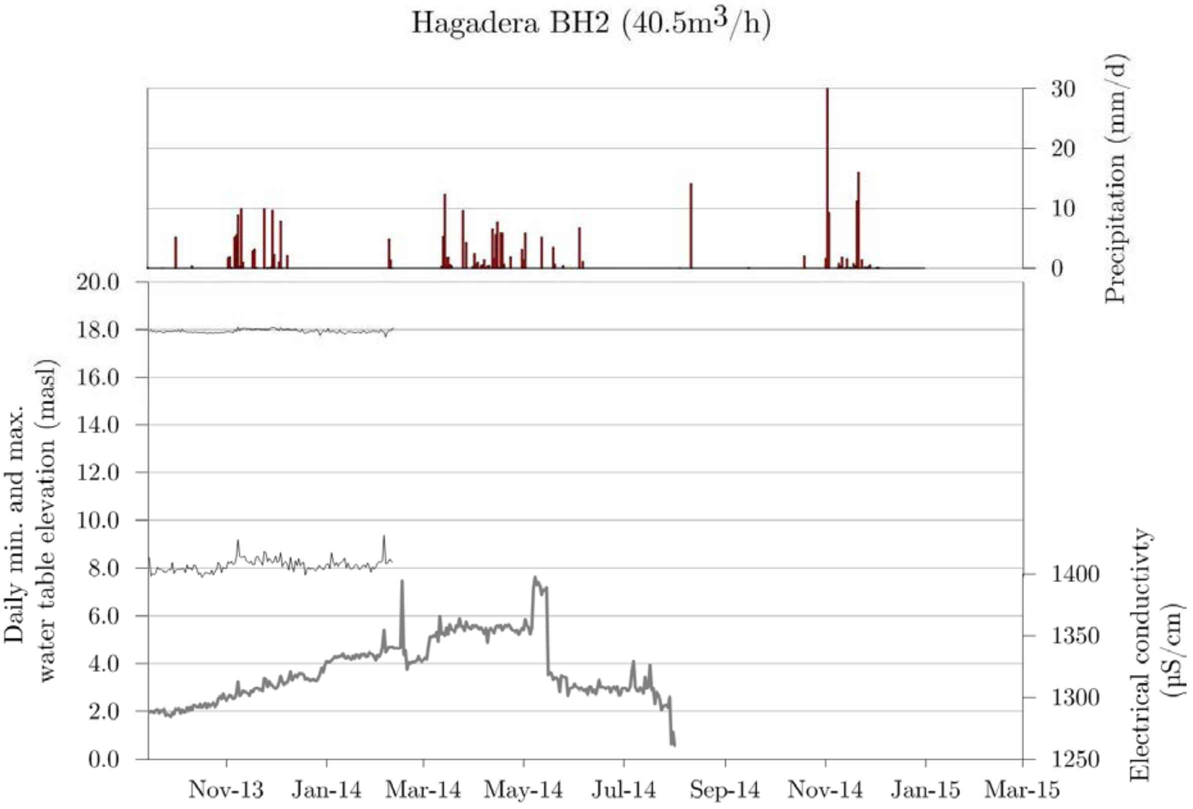
Hagadera BH2 (40.5m³/h)
Precipitation (mm/d)
30
20
10
0
Daily min. and max. water table elevation (masl)
20.0
18.0
16.0
14.0
12.0
10.0
8.0
6.0
4.0
2.0
0.0
Electrical conductivty (µS/cm)
1400
1350
1300
1250
Nov-13
Jan-14
Mar-14
May-14
Jul-14
Sep-14
Nov-14
Jan-15
Mar-15

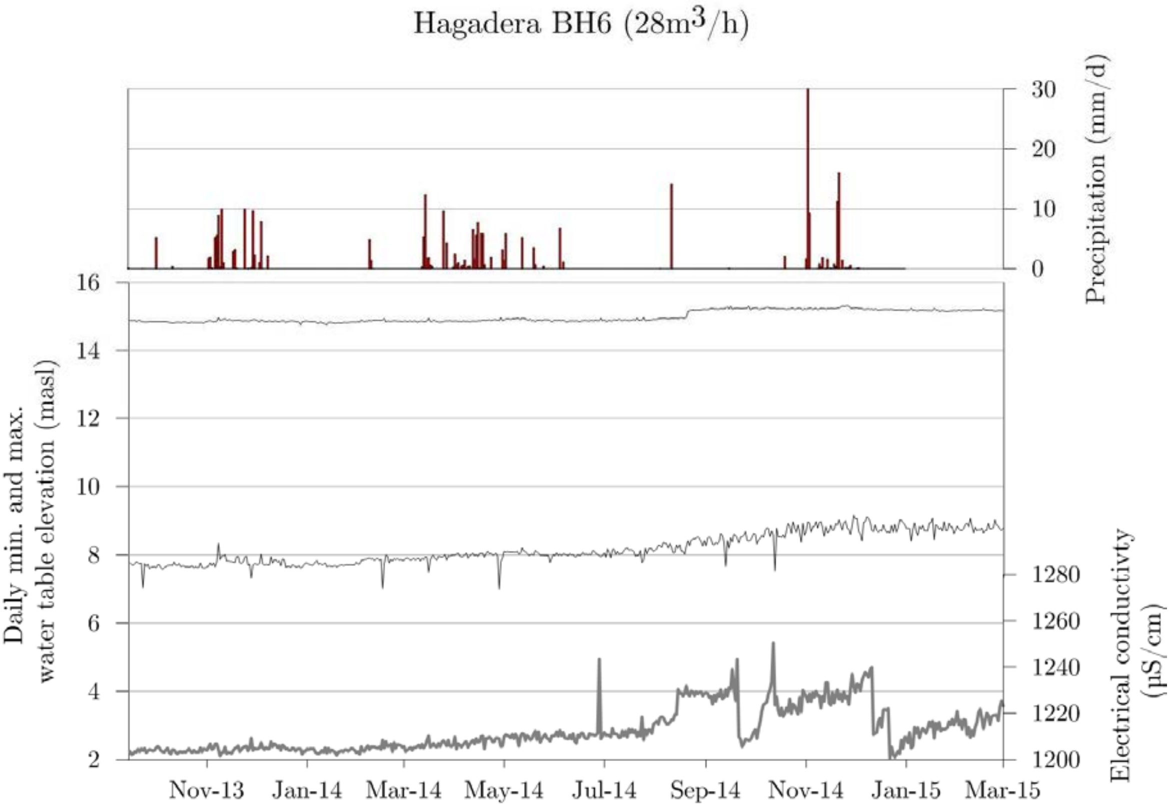
Hagadera BH6 (28m³/h)
Precipitation (mm/d)
30
20
10
0
Daily min. and max. water table elevation (masl)
16
14
12
10
8
6
4
2
Electrical conductivty (µS/cm)
1280
1260
1240
1220
1200
Nov-13
Jan-14
Mar-14
May-14
Jul-14
Sep-14
Nov-14
Jan-15
Mar-15

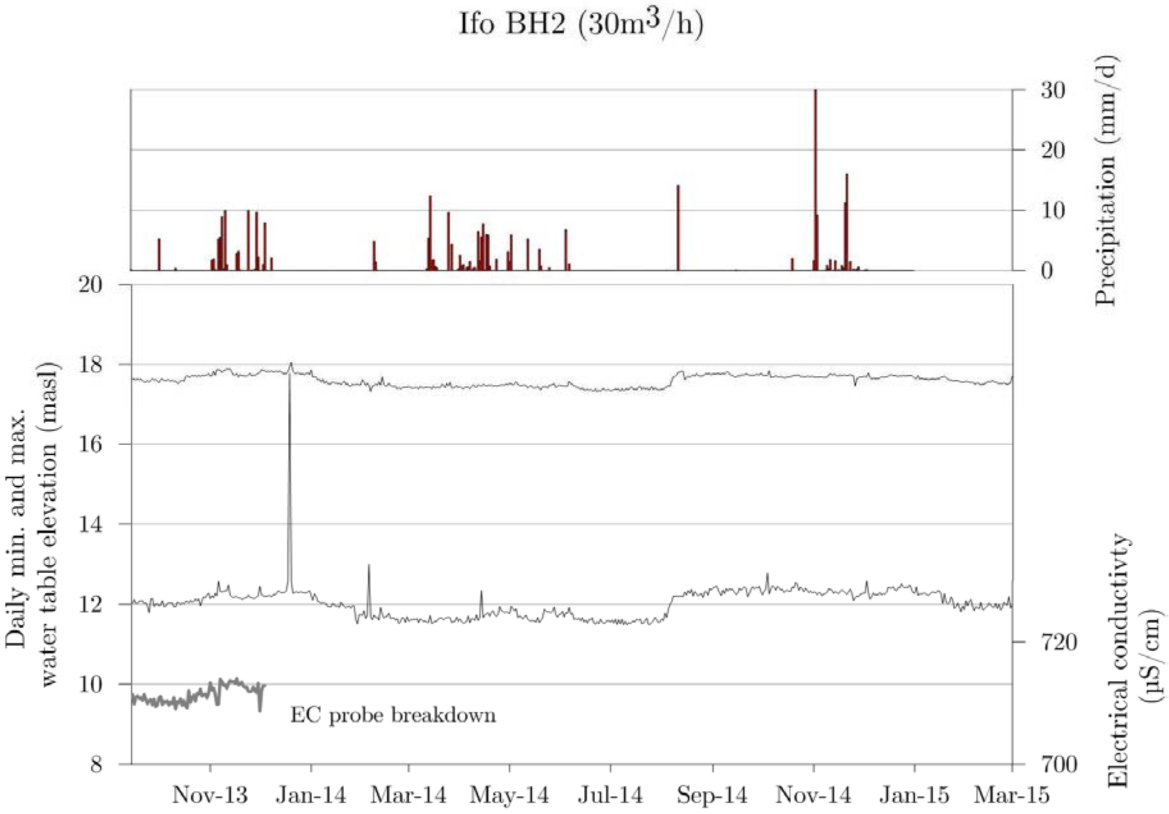
Ifo BH2 (30m^3/h)
30
20
10
0
Precipitation (mm/d)
20
18
16
14
12
10
8
Daily min. and max. water table elevation (masl)
720
700
Electrical conductivty (µS/cm)
EC probe breakdown
Nov-13
Jan-14
Mar-14
May-14
Jul-14
Sep-14
Nov-14
Jan-15
Mar-15

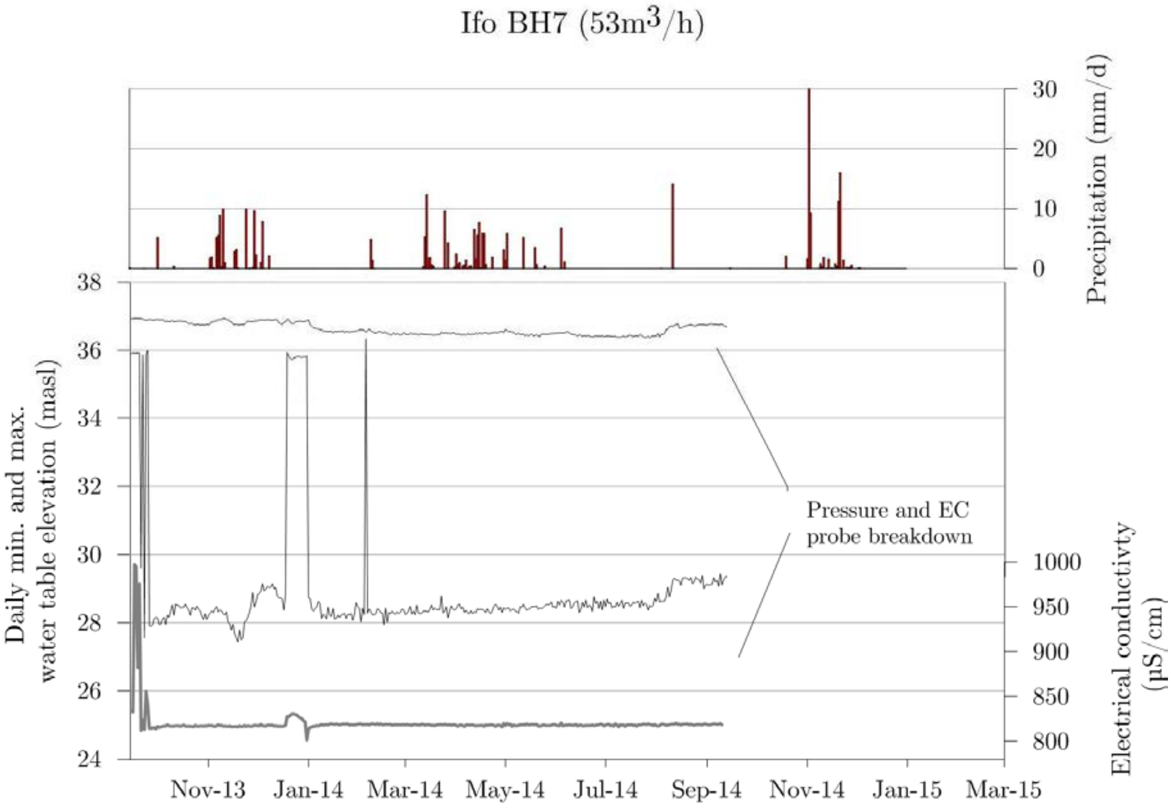
Ifo BH7 (53m^3/h)
30
20
10
0
Precipitation (mm/d)
38
36
34
32
30
28
26
24
Daily min. and max. water table elevation (masl)
1000
950
900
850
800
Electrical conductivty (µS/cm)
Pressure and EC probe breakdown
Nov-13
Jan-14
Mar-14
May-14
Jul-14
Sep-14
Nov-14
Jan-15
Mar-15

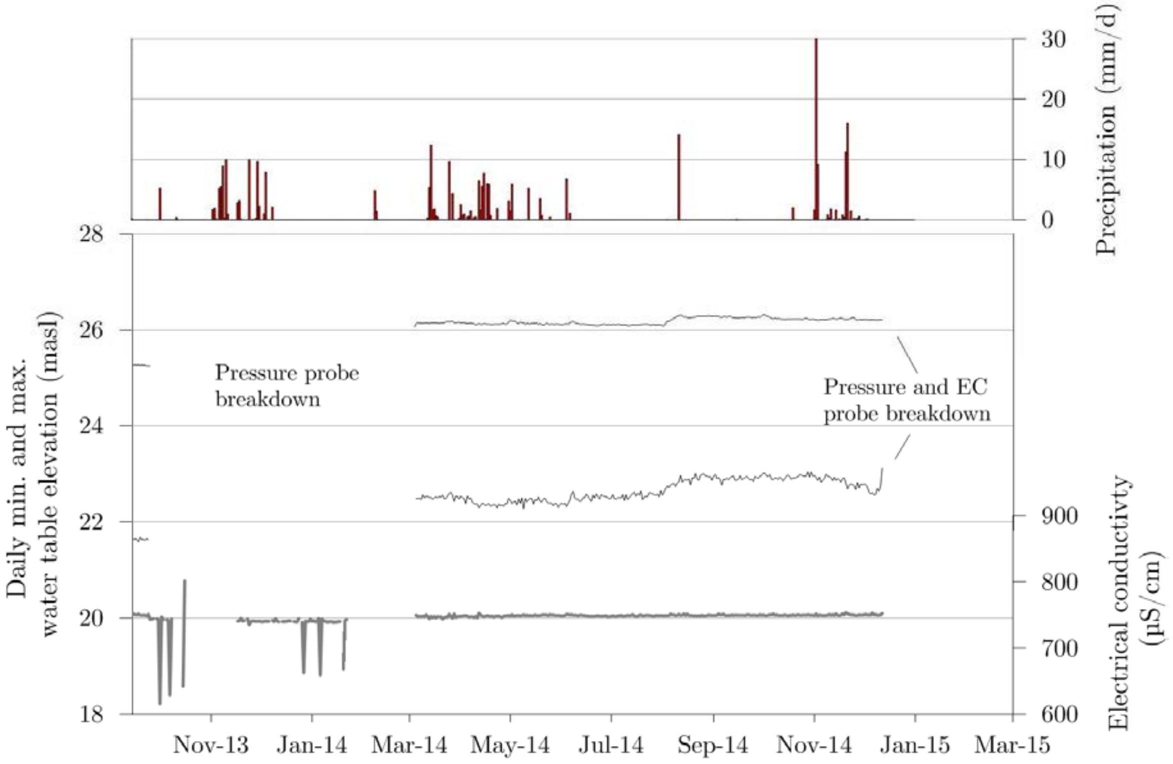

Ifo2 West BH1 ($56 m^3/h$)

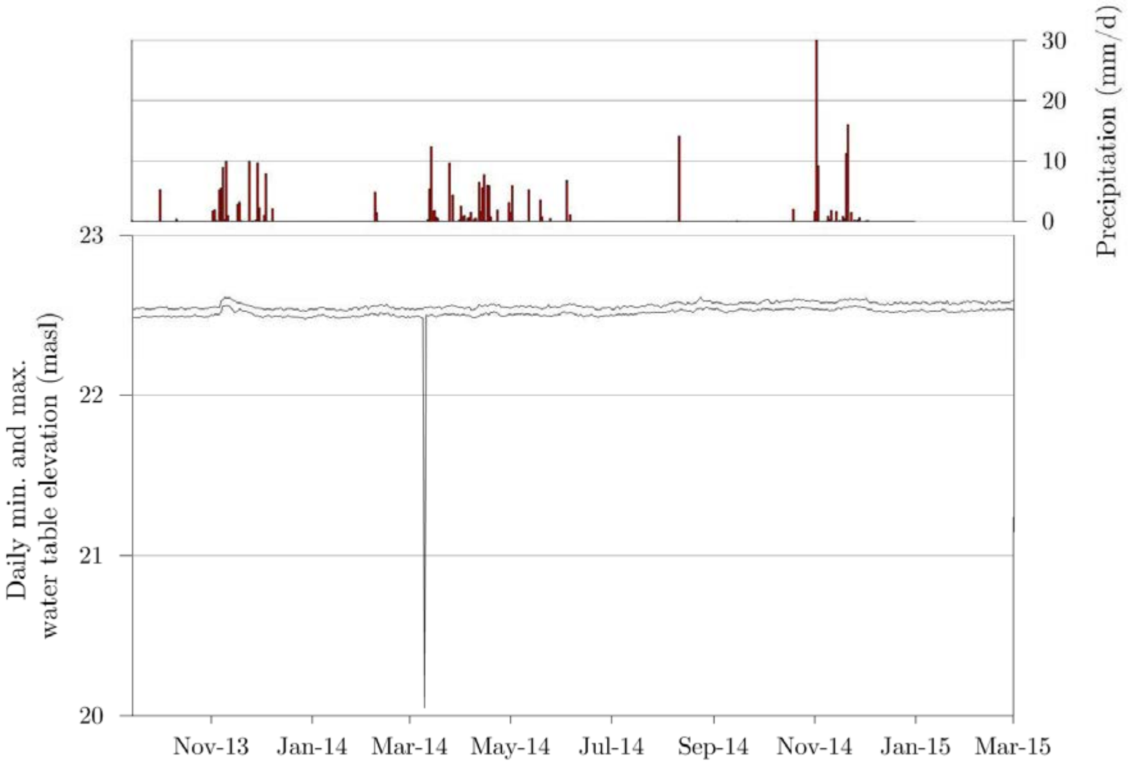

Kambioos (no pumping)

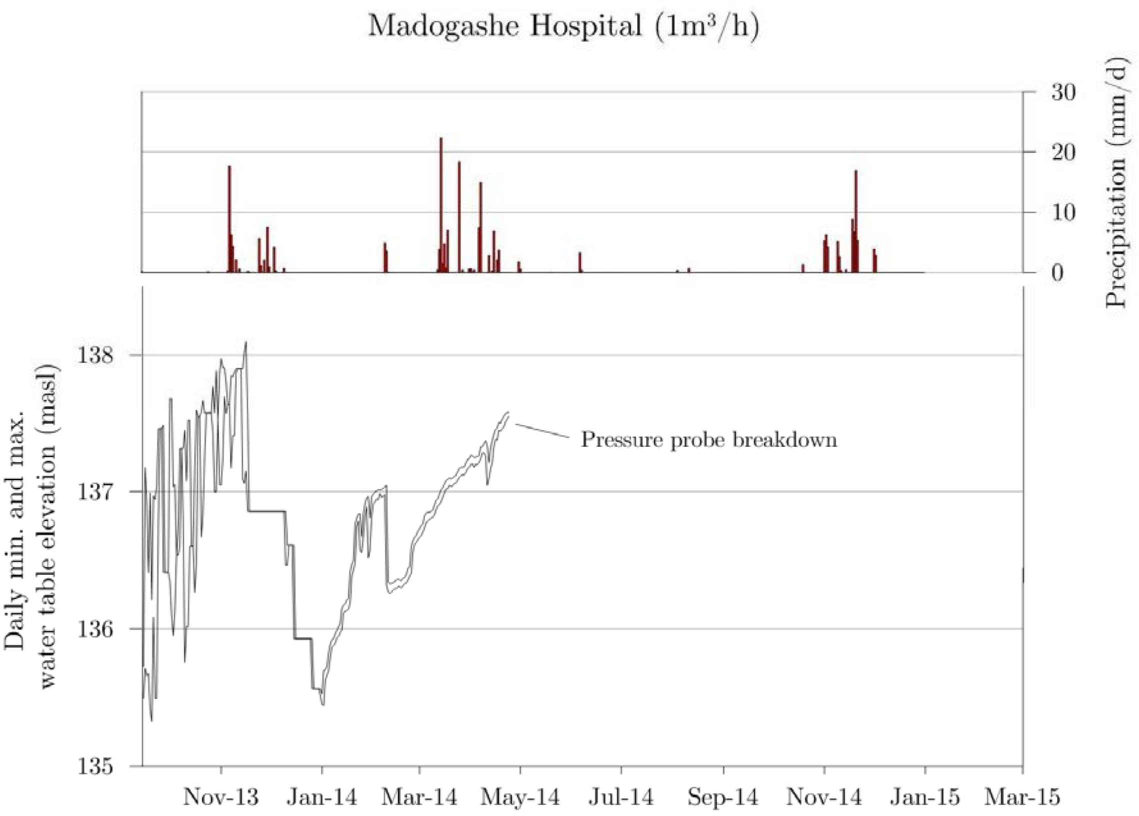
Madogashe Hospital (1m³/h)
30
20
10
0
Precipitation (mm/d)
138
137
136
135
Daily min. and max. water table elevation (masl)
Pressure probe breakdown
Nov-13
Jan-14
Mar-14
May-14
Jul-14
Sep-14
Nov-14
Jan-15
Mar-15

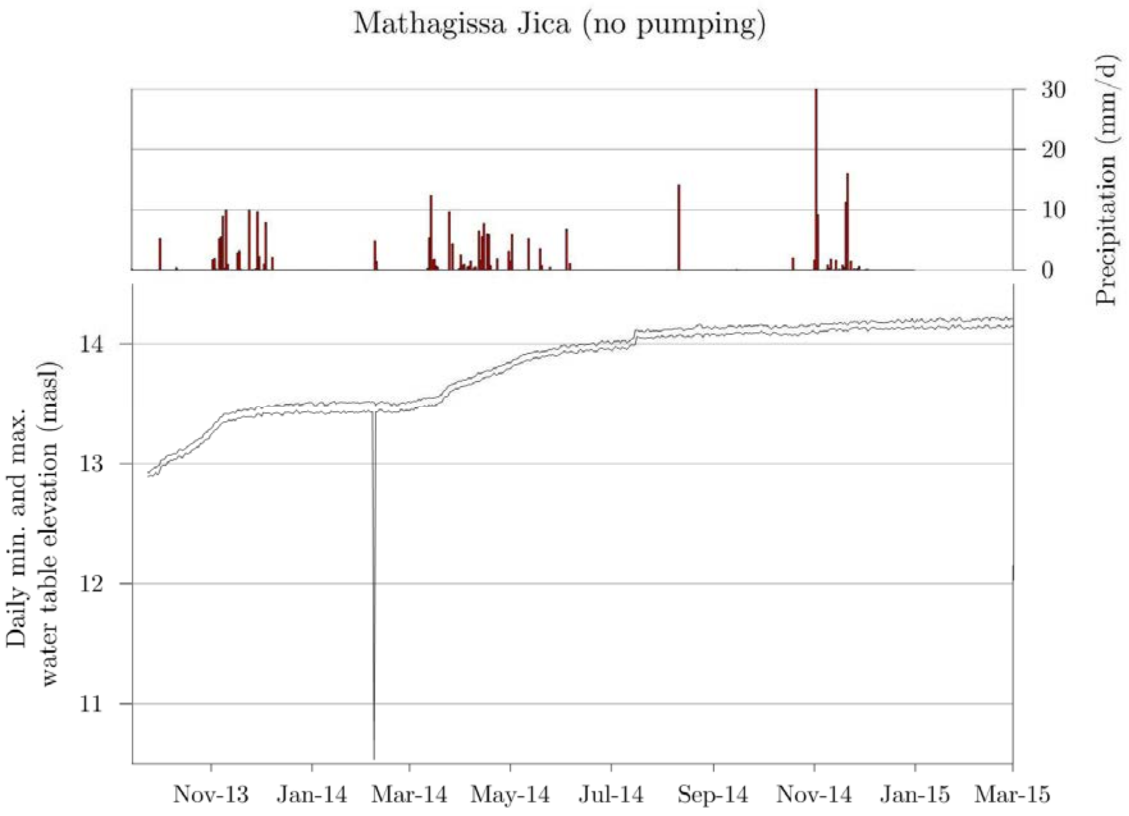
Mathagissa Jica (no pumping)
30
20
10
0
Precipitation (mm/d)
14
13
12
11
Daily min. and max. water table elevation (masl)
Nov-13
Jan-14
Mar-14
May-14
Jul-14
Sep-14
Nov-14
Jan-15
Mar-15

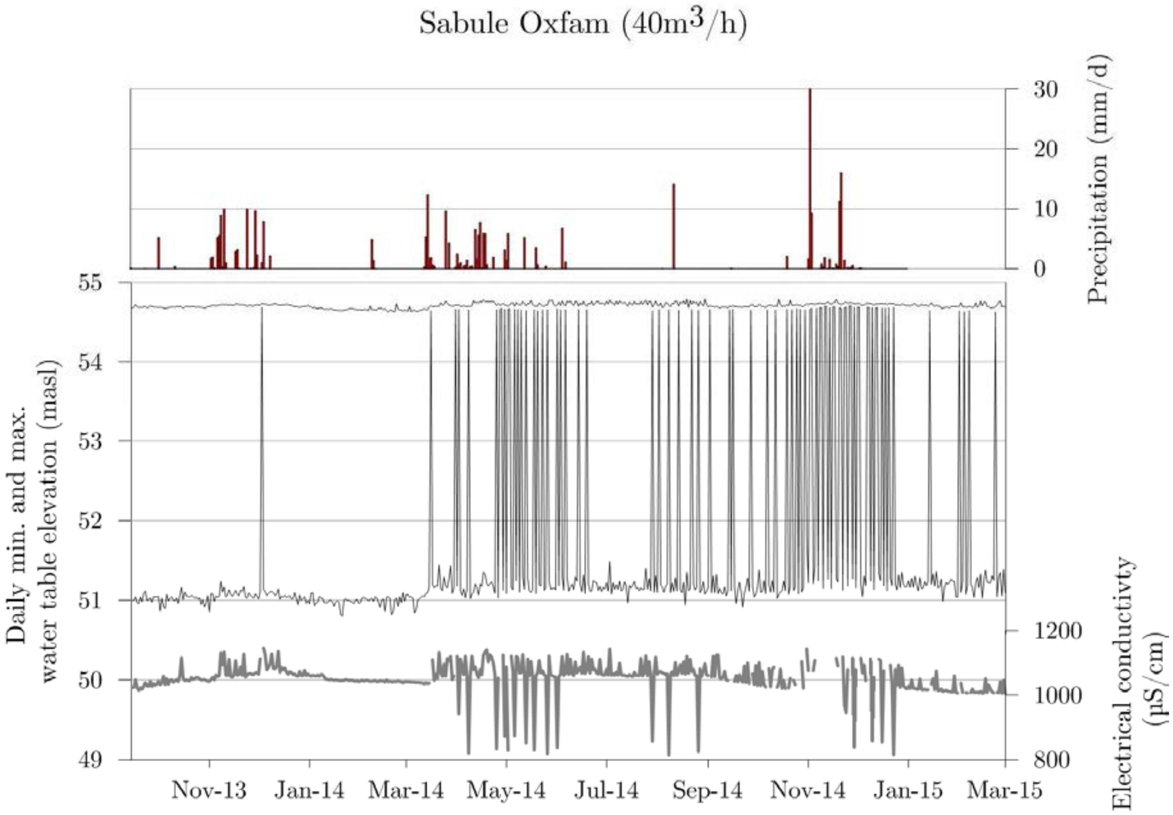
Sabule Oxfam (40m^3/h)
Precipitation (mm/d)
30
20
10
0
Daily min. and max. water table elevation (masl)
55
54
53
52
51
50
49
Electrical conductivty (µS/cm)
1200
1000
800
Nov-13
Jan-14
Mar-14
May-14
Jul-14
Sep-14
Nov-14
Jan-15
Mar-15

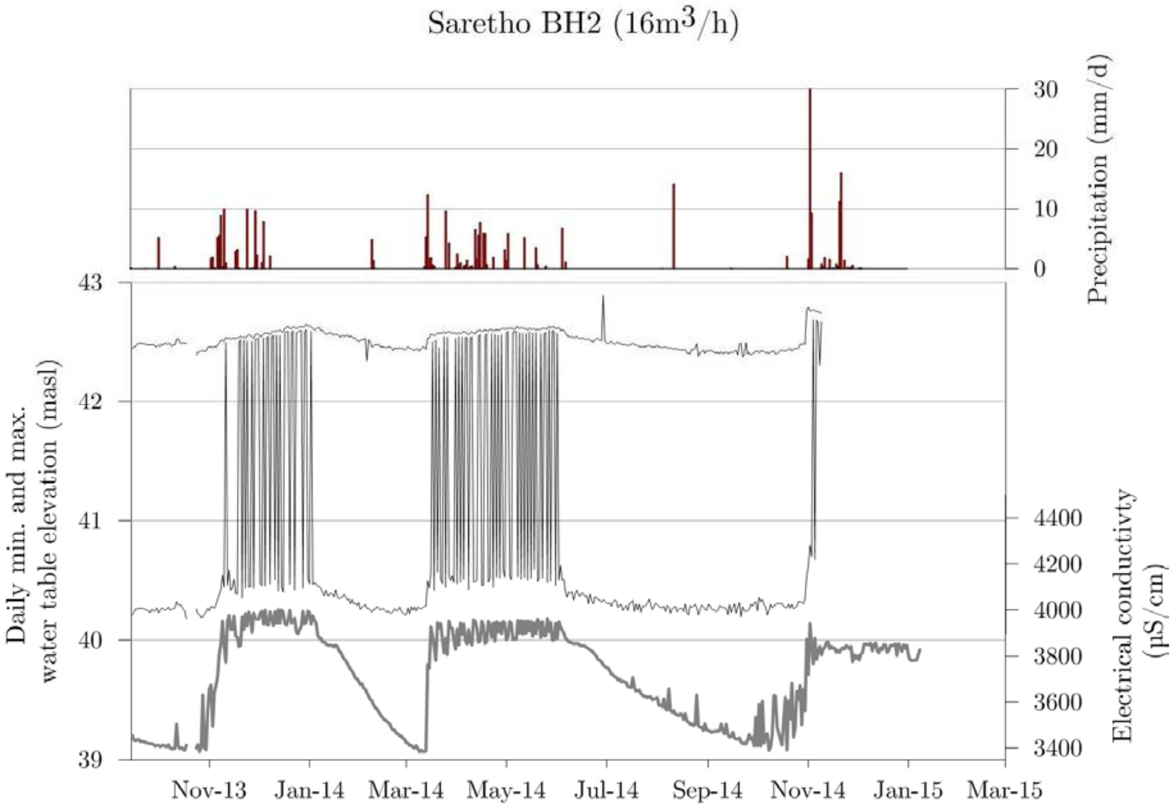
Saretho BH2 (16m^3/h)
Precipitation (mm/d)
30
20
10
0
Daily min. and max. water table elevation (masl)
43
42
41
40
39
Electrical conductivty (µS/cm)
4400
4200
4000
3800
3600
3400
Nov-13
Jan-14
Mar-14
May-14
Jul-14
Sep-14
Nov-14
Jan-15
Mar-15

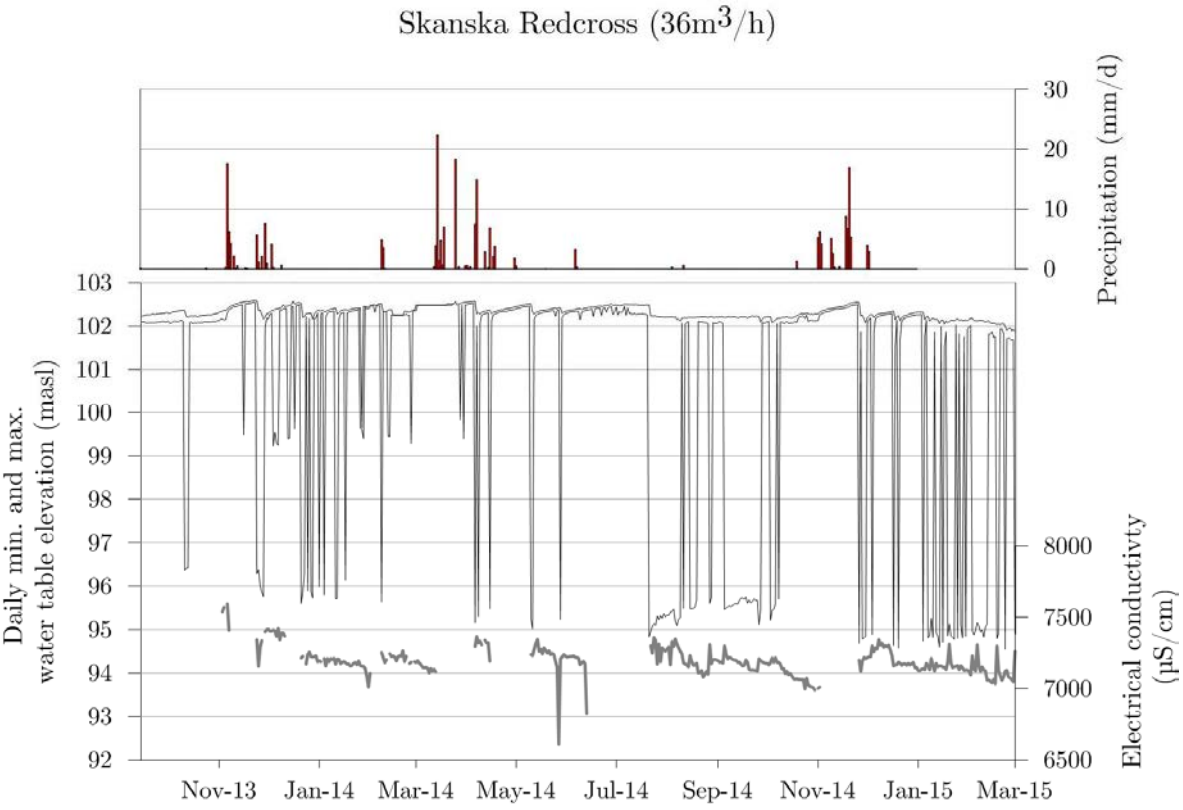

Remark: Dagahaley BH9 monitoring devices broke down few days after the installation and is therefore not presented in the study.

Appendix D

Drilling logs

Geological Log Hagadera borehole 1

Depth (m)	Description
0 - 4	top loose sandy soil
4 – 12	weathered limestones
12 – 56	highly weathered limestones.
56 – 70	fractured limestones intercalated with coarse grits.
70 – 90	weathered limestones.
90 - 102	fractured limestones intercalated with Lake Grits (aquiferous at 96 – 102 m).
102 - 120	highly Weathered limestones.
120 - 160	Weathered and fractured limestones mixed with coarse sands and gravel (aquiferous).
160 - 180	clayey deposits interbedded with limestones grits (aquiferous from 162 - 174).

Geological Log Hagadera borehole 2

Depth (m)	Description
0 - 4	loose top soils mixed with sand.
4 - 6	Fine sands.
6 - 12	Very fine sands mixed with silts.
12 - 18	Silty weathered sediments, sands and gravel.
18 - 28	Fine sands mixed with clays.
28 - 36	Pebbles, loose sands and gravel.
36 - 42	Old land surfaces – buried river channel.
42 - 60	Clays intercalated with sediments and silts.
60 - 74	Clays mixed with sands.
74 - 80	loose sands mixed with coarse gravel.
80 - 90	Fine sands and silts.
90- 122	slightly weathered and fractured limestones.
122 - 140	loose silts and fine sands.
140 – 152	Old land surfaces mixed with coarse gravel and sands - aquiferous.

Geological Log –Ifo replacement borehole 1

Depth(m bgl)	Description
0 - 2	top red soils mixed with silt.
4 - 6	Fine silt and clay Particles.
6 - 16	Sands, silts and gravel mixed with clays.
16 - 38	Compact Sediments.
38 - 46	highly weathered sediments.
46 - 62	slightly weathered and fractured sediments.
62 - 72	slightly weathered sediments mixed with fine quartzite sands.
72 - 74	clayey limestones.
74 - 82	weathered limestones.
82 - 88	clayey limestones mixed with fine sands, clays and silt particles.
88 - 96	Slightly weathered limestones.
96 - 106	highly weathered limestones, mixed with coarse sands, silts and gravel. Aquiferous at 94 – 106 m.
106 - 114	Clayey limestones, highly decomposed.
114 - 122	Weathered limestones mixed with fine to coarse gravel, sands and silts. Aquiferous zone.
122 - 132	Clayey sands and silts.
132 - 142	Pebblish limestones, fractured and aquiferous.
142 - 152	Clayey sands, silts and fine gravel particles.

152 - 162	Coarse sediments, sands and and gravel mixed with pebble stones. Aquiferous. Coarse in nature and porous. Main aquifer zone.

Geological Log –Ifo replacement borehole 1

Depth (m)	Description
0 - 2	Top red soils mixed with silt.
4 - 6	Fine silt and clay Particles.
6 - 16	Sands, silts and gravel mixed with clays.
16 - 38	Compact Sediments.
38 - 46	highly weathered sediments.
46 - 62	slightly weathered and fractured sediments.
62 - 72	slightly weathered sediments mixed with fine quartzite sands.
72 - 74	clayey limestones.
74 - 82	weathered limestones.
82 - 88	clayey limestones mixed with fine sands, clays and silt particles.
88 - 96	Slightly weathered limestones.
96 - 106	highly weathered limestones, mixed with coarse sands, silts and gravel. Aquiferous at 94 – 106 m.
106 - 114	Clayey limestones, highly decomposed.
114 - 122	Weathered limestones mixed with fine to coarse gravel, sands and silts. Aquiferous zone.
122 - 132	Clayey sands and silts.
132 - 142	Pebblish limestones, fractured and aquiferous.
142 - 152	Clayey sands, silts and fine gravel particles.
152 - 160	Coarse sediments, sands and and gravel mixed with pebble stones. Aquiferous. Coarse in nature and porous. Main aquifer zone.

Geological Log – Dagahaley replacement borehole 6

Depth (m)	Description
0 - 2	Top soils mixed with sand.
2 - 4	slightly compacted sands mixed with fine silts.
4 - 6	Greyish sands.
6 - 10	Silty clays.
10 – 12	Fine silts
12 – 14	Coarse gravel and sands
14 - 22	Silty clays mixed with coarse gravel and fine sands
22 – 26	Coarse gravel and sands.
26 – 40	Silty clays
40 - 60	slightly weathered limestones sediments mixed with sand and fine silt.
60 - 74	Silty clays.
74 - 76	Coarse sands, old river channel.
76 - 78	Silty clays.
78 – 100	Fine silts mixed with sands.
100 – 106	Coarse sands and gravel – aquiferous
106 - 122	Clayey limestones mixed with fine sands, clays and silt particles.
122 - 126	Coarse sands mixed with pebbles. Aquiferous zone.
126 - 146	silty clays.
146 - 154	highly decomposed limestones. Aquiferous zone.
154 - 160	Silty clays.

160 - 176	Coarse sands mixed with fine gravel. Main aquifer zone..
176 - 180	Clayey sands, silts and fine gravel particles.

Geological Log – Dagahaley replacement borehole 1

Depth (m)	Description
0 - 2	Top soils mixed with fine sand particles.
2 - 10	Whitish to brownish limestones mixed with fine silts.
10 - 12	Unconsolidated sandy silts.
12 - 16	Fine sands and silts, coarse in nature.
16 – 24	Silty sands and gravel
24 – 26	Coarse quartzite sands mixed with pebbles.
26 - 30	No samples collected
30 – 44	Coarse gravel and sands.
44 – 50	Silty sands mixed with clays
50 - 52	Coarse gravels mixed with pebbles, sands and gravel.
52 - 54	Silty sands.
54 – 56	Coarse sands mixed with gravel.
56 – 62	Silty sands and fine silts.
62 – 64	Sands and gravel (Coarse in nature)
64 - 70	Fine silty sands mixed with clays.
70 - 74	Coarse sand particles.
74 – 86	Clays mixed with silts.
86 – 92	Silts and coarse sands, slightly aquiferous.
92 – 100	Fine sands intercalated with silts and clays. Slightly aquiferous.
100 – 108	Coarse sands and gravel, aquiferous.
108 - 112	silty clays and fine sands.
112 - 118	coarse sands.
118 - 124	fine sands, medium sized.
124 - 146	Silty clays.
146 - 164	Weathered limestones mixed with silts, sands and gravel. Main aquifer zone.
164 - 180	Coarse sands and gravel. Aquiferous.

Appendix E

Pumping test at Dagahaley BH3

The analysis was carried out with the matlab hytool library, version 2.03.

Drawdown data:

Time	Time (s)	Drawdown (m)	Time	Time (s)	Drawdown (m)
02.10.2013 4:15	0	0.000	02.10.2013 7:45	12'600	1.655
02.10.2013 4:30	900	0.930	02.10.2013 8:00	13'500	1.669
02.10.2013 4:45	1'800	1.257	02.10.2013 8:15	14'400	1.667
02.10.2013 5:00	2'700	1.383	02.10.2013 8:30	15'300	1.676
02.10.2013 5:15	3'600	1.445	02.10.2013 8:45	16'200	1.675
02.10.2013 5:30	4'500	1.493	02.10.2013 9:00	17'100	1.671
02.10.2013 5:45	5'400	1.541	02.10.2013 9:15	18'000	1.683
02.10.2013 6:00	6'300	1.571	02.10.2013 9:30	18'900	1.682
02.10.2013 6:15	7'200	1.586	02.10.2013 9:45	19'800	1.676
02.10.2013 6:30	8'100	1.616	02.10.2013 10:00	20'700	1.674
02.10.2013 6:45	9'000	1.614	02.10.2013 10:15	21'600	1.669
02.10.2013 7:00	9'900	1.629	02.10.2013 10:30	22'500	1.650
02.10.2013 7:15	10'800	1.643	02.10.2013 10:45	23'400	1.662
02.10.2013 7:30	11'700	1.656			

Complete report diagnostic:

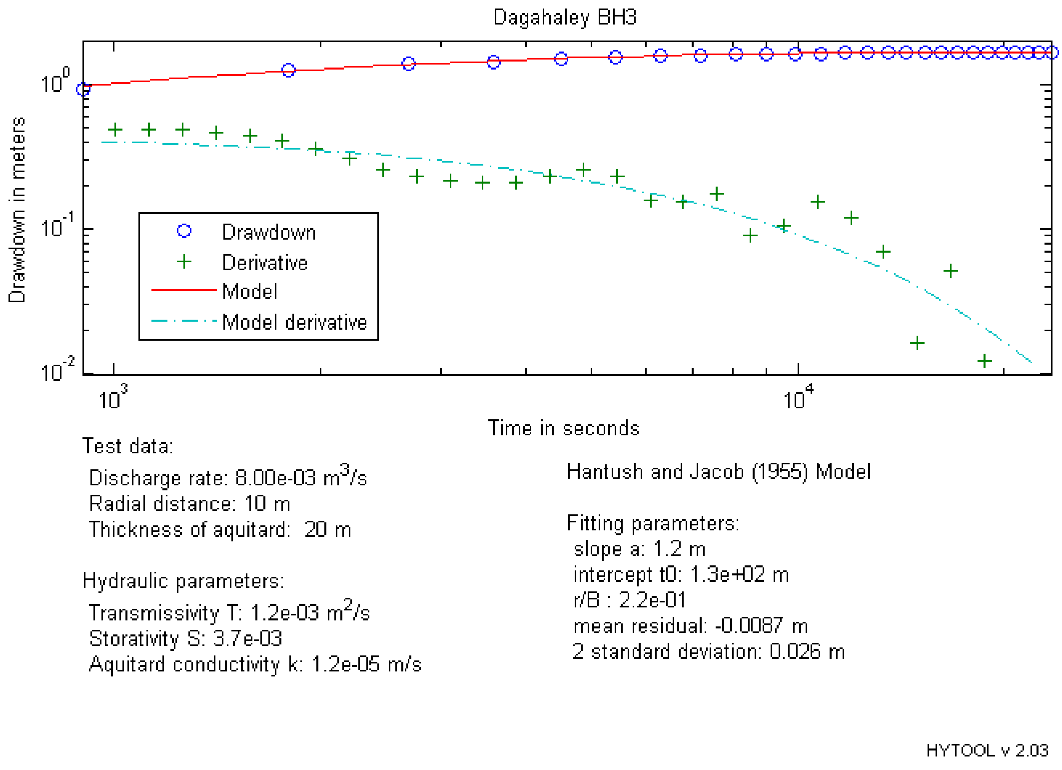

Test data:
Discharge rate: 8.00e-03 m^3/s
Radial distance: 10 m
Thickness of aquitard: 20 m

Hydraulic parameters:
Transmissivity T: 1.2e-03 m^2/s
Storativity S: 3.7e-03
Aquitard conductivity k: 1.2e-05 m/s

Hantush and Jacob (1955) Model

Fitting parameters:
slope a: 1.2 m
intercept t0: 1.3e+02 m
r/B : 2.2e-01
mean residual: -0.0087 m
2 standard deviation: 0.026 m

Appendix F

Synthesis of hydrochemical analyses for the period 1956-2011

BH	Name/type	Date	Coord X	Coord Y	EC [uS/cm]	TDS [mg/l]	Fe [mg/l]	Ca [mg/l]	Mg [mg/l]	Na [mg/l]	K [mg/l]	Sr [mg/l]	HCO3 [mg/l]	CO3 [mg/l]	SO4 [mg/l]	Cl [mg/l]	NO3 [mg/l]	NO2 [mg/l]	F [mg/l]	T [°C]	From
2485	Dadaab	Aug.1955	40.398	0.058	1190	720	0.3						470		23	94	0.01	0.01	0.7		GIBB 2004
2643	Dif	Feb.1957	40.991	0.982	24641	15100	0.7	495	501				200		1415	8170	0.01	0.01	1.2		GIBB 2004
2685	Liboi	Jun.1957	40.876	0.357	1174	710	1.5	71	45				400	0	31	142	0.01	0.01	3		GIBB 2004
2686	Alunjugul	Jun.1957	40.456	-0.029	1331	805	1.5						660		25	65	0	0.01	1.8		GIBB 2004
2687	Garissa	Jul.1957	39.667	-0.473	36064	22100	0.8						1330		1580	11400	0.01	0.01	9.4		GIBB 2004
2718	Kolbio	Aug.1957	41.076	-1.151	57768	35400	0.7	315	437				610		2450	11900	0	0.01	15.2		GIBB 2004
3033	Fafi	Jul.1960	40.303	-0.384	11276	6910	0	22							671	3180	16	1.2	2.3		GIBB 2004
3038	Galma Galla	Jul.1960	40.809	-1.182	20888	12800	0.2	126							2130	5500	0	0	1.1		GIBB 2004
3041	Lagh Bogal	Jul.1960	39.846	1.291	18603	11400	0.01	428							572	6080	0.6	0.09	1.8		GIBB 2004
2719	Kolbio	Feb.1961	41.157	-1.151	33000	25900	0	392							2430	12900	6.6	0	3.3		GIBB 2004
3110	N Sabule	Feb.1961	40.227	0.309	1150	730	0.1	70	47						42	148	42	2	2.5		GIBB 2004
3085	Wel Merer	Dec.1961	40.580	-0.174	1550	1040	0.3								107	164	0	0	2		GIBB 2004
3218	Habaswein	Mar.1963	39.384	0.964	1100	765	0	27		220					56	88	0.4	0	1		GIBB 2004
3240	Darken	Jun.1963	40.436	0.133	540	380	0	16	10	118	9				23	28	0	0	0.5		GIBB 2004
3155	Wajir	Aug.1963	40.091	1.742	2600	1450		9		455	36				123	690	3.8	1.4	8.2		GIBB 2004
3306	Wajir: (119m)	Aug.1964	40.091	1.782	2400	1480	0	82	58	333	45				85	644	27.5	2.3	1.1		GIBB 2004
3306	Wajir: (146m)	Aug.1964	40.091	1.782	2400	1540	0	90	67	333	45				92	644	27.5	5.5	1		GIBB 2004
3306	Wajir: (263m)	Sep.1964	40.091	1.782	6181	3750	0	309	118	860	44				73	2010	38	0.06	1.3		GIBB 2004
3411	Kurdi	Jun.1966	40.673	-0.738	21867	13400	0	560	170	3620	43		460		4800	3570	0	0	1.5		GIBB 2004
3591	Garissa E	Jan.1968	39.821	-0.376	9432	5780							338	48	1440	1880					GIBB 2004
3636	Madogashe	Nov.1969	39.169	0.718	17000	10600	0.1	50	0	3600	13		3100	422	1630	3100	57	3.3	2		GIBB 2004
3656	Giriftu	Jan.1970	39.742	1.991	650	472	0.1	15	57	30	10		366	0		18	22	0.3			GIBB 2004
3655	Habaswein	May.1970	39.432	1.061	1000	795	0.4	31	17	184	13		586	0	47	100	2.2	0.03	2.3	34	GIBB 2004
3667	Liboi	May.1970	40.876	0.357	950	716	0	58	46	62	15		396		51	140	5.3	0.03	1.2	35.5	GIBB 2004
3684	Kulan	May.1970	40.641	0.215	1800	1180	0	71	63	240	20		390	0	59	336	67	0.03	0.5	37	GIBB 2004
3697	W Meri	May.1970	39.824	0.382	1800	1200	0.05	10	46	520	5		854	0	87	150	2.7	0.03	2.2	37.3	GIBB 2004
3685	Dilmanyale	Aug.1970	39.604	0.811	1200	920	0.01	19	25	320	20		586	0	105	109	22	0.03	1.6	34	GIBB 2004
3687	Meri	Aug.1970	39.925	0.482	700	420	0.15	22	7	96	11		390	0	43	34	0.6	0	0.4	36.7	GIBB 2004

BH	Name/type	Date	Coord X	Coord Y	EC [uS/cm]	TDS [mg/l]	Fe [mg/l]	Ca [mg/l]	Mg [mg/l]	Na [mg/l]	K [mg/l]	Sr [mg/l]	HCO3 [mg/l]	CO3 [mg/l]	SO4 [mg/l]	Cl [mg/l]	NO3 [mg/l]	NO2 [mg/l]	F [mg/l]	T [°C]	From
3769	Hara Khto Khot	Aug.1970	39.901	0.891	4500	2750	0	12	31	880	17		644	0	192	816	0	0.07	1.9		GIBB 2004
3695	Dadaab	Oct.1970	40.308	0.058	710	520	0	34	29	80	14		476	0	41	38	5	0.03	0.7		GIBB 2004
3752	NW Meri	Mar.1971	39.557	0.636	1750	1190	0.04	4	6	456	6		776	0	77	182	0.09	0.03	0.8		GIBB 2004
3727	Abakorey	May.1971	39.627	0.754	750	545	0.4	17	11	174	7		478	0	30	50	0	0	1.4		GIBB 2004
3751	Shantabak	Jul.1971	39.741	0.464	1760	1080	0.3	20	17	368	11		573	0	56	278	0.04	0.02	0.6	37.5	GIBB 2004
3654	Habaswein	Aug.1971	39.432	1.061	1080	740	0.4	25	39	190	16		617	65	59	67	0	0.03	1.2	36.2	GIBB 2004
3218	Habaswein	Sep.1971	39.384	0.964	1080	720	0.2	27	18	240	16				55	67	0	0.01	1.1	36.2	GIBB 2004
3753	Lorian Swamp	Oct.1971	39.432	0.865	1530	1010	0.8	19	8	338	46		744	0	73	130	0	0.01	3		GIBB 2004
3770	W Dadaab	Oct.1971	39.977	-0.034	11800	8370	0.8	10	13	5275	18		994	152.3	933	3650	1.7	1.4	5.2		GIBB 2004
3781	Lorian Swamp	Jan.1972	39.437	0.800	1550	1130	0.2	12	9	425	7		847	0	83	136	1.1	0.03	1.5	35.1	GIBB 2004
3788	Fini	Feb.1972	40.013	0.416	710	460	0.1	30	25	100	15		344	29	21	40	0.4	0.01	0.7	37.6	GIBB 2004
3805	Sericho	Feb.1972	39.099	1.146	8000	5660	0.2	3	1	2200	8		2050	552	827	1080	0	0.6	20		GIBB 2004
3792	Kalalut	Mar.1972	39.639	0.754	1220	740	0	40	43	176	21		512	48	55	140	4.4	0	0.4		GIBB 2004
3814	Sericho	Mar.1972	39.099	1.146	14000	10000	0	16	0	3860	18		2430	996	973	2550	4.4	0.7	12		GIBB 2004
3804	W Kalakut	Apr.1972	39.471	0.694	10200	7600	0.6	17	19	2540	13		1698	98	850	2700	2.8	2.9	6.7	37.8	GIBB 2004
3811	Giriftu	Apr.1972	39.742	1.990	15500	11000	0.1	200	390	2740	34		220	0	467	5200	199	0.4	0.7		GIBB 2004
3820	Sabuli	May.1972	40.111	0.351	820	535	0	30	14	132	13		434	0	19	58	0	0	0.7	37.5	GIBB 2004
3821	Dagahaley N	Jun.1972	40.369	0.229	1550	938	0	105	51	104	16		371	0	31	256	24	0.04	0.2		GIBB 2004
3726	Khot Khot	Jul.1972	40.018	0.636	2050	1290	0.4	2	0	490	8		932	118	24	150	0	0.03	4.2		GIBB 2004
3822	Sericho (Hiloble)	Jul.1972	39.094	1.028	10400	7970	0.8	3	1	2860	26		2920	312	800	2470	1.3	0.1	37		GIBB 2004
3831	Alunjugul	Jul.1972	40.456	-0.029	1200	725	0.2	8	7.7	245	9		569	0	60	82	0	0	1.3	36.7	GIBB 2004
3852	Hag 0	Sep.1972	40.373	0.006	930	700	0.1	9	7	236	8		508	24	133	49	1.3	0.01	0.9		GIBB 2004
3860	S Meri	Nov.1972	39.969	0.347	750	525	0.1	30	16	123	15		359	31	17	69	4.4	0.01	0.2	39.2	GIBB 2004
3830	NW Habaswein	Feb.1973	39.234	1.208	10000	8080	0.3	8	3	2900	32		1680	312	1230	2720	4.4	0.13	7.6		GIBB 2004
3877	Kumahumato	Feb.1973	40.080	0.316	850	505	0.5	32	21	120	15		485	0	8	36	2.6	0.01	0.4		GIBB 2004
3902	Liboi	Apr.1973	40.872	0.356	1040	1040	0.1	85	40	76	14		434	0	61	124	8	0	0.7		GIBB 2004
3893	Hadado	May.1973	39.302	1.486	2550	1500	0.1	7	6	524	16		508	2.4	183	576	3.5	0	1.2		GIBB 2004
3915	Hadado	Jun.1973	39.419	1.532	6550	5000	0	56	65	1200	116		486	24	267	2850	0	0.01	0.7		GIBB 2004

BH	Name/type	Date	Coord X	Coord Y	EC [uS/cm]	TDS [mg/l]	Fe [mg/l]	Ca [mg/l]	Mg [mg/l]	Na [mg/l]	K [mg/l]	Sr [mg/l]	HCO3 [mg/l]	CO3 [mg/l]	SO4 [mg/l]	Cl [mg/l]	NO3 [mg/l]	NO2 [mg/l]	F [mg/l]	T [°C]	From
4514	Merti W/S	Aug.1986	38.647	1.061	930	560	0.1	1.1	1.7	206	13		376		30	54	0.01	0.01	2.1		GIBB 2004
4543	Merti CM	Aug.1986	38.647	1.061	890	533	0.1	1.2	1	230	13		364		29	46	0.01	0.01	1.8		GIBB 2004
nk	Logologo BH	Aug.1986	37.917	1.983	800	480	0.7	8.1	34	97	15		312		11	61	1.2	0.01	0.28		GIBB 2004
ShW	Garbatula	Aug.1986	38.516	0.538	1780	1066	0.3	7.6	87	220	18		740		40	164	1.4	0.01	0.74		GIBB 2004
River	Ewaso at Archer's	Sep.1986	37.672	0.637	185	112	2.8	2.8	4.8		11		70		0.3	9	0.61	0.01	0.31		GIBB 2004
ShW	Boji ShW	Sep.1986	38.339	0.568	1410	845	0.3	32	103		55		750		18	79	2	0.02	0.41		GIBB 2004
3864	Merti	Sep.1988	38.648	1.062	961	577	0.1	2	3	746	6		172	0	25	52			0.1		GIBB 2004
4543	Merti CM	Sep.1988	38.647	1.061	937	562	0.1	2	1	231	6		164		32	44			1.1		GIBB 2004
5795	Habaswein	Sep.1988	39.487	0.994	1922	1153	0.1	16	25	735	8		340	0	24	43			0.8		GIBB 2004
4176	Arbajahan	Oct.1988	38.958	2.097	1200	726															GIBB 2004
3915	Hadado	Jun.1989	39.419	1.532	8010	4803	0.2	43	59	1300	38		406	0	492	2225	0.7				GIBB 2004
4699	Yamicha	Mar.1991	38.612	1.724	620	372	0.01	8	8	137	17		264	0	4.8	27			0.6		GIBB 2004
9009	Liboi	Aug.1991	40.876	0.357	940	680	0.4	62	22	100	28		316	0	40	112	4.4	0	0.4	35	GIBB 2004
3852	Hag 0	Jun.1992	40.373	0.006	1400	900	1.4	45	62	165	30		468	0	12	130	13.3	0.01	0.4		GIBB 2004
9761	Hag 2	Jun.1992	40.374	0.008	930	650	0.1	9	8	192	7		450	0	4	53	0.8	0.01	0.7	36.2	GIBB 2004
9760	Hag 1	Aug.1992	40.373	0.004	1100	800	0	10	12	242	10		496	0	46.3	86	1.1	0.01	0.9		GIBB 2004
10094	Dag 1	Oct.1992	40.285	0.191	720	432		54	24	84	11		448	0	14	25	0	0	0.3		GIBB 2004
10095	Dag 2	Oct.1992	40.279	0.195	600	360		39	16	84	11		382	0	13	23	0	0	0.3		GIBB 2004
10096	Dag 3	Oct.1992	40.300	0.190	700	420		52	25	69	8		392	0	13	19	0	0	0.1		GIBB 2004
10098	Hag 4	Oct.1992	40.357	0.000	970	582		10	10	252	8		566	0	36	63			0.5		GIBB 2004
9384	Diri	Feb.1993	39.302	1.268	4600	3300	0.2	0.4	4	1120	22		1240	0	600	480	0		3		GIBB 2004
10418	Dadaab	May.1993	40.308	0.058	1050	800	0	20	14	229	11		400	0	49	124	2.2	0	1	37.1	GIBB 2004
10420	Alunjugul	May.1993	40.456	-0.029	1200	800	0	10	11	261	13		496	0	90	66	1.1	0.01	0.6	38.3	GIBB 2004
10421	Hag 5	May.1993	40.350	0.004	1050	800	0	15	12	270	12		506	0	36	59	1.1	0.01	0.8	39	GIBB 2004
10419	Dag 5	Jun.1993	40.284	0.176	665	470	0	30	28	95	18		370	0	11	15	0	0.01	0.1		GIBB 2004
10436	Liboi Mon. BH	Jun.1993	40.874	0.356	1300	787		81	33	221	15		390	0	87	224		0.01	1.5		GIBB 2004
9760	Hag 1	Jul.1994	40.373	0.004	1040	624		13	11	210	7		470	0	52	90			0.8		GIBB 2004
9761	Hag 2	Jul.1994	40.374	0.008	900	540		12	7	168	6		430	0	47	55	0	0	0.8	35.2	GIBB 2004

BH	Name/type	Date	Coord X	Coord Y	EC [uS/cm]	TDS [mg/l]	Fe [mg/l]	Ca [mg/l]	Mg [mg/l]	Na [mg/l]	K [mg/l]	Sr [mg/l]	HCO3 [mg/l]	CO3 [mg/l]	SO4 [mg/l]	Cl [mg/l]	NO3 [mg/l]	NO2 [mg/l]	F [mg/l]	T [°C]	From
10094	Dag 1	Jul.1994	40.285	0.191	710	426		54	23	74	10		388	0	19	22	0	0	0.1	34.6	GIBB 2004
10095	Dag 2	Jul.1994	40.279	0.195	620	372		43	15	75	10		392	0	18	21	0	0	0.1		GIBB 2004
10096	Dag 3	Jul.1994	40.300	0.190	680	408		55	13	74	10		346	0	18	18	0	0	0.1	34.4	GIBB 2004
10097	Hag 3	Jul.1994	40.362	-0.003	1240	744		18	14	242	6		442	0	1	160	0	0	0.9	36.5	GIBB 2004
10098	Hag 4	Jul.1994	40.357	0.000	1020	612		12	14	231	5		474	0	53	74			0.8	35.5	GIBB 2004
10099	Dag 4	Jul.1994	40.276	0.193	690	414		55	20	80	10		400	0	17	20			0.1		GIBB 2004
4341	Jarajilla: UCL	Jun.1995	40.782	-0.472	5580	3376	0.34	18	28	1327	33		970	0	530	1272	0	0	0	36.5	GIBB 2004
9760	Hag 1 UCL	Jun.1995	40.373	0.004	1210	732	0.01	10	11	239	8		531	0	35.3	68.3	0	0	0	36.2	GIBB 2004
9761	Hag 2 UCL	Jun.1995	40.374	0.008	1090	659	0.01	8	8	220	7		517	0	27	56	0	0	0	35.2	GIBB 2004
10094	Dag 1 UCL	Jun.1995	40.285	0.191	785	475	0.01	57	24	88	12		473	0	10.8	18.2	0	0	0	34.6	GIBB 2004
10096	Dag 3 UCL	Jun.1995	40.300	0.190	755	457	0.01	56	26	80	12		478	0	10.9	16.6	0	0	0	34.4	GIBB 2004
10097	Hag 3 UCL	Jun.1995	40.362	-0.003	1410	853	0.01	15	16	262	11		523	0	41.1	134.7	0	0	0	36.5	GIBB 2004
10098	Hag 4 UCL	Jun.1995	40.357	0.000	1210	732	0.01	12	12	237	10		551	0	41.6	85.6	0	0	0	35.5	GIBB 2004
3684	Kulan: GoK	Jul.1995	40.641	0.215	1500	1000	0	80	70	216	23		360	0	50	320	5.54	0	0.4		GIBB 2004
3684	Kulan: UCL	Jul.1995	40.641	0.215	1800	1089	0.01	66	61	199	20		362	0	35.1	278.5	97.1	0	0	36.8	GIBB 2004
3820	Sabuli: GoK	Jul.1995	40.111	0.351	700	490	0.01	28	19	129.7	15		350	0	20	70	0	0	0.3		GIBB 2004
3820	Sabuli: UCL	Jul.1995	40.111	0.351	805	487	0.01	30	19	125	13		394	0	18	50.1	0	0	0	36.3	GIBB 2004
3877	Kumahumato: GoK	Jul.1995	40.080	0.316	680	480	0.04	30	20	127.5	15		396	0	12	20	0	0	0.1		GIBB 2004
4313	Yumbis: GoK	Jul.1995	40.381	-0.186	3400	2057	0.1	4	53	846	4		700	40	400	585	0.6	0	2		GIBB 2004
4313	Yumbis: UCL	Jul.1995	40.381	-0.186	4130	2499	0.01	6	6	783	5		916	0	290	599.5	0	0	0	37.5	GIBB 2004
9009	Liboi: GoK	Jul.1995	40.876	0.357	960	670	0	81.6	38.4	87.2	16.3		328	0	40	155	1.66		0.4		GIBB 2004
9009	Liboi: UCL	Jul.1995	40.876	0.357	1190	720	0.01	71	48	84	14		393	0	36.6	121.6	7.75	0	0	33.8	GIBB 2004
9740	Ifo 1 GoK	Jul.1995	40.306	0.105	859	500	0.004	28	24	121.3	12		410	0	30	30	0.44		0.6		GIBB 2004
9740	Ifo 1 UCL	Jul.1995	40.306	0.105	810	490	0.01	30	25	118	13		454	0	25	32.5	0	0	0	36.7	GIBB 2004
9749	Ifo 2 GoK	Jul.1995	40.305	0.121	765	550	0	32	29	120.6	16		410	0	39	30	2.44		0.4		GIBB 2004
9749	Ifo 2 UCL	Jul.1995	40.305	0.121	872	528	0.01	39	29	116	14		458	0	25.7	35.8	6.6	0	0	33.9	GIBB 2004
9760	Hag 1 GoK	Jul.1995	40.373	0.004	1000	700	0	16	22	243	7		490	0	44	45	1.7	0	0.8		GIBB 2004
9761	Hag 2 GoK	Jul.1995	40.374	0.008	880	620	0.02	7.2	7.7	221.7	5		440	0	44	35	0.6	0	0.6		GIBB 2004

BH	Name/type	Date	Coord X	Coord Y	EC [uS/cm]	TDS [mg/l]	Fe [mg/l]	Ca [mg/l]	Mg [mg/l]	Na [mg/l]	K [mg/l]	Sr [mg/l]	HCO3 [mg/l]	CO3 [mg/l]	SO4 [mg/l]	Cl [mg/l]	NO3 [mg/l]	NO2 [mg/l]	F [mg/l]	T [°C]	From
9999	Ifo 5 GoK	Jul.1995	40.316	0.115	710	500	0	28	24	119.7	15		410	0	25	10	0.22		0.4		GIBB 2004
10097	Hag 3 GoK	Jul.1995	40.362	-0.003	1200	850	0.01	12	16.8	277.4	7.1		450	0	50	100	4.4	0.01	0.6		GIBB 2004
10098	Hag 4 GoK	Jul.1995	40.357	0.000	1000	705	0.02	8	13.4	242.1	6.3		474	0	50	40	0.7	0	0.6		GIBB 2004
10418	Dadaab	Jul.1995	40.308	0.058	1143	692	0.01	18	17	220	12		457	0	45	135.8	22.4	0	0	37.1	GIBB 2004
10420	Alunjugul: GoK	Jul.1995	40.456	-0.029	1000	700	0	10	19	246	9		470	0	50	40	1.1	0	2		GIBB 2004
10420	Alunjugul: UCL	Jul.1995	40.456	-0.029	1220	738	0.01	9	11	249	14		567	0	60.8	83.2	0	0	0	38.3	GIBB 2004
10422	Shantabak: GoK	Jul.1995	39.740	0.464	1600	1100	0.004	24	14.4	374.5	11.7		490	0	45	290	0		0.3		GIBB 2004
10422	Shantabak: UCL	Jul.1995	39.740	0.464	1800	1089	0.01	19	10	353	10		526	0	40.6	247.2	0	0	0	36.6	GIBB 2004
10437	Liboi L/S GoK	Jul.1995	40.864	0.352	900	630	0	50	46.3	83	18		296	0	50	105	3.76	0	0.6	36	GIBB 2004
Hag	Hag Pan UCL	Jul.1995	40.374	0.001	239	127	0.14	12	6	19	24		101	0	4.34	12.76	1.98	0	0	25.4	GIBB 2004
3685	Dilmanyale BH	Dec.1999	39.568	0.840	1439			25	80	210	5		720		110	127			1.3	33.4	GIBB 2004
4543	Merti CM BH	Dec.1999	38.663	1.053	1000			3	3	260	5		630		30	54			1.6		GIBB 2004
8692	Ademasajida BH	Dec.1999	39.448	1.039	1200			41	108	100	5		810		37	63			1.3	35	GIBB 2004
9009	Liboi BH	Dec.1999	40.873	0.350	1035			79	173				450		30	135			0.7	34.7	GIBB 2004
9380	Merti AA BH	Dec.1999	38.670	1.061	800			25	16	100	5		540		32	63			1.6	30.4	GIBB 2004
9573	Garbatulla W/S BH	Dec.1999	38.516	0.538	2300			130	360				1620		55	267			0.8	30.7	GIBB 2004
10418	Dadaab BH	Dec.1999	40.309	0.055	1217			32	61	180	5		630		35	137			1	35.6	GIBB 2004
10420	Alinjugul BH	Dec.1999	40.458	-0.032	1140			8	27	280	5		720		60	74			1.3	35	GIBB 2004
10527	Merti Muslim BH	Dec.1999	38.663	1.053	2100			11	25	490	5		900		70	295			1.4		GIBB 2004
10573	Habaswein ASAL	Dec.1999	39.511	1.015	1200			36	49	210	5		810		26	63			1		GIBB 2004
11730	SCE BH	Dec.1999	37.683	0.622	1300			93	281				1170		9	45			0.7	30.3	GIBB 2004
-1998	Lagh Boghal	Dec.1999	39.834	1.297	17770			352	1147	3000	100		360		800	8335			1	35.4	GIBB 2004
3820+	Sabule BH	Dec.1999	40.111	0.351	793			35	75	90	5		540		18	106			0.6	35.5	GIBB 2004
	Badhana ShW	Dec.1999	38.921	1.114	1000			51	67	140	5		810		18	40			1.4	26	GIBB 2004
	Boji ShW	Dec.1999	38.339	0.568	1900			98	366				1710		12	142			0.7	28.4	GIBB 2004
	Chandler's Spring	Dec.1999	38.079	0.780	1700			73	353				1440		10	70			0.6	31.2	GIBB 2004
	Dagahaley BH	Dec.1999	40.301	0.187	745			65	86	10	5		630		10	19			0.5	35	GIBB 2004
	El Dera	Dec.1999	38.835	0.603	1700			32	47	310	5		630		95	255			1.7		GIBB 2004

BH	Name/type	Date	Coord X	Coord Y	EC [uS/cm]	TDS [mg/l]	Fe [mg/l]	Ca [mg/l]	Mg [mg/l]	Na [mg/l]	K [mg/l]	Sr [mg/l]	HCO3 [mg/l]	CO3 [mg/l]	SO4 [mg/l]	Cl [mg/l]	NO3 [mg/l]	NO2 [mg/l]	F [mg/l]	T [°C]	From
	Hagadera BH	Dec.1999	40.357	-0.004	1260			18	46	230	5		720		30	98			0.8	36.5	GIBB 2004
	Ifo BH	Dec.1999	40.306	0.118	846			42	103	50	5		720		18	43			0.6	34.6	GIBB 2004
	Issack Abdile's	Dec.1999	40.061	1.757	1420			114	203				270		55	200			0.7	32.2	GIBB 2004
	Kula Mawe BH	Dec.1999	38.202	0.568	1800			86	357				1350		10	99			0.7	30.2	GIBB 2004
	Malka Daka ShW	Dec.1999	38.475	0.871	1000			65	117	30	5		720		6	99			1.1		GIBB 2004
	Malka Galla	Dec.1999	38.933	1.183	800			19	5	220	5		630		75	71			1.2	28.9	GIBB 2004
	MDG Galana Gof	Dec.1999	39.172	0.725	1100			86	129				540		80	77			0.7		GIBB 2004
	Sericho BH	Dec.1999	39.120	1.169	1200			30	39	250	5		900		16	33			1	28.9	GIBB 2004
	Wajir Girls ShW	Dec.1999	40.037	1.754	2330			174	375				450		45	535			0.8	32.6	GIBB 2004
	Wajir Minor	Dec.1999	40.060	1.745	3520			208	388				450		110	386			0.6	31.7	GIBB 2004
	Yuhud (qarry)	Dec.1999	40.104	1.725	1130			104	157				450		24	201			0.5	29.6	GIBB 2004
WRAP	Ewaso Ngiro	Mar.2000	37.664	0.633	275	165	7.9	16	10	24	6		126	0	0.3	11	0.12		0.28		GIBB 2004
3685	Dilmanyale BH	Nov.2000	39.568	0.840	1507	1131		29	28	330	15		519		70	140				32.7	GIBB 2004
3727	Abakorey BH	Nov.2000	39.708	0.630	866	729		30	21	160	10		427		20	61				35.2	GIBB 2004
5795	Habaswein BH	Nov.2000	39.492	1.012	1023	789		20	23	215	15		561		24	44				33.7	GIBB 2004
10418	Dadaab BH	Nov.2000	40.309	0.055	1174	871		22	6	240	10		451		18	124				36.8	GIBB 2004
10420	Alunjugul BH	Nov.2000	40.458	-0.032	1142	928		11	10	280	10		512		30	75				30.7	GIBB 2004
10422	Shantabak BH	Nov.2000	39.741	0.462	1731	1097		23	12	200	10		519		45	288				36.9	GIBB 2004
12412	Garfasa BH	Nov.2000	38.594	0.944	3760	2785		10	23	1225	23		549		300	663				31.5	GIBB 2004
3687+	Meri BH	Nov.2000	39.848	0.492	827	658		49	29	115	10		366		14	75				35.8	GIBB 2004
3820+	Sabule BH	Nov.2000	40.111	0.351	795	757		38	17	113	10		519		0	61				34.9	GIBB 2004
	Badhana BH	Nov.2000	38.921	1.114	11600	10462		6	31	4250	55		2745		450	2925				32.4	GIBB 2004
	Boji BH	Nov.2000	38.340	0.568	1135	1112		25	46	65	20		903		10	44					GIBB 2004
	Boji ShW	Nov.2000	38.339	0.568	1591			68	126	148	50		915		12	114				29.6	GIBB 2004
	Dgahaley BH	Nov.2000	40.301	0.187	746	661		46	26	88	10		458		10	23				35.2	GIBB 2004
	Hagadera BH	Nov.2000	40.357	-0.004	1004	839		10	12	245	8		488		18	58				36.6	GIBB 2004
	Ifo BH	Nov.2000	40.306	0.118	842	622		16	9	68	8		476		20	25				35.1	GIBB 2004
	Kula Mawe BH	Nov.2000	38.202	0.568	1164	1241		68	111	168	63		939		45	101				30.6	GIBB 2004

BH	Name/type	Date	Coord X	Coord Y	EC [uS/cm]	TDS [mg/l]	Fe [mg/l]	Ca [mg/l]	Mg [mg/l]	Na [mg/l]	K [mg/l]	Sr [mg/l]	HCO3 [mg/l]	CO3 [mg/l]	SO4 [mg/l]	Cl [mg/l]	NO3 [mg/l]	NO2 [mg/l]	F [mg/l]	T [°C]	From
	MDG Galana Gof	Nov.2000	39.173	0.728	1196			42	24	225	23		433		140	71				30.9	GIBB 2004
	Sericho BH	Nov.2000	39.120	1.169	1460	1392		12	6	410	6		903		16	39				28.5	GIBB 2004
	Sericho ShW	Nov.2000	39.123	1.170	1010			21	9	235	9		506		22	53				25.7	GIBB 2004
	Shantabak ShW	Nov.2000	39.695	0.416	937			84	39	140	18		290		120	79				30.8	GIBB 2004
	Spring at Garbatula	Nov.2000	38.517	0.534	3000			93	151	395	83		760		150	538				31	GIBB 2004
13313	Elan BH	Aug.2001	39.319	0.767	12100			12	3		5		445		202	32	0		8.3	39.6	GIBB 2004
4543	Merti CM BH	Sep.2001	38.663	1.053	983			3	2		9		254		26	64	0		1.4	33	GIBB 2004
5795	Habaswein BH	Sep.2001	39.568	0.840	1022			18	23		11		367		22	44	0		1	35.2	GIBB 2004
6951	Bulesa BH	Sep.2001	38.560	0.956	1469			18	8		8		302		142	131	0		2.1	31.5	GIBB 2004
8693	Ademasajida BH	Sep.2001	39.448	1.039	1150			22	27		8		263		25	62	0		1.3	32.8	GIBB 2004
8693	Hadado BH	Sep.2001	39.498	1.037	1103			27	31		10		272		34	60	0		1.2	34.2	GIBB 2004
9380	Merti AA BH	Sep.2001	38.670	1.061	860			11	6		9		207		24	54	0		1.9	31	GIBB 2004
9573	Garbatula Community	Sep.2001	38.516	0.538	2060			55	127		57		445		52	218	42		0.4	29	GIBB 2004
10573	Habaswein	Sep.2001	39.511	1.015	1077			22	24		13		274		22	63	0		0.6	35.3	GIBB 2004
13332	Gurufa BH	Sep.2001	39.464	0.799				13	10		7		365		110	70	7		7.9		GIBB 2004
	Boji ShW	Sep.2001	38.339	0.568	1573			64	112		54		488		11	74	18		0.5	29.1	GIBB 2004
	Chandler's Spring	Sep.2001	38.079	0.780	1703			60	112		61				9	62	22		0.3	32	GIBB 2004
	Elsaboru BH	Sep.2001	38.847	1.091	472			36	14		13		128		11	21	9		0.9	37	GIBB 2004
	Garbatula Spring	Sep.2001	38.517	0.534	5380			24	169		130		440		420	1200	44		1.1	29.4	GIBB 2004
	Kula Mawe BH	Sep.2001	38.202	0.568	1695			60	109		58		495		26	75	20		0.4	31	GIBB 2004
	Malka Daka ShW	Sep.2001	38.483	0.871	442			20	11		6		120		11	20	0		0.9	26.7	GIBB 2004
	MDG Galana Gof	Sep.2001	39.169	0.722	804			67	18		12		135		67	50	48		0	31.2	GIBB 2004
	MDG Galana Gof	Sep.2001	39.173	0.724	864			46	10		12		250		65	48	22		0.5	29.7	GIBB 2004
	Muchuro BH	Sep.2001	38.618	0.965	2900			20	34		17		515		345	266	10		2.2	32.5	GIBB 2004
	Urura (Hururu Merti)	Sep.2001	38.790	0.542	2900			9	5		13		366		300	442	4		1.2	37	GIBB 2004
	Waliyana-Garbatula	Sep.2001	38.513	0.540	2400			58	144		66		436		83	320	40		0.6	31.9	GIBB 2004
13331	Kumahumato BH	Oct.2001	40.081	0.314	664			31	20		9		209		9	35	0		7.6	35.4	GIBB 2004
13387	Welmerer BH	Oct.2001	40.580	-0.177	1642			0.03	0.5				46			931				39.6	GIBB 2004

BH	Name/type	Date	Coord X	Coord Y	EC [uS/cm]	TDS [mg/l]	Fe [mg/l]	Ca [mg/l]	Mg [mg/l]	Na [mg/l]	K [mg/l]	Sr [mg/l]	HCO3 [mg/l]	CO3 [mg/l]	SO4 [mg/l]	Cl [mg/l]	NO3 [mg/l]	NO2 [mg/l]	F [mg/l]	T [°C]	From
nk	Goriale (Malaamin)	Nov.2001	39.333	0.441	18000	8366	0.2	32	29	3410	13		580	50	500	4300	0		2		GIBB 2004
9758	Liboi	Jan.2002	40.878	0.357	990	690	0.6	0	29	170	14		310	0	50	76	0	0.16	0.6		GIBB 2004
3033	Fafi: MUDCSE	Jul.2002	40.303	-0.384	1167	382	0.036	70	114	60			69			0			1.1	31.2	GIBB 2004
4313	Yumbis: MUDCSE	Jul.2002	40.381	-0.186	405	428	0.044	23	38	10			86			0			1.1	31.2	GIBB 2004
10420	Alunjugul: MUDCSE	Jul.2002	40.456	-0.029	1216	350	0.058	9.8	16.2	61			66			0			1.3	31.2	GIBB 2004
3685	Dilmanyale BH	Aug.2002	39.568	0.840	1500	696		23	21	320	14		280			138	164		1.6	33.5	GIBB 2004
3727	Abakorey BH	Aug.2002	39.708	0.630	900	393		26	16	170	10		230			55	37		0.6	35.7	GIBB 2004
5795	Habaswein BH	Aug.2002	39.568	0.840	1100	477		18	22	220	16		300			95	36		1.4	34.1	GIBB 2004
9573	Garbatula Community	Aug.2002	38.516	0.538	2100	985		54	130	235	62		440			209	78		0.7	30.4	GIBB 2004
10418	Dadaab BH	Aug.2002	40.309	0.055	1200	537		22	15	235	12		230			118	53		1	34.5	GIBB 2004
3687+	Meri BH	Aug.2002	39.848	0.492	800	362		44	18	123	11		190			65	29		0.5	34.6	GIBB 2004
3781+	Gurufa BH	Aug.2002	39.464	0.799	2000	944		19	7	500	7		390			204	175		1.7	35	GIBB 2004
3820+	Sabule BH	Aug.2002	40.111	0.351	900	414		17	7	205	7		200			68	36		0.9	34.6	GIBB 2004
8693 ?	Hadado BH	Aug.2002	39.498	1.037	1100	517		25	28	205	12		320			62	61		1.3	35.7	GIBB 2004
	Boji ShW	Aug.2002	38.339	0.568	1500	735		64	103	145	52		450			75	23		0.5	27.2	GIBB 2004
	Ifo BH	Aug.2002	40.306	0.118	900	387		44	20	130	14		230			46	40		0.6	32.6	GIBB 2004
	Malka Daka ShW	Aug.2002	38.483	0.871	500	250		28	16	78	10		140			33	1		0.8	27.9	GIBB 2004
	MDG Galana Gof	Aug.2002	39.169	0.722	700	278		48	14	65	14		130			49	38		0.6	30.6	GIBB 2004
	Sericho BH	Aug.2002	39.120	1.169	1500	683		8	5	390	5		470			35	38		1.7	29.3	GIBB 2004
	Waliyana-Garbatula	Aug.2002	38.513	0.540	2400	1139		58	144	260	68		420			324	114		0.7	31.4	GIBB 2004
8693	Hadado South	Apr.2003	39.498	1.037	1105	786	0.17	21	36	175	14		466		51	67	7		1.3		GIBB 2004
13777	Damajale	Apr.2003	40.784	0.106	1364	774	0.18	14	32	210	14		264	0	70	224	16		0.5		GIBB 2004
nk	Habaswein	Apr.2003	39.568	0.840	1004	760	0.18	14	26	180	16		462		28	50	11		1.5		GIBB 2004
nk	Lagh Bghal BH	Apr.2003	39.834	1.297	20000	13453	0.21	361	534	4500	36		242		976	7750	29		0.6		GIBB 2004
3033	Fafi	Jul.2003	40.324	-0.391	10910	7034	0.03	19	27	2587	27		793	0	255	3546	32		2.7	37	GIBB 2004
3781	Gurufa	Jul.2003	39.464	0.804	2140	1582	0.01	11	11	486	12		793	0	41	256	13			35	GIBB 2004
4176	Arbajahan	Jul.2003	39.003	2.071	1390	968	0.01	14	12	254	5		458	0	29	216	9		0.8	32	GIBB 2004
4261	Sarif	Jul.2003	40.601	0.598	3050	2326	0.01	8	15	726	22		1159	0	48	373	20		3.6	37	GIBB 2004

BH	Name/type	Date	Coord X	Coord Y	EC [uS/cm]	TDS [mg/l]	Fe [mg/l]	Ca [mg/l]	Mg [mg/l]	Na [mg/l]	K [mg/l]	Sr [mg/l]	HCO3 [mg/l]	CO3 [mg/l]	SO4 [mg/l]	Cl [mg/l]	NO3 [mg/l]	NO2 [mg/l]	F [mg/l]	T [°C]	From
4270	Abakailey	Jul.2003	40.096	0.078	1620	1307	0	3	3	368	7		854	0	24	71	1			34	GIBB 2004
4524	Biamadhow	Jul.2003	40.415	0.617	2530	2168	0	3	5	639	12		1281	0	21	204	24			36	GIBB 2004
6885	Diff	Jul.2003	40.954	0.996	13610	8271	0.09	249	243	2600	42		122	0	265	4871	143		0.8	37.5	GIBB 2004
9380	Merti Action Aid	Jul.2003	38.665	1.073	990	719	0.01	7	6	183	12		445	0	9	62	1		2.3	32.5	GIBB 2004
9740	Ifo BH 1	Jul.2003	40.306	0.105	940	725	0.02	30	26	119	14		488	0	10	46	1		0.7	36.5	GIBB 2004
9760	Hagadera 1	Jul.2003	40.373	0.003	1250	912	0.01	10	12	237	10		549	0	14	89	4		1.1	38	GIBB 2004
10094	Dagahaley BH 1	Jul.2003	40.285	0.190	890	683	0.03	53	23	86	12		470	0	4	37	1		0.4	36.5	GIBB 2004
10418	Dadaab Centre	Jul.2003	40.308	0.058	1270	867	0.02	17	17	219	15		458	0	13	133	7		1.1	34	GIBB 2004
13387	Welmerer	Jul.2003	40.579	-0.174	1740	1260	0	6	5	373	7		671	0	35	197	1			35.5	GIBB 2004
nk	Alikune	Jul.2003	40.017	0.348	860	547	0.01	18	13	124	9		336	0	6	46	1			36	GIBB 2004
nk	Athibohol	Jul.2003	39.214	1.707	2730	1719	0.02	12	17	596	27		641	0	98	419	5		1.7	33	GIBB 2004
nk	Baraki	Jul.2003	39.580	0.657	1580	1278	0	5	4	347	6		763	0	21	151	2			35.5	GIBB 2004
nk	Dadajibula	Jul.2003	40.873	0.540	6790	4147	0.04	17	35	1624	55		1159	0	126	1192	65			37.1	GIBB 2004
nk	Garse Kofte	Jul.2003	39.158	1.815	1470	925	0.03	22	30	239	16		427	0	55	185	5		1.2	32	GIBB 2004
3877	Kumahumato	Jun.2005	40.080	0.316	743	382	0.14	368	103	50			1000			65			0.06		
4313	Yumbis: MUDCSE	Jun.2005	40.381	-0.186	1369	398	0.054	176	30	58			2050			68			0.052		
10417	Liboi	Jun.2005	40.872	0.356	1000																
10573	Habaswein	Jun.2005	39.500	1.075	800	560	0.1	21	19	225	15		520	0	25	60	0	0	0.9	38	
	Dagahaley BH 1	Oct.2010	40.286	0.188	754			53	22	85	11	0.5	488		12	20	2.1	0	0.3	35.8	Milnes 2010
	Dagahaley BH 3	Oct.2010	40.301	0.187	738			55	25	79	11	0.7	484		11	17	1.6	0	0.3	34.9	Milnes 2010
	Dagahaley BH 4	Oct.2010	40.277	0.191	750			47	20	94	13	1	478		16	24	2.5	0	0.2	36.1	Milnes 2010
	Dagahaley BH 6	Oct.2010	40.284	0.193	726			49	21	86	11	0.7	467		11	20	1.8	0	0.3	36.5	Milnes 2010
	Dagahaley BH 8	Oct.2010	40.287	0.202	854			64	29	91	13	0.9	510		16	46	3.8	0	0	35.6	Milnes 2010
	Dagahaley BH 9	Oct.2010	40.280	0.177	740			43	19	104	13	1.1	484		13	21	1.8	0	0.2	37.5	Milnes 2010
	Hagadera BH 2	Oct.2010	40.375	0.005	1092			11	12	232	8	1	565		41	71	9	0	1.1	37.2	Milnes 2010
	Hagadera BH 3	Oct.2010	40.362	-0.006	1273			15	15	266	10	0.9	576		46	116	13.2	0	0.7	37.3	Milnes 2010
	Hagadera BH 4	Oct.2010	40.357	-0.003	1243			13	14	259	10	0.7	591		46	105	11.1	0	0.8	37.4	Milnes 2010
	Hagadera BH 6	Oct.2010	40.376	0.008	1176			11	12	248	8	1.2	578		42	90	15.2	0	1.7	37.8	Milnes 2010

BH	Name/type	Date	Coord X	Coord Y	EC [uS/cm]	TDS [mg/l]	Fe [mg/l]	Ca [mg/l]	Mg [mg/l]	Na [mg/l]	K [mg/l]	Sr [mg/l]	HCO3 [mg/l]	CO3 [mg/l]	SO4 [mg/l]	Cl [mg/l]	NO3 [mg/l]	NO2 [mg/l]	F [mg/l]	T [°C]	From
	Hagadera BH 7	Oct.2010	40.372	-0.012	1180			9	9	266	6	0.8	555		57	89	9.1	0	0.8	38.5	Milnes 2010
	Hagadera BH 8	Oct.2010	40.383	0.001	1008			6	6	238	6	0.5	545		43	50	1.7	0	0.9	37.8	Milnes 2010
	Ifo 1	Oct.2010	40.307	0.102	821			30	25	118	13	0.6	489		29	28	2.9	0	0.5	36.7	Milnes 2010
	Ifo 2	Oct.2010	40.306	0.118	891			37	28	117	13	0.6	489		30	51	12.4	0	0.4	36.6	Milnes 2010
	Ifo 2 -A	Oct.2010	40.306	0.118	756			39	21	110	12	1	454		19	32	6.9	0	0.3	37.3	Milnes 2010
	Ifo 4	Oct.2010	40.318	0.106	846			32	24	123	13	0.9	486		28	41	4.7	0	0.4	37	Milnes 2010
	Ifo 5	Oct.2010	40.316	0.112	803			34	25	117	13	0.8	491		28	27	2.7	0	0.8	36.9	Milnes 2010
	Ifo 6	Oct.2010	40.313	0.121	923			42	29	121	14	0.9	483		30	61	16.5	0	0.6	37	Milnes 2010
	Ifo 7	Oct.2010	40.328	0.113	792			35	24	117	13	0.9	488		27	24	2.4	0	0.5	36.3	Milnes 2010
	Ifo 8 - A	Oct.2010	40.308	0.129	890			43	27	119	14	0.9	461		29	58	15.6	0	0.5	37	Milnes 2010
	Ifo 8 - B	Oct.2010	40.308	0.129	890			44	27	117	13	0.9	472		29	62	16	0	0.5	37	Milnes 2010
	Abakore new	Nov.2011	39.706	0.631	904			32	23	152	13	1.7	447		28	62	0	0	0.5		Blandenier
	BH O P/S IFO	Nov.2011	40.304	0.112	805			32	27	118	14	0.9	470		30	33	5	0	0.6		Blandenier
	Dagahaley BH 1	Nov.2011	40.286	0.188	741			47	19	99	12	0.9	453		13	26	2.2	0	0.3		Blandenier
	Dagahaley BH 4	Nov.2011	40.277	0.191	791			49	20	98	13	1	466		13	27	2.8	0	0.4		Blandenier
	Dagahaley BH 6	Nov.2011	40.284	0.193	785			47	19	97	12	0.9	457		13	30	2.7	0	0.4		Blandenier
	Dagahaley BH 8	Nov.2011	40.287	0.202	886			65	27	91	13	0.9	490		17	51	4.4	0	0.3		Blandenier
	Dagahaley BH 9	Nov.2011	40.280	0.177	806			48	23	96	12	1	488		13	21	1.6	0	0.3		Blandenier
	Dertu Old	Nov.2011	39.802	0.274	3030			3	3	772	5	0.2	1450		63	130	3.7	0	1.7		Blandenier
	Dimanyace new	Nov.2011	39.566	0.843	1654			22	27	308	18	0.8	552		136	178	24.4	0	1.2		Blandenier
	Gurufa	Nov.2011	39.443	0.814	3650			7	6	876	5	0.5	1201		261	474	9.2	0	4		Blandenier
	Gurufa Mowi	Nov.2011	39.465	0.804	2150			11	10	487	9	0.6	794		120	215	19.9	0	2.3		Blandenier
	Habaswein Hospital	Nov.2011	39.509	1.029	1275			25	35	217	15	0.8	623		48	95	1.7	0	0.8		Blandenier
	Habaswein KPLC	Nov.2011	39.506	1.028	1202			25	32	208	14	0.8	620		37	76	2	0	1.1		Blandenier
	Habaswein Waso	Nov.2011	39.474	1.016	1118			20	26	208	12	0.4	574		36	74	5	0	1.5		Blandenier
	Hadado S. new	Nov.2011	39.496	1.139	1117			24	31	205	13	0.7	610		48	66	3.1	0	1.1		Blandenier
	Hadado UNHCR	Nov.2011	39.437	1.540	6390			24	29	1350	29	1	466		297	1658	23.6	0	0.7		Blandenier
	Hagadera BH 2	Nov.2011	40.375	0.005	1291			16	17	258	10	1.5	556		46	114	21.5	0	0.9		Blandenier

BH	Name/type	Date	Coord X	Coord Y	EC [uS/cm]	TDS [mg/l]	Fe [mg/l]	Ca [mg/l]	Mg [mg/l]	Na [mg/l]	K [mg/l]	Sr [mg/l]	HCO3 [mg/l]	CO3 [mg/l]	SO4 [mg/l]	Cl [mg/l]	NO3 [mg/l]	NO2 [mg/l]	F [mg/l]	T [°C]	From
	Ifo 2	Nov.2011	40.306	0.118	903			39	27	122	14	0.9	473		30	47	8.9	0	0.5		Blandenier
	Ifo 5	Nov.2011	40.316	0.112	801			33	21	121	13	0.9	470		29	26	2.6	0	0.5		Blandenier
	Ifo 7	Nov.2011	40.328	0.113	790			35	23	117	13	0.9	470		28	26	2.7	0	0.5		Blandenier
	L. Bogo REF 70	Nov.2011	39.853	1.299	21100			339	344	4096	37	12.6	303		1147	6873	0	0	0		Blandenier
	Madogashe Hospital	Nov.2011	39.185	0.730	15430			10	11	4024	11	3.3	3616		1253	2614	97.1	0	1.5		Blandenier
	Mochefa	Nov.2011	40.274	1.008	1211			233	132	2334	25	6.9	299		621	3596	129.9	0	0.2		Blandenier
	Shantabaq Old	Nov.2011	39.747	0.461	1667			21	11	354	10	2.2	553		23	133	0.8	0	0.3		Blandenier
3715	SW Meri	unk.	39.847	0.495	700	480	0.2	39	25	102	11		440	0	24	64	1	0.01	0.7		GIBB 2004
4424	Kune	unk.	39.289	0.898	10900	6680	1.8	4	8	2400			2252			2067			8		
4425	Korbesa E	unk.	38.889	1.211	13000	7966															
4475	Malka Daka	unk.	38.471	0.840	6000	3600	2.96	48	48	1131			1053	0		1156			0.3		
4514	Merti E	unk.	38.817	1.039	4100	2512															
4586	Boji 3	unk.	39.133	1.365	4700	2844															
4587	Bule	unk.	38.968	1.566	1800	1089															
4588	Bule 2	unk.	38.792	1.404	18000	11030															
4643	Hururu Merti	unk.	38.769	1.551	1100	666															
6712	Wajir Girls	unk.	40.064	1.734	1900	1153	0														
9380	Merti	unk.	38.663	1.056	949	582															

Appendix G

Freshwater lens dynamics - Transient analysis

- **formation of a freshwater lens under various recharge and aquifer settings**
- **Cyclical recharge**

1. Transient analysis – formation of a freshwater lens under various recharge and aquifer settings

The durations to form a freshwater lens are investigated starting from an entirely saline aquifer. For transient simulations including transport, the couple recharge/transmissivity could not be simplified by the recharge ratio R_r. The impact of these two parameters on the freshwater lens size has to be assessed individually, as well as the impact of the aquifer thickness.

Based on the ponding model (experiment *C*) a series of simulations are carried out by varying the recharge rate R, the transmissivity T and the aquifer thickness D. For this transient analysis, the base model *C*, is defined with a recharge consistent with the results obtained in Chapter 3, that is of 120 x 10^6 m^3/y for the half model, a transmissivity of 0.2 m^2/s and a thickness of 500 m. For transport transient simulations, the porosity also plays a role on the freshwater lens dynamics; a value of 0.3 was defined for all models.

Influence of each parameter (except the porosity) on the freshwater lens surface is tested, firstly by doubling, and secondly by dividing by two the value of the parameter. The hydraulic gradient ∇H is not considered in this analysis since it influences the lens dynamics in the same way as the transmissivity (doubling the flux yields to the same result as doubling the transmissivity). Furthermore, this analysis can be transposed to thicker or thinner similar models by multiplying the recharge, the transmissivity and the aquifer thickness by the same factor.

The first observation is that the time required for reaching a steady state is for all simulations at least several thousands of years (Fig 1). This time is mainly controlled by the transmissivity and the aquifer thickness and less by the recharge rate. Increasing transmissivity shortens the time for reaching a steady state (Fig 1b), while greater aquifer thickness increases this time (Fig 1c). The transmissivity has also an effect on the size lens, with an inverse relation as the recharge rate. Aquifer thickness only influences the formation time of the lens but not its size.

The shorter time needed to reach steady state with a recharge of 240 x 10^6 m^3/y (Fig 1a) is explained by the model size that constrains and shortens the duration of the lens development compared to a model with a recharge of 120 x 10^6 m^3/y. Compared to the model with a recharge of 60 x 10^6 m^3/y, the effect of the model size also exists for the 120 x 10^6 m^3/y recharge model but in a lesser extent. This effect of the model size on the freshwater lens development is well highlighted with the variation of transmissivity. If the lens developments were not constrained by the model size, the curves on Fig 1b may have an identical slope before reaching steady state, but a slight increase of the slope is observable by decreasing the transmissivity.

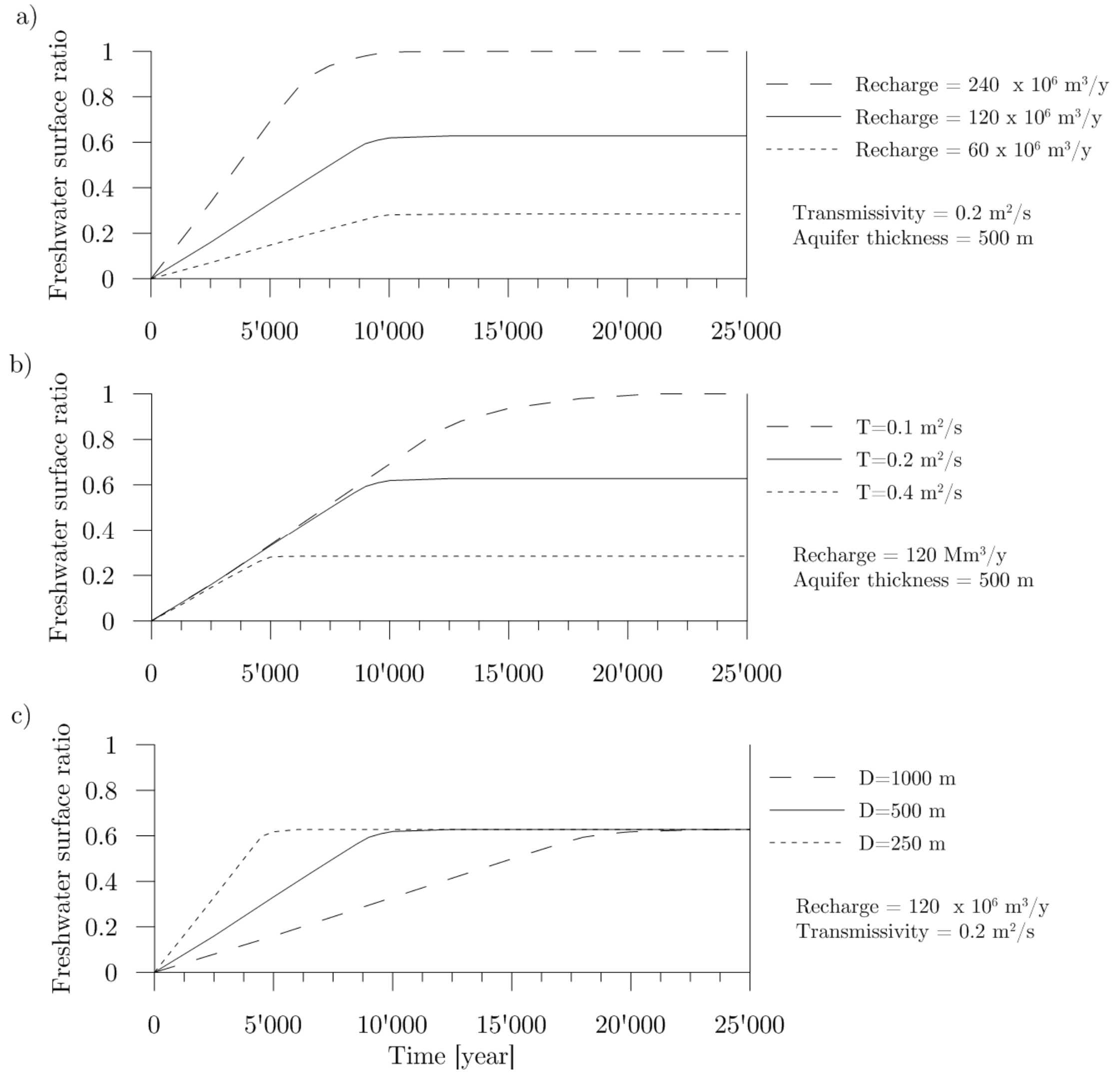

Fig. 1 : Formation a freshwater lens from a complete saline aquifer under various recharge rate R (a), transmissivities T (b) and aquifer thickness D (c). Simulations are based on the ponding model (experiment C).

If these curves are plotted in function of a normalised time t divided by the mean residence time $\bar{t}$ of the fresh water (Fig 2), it can be observed that the required time for reaching a steady state ranges around 1.1 times the mean residence time of the fresh water for all curves (Fig 2). Only changes on transmissivity have a little effect of the time for reaching the steady state (Fig 2b).

For different aquifer thicknesses, normalising the time by $\bar{t}$ yields to identical curves if recharge and transmissivity remain the same (Fig 2c).

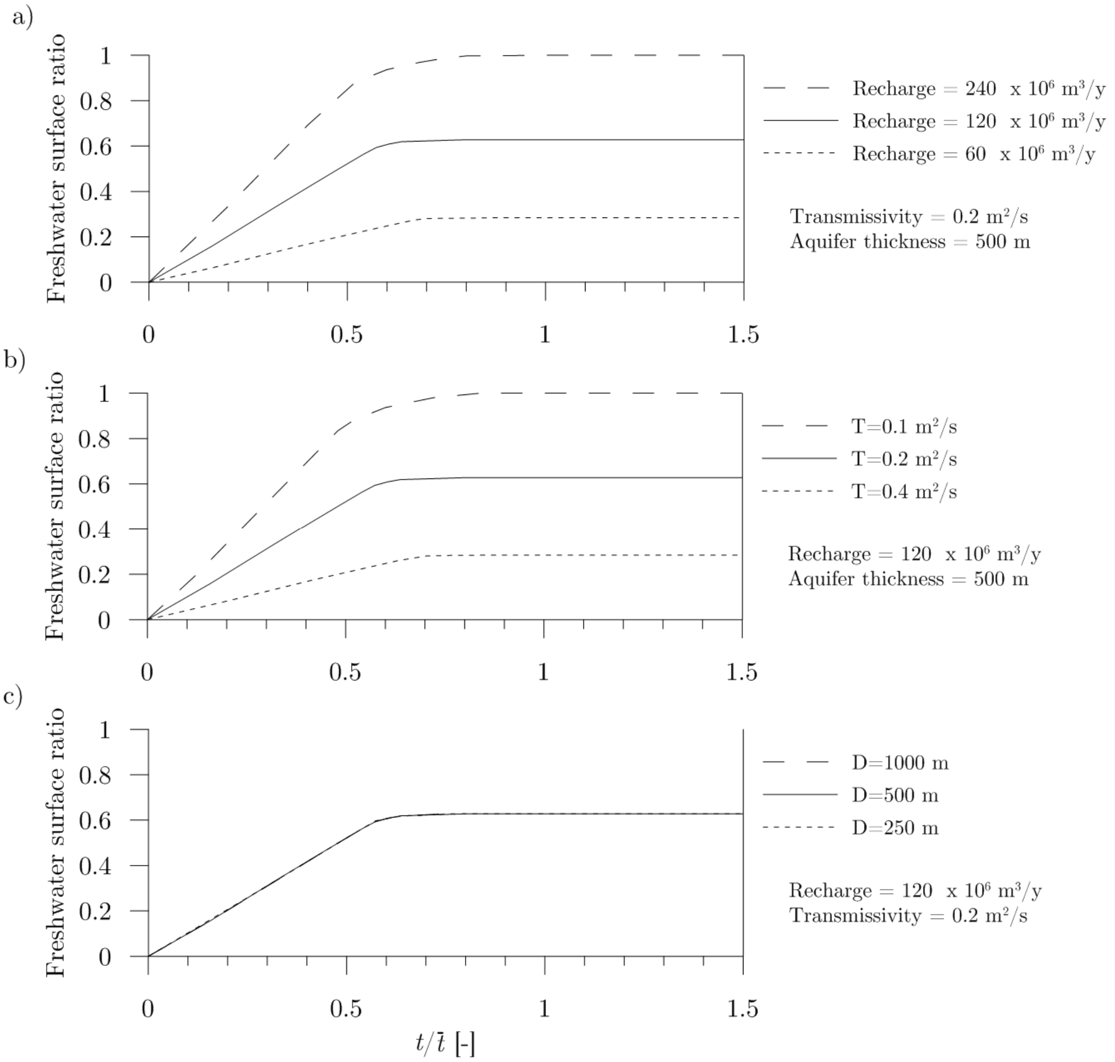

Fig. 2 : Same simulations as those in Fig. but with a normalised time divided by the mean residence time of the fresh water.

Similar simulations were carried out with a combined ponding/rainfall mechanism (experiment *G*) in order to assess the effect of rainfall on the duration of lens formation. As discussed in the steady state analysis (section 4.3), replacing part of concentrated recharge by rainfall has as effect to diminish the final size of the freshwater lens (freshwater surface ratio passes from 0.63 for a recharge of 120 x 10^6 m^3/y and a ponding recharge to 0.37 with a combined ponding/rainfall mechanism). The results shown on Fig. reveal that for freshwater lenses that are not highly constrained by the model size, the time to reach the steady state is the same as for the ponding model *C* (Fig 1).

Thus, these times do not change for the models with a recharge rate of 120 x 10^6 m^3/y, a transmissivity of 0.2 m^2/s and various aquifer thicknesses (Fig 3c). On the other hand, this time is significantly longer for the transmissivity curve of 0.1 m^2/s (Fig 3b). The recharge curve of 60 x 10^6 m^3/y (Fig 3a) and the transmissivity curve of 0.4 m^2/s (Fig 3b) are not displayed on the graphics because no lens forms with the combined ponding/rainfall mechanism and these recharge and transmissivity conditions.

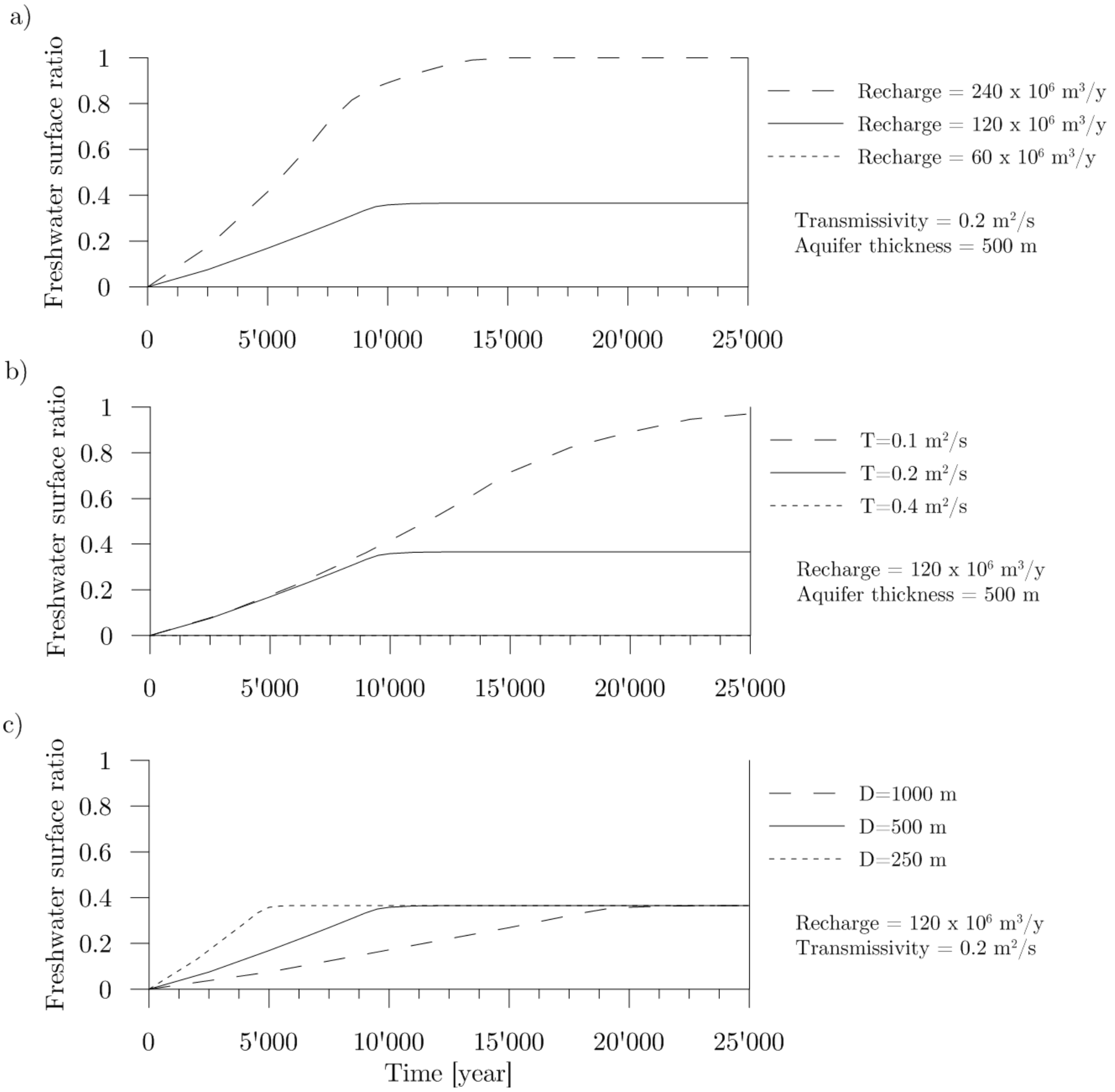

Fig. 3: Formation a freshwater lens from a complete saline aquifer under various recharge rate *R* (a), transmissivities *T* (b) and aquifer thickness *D* (c), based a combined ponding/rainfall recharge mechanism (experiment *G*).

2. Transient analysis – cyclical recharge

The analysis of recharge carried out in previous chapter revealed that, according to the recharge-discharge distribution model (Chapter 3), half of the concentrated recharge is controlled by events having a return period ranging at least between 2.9 and 6.7 years. In order to assess the impact of major flood events on the lens geometry variation, a model with cyclical extremes events is developed with a 50-years ponding recharge rate cycles.

During the 50-years low recharge period, a combined recharge is applied with ponding and rainfall mechanisms, each with an annual average recharge of 80 x 10^6 m^3/y. Then extreme cyclical recharge events 50 times higher than the base ponding recharge are simulated every 50 years. Ponding recharge during this extreme event contributes to half of the average annual concentrated recharge. Total recharge over the 50-years cycle for the half lens domain is 160 x 10^6 m^3/y. The model is run several times until reaching a dynamic steady state (concentrations and water levels are identical at the beginning and the end of the cycles). The dynamics of the lens is assessed by measuring the changes of the freshwater surface ratio and the evolution of the concentration along the limit between the freshwater lens and the brackish water at three lengths from the upstream boundary (10, 20 and 50 km).

As for previous transient analyses, this model shows the great inertia of the lens whose size variation remains imperceptible on the large scale during the entire cycle (Fig 4). Only small changes on the concentrations are observable along the 0.1 concentration line. A diminishing of about 0.01 occurs at a length of 10 km from the beginning of the lens, while at a distance of 50 km, the variation of concentration is imperceptible. This indicates that, even major recharge events do not affect the geometry of the lens. Thus, changes of the lens geometry are only expected on the long term (more than hundreds of years) if the annual average recharge varies, for instance due to climate changes or due to land or water use changes in the catchment area.

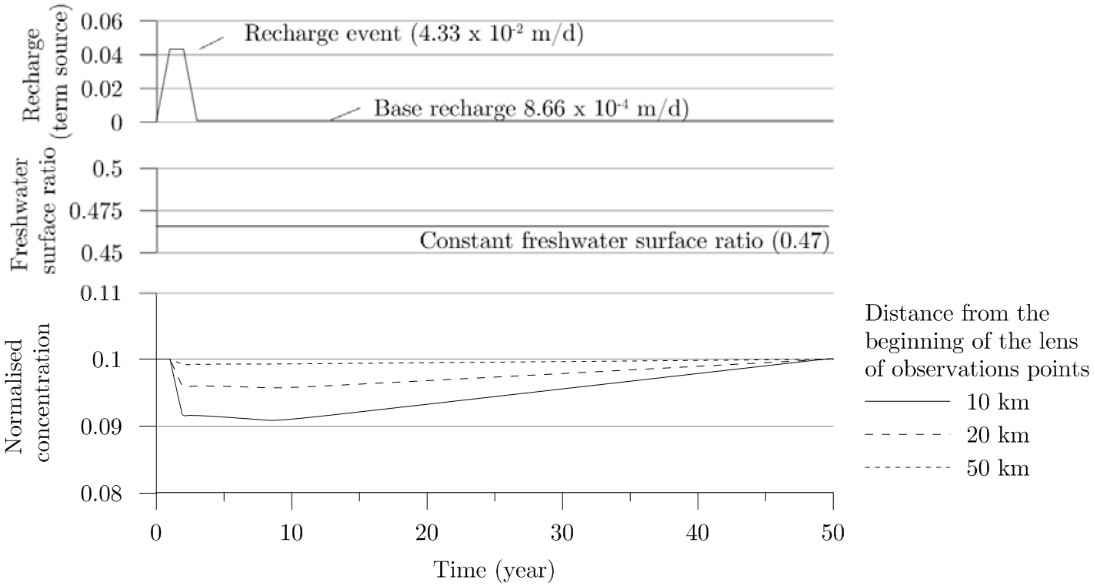

Fig. 4 : Evolution of the freshwater lens with 50-years cyclical recharge. Every 50 years, an equivalent freshwater recharge volume to the "base ponding" recharge of the 50 years is applied. The change on the lens size is not observable. Concentration along the 0.1 concentration line (the limit between the fresh and the brackish water) varies at a distance of 10 km of the beginning of the lens of only 0.01. At a distance of 50 km, no significant variations are observable.

Appendix H

Observations points used for the calibration of the regional numerical model

Location	Groundwater level	Longitude	Latitude	Location	Groundwater level	Longitude	Latitude
Alango	35	609242	10333	Hururu Merti	208.9	474245	171535
Alinugur	20.2	662127	-1929	Ifo2	19.2	645327	13428
Boji	120	514756	151099	Kalakut	87.8	552262	76929
Bule	141	496364	173218	Khot Khot	51.2	613088	70438
Bule 5	162	476529	155307	Korbesa	218	487589	133909
Buna	444.3	525816	308815	Lagh Bogal	107.1	594095	142925
D Galla	213	457536	174540	Liboi	11	708776	39664
Dagahaley	20.5	642330	20010	Madogash	134	520526	80776
Damajale	12.2	699880	11294	Matasadeni	267	436499	152181
Dertu Redcross	56.3	586642	34976	Mathagisse	19.3	658641	18507
Duma	238	445395	189927	Merti	278	462344	116839
El Dera	245	481097	65389	Merti E	231.6	479775	114796
Elan	120	535192	84743	Merti NE	267	467273	118161
Fafi	23.5	645064	-42440	Mochesa	57.8	641939	111790
Fini	49.8	612127	46155	NW Habaswein	110	533870	140641
Galaboba Merti	251	433013	171174	Saretho	31.7	626071	2158
Giriftu	288.9	582795	220340	Sericho C	216	510789	126817
Gurufa	95	548535	88470	Sericho N	214	514997	130663
Habaswein	97.1	553103	114796	Sericho S	149	510429	113714
Hadado	158	546372	169371	Shantabak	58	582795	51445
Hagadera	19.5	652277	956	Wel Merer	13.6	675598	-19479
Hara	77.6	600346	98567				

Coordinates are in the UTM 37N system, based on the WGS 84 geoid.

Appendix I

Transmissivity maps and scatter plots of the regional numerical model

Transmissivity map for the reference model with a diffuse recharge 2 times higher

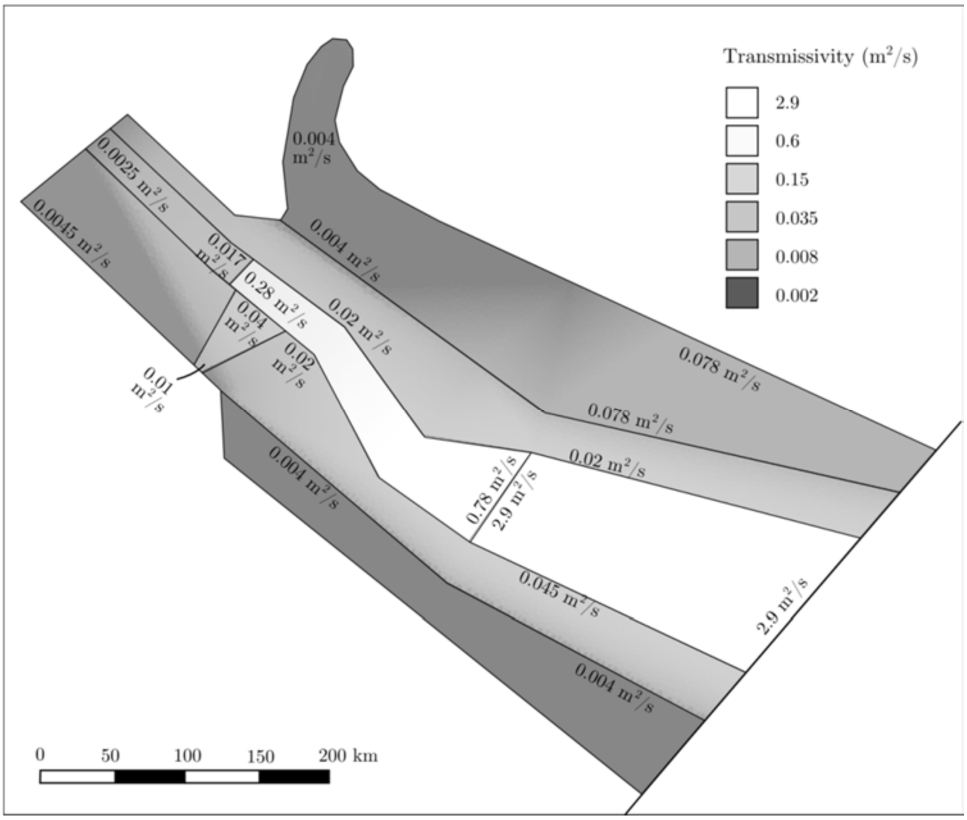

Transmissivity map for the reference model with diffuse recharge two times lower.

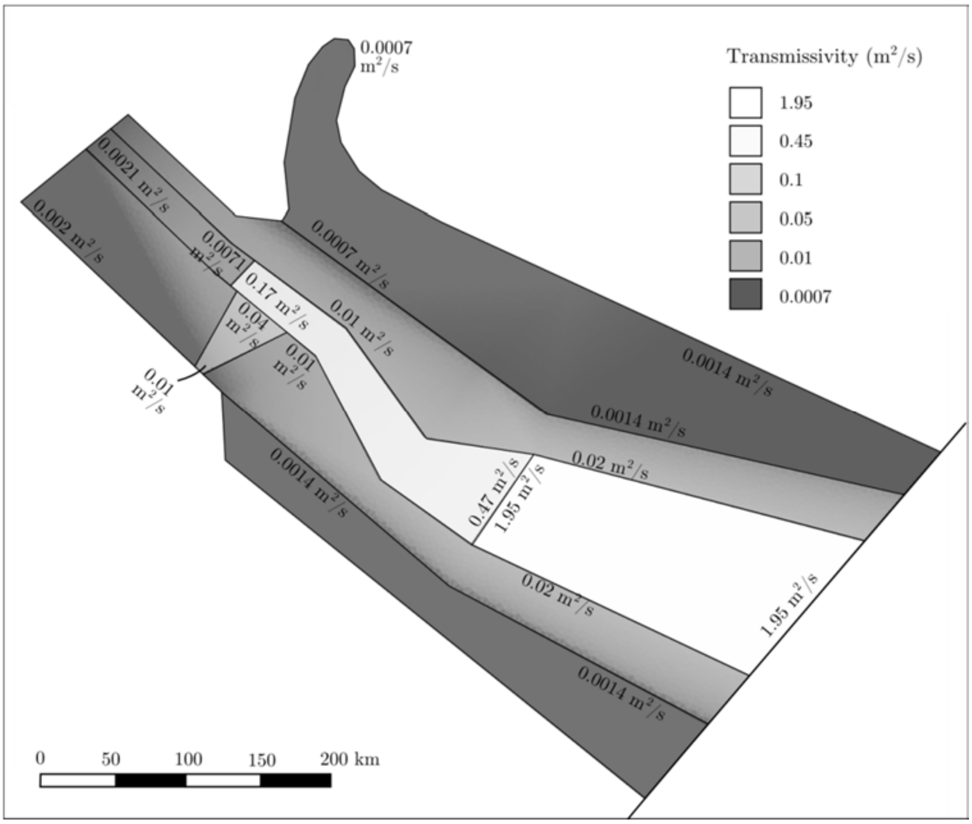

Transmissivity map with the new concentrated recharge area

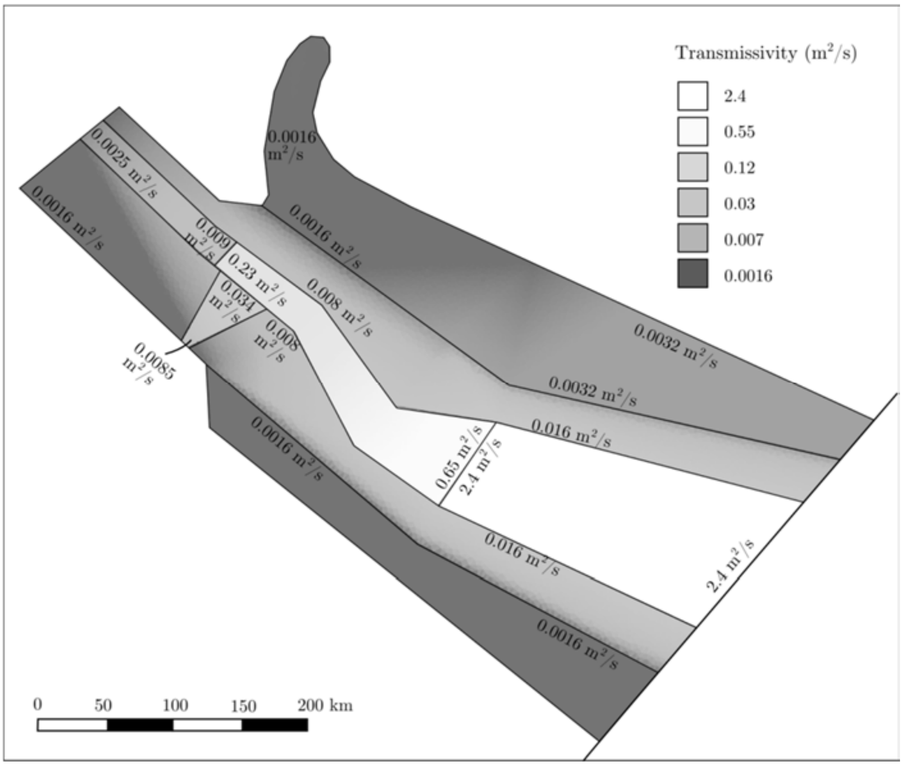

Scatter plot between the observed and simulated hydraulic head for the model with the new concentrated area.

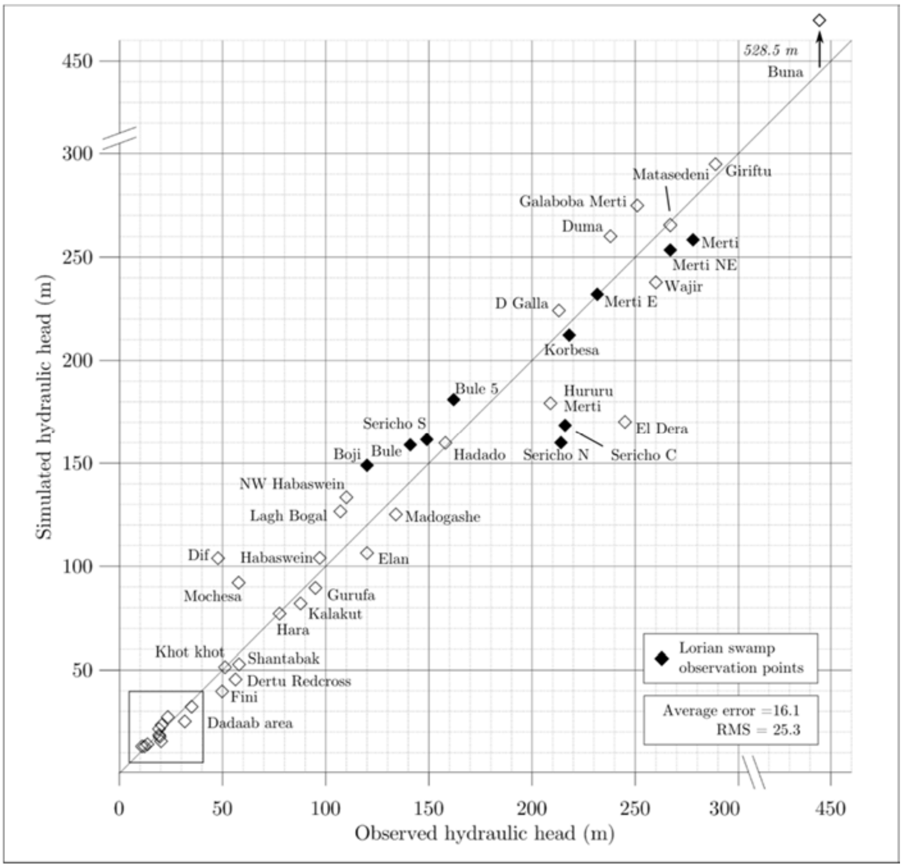

Scatter plot of the inter-aquifer recharge model.